DISSERTATION / DOCTORAL THESIS

Titel der Dissertation/ Title of the Doctoral Thesis

"The Photon as New Physics Messenger:
From the Standard Model to the Dark Sector"

verfasst von/ submitted by

Dipl.Ing. Lukas Semmelrock, BSc

angestrebter akademischer Grad/in partial fulfilment of the requirements for the degree of

Doktor der Naturwissenschaften (Dr. rer. nat.)

Wien, 2020/ Vienna, 2020

Studienkennzahl lt. Studienblatt/ degree programme code as it appears on the student record sheet:	A 796 605 411
Dissertationsgebiet lt. Studienblatt/ field of study as it appears on the student record sheet:	Physik
Betreut von / Supervisor:	Dr. Josef Pradler Univ.-Prof. Dr. André Hoang

Statement of the thesis advisor

I hereby confirm that Lukas Semmelrock has contributed substantially to the following three publications, which are part of his thesis:

[1] X. Chu, J. Pradler and L. Semmelrock, *Light dark states with electromagnetic form factors.* Phys. Rev. D99 (2019) no. 1, 015040, arXiv:1811.04095 [hep-ph].

[2] X. Chu, J.-L. Kuo, J. Pradler and L. Semmelrock, *Stellar probes of dark sector-photon interactions.* Phys. Rev. D100 (2019) no. 8, 083002, arXiv:1908.00553 [hep-ph].

[3] J. Pradler and L. Semmelrock, *Exact Theory of Non-relativistic Electron-Electron Bremsstrahlung.* arXiv:2007.06592 [hep-ph]

According to the common practice in particle physics, the authors are listed in alphabetical order.

Dr. Josef Pradler

Abstract

While gravity is the driving force in the universe—dictating its expansion and forming galaxies under the influence of dark matter—it is electromagnetism that brings information about the universe to us. This thesis studies emission processes induced or mediated by photons as they occur in the scattering of electrically charged particles and may occur in the scattering with dark matter. First, we analyze a dark matter model of light (sub-GeV) particles that are electrically neutral but couple to the electromagnetic current via higher dimensional operators. Such particles—in addition to being dark matter candidates—can potentially alleviate the tension between the measured and predicted value of the magnetic moment of the muon. They can be produced in terrestrial experiments or in stellar objects via bremsstrahlung in collisions of charged particles, allowing us to constrain the parameter space of the model. We show that the parameter space capable of solving the tension of the magnetic moment of the muon is ruled out by experiments. Furthermore, the viability of such particles to make up all of the dark matter in a standard freeze-out scenario is strongly constrained, yet not completely ruled out. Second, we investigate the emission of photons in fermion collisions. We present an analytical calculation of the emission cross-section and energy loss rate for the scattering of two identical non-relativistic charged particles. This calculation is exact to all orders in the Coulomb interaction and closes the gap between the Born and quasi-classical limits. The obtained results are relevant for electron-electron bremsstrahlung in non-relativistic astrophysical environments as well as for dark photon emission in self-interacting dark matter models.

Zusammenfassung

Während die Schwerkraft die treibende Kraft im Universum ist, seine Expansion vorschreibt und unter dem Einfluss Dunkler Materie Galaxien bildet, bringt der Elektromagnetismus diese Informationen über das Universum zu uns. In dieser Arbeit werden durch Photonen induzierte oder vermittelte Emissionsprozesse untersucht, wie sie bei der Streuung elektrisch geladener Teilchen auftreten, aber auch bei deren Streuung mit dunkler Materie auftreten könnten. Zunächst wird ein Modell leichter (sub-GeV) Dunkle-Materie-Teilchen analysiert, die elektrisch neutral sind, aber über höherdimensionale Operatoren an den elektromagnetischen Strom koppeln. Solche Teilchen sind nicht nur Dunkle Materie Kandidaten, sondern können potentiell auch die Diskrepanz zwischen gemessenem und vorhergesagtem Wert des magnetischen Moments des Myons auflösen. Sie können in Experimenten oder in Sternen durch Bremsstrahlung in Kollisionen geladener Teilchen erzeugt werden, was es möglich macht, deren Parameterraum einzuschränken. Es wird gezeigt, dass der Parameterraum, der die Diskrepanz des magnetischen Moments des Myons lösen kann, durch Experimente ausgeschlossen ist. Die Möglichkeit, dass solche Teilchen die gesamte Dunkle Materie ausmachen, ist in einem Standard-Freeze-Out Szenario stark eingeschränkt, jedoch nicht vollständig ausgeschlossen. Weiters wird die Emission von Photonen in Kollisionen von Fermionen untersucht. Eine analytische Berechnung des Emissionswirkungsquerschnitts für die Streuung zwei identischer nicht-relativistischer geladener Teilchen, die exakt in allen Ordnungen in der Coulomb-Wechselwirkung ist und somit die Lücke zwischen Born- und der quasi-klassischer Näherung schließt, wird präsentiert. Die erhaltenen Ergebnisse sind sowohl relevant für Elektron-Elektron-Bremsstrahlung in nicht-relativistischen astrophysikalischen Umgebungen, als auch für die Abstrahlung dunkler Photonen in Modellen selbstwechselwirkender Dunkler Materie.

Acknowledgements

First and foremost, I would like to thank my research supervisor, Josef Pradler, for always having an open door for me and intensively trying to figure out how to solve my problems whenever I got stuck. Thank you for giving me the opportunity to do my PhD in the New Physics group of the Institute of High Energy Physics and for supporting me over the past five years. In addition, I want to thank André Hoang from the University of Vienna for the official university supervision of my thesis.

I am grateful for the people I have met during my studies, Johannes, Thomas, Willi, Matthias, Jakob, Philipp, Andi and Max, who not only made many courses and lunch breaks a lot of fun, but have also become great friends over the years. Thanks to all my colleagues from the Institute of High Energy Physics for many interesting discussions about physics and beyond and for the occasional bouldering session.

I also want to express my gratitude to my parents for encouraging me to study and for listening to my stories of the strange and complex world of physics. Thank you for supporting me in finding my own way. Finally, I want to thank Kathrin for always being there for me, for talking through my day-to-day physics problems with me and lightening my mood whenever I hit bumps on the road. I am especially grateful for you helping me through the challenging final phase of my PhD.

Contents

List of Figures

Preface

This thesis deals with emission processes and how they can be used to test possible implications of dark matter properties, specifically terrestrial, astrophysical and cosmological signatures of light dark particles. It is structured as follows: In Part I, the most important theoretical concepts relevant for this work are presented and an overview of the current experimental status is given. Furthermore, the topics of the publications presented in Part II are introduced and their relation in the context of new physics and dark matter is pointed out.

Part II contains the publications produced during the course of the author's PhD studies. Each chapter shows the publications' status or journal of publication, followed by the original published (or preprint) version. First, Chapter 3 presents two papers which investigate a model of light dark fermions that couple to the standard model photon via electromagnetic form factors. The first publication [1] tests the model with respect to electron accelerator-based experiments, where constraints from existing experiments as well as sensitivity projections for future experiments are derived. In addition, astrophysical and cosmological constraints for this model are investigated, if these light dark fermions make up all of the dark matter in the universe. The second publication [2] extends the model parameter space of interest and tests even lighter dark states via their possible production in stellar objects. In Chapter 4, paper [3] discusses the exact theory of bremsstrahlung in electron-electron collisions, a process which has not been studied in full detail before. The obtained results are interesting for the analysis of photon spectra from electron-electron scattering in non-relativistic astrophysical environments. Additionally, they can also be applied to models of self-interacting dark matter, i.e. dark particles that interact with each other via a light vector mediator.

Part III summarizes the main findings of this thesis. It gives an outlook on work in preparation based on [3], which will be finished after the defense of this thesis. Moreover, the reader is pointed to subsequent work of the co-authors of the publications [1] and [2]. Finally, some additional unfinished efforts of the author of this thesis are mentioned, which have not been published and are detailed in the Appendix.

The Appendix presents more detailed calculations that did not make it into the published version of the publications, but which the author deems instructive to the reader. The sections in the appendix are therefore named analogously to the sections in Part II to emphasize their association with the publications. Additionally, App. C describes some efforts in addition to the ones that lead to the publications in Part II, which were not finished due to numerical issues that could not be resolved before investigations on the same topic were published by another group. They are, however, a fitting addition to the topics regarding self-interacting dark matter discussed in this thesis and therefore shall not go unmentioned.

Part I

Introduction

CHAPTER 1

The need for new physics

The universe we live in can be explained to great detail by two independent theories that produce very accurate predictions on different scales, Quantum Field Theory (QFT) on small scales and General Relativity (GR) on large scales. Even though no unification of these theories has been found to this date, using their machinery to produce models describing how the world works has been proven a tremendous success. Physicists explain the world in terms of *Standard Models* that make predictions of high accuracy and have survived many decades of testing in experiments and astrophysical observations. Here, we will mainly discuss two standard models, namely the *standard model of particle physics* (hereafter standard model or SM) and the *standard model of cosmology* (hereafter standard cosmology or ΛCDM).

The SM is built on the framework of QFT and has been developed over the past century. It explains the smallest constituents of the world we live in, in terms of matter fields (i.e. fermions which can be grouped into quarks and leptons) interacting with each other through force mediators (i.e. gauge bosons). The SM contains four types of fermions, i.e. two quarks and two leptons. These four fermions come in three flavours each, making a total of twelve particles. These twelve particles interact with each other through gauge bosons which can be split into three forces, i.e. the eight gluons that mediate the strong interaction, the $W^{\pm}$ and Z bosons that mediate the weak interaction and the photon that mediates the electromagnetic interaction. A mechanism designed to allow some of the force carriers gain mass, the Higgs mechanism, gives rise to one more boson, the scalar Higgs boson, mediating interactions between massive particles (see left panel of Fig. 1.1 for an overview). Including all fermions, gauge bosons and the Higgs boson, the SM contains 25 particles, all of which have been found and analysed in various ways over the past 100 years. The SM has been studied with unequalled precision by numerous experiments built over the last century—many of which are currently running and have produced an enormous amount of data—which are putting the model's predictions to the test.

The ΛCDM model is the standard cosmological model describing the universe in the framework of GR as an expanding, largely homogeneous and isotropic, space which is currently filled with an energy content of roughly 68% dark energy (Λ), 27% cold collisionless dark matter (CDM) and 5% visible matter [4]. Even though there are many open questions from a bottom up perspective regarding the true physical nature of dark energy (DE) and dark matter (DM), ΛCDM explains—with simple top down assumptions about the two, and utilising our knowledge about the visible matter from the SM—how the universe evolves (see right panel of Fig. 1.1 for an illustration). It started about 13.8 billion years ago with the Big Bang and was presumably followed by a short period of rapid expansion called inflation. After that, the universe was so hot and dense that it was impossible for light to travel through until 379,000 year after the Big Bang when it had cooled down enough for electrons and protons to combine into neutral atoms making it permeable to light. The light from this time of history can still be observed today and is called the *cosmic microwave background* (CMB). From that point on, the universe was dark for hundreds of millions of years until the first stars formed, that during the rest of their lifetime — driven by the movement of dark matter — got arranged into huge structures of galaxies containing billions of stars and planets. Recently, the dark energy has gained more and more importance and has led the universe into an era of accelerated expansion. Given its simplicity, it is amazing how well this model is able to explain phenomena such as the per mille fluctuations in the CMB, the formation of structures like galaxies and stars, as well as the recent onset of accelerated expansion of the universe.

At this point the reader might have been mislead into believing that today's physics is complete and that not much is missing (except perhaps a theory of everything that unifies all we know into one grand theory). However, the SM and ΛCDM are far from the endgame. First of all, they do not fulfil a theorist's wish for simplicity and beauty because some of their features are added in an ad hoc way. The SM has 26 parameters that cannot be predicted by theory and therefore have to be determined from experiments. In addition, some of these parameters are subject to quantum corrections which can be much larger than its original values. In order to "tame" these corrections, some other parameters have to be fine tuned in such a way that they almost exactly cancel the quantum corrections, which is deemed unnatural by many. Similarly, very little is known about the two dominant entities that together make up approximately 95% of the universe's energy content, dark matter and dark energy. They are added to ΛDCM as parameters but no further assumption about their quantum or particle nature is made. Secondly, there are some measurements and observations that seem to be in tension with the predictions from the SM and ΛDCM, like the magnetic moment of the muon [5–8], the proton radius [9–12], anomalies in the decay of rare mesons [13–15] as well as the value of the Hubble constant describing the expansion rate of the universe [4, 16–21] and the density distribution of dark matter on small scales [22, 23], just to name a few. There is still an ongoing debate whether these tensions point to underestimated systematic uncertainties in experiments and observations or to the models being incomplete and needing an introduction of new physics.

In the following, we will explain the concepts of the standard models in particle physics, astrophysics and cosmology and go into detail of some of their shortcomings relevant for this thesis. We will then use these shortcomings as a motivation to introduce new physics models, i.e. new particles that in some way interact with the SM particles, that solve one or a combination of a few of these shortcomings. We will argue that it is desirable to make predictions for new physics models and test them in experiments to narrow down the parameter space of possibilities until nature decides to reveal itself.

1.1 Dark Matter and the Standard Cosmology

To this date, we know very little about the properties of dark matter and dark energy. To leading order, they are parameters in the Friedmann equations, that describe the evolution of the universe in the framework of GR,

$$\left(\frac{\dot{a}(t)}{a(t)}\right)^2 = \frac{8\pi G}{3}\rho(t) - \frac{K}{a(t)^2} + \frac{\Lambda}{3}\,, \qquad \frac{\ddot{a}(t)}{a(t)} = -\frac{4\pi G}{3}\big[\rho(t) + 3p(t)\big] + \frac{\Lambda}{3}\,, \tag{1.1}$$

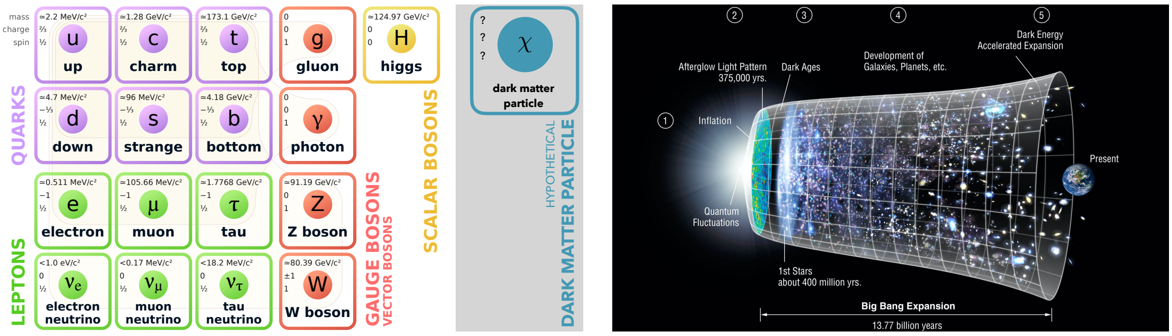

Figure 1.1: *Left:* Table containing all particles and interactions of the standard model of particle physics. The gray shaded area depicts a speculative new particle, which has up to now evaded detection. The figure is adapted from `https://en.wikipedia.org/wiki/Standard_Model`. *Right:* Evolution of the universe in the standard ΛCDM cosmology. Image credit: NASA/WMAP Science Team.

where Λ is the dark energy also known as cosmological constant, K is the curvature of the universe (which observationally seems to be very close to zero although lately there have been reports for a small positive curvature [24]), $\rho = \rho_{SM} + \rho_{DM}$ is the sum of the energy densities of the dark matter and all the standard model particles in the universe and p is the relativistic pressure related to ρ via the equation of state of the particle content. The scale factor $a(t)$ increases as the universe expands and therefore gives a measure of how distances grow.

There is evidence for a non-zero Λ from several independent observations. Historically, the luminosities and redshifts of type Ia supernovae accelerating away from us, was the first probe of dark energy [25–27]. In addition, Λ can also be inferred from CMB data [4, 16] in combination with low redshift measurements of the expansion rate H_0 from, e.g., gravitational lensing [18, 20, 21], distances to red giant stars [19] or gravitational wave events [28]. Other probes of dark energy exist, including Baryon Acoustic Oscillations, weak gravitational lensing and the distribution of galaxy clusters, a discussion of which can be found in Ref. [29] All measurements find an accelerating expansion of the universe pointing to the existence of dark energy. Interestingly, however, there have been recent reports that they disagree on the value of H_0 [30, 31], i.e. measurements that infer H_0 from far away observations, corresponding to the early universe, disagree with the ones that infer it from close-by observations, corresponding to the late universe. This discrepancy could point to some sort of new physics that would change one of the inferred values [32–38] or even alter the model in a way that we cannot speak of a global acceleration anymore [39].

However, we will not go into details about the nature of dark energy here (the interested reader is pointed to the review article [40]). The following sections focus on the nature of dark matter which, in some sense, is a little easier to grasp since it might be similar in nature to the visible matter we know from our day to day life.

1.1.1 Evidence for Dark Matter

Similarly to dark energy, the argument for the existence of dark matter is not only backed by one, but by a multitude of observations as well as a great predictive power regarding the formation and evolution of the universe that comes with it. Since many of the observations are equally important for the argument for the existence of dark matter, we will now list a few of them in chronological order of their discovery following the review article [41].

Velocity Dispersion of Galaxies and Galaxy Clusters. In 1933, the Swiss astronomer Fritz Zwicky published the first article that used the phrase dark matter [42]. Using the virial theorem to calculate the total mass of the Coma galaxy cluster, which to within constants of order unity is

$$M_{\text{vir}} \approx \frac{R}{G} \langle v^2 \rangle \ , \tag{1.2}$$

with R being the cluster radius, G the gravitational constant and $\langle v^2 \rangle$ the mean squared velocity of the observed galaxies, he found that M_{vir} is roughly two orders of magnitude larger than the cluster mass M_{lum} inferred from its total luminosity. Zwicky concluded from this, that there must be some additional dark (non luminous) matter in the cluster attributing for the high velocity of the galaxies. Some similar observations were made in the 1930s [43–45] but not much attention was given to them and the discrepancies were attributed to large measurement uncertainties.

Rotation Curves of Galaxies. Only in the early 1970s, with similar discrepancies arising in the rotation curves [46–49] the opinion of the community shifted because there were two unexplained phenomena—the velocity dispersions of galaxies and galaxy clusters and the rotation curves of spiral galaxies. Both could be explained with the same solution, i.e. the existence dark matter. Explicitly, the problem with the rotation curves of galaxies is that the velocity of stars around the center of the galaxy v as a function of the distance from the center r should be given by

$$v(r) = \sqrt{\frac{GM(r)}{r}} \ , \qquad M(r) = 4\pi \int_0^r \rho(r') r'^2 dr' \ , \tag{1.3}$$

where $\rho(r)$ is the matter density profile and $M(r)$ is the mass within the star's orbit. Therefore, the velocity is expected to decrease with $r^{-1/2}$ beyond a certain radial distance where most of the mass is in the interior and $M(r)$ is constant. Observations, however, pointed to flat rotation curves, i.e. $v(r) = \text{const.}$, suggesting that $M(r)$ was rising with r beyond the point where almost no stars were visible anymore (see left panel of Fig. 1.2 as an example). From this point on this was interpreted by the community as some kind of non-luminous, possibly only gravitationally interacting, matter forming a halo around the galaxy extending beyond the visible galactic disk.

Anisotropies of the Cosmic Microwave Background. The discovery of the CMB in 1964 [50] opened an observational window to the very early universe, i.e. $379,000$ years after the Big Bang, when the universe's temperature had dropped so far that most of the electrons and protons had combined to neutral Hydrogen, ridding the universe of free charged particles and making it translucent. Photons that were set free at this time have been red shifted since then and can be measured today as microwaves with a spectrum corresponding to a

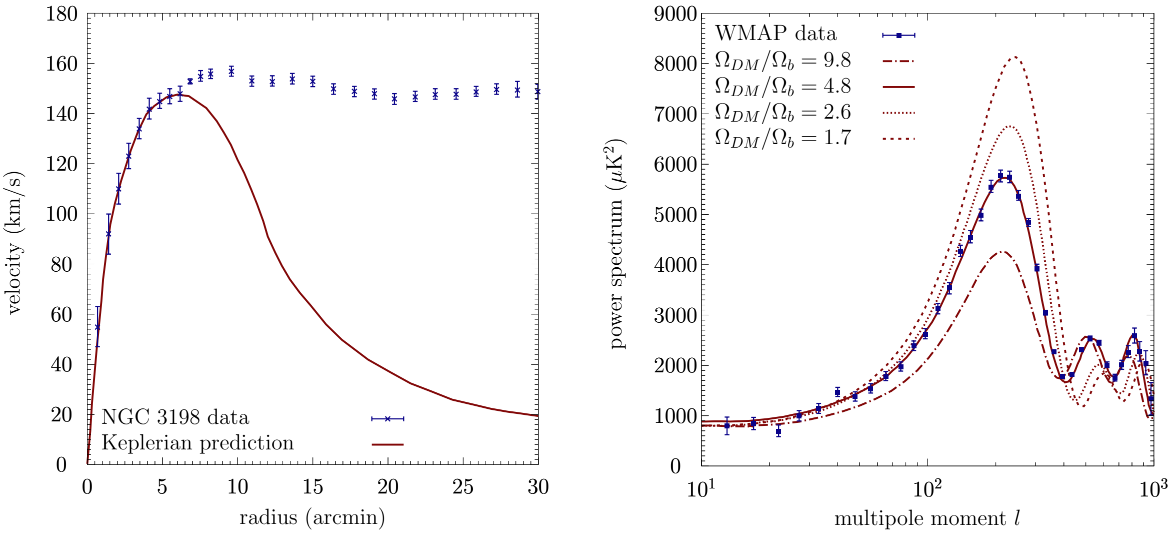

Figure 1.2: Evidence for dark matter from rotation curves (left) and the CMB power spectrum (right). The figures are reproduced from [53].

black body radiation with a temperature of 2.725(48) K. From the early 2000s onward, the satellite telescopes WMAP [51] and its successor Planck [52] started picking up on small fluctuations in the CMB temperature, depending on the position in the sky. The reason for these fluctuation are matter density fluctuations at the moment of recombination. The CMB photons that were emitted in an over-density, had to climb out of a deeper gravitational well than the photons that were emitted in an under-density. Therefore the former have a slightly lower energy (or temperature) than the latter when measured today. The magnitude of these fluctuations are a direct probe of the fraction of the universe that is made up of dark matter, since their formation is suppressed by radiation pressure building up in standard matter but not present in dark matter. The density fluctuations are usually analyzed by looking at the power spectrum of the CMB, i.e. the Fourier components of the spatial correlations of the temperature fluctuations, as shown in the right panel of Fig. 1.2 where the theoretical power spectrum is shown for four different ratios of the dark matter vs. baryon density with the best fit to WMAP data at $\Omega_{DM}/\Omega_b \approx 4.8$ [53].

Gravitational Lensing. Since the formulation of Einstein's general theory of relativity, it is known that mass bends light, or—more precisely—mass curves space-time and light moves in the latter on the shortest path between points. If light from a faraway source traverses a massive halo on its way to us, it gets bent in the gravitational field of the halo. Therefore, the image of the original source gets distorted. The magnitude of the distortion can then be used to calculate the mass of the halo. The mass of the luminous matter can be deduced from its total luminosity. The difference between the two is the amount of dark matter in the observed halo. Depending on the mass and size of the traversed halo, as well as the distance to the source, the techniques to derive the dark matter content are very different (the interested reader is pointed to the review article [54]). One of the most famous observations, where evidence for dark matter was found through gravitational lensing, is the Bullet cluster [55, 56]. It owes its fame to the fact that its observation did not only give direct evidence for dark matter but also allowed for the derivation of an upper limit on possible dark matter self-interactions, which will be mentioned in Sec. 1.2.2.

1.1.2 Shortcomings of the Cold Collisionless Dark Matter Paradigm

Cold collisionless dark matter (CDM) seems to explain many observations we make about our universe very well, with a multitude of hints for its existence, as summarized in the previous section. In addition, starting in the 1990s, numerical N-body simulations [57] of the universe were made, where gravitationally interacting clumps of matter were set into an expanding volume to study structure formation. These simulations usually start out with a random gaussian field of matter over- and under densities in the early universe which get amplified and evolve into the structures we can see today. Surprisingly, even with very simple Newtonian dynamics and no other SM physics added, one of the first big simulation projects that simulated a volume with the size of the universe, the Millenium simulation [58–60], yielded tremendous results which matched observations of large scale structure in the universe very well.

In later simulations, e.g. the Illustris simulation [61–63], additional processes, like black hole and star formation, supernovae, magnetic fields etc. were taken into account. These effects are not added on a particle physics level, but through simplified models which can be handled by the simulations. Still, adding all the above improved the simulations a lot and made them more realistic in many aspects.

It turns out, however, that while the simulations agree with observations very well on large scales, i.e. on scales larger than Mpc, there seem to be discrepancies between the two on galactic and sub-galactic scales, i.e. on scales smaller than Mpc. The discrepancies between N-body simulation and observations on small scales have been coined the four unsolved problems of structure formation in the universe. They involve the density distribution of dark matter halos, where structures of ordinary matter are embedded in and can be observed via gravitational effects on the latter. These unsolved problems will be discussed in the following.

Missing Satellite problem. In early N-body simulations, it was found that halos with a similar mass to the Milky Way host a large number of satellite halos, only a fraction of which were found by observations looking for satellite galaxies of the Milky Way [64–66]. Since galaxies of luminous matter are expected to be hosted by halos of dark matter, the numbers were expected to coincide. More satellite galaxies have been found by optical surveys over time and it was also soon realized that the neglected baryonic physics in early simulations might alter the density distribution of dark and luminous matter [67, 68]. In this context supernova explosions, for example, lead to an outward particle flux and can possibly strip a small galaxy of a fraction of its luminous matter. More recent simulations, like the Illustris simulation mentioned above, have taken baryonic physics into account to some extend and found that the discrepancy in missing satellites decreases and the problem is possibly alleviated by baryonic physics.

Too big to fail problem. The second problem of small structures emerged briefly after the missing satellite problem. In the context of the missing satellite problem, it was argued that the large number of satellite halos in simulations might be so small, that they fail to host visible galaxies because their gravitational potential is not large enough to attract enough luminous matter. However, it was found that simulations also predict a number of larger satellite galaxies, which are "too big to fail" to host stars [69, 70]. The simulations predicted a number of very massive satellite halos, which should find their counterparts in massive satellite galaxies in our local group. But comparing the masses of these halos from simulations and galaxies from observations, leads to a discrepancy. Therefore, this problem was named the too big to fail problem and is closely related to the missing satellite problem.

Cusp vs Core problem. Like the previous problems of small structures in the universe, the cusp vs. core problem [71] is related to the density distribution of dark matter at small scales. Navarro, Frenk and White (NFW) identified that the halos in N-body simulations followed a specific radial density distribution [72]

$$\rho(r) = \frac{\rho_0}{\frac{r}{r_s}\left(1 + \frac{r}{r_s}\right)}, \tag{1.4}$$

where r_s is the scale radius and $\rho_0/4$ the density at the scale radius which are parameters that vary from halo to halo. This profile is called the NFW profile and stands for the generic behavior of halo densities in N-body simulations. The density in an NFW profile scales as $1/r^2$ for large radii and as $1/r$ in the central region. This $1/r$ behavior of the density at the center is usually referred to as a cuspy density profile. Observations, however, seem to indicate an approximately constant dark matter density profile $\rho(r) = \text{const.}$ in the inner parts of galaxies, which is referred to as a cored density profile.

Diversity problem. The diversity problem was only found recently and stands out a bit with respect to the former three. It was shown in Ref. [73] that the inner rotational velocity profiles of dwarf galaxies can be very diverse even though their masses are similar. In other words, small galaxies which are expected to have similar density distributions, in fact have very different ones. At first sight, this seems to be a much more complicated problem than the previous three, since the other problems are always related to some kind of "mass deficit" at small scales with respect to simulations, whereas in the diversity problem this is more complex and cannot simply be relegated to missing mass.

Still, all the above mentioned problems can be resolved with a single solution, the introduction of self-interactions between dark matter particles. These self-interactions, which were first introduced in Ref. [74] to solve the cusp vs. core problem, lead to a momentum transport to the central regions of dark matter halos. In recent simulations, see e.g. Refs. [75–77], it was shown that dark matter self-interactions lead to a decrease in small structures, meaning they can also solve the too big to fail and missing satellite problem (some halo projections for visualization of the structure suppression from Ref. [77] are shown in Fig. 1.3). In addition, recently Ref. [78] numerically analysed halo formation with self-interacting dark matter using a simple model. They found that self-interactions lead to a large spread in rotational velocities for dwarf galaxies similar to the observed galaxies that have caused the diversity problem. They conclude that the diversity problem can, as well, be solved by dark matter self-interactions. Some further details of self-interacting dark matter will be discussed in Sec. 1.2.2.

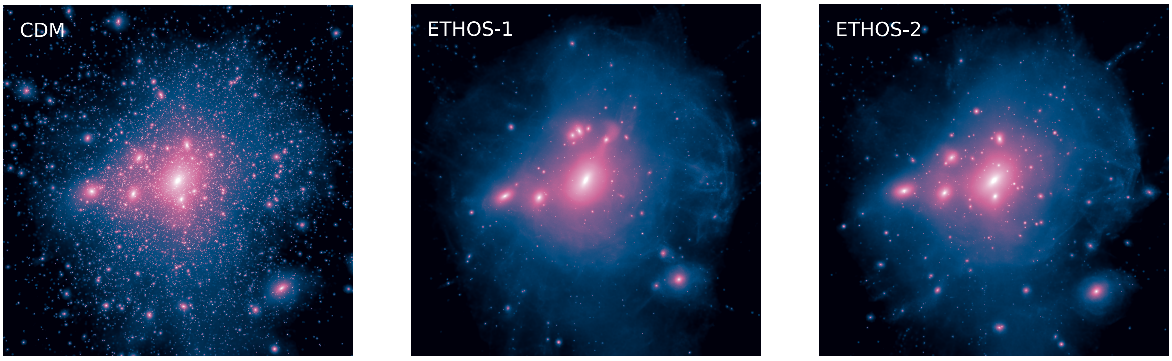

Figure 1.3: Galaxy simulated with an N-body simulation [77] with the standard non-interacting cold dark matter (left) and with self-interacting dark matter with larger (center) and (smaller) coupling. The larger the self-coupling, the more small scale structure ist washed out.

1.2 Dark Matter Interactions

All properties of dark matter that we have deduced so far are inferred from the gravitational effect it has on the structures we see. We know that for ΛCDM to work, dark matter has to behave like matter, i.e. its density has to scale with the scale parameter as $\rho_{\mathrm{DM}} \propto a^{-3}$. Since the world we know and perceive is made up of standard model particles, very well described by the framework of QFT, it stands to reason that dark matter is also made up of particles, similar to the ones we already know.

From a particle physics perspective, however, we know very little about dark matter. If dark matter is made up of particles, the imminent questions arise, do dark matter particles have interactions other than gravity, like SM particles have? Do they interact in some way with the standard model? Do they interact with themselves? These questions are largely unanswered to this date, but there are some hints that a self-interaction of dark matter particles might be favored while a huge parameter space of interactions with the standard model is already excluded. In the following, we will give a short overview of the current experimental and observational status.

1.2.1 Dark Matter Interactions with the Standard Model

The only way we can be able to detect dark matter in particle physics experiments, is if dark matter interacts with the standard model via an additional force apart from gravity. While gravity is the driving force on large scales, this is only the case because stellar objects, galaxies and galaxy clusters, are electrically neutral overall. For a single charged particle, the gravitational force is about 38 orders of magnitude smaller than the electromagnetic force.

In the spirit of "looking under the lamp post", there are dozens of dedicated particle physics experiments trying to find such an additional interaction between dark matter and the standard model. There are three orthogonal ways of testing DM-SM interactions, i.e. direct detection (DM+SM $\to$ DM+SM), indirect detection (DM+DM $\to$ SM+SM) and production (SM+SM $\to$ DM+DM). Direct detection experiments, like XENON [79], DAMA/LIBRA [80], CRESST [81] just to name a few, are looking for nuclear (or electron) recoils from dark matter particles present in our galaxy hitting a target material in the experimental setup. In this kind of setup, the dark matter particle has to deposit a minimum amount of energy to the target material in order for the recoil to be registered by the detector. Therefore, direct detection is especially well suited for heavy dark matter with masses larger than roughly a few GeV. However, more recent experiments using semi-conductor technology, like SENSEI [82, 83], can test DM masses down to 500 keV. Indirect detection experiments, on the other hand, try to find dark matter signals by analyzing the SM particle flux hitting earth. Examples for indirect detection experiments are the earth based imaging atmospheric Cherenkov telescopes MAGIC [84], HESS [85] and VERITAS [86], the satellite based γ-ray telescope Fermi-LAT [87] or the charged-particle detectors PAMELA [88] and AMS [89]. Finally, dark matter can be produced in particle accelerators, if more energy than the dark matter mass is set free in the collision. Examples are collider experiments such as BaBar [90], Belle [91], ATLAS [92], CMS [93], or fixed target experiments such as NA64 [94], mQ [95] or COHERENT [96]. Dark matter particles are usually looked for by analysing all final states produced in the collisions in a detector. Since it is assumed that the DM-SM interactions is so weak that the DM particles leave the detector without a signal, one can look for missing energy or missing momentum in a certain direction by reconstructing the process.

Up to now, most of the experiments above have reported only negative results and were able to constrain the parameter space of dark matter mass and coupling strength to the standard model. There have been some experiments, however, reporting an excess of data above the expected background. One heavily disputed report of a signal is the one by DAMA/LIBRA [97, 98] claiming to see a signal in the region of parameter space which other experiments have already constrained. Experiments are being set up to this date, that try to use the same detector material as DAMA/LIBRA to cross check their result, e.g. SABRE [99] which is set up on the southern hemisphere in order to crosscheck possible seasonal effects as well. Moreover, the AMS-02 spectrometer at the international space station has measured an unexpected positron flux [100, 101], which allows for a dark matter interpretation. Very recently, the XENON-1T collaboration has announced an excess in nuclear recoils at small energies [102], which lines up in a history of previous excesses.

1.2.2 Dark Matter Self-Interactions

Apart from interactions with SM particles, dark matter particles could also have self-interactions. As mentioned above, they were first hypothesized in Ref. [74] to solve the cusp vs. core and missing satellite problems. Dark matter self-interactions lead to a momentum transfer from the inner to the outer regions of dark matter halos and therefore suppress the formation of small scale structures. One can get a rough estimate of the self-interacting dark matter (SIDM) cross section needed for this mechanism to work by calculating the local collision rate in a dwarf halo [103],

$$R_{\mathrm{scatt}} = \frac{\sigma_{\mathrm{SI}}\, v_{\mathrm{rel}}\, \rho_{\mathrm{DM}}}{m_{\mathrm{DM}}} \approx 0.1\ \mathrm{Gyr}^{-1} \times \left(\frac{\rho_{\mathrm{DM}}}{0.1\ \mathrm{M}_\odot/\mathrm{pc}^3}\right)\left(\frac{v_{\mathrm{rel}}}{50\ \mathrm{km/s}}\right)\left(\frac{\sigma_{\mathrm{SI}}/m_{\mathrm{DM}}}{1\ \mathrm{cm}^2/\mathrm{g}}\right), \tag{1.5}$$

with σ_{SI} being the self-interaction cross section, v_{rel} the relative velocity, ρ_{DM} the dark matter density and m_{DM} the dark matter mass. In order to have an effect on the halo, approximately one scattering event per Hubble time should occur. Hence, the cross section per unit mass must have a value of $\sigma_{\mathrm{SI}}/m_{\mathrm{DM}} \approx 1\ \mathrm{cm}^2/\mathrm{g}$. In the literature, a cross section between 0.1 and

1 cm^2/g at dwarf galaxy scales is often assumed to test the parameter space of SIDM models where the small structure problems are solved, see e.g. [104, 105]. A cross section of this size is comparable to the electron Thomson scattering cross section, which is huge compared to weak scale interactions like the DM-SM cross sections looked for in DM direct detection experiments.

There are, however, also constraints on the magnitude of the self-scattering cross section of DM from astrophysical observations. The Bullet cluster—which was already mentioned previously as an observation that supplied evidence for the existence of dark matter—is an important observation in the context of dark matter, because it also gives an upper bound on the self-interaction cross section [106]. The upper bound derived from the Bullet cluster is also roughly 1 cm^2/g. Due to the constraints on the cross section on cluster scales, where DM particles collide at a typical velocity of $v_{\rm rel} \approx 1000$ km/s and the necessity of having a large cross section at dwarf scales with typical velocities of $v_{\rm rel} \approx 50$ km/s to solve the small structure problems, SIDM models often incorporate velocity dependent cross sections. Simple particle physics models, that yield velocity dependent cross sections—with a large cross section at small velocities and vice versa—are models with light mediator particles. With light mediators, the cross section scales as $v_{\rm rel}^{-4}$ in the kinematic regime, where the typical momentum transfer between the colliding particles is larger than the mediator mass and is constant in $v_{\rm rel}$ if the typical momentum transfer is smaller. Recently, velocity dependent cross sections were also studied in simulations [77], comparing several models and investigating the extent to which they suppress small scales. In addition to the $v_{\rm rel}^{-4}$ velocity scaling which yields large cross sections at small velocities, resonance effects can enhance the cross section in certain kinematic regimes by several orders of magnitude [104].

In conclusion, one may say that light mediator models work very well in evading constraints at cluster scales while solving the small structure problems at small scales. However, if the mediator particle has a mass $m_{\rm med} < \mu v_{\rm rel}^2/2$, μ being the reduced mass of the colliding particles, the mediator can be emitted in collisions leading to the fact that the DM halo dissipates energy. In the publication [3] in Ch. 4, we present the exact calculation of a photon emission process, which is relevant for the SM photon, but can also be applied to SIDM models with a dark photon mediator. In these models, the emission of the dark photon can counteract the solution to the small structure problems determined by elastic processes, which will be discussed in Sec. 2.2.

1.3 The Standard Model of Particle Physics and Beyond

In the previous sections, we have motivated the necessity of dark matter and—under the premise of its existence—laid down the shortcomings of a CDM model. Moreover, we motivated why it is reasonable to describe dark matter as a particle and look for it in experiments and astrophysical signatures. This section shall be dedicated to shortcomings of the standard model of particle physics. According to Occam's razor, a superior model is one that explains the most with simple assumptions. In this spirit, it seems natural to look for a particle dark matter model that also tackles shortcomings of the SM. This is the motivation for dark matter models discussed in Ch. 3. A compilation of anomalies in the standard model, that might hint to new physics is outlined in Ref. [107] and we briefly summarize them here (in alphabetical order and not ordered in terms of apparent severeness; we base this summary on the anomalies deemed most intriguing in Ref. [107]).

B-anomalies. The standard model of particle physics predicts that the couplings of leptons to all types of gauge bosons is independent of the flavor (e, μ, τ) of the lepton. This is a cornerstone of the SM and is confirmed in many experiments. However, in measurements of B-meson decays into leptons, it seems that this universality is violated with a 2–3σ deviation from the standard model prediction [108].

Beryllium anomaly. Experiments in the Atomki facility have found an excess of e^+e^- emission at large angles between e^+ and e^- from excited Beryllium [109] and Helium [110] decays with respect to the SM prediction. A new heavy boson, was hypothesized as a possible solution to this excess [109–111].

Cooling anomaly. Several observations show that stellar objects cool slightly faster than expected [112, 113]. Stellar objects that allow for such observations are horizontal branch and red giant stars, white dwarfs, as well as the supernova SN1987A and neutron stars. New particles that can be emitted inside the stellar objects and freely stream out, like axions or sterile neutrinos, can contribute to the energy loss of the star and therefore lead to faster cooling [114].

γ-ray transparency. There are more high-energy γ-rays from extra-galactic sources than expected. These γ-rays should be depleted through annihilations into e^+e^--pairs, when they propagate through the universe. However, this depletion mechanism does not seem to be as efficient as predicted. Again this could be explained by axion models, which allow for a conversion back into photons [114].

Magnetic moment of the muon. The anomalous magnetic moment of the muon, or short $(g-2)_\mu$, is a quantity that can be calculated with very high precision in the standard model. Currently the most precise QFT calculation of $(g-2)_\mu$ takes into account corrections up to 5-loop order in quantum electrodynamics (QED) and the predicted value is precise to 9 digits [115]. In addition, it can be measured very precisely, the best measurement to this date stems from the Brookhaven experiment [116], but much anticipated upcoming experiments [117, 118] will further weigh in on the anomaly in the near future. To this date, there is a tension of 3.7σ between the predicted and measured value. New particles that couple to the SM can give loop corrections to the muon's magnetic moment and therefore there are particle dark matter models that can alleviate this tension [119–122].

For all of the above anomalies, different extensions of the SM can alleviate the tensions. However, it is very difficult to find one easy solution, that explains all tensions. In Ch. 3, we will motivate a model of dark states that might be able to solve the $(g-2)_\mu$ anomaly and test its viability as a dark matter candidate. These dark states can also be produced in stellar objects, yielding a possible solution to the stellar cooling anomaly.

CHAPTER 2

Probing the known and unknown

After summarizing some of the shortcomings of the standard model of particle physics and the standard cosmological model as well as introducing the possibility for dark matter particles to interact with the standard model particles or with themselves in ways other than via gravity in the previous chapter, we will now discuss more specifically, how dark matter models can be tested. We will focus on emission processes—induced or mediated by the SM or dark photon—through which dark states can be produced. We will take the concepts introduced in Ch. 1 and introduce the topics discussed in the publications in Part II of this thesis.

2.1 Light dark particles - the unexplored regime

For dark matter particles heavier than roughly 1 GeV, the best constraints on various models come from direct detection experiments. For lighter (i.e. sub-GeV) dark matter, direct detection experiments that search for DM-nucleus scattering are stretched to their limits due to the fact that these experiments look for recoils from dark matter particles in our galaxy hitting the nuclei of their target material. The Milky Way has an escape velocity of 550 km/s while our solar system has a circular velocity in the galaxy of roughly 220 km/s. Hence, dark matter bound to the Milky Way can hit earth with a maximum velocity of the sum of the above, i.e. 770 km/s. The maximum recoil energy a light dark matter particle with mass $m_{\rm DM}$ can transfer to a nucleus at rest with mass m_N, if $m_{\rm DM} \ll m_N$, is

$$E_R^{\rm max} = \frac{m_{\rm DM} v_{\rm lab}^2}{2} \approx 3~{\rm keV} \times \left(\frac{v_{\rm lab}}{770~{\rm km/s}}\right)^2 \left(\frac{m_{\rm DM}}{1~{\rm GeV}}\right), \tag{2.1}$$

with the velocity of dark matter as measured on earth $v_{\rm lab}$ which we have set to its maximum possible value. In order for the experiment to be able to detect the recoil, its threshold energy has to be larger than the maximum recoil energy, i.e. $E_{\rm th} < E_R^{\rm max}$. Thus, for smaller $m_{\rm DM}$ the constraints from direct detection experiments get weaker, because fewer events are expected until $E_R^{\rm max} < E_{\rm th}$ where the constraints vanish completely. By looking at electron recoils, however, the maximum recoil energy in Eq. (2.1) is set by the electron mass and velocity instead, allowing to probe smaller DM masses [123–125]. In many of the more conventional models DM shares interactions with both nucleons and electrons, but there are models where DM only interacts with one of the above [126, 127].

Particle accelerators where DM can be tested by producing it in collisions, however, have difficulties with large $m_{\rm DM}$. Here, the DM particle can only be produced if the energy set free in the collision is larger than the dark matter mass. Therefore, accelerator experiments are especially well suited for searches for light dark matter particles.

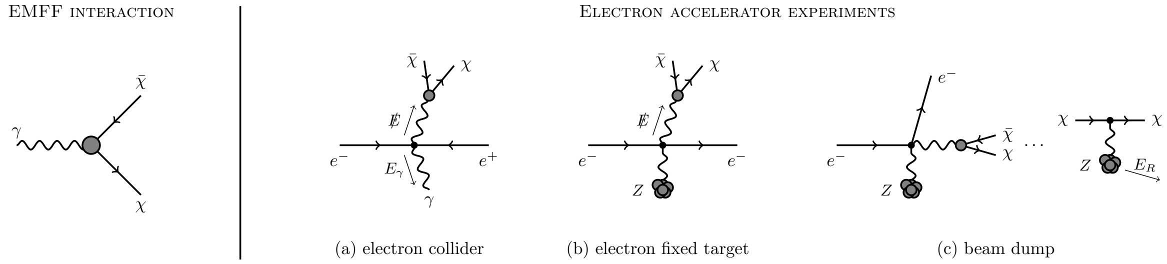

Figure 2.1: *Left:* Vertex depicting the coupling of dark states χ to the SM photon via electromagnetic form factor interactions. *Right:* Types of electron accelerator experiments to test electromagnetic form factor interactions of dark states. The three types discussed in this thesis are (a) electron colliders such as BaBar and Belle II, (b) fixed target experiments such as NA64 and LDMX and (c) beam dump experiments such as mQ and BDX.

In the following, we will introduce a model of light (sub-GeV) dark fermions χ, which can be tested with particle accelerators. These fermions couple to the photon via electromagnetic form factors, the vertex of which is shown in the left panel of Fig. 2.1. These models are analysed in Ch. 3. The electromagnetic form factor coupling of χ to a single photon A_μ can be written as $\bar{\chi}\Gamma^\mu\chi A_\mu$, where the vertex function can be split into a parity-even and a parity-odd part,

$$\Gamma^\mu_{\text{even}} = F_E(q^2)\gamma^\mu + iF_M(q^2)\sigma^{\mu\nu}q_\nu \qquad \text{(P-even)}, \tag{2.2a}$$
$$\Gamma^\mu_{\text{odd}} = F_A(q^2)(q^2\gamma^\mu - q^\mu \not{q})\gamma^5 + iF_D(q^2)\sigma^{\mu\nu}q_\nu\gamma^5 \qquad \text{(P-odd)}. \tag{2.2b}$$

Here, q is the ingoing photon momentum, γ the Dirac gamma matrix, $\sigma^{\mu\nu} = \frac{i}{2}[\gamma^\mu, \gamma^\nu]$ and the functions $F(q^2)$ are electromagnetic form factors. Assuming that χ is electrically neutral, in the static limit the form factors yield the magnetic and electric dipole moment, the anapole moment and the charge radius,

$$\mu_\chi = F_M(0), \quad d_\chi = F_D(0), \quad a_\chi = F_A(0), \quad b_\chi = F_E(0). \tag{2.3}$$

As mentioned in Sec. 1.3, these models can potentially solve the $(g-2)_\mu$ anomaly since the χ-particles can give loop contributions to the respective Feynman diagrams. The lowest-order contribution to $(g-2)_\mu$ enters through the vacuum polarization diagram, Fig. 9b in [1], where χ is in the loop of the internal photon line.

The couplings in Eq. (2.3) can be tested by terrestrial experiments or astrophysical observations, where a $\chi\bar{\chi}$-pair is produced via emission of a SM photon in the collision of charged particles. In the following, we give an introduction to the main ideas of testing these electromagnetic form factor couplings, which are discussed in more detail in the publications [1] and [2].

2.1.1 Production of particle-pairs in electron-accelerators

One promising way of producing a particle carrying one or more of the electromagnetic form factors in Eq. (2.2) is in high intensity electron beam facilities. There are three main types of experiments, that can test the models discussed in this thesis, which are outlined in the right panel of Fig. 2.1.

First, in electron-positron collider experiments, like BaBar or Belle II, two photons can be produced in the collision of electrons and positrons, one of which is detected while the other one produces an $\chi\bar{\chi}$-pair (as shown in Fig. 2.1a). This process can be analyzed by looking for mono-photon signals and missing energy in the detector. Second, in electron fixed target experiments, like NA64 or LDMX, electrons hit the nuclei of a traget material and emit a pair of dark states mediated by a photon in the process (as shown in Fig. 2.1b). Here the electron can lose energy by emitting dark states, so again we look for missing energy in the detector. In this case, the electron can also lose energy by inelastically scattering on the nucleus, but this would produce hadronic events in the detector which can be vetoed. Third, in beam dump experiments, like mQ and BDX, dark states can be produced as before by scattering on nuclei. In this case, however, all SM particles are stopped by a thick layer of gravel and there is a detector several dozens of meters away from the collision site, where the produced dark states can be detected via elastic scattering on nuclei (as shown in Fig. 2.1c).

In publication [1] in Ch. 3, we test the electromagnetic form factors outlined above with data from the electron beam facilities Babar, NA64 and mQ and show sensitivity projections for the recently started experiment Belle II, and the upcoming LDMX and BDX. Furthermore, we show constraints from SM precision observables and investigate the possibility of particles with electromagnetic form factors making up all of dark matter. A thorough derivation of the phase space integral for $\chi\bar{\chi}$-production in electron fixed target experiments is shown in App. A.

2.1.2 Production of particle-pairs in stellar objects

Aside from accelerator experiments, a $\chi\bar{\chi}$-pair can also be produced in stellar objects, like the sun, horizontal branch (HB) and red giant (RG) stars and supernovae (SN). The χ-particles can be produced via plasmon decay, e^+e^--annihilation, $2 \to 3$ Compton scattering, electron bremsstrahlung and nucleon bremsstrahlung, as depicted in Fig. 2.2. The dark particles then stream or diffuse out of the stellar environment and carry away energy leading to anomalous energy loss in addition to the energy loss from SM processes.

Constraints can be set on anomalous energy loss channels because they would alter certain stellar observables [112]. In the sun, for example, the emission of χ-particles would alter nuclear fusion rates which are inferred through the measurement of the solar neutrino flux. A constraint in HB stars can be derived, because anomalous energy loss would shorten their helium burning lifetime altering the observed number ratio of HB and RG stars. Moreover, in RG stars the core mass before helium burning—which can be deduced from the RG's luminosity since in this phase of stellar evolution the luminosity is determined almost entirely by the core mass—gets altered if energy is emitted via χ-pairs. Finally, in supernovae, anomalous energy loss quenches neutrino emission. Since there has only been one nearby supernova in history where the neutrino flux was observed with a sparse amount of data, i.e. SN1987A, one can only use very conservative constraints on the anomalous energy loss. Often the Raffelt criterion [112] is used requiring that the total dark particle luminosity is smaller than the total neutrino luminosity.

While stars have a core temperature of $\mathcal{O}$(keV), and can therefore only test models of dark states up to masses of around this scale, supernovae have temperatures of $\mathcal{O}$(MeV) and can

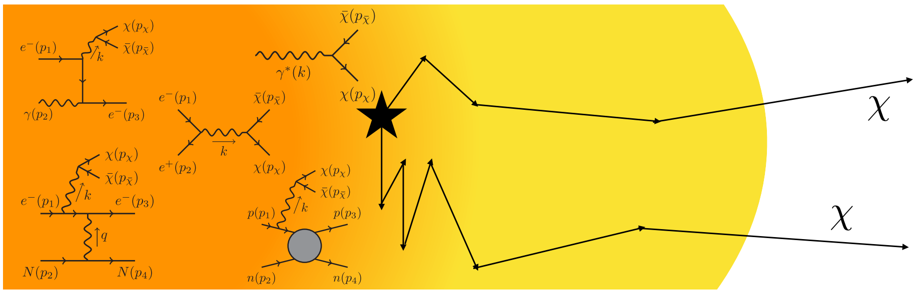

Figure 2.2: Production of dark states χ in the stellar object depicted by the yellow/orange shaded region. The dark states then stream or diffuse out of the stellar object and thereby contribute to anomalous energy loss and induce a feedback altering the rate of SM processes inside the stellar object.

therefore produce heavier particles. We investigate the production of $\chi\bar{\chi}$-pairs in the above environments in publication [2] in Ch. 3.

2.2 (Dark) photon emission

After analyzing the emission of a pair of dark states mediated by a photon, we want to turn our attention to emission processes of a photon or of a dark photon—without attaching a pair of dark states to the external photon line. Such bremsstrahlung processes are of ample importance in astrophysics as they are a dominant channel of energy loss in many systems and therefore play a key role in the cooling of stellar objects [112]. Moreover, they are the main source of diffuse X-rays emitted from galaxy clusters [128]. In self-interacting dark matter models with a light dark photon mediator, the dark photon can be emitted as bremsstrahlung in collisions, as already mentioned in Sec. 1.2.2. In this case the emission process leads to energy loss in the dark sector, which—depending on its magnitude—can have very interesting implications for cosmology and structure formation [129–145], like the formation of dark discs or dark clumps due to cooling.

Dark matter needs to move at non-relativistic speeds early in the universe's history in order to form structures and bind the luminous matter to its gravitational potential. In addition, many astrophysical environments that can be observed today, e.g. a hot galaxy cluster gas, have a temperature low enough for SM particles to move non-relativistically. Therefore we put our focus on a non-relativistic description of the scattering processes making it possible to treat the problem in an exact way, as will be outlined in the following.

2.2.1 Scattering with light mediators

Light mediators give rise to velocity dependent elastic scattering cross sections. In order for perturbative calculations to be possible, the interaction has to be weak and/or short ranged. To be more precise, the condition for calculating the cross section to lowest order in perturbation theory (left diagram in Fig. 2.3) is $m_{\rm med}/(\mu v_{\rm rel}) \ll 1$, where $m_{\rm med}$ is the mediator mass and μ and $v_{\rm rel}$ are the reduced mass and relative velocity of the colliding particles respectively. If this condition is not fulfilled, i.e. the potential is not short ranged, perturbative calculations are still valid if $\alpha Z_1 Z_2/v_{\rm rel} \ll 1$, where α is the coupling strength and $Z_{1,2}$ are the charges of the colliding particles. The transfer cross section $\sigma_T = \int d\Omega\,(1-\cos\theta)\,d\sigma/d\Omega$ valid, in both the above regimes (hereafter subsumed as Born regime), for a scalar or vector mediator perturbative in α and in the non-relativistic limit is given by [104]

$$\sigma_T^{\rm Born} = \frac{2\pi\alpha^2 Z_1^2 Z_2^2}{\mu^2 v_{\rm rel}^4}\left[\ln\left(1+\frac{4\mu^2 v_{\rm rel}^2}{m_{\rm med}^2}\right) - \frac{4\mu^2 v_{\rm rel}^2}{m_{\rm med}^2 + 4\mu^2 v_{\rm rel}^2}\right], \tag{2.4}$$

which, as already mentioned in Sec. 1.2.2, scales as $v_{\rm rel}^{-4}$ in the kinematic regime, where the typical momentum transfer between the colliding particles is larger than the mediator mass and is constant in $v_{\rm rel}$ if the typical momentum transfer is smaller.

In dark matter scattering, as well as in the scattering of standard model particles in astrophysical environments where the relative velocity of the colliding particles is small, the Born conditions above are not necessarily fulfilled. In this case, the leading order perturbative calculation is not valid anymore and the full calculation would involve the resummation of an infinite number of diagrams of the kind in Fig. 2.3b. Equivalently, one can go to a non-relativistic ansatz and calculate the scattering cross section to all orders in the scattering potential (see e.g. [146]). For scalar or vector mediator particles the scattering potential is given by the Yukawa potential

$$V(r) = \frac{\alpha Z_1 Z_2}{r} e^{-m_{\rm med} r}, \tag{2.5}$$

where $r = |\boldsymbol{r}|$ is the inter-particle distance. In QED $\alpha \approx 1/137$ is the fine structure constant and $m_{\rm med} = 0$ the photon mass, whereas in SIDM models the dark coupling and charges as well as the mediator mass can be free parameters that are possibly constrained by observations, like the Bullet cluster mentioned above. The sign of the potential in Eq. (2.5) is determined by the relative sign of the couplings (or charges) of the scattering particles. Ref. [104] has numerically evaluated the elastic scattering cross section away from the Born regime by solving the Schrödinger equation corresponding to the potential (2.5) in a partial wave decomposition and summing up all partial waves until convergence is reached. They found that the cross section shows a resonance behavior for attractive interactions with large enhancements with respect to the Born cross section at the resonances. An obvious extension of this kind of calculation is to go from the spin-independent Yukawa interaction to spin-dependent interactions induced by, e.g., pseudo scalar or axial vector mediators. The author of this thesis has worked on this topic until he was outpaced by others [147] and a compilation of the corresponding work is attached in App. C.

If the mediator is light enough, i.e. $m_{\rm med} < \mu v_{\rm rel}^2/2$, the mediator particle can be emitted as bremsstrahlung during the collision, as depicted in Fig. 2.3c. In this case, the exponential term in Eq. (2.5) can be neglected. This can be seen by evaluating the potential at the distance r, which equals the de Broglie wavelength of the relative motion. This is the typical distance tested in collisions of two colliding particles. Since $m_{\rm med} \ll \mu v_{\rm rel}$ for $v_{\rm rel} \ll 1$, the interaction is in this case effectively a Coulomb interaction.

2.2.2 Bremsstrahlung in a Coulomb potential

For Coulomb interactions, the scattering problem can be solved analytically—exact to all orders in the potential. For elastic scattering, the exact cross section is given by the Ruther-

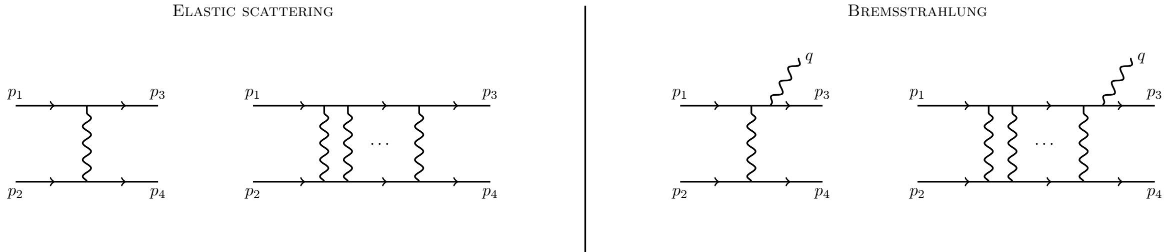

(a) perturbative (b) non-perturbative (c) perturbative (d) non-perturbative

Figure 2.3: Scattering (left) and emission (right) processes relevant for self-interacting dark matter as well as bremsstrahlung in standard model scattering events. In the Born limit, perturbative calculations (a) and (c) are valid while beyond the Born limit, resummation techniques have to be used to sum up an infinite number of diagrams of the kind (b) or (d) respectively.

ford cross section (and a symmetrized version of it for identical particle scattering; see e.g. Ref. [148]). For bremsstrahlung, we can treat the particle emission perturbatively with an emission operator $\hat{\mathcal{O}}_{\text{emm}} \propto e^{-i\boldsymbol{q}\cdot\boldsymbol{r}_n}$ stemming from the photon wave function with momentum $\boldsymbol{q}$ and the scattering particles' positions $\boldsymbol{r}_n$, while we treat the particle interaction in an exact manner. The matrix element for the emission of bremsstrahlung is given by

$$\mathcal{M} = \sum_{I=\text{multipoles}} \langle \chi_{\boldsymbol{p}_f} | \hat{\mathcal{O}}_I | \chi_{\boldsymbol{p}_i} \rangle, \tag{2.6}$$

where $\chi_{\boldsymbol{p}_{i,f}}$ are the ingoing (outgoing) wave function solutions to the Schrödinger equation of the relative motion with the respective scattering potential. The initial (final) state particles have the relative momentum $\boldsymbol{p}_{i,f}$. The operator $\hat{\mathcal{O}}_I$ originates from the multipole expansion of $\hat{\mathcal{O}}_{\text{emm}}$. The dipole and quadrupole emission cases assemble themselves through the respective leading and next-to-leading order terms in said expansion. Using for $\chi_{\boldsymbol{p}_{i,f}}$ in Eq. (2.6) the first order Born wave functions,

$$|\chi^{(1)}_{\boldsymbol{p}_{i,f}}\rangle = |\chi^{(0)}_{\boldsymbol{p}_{i,f}}\rangle + \int \frac{d^3p}{(2\pi)^3} \frac{\langle \chi^{(0)}_{\boldsymbol{p}} | \, \hat{V} \, | \chi^{(0)}_{\boldsymbol{p}_{i,f}} \rangle}{E_{i,f} - E_{\boldsymbol{p}}} \, |\chi^{(0)}_{\boldsymbol{p}}\rangle \,, \tag{2.7}$$

where $\chi^{(0)}_{\boldsymbol{p}_{i,f}}$ and $\chi^{(0)}_{\boldsymbol{p}}$ are plane waves, one obtains an expression valid in the Born limit, which can also be obtained from the Feynman diagrammatic perturbative calculation. We show this calculation in App. B.1.

Starting from Eq. (2.6) and taking for $\chi_{\boldsymbol{p}_{i,f}}$ the ingoing and outgoing Coulomb wave functions with the correct asymptotic behavior, which in position space read [149]

$$\chi^{(+)}_{\boldsymbol{p}_i}(\boldsymbol{r}) = \Gamma\left(1 - i\nu_i\right) \, e^{\frac{\pi}{2}\nu_i} e^{i\boldsymbol{p}_i\cdot\boldsymbol{r}} \, {}_1F_1(i\nu_i, 1; i(p_i r - \boldsymbol{p}_i\cdot\boldsymbol{r})) \,, \tag{2.8}$$

$$\chi^{(-)}_{\boldsymbol{p}_f}(\boldsymbol{r}) = \Gamma\left(1 + i\nu_f\right) \, e^{\frac{\pi}{2}\nu_f} e^{i\boldsymbol{p}_f\cdot\boldsymbol{r}} \, {}_1F_1\big(-i\nu_f, 1; -i(p_f r + \boldsymbol{p}_f\cdot\boldsymbol{r})\big) \,, \tag{2.9}$$

the emission cross section can be calculated in an exact way. Here, $p_{i,f} = \mu v_{i,f}$ are the initial (final) state relative momenta with $\nu_{i,f} = \alpha Z_1 Z_2 / v_{i,f}$. This was done for dipole emission in Ref. [150]. We extend this calculation to quadrupole emission—including the scattering of identical particles—in publication [3] in Ch. 4. For this calculation, the analytical solution to the following integral over the hypergeometric functions,

$$\mathcal{I}_N = \int d^3r \frac{e^{-\lambda r}}{r} e^{i\boldsymbol{k}\cdot\boldsymbol{r}} {}_1F_1\Big(i\nu_f, 1, i(p_f r + \boldsymbol{p}_f \cdot \boldsymbol{r})\Big) {}_1F_1\Big(i\nu_i, 1, i(p_i r - \boldsymbol{p}_i \cdot \boldsymbol{r})\Big), \tag{2.10}$$

and derivatives thereof are used. The solution to $\mathcal{I}_N$, originally found by Ref. [151], is sketched in App. B.2.

Part II

Publications

CHAPTER 3

Terrestrial and stellar probes of dark sector-photon interactions

Light dark states with electromagnetic form factors

Xiaoyong Chu, Josef Pradler and Lukas Semmelrock

Published in: Physical Review D 99 (2019) no.1, 015040

Preprint version: arXiv:1811.04095 [hep-ph]

Stellar Probes of dark sector-photon interactions

Xiaoyong Chu, Josef Pradler, Jui-Lin Kuo and Lukas Semmelrock

Published in: Physical Review D 100 (2019) no.8, 083002

Preprint version: arXiv:1908.00553 [hep-ph]

Light dark states with electromagnetic form factors

Xiaoyong Chu,[1,*] Josef Pradler,[1,†] and Lukas Semmelrock[1,2,‡]
[1]*Institute of High Energy Physics, Austrian Academy of Sciences, Nikolsdorfergasse 18, 1050 Vienna, Austria*
[2]*Department of Physics and Astronomy, Johns Hopkins University, 3400 N. Charles St., Baltimore, MD 21218, USA*

(Received 19 November 2018; published 31 January 2019)

New particles χ that are electrically neutral but couple to the electromagnetic current via higher-dimensional operators and that are sufficiently light, at or below the GeV-mass scale, can be produced in pairs in a number of dedicated high-intensity experiments. In this work we consider the production of χ through magnetic- and electric-dipole moments as well as through an anapole moment and charge radius interactions in electron beams. We derive new constraints from *BABAR*, NA64 and mQ and forecast the future sensitivity on the existence of such states, from Belle-II, LDMX and BDX. We present for the first time a detailed treatment of the off shell production of photons in electron beams with subsequent decay into a $\chi\bar{\chi}$ pair in a 2-to-4 process. These direct limits are then compared to the effects on SM precision observables, as well as to bounds from flavor physics and high energy colliders. Finally, we consider the possibility that χ is dark matter and study ensuing astrophysical and cosmological constraints. We find that a combination of all considered probes rule out χ particles with mass-dimension five and six photon interactions as dark matter when assuming a standard freeze-out abundance.

DOI: 10.1103/PhysRevD.99.015040

I. INTRODUCTION

Through a long history of astronomical and cosmological observations that date back into the first half of the previous century, it has now firmly been established that Newton's laws—when applied to the observed distribution of luminous matter—fail on galactic (kpc) length scales and beyond. Whereas there is an ongoing debate whether the gravitational force on small acceleration scale requires modification or if the Standard Model (SM) of particle physics is incomplete, predictions that are based on the existence of a new, neutral, and cold matter component stand unchallenged in explaining the precision observations of the cosmic microwave background (CMB). Indeed, the success of a model in which the Universe is filled with baryons, photons, neutrinos, dark matter (DM), and dark energy is so distinct that it has become a cornerstone of modern physics, termed the "standard cosmological model" or ΛCDM [1,2]. This new paradigm that purports the existence of a new form of matter, dark matter, has become the center of much experimental and theoretical activity [3].

Even if gravity as it stands today will pass the test of time, new forces are likely at play in a dark sector of particles. While the electromagnetic interaction and the photon as its carrier stand out as the most important messengers in astronomy, dark matter—as the name suggests—must be to a large degree electrically neutral and hence be nonluminous. However, even if DM carries no charge, it may still be coupled to the photon e.g., through various moments such as magnetic- or electric-dipole moments (MDM or EDM), through an anapole moment (AM) or through a charge radius interaction (CR). Indeed, "how dark" neutral DM needs to be in terms of its coupling to photons is a quantifiable question that has been addressed previously in Refs. [4–6]. In this work we will revisit those ideas in light of the much recent interest in sub-GeV dark sector searches, notably at the intensity frontier [7,8]. This interest not only spans DM detection, but more generally aims to probe light new particles and in this spirit we do not require that χ is DM *per se* but only long-lived on timescales pertinent to terrestrial experiments.

In this paper we shall consider Dirac fermions χ that interact with an external electromagnetic field or current through MDM, EDM, AM and CR. In the nonrelativistic limit, the corresponding respective Hamiltonian operators for the particle χ are $\mathcal{H}_{\rm MDM} = -\mu_\chi(\boldsymbol{B}\cdot\boldsymbol{\sigma}_\chi)$, $\mathcal{H}_{\rm EDM} = -d_\chi(\boldsymbol{E}\cdot\boldsymbol{\sigma}_\chi)$, $\mathcal{H}_{\rm AM} = -a_\chi(\boldsymbol{J}\cdot\boldsymbol{\sigma}_\chi)$ and $\mathcal{H}_{\rm CR} = -b_\chi(\boldsymbol{\nabla}\cdot\boldsymbol{E})$.

*xiaoyong.chu@oeaw.ac.at
†josef.pradler@oeaw.ac.at
‡lukas.semmelrock@oeaw.ac.at

We will refer to μ_χ, d_χ, and a_χ as the magnetic dipole-, electric dipole-, and anapole moment, respectively, and to b_χ as the charge radius. These operators differ most notably in the symmetry properties with respect to space reflection (P), charge conjugation (C), and time reversal (T). Since the magnetic field $\boldsymbol{B}$ and the spin $\boldsymbol{S}_\chi = \boldsymbol{\sigma}_\chi/2$ are axial vectors, an MDM interaction is P- and T-even. Hence CP is a good symmetry, and, as is inherent in the field-theoretical description of particles, any state χ that has electromagnetic charge Q_χ will automatically carry a magnetic moment $\boldsymbol{\mu} = gQ_\chi/(2m_\chi)\boldsymbol{S}_\chi$ with $g = 2$ up to anomalous contributions; m_χ is the mass of χ. In turn, any EDM interaction with the electric field $\boldsymbol{E}$ maximally violates P and T and is a new source of flavor-diagonal CP violation—one that has not been observed in any SM particle yet. Hence, searches for EDMs are considered essentially "background free" probes of new physics [9] and any detection of a dark particle through its EDM would be particularly striking. If χ has a nonvanishing anapole moment, it will interact with external electromagnetic currents $\boldsymbol{J}$; in that case χ may even be a Majorana particle. Unlike MDM and EDM, AM does not correspond to a multipolar distribution of charge. It was first proposed by Zel'dovich [10] as a P-violating (but CP conserving) electromagnetic interaction, and has since been discovered in atomic nuclei [11]. Finally, the CR interaction appears at the second order in the expansion of a charge form factor, and as such it is a quantity e.g., well present in composite particles of the SM, and it is a searched for property of neutrinos [12]. Its transformation property with respect to discrete symmetries is one of a scalar.

The effective interactions of neutral χ with the photon field may arise in a variety of UV-complete descriptions. An imminent possibility is that χ is a composite particle so that a dipole moment arises through the particle's internal structure, such as, e.g., in technicolor theories [13–15]. Another possibility are frameworks with an extended set of particles such that electromagnetic moments are produced perturbatively, by the loops of charged states [16]. Here, a sizable MDM can be generated e.g., through axial or vector type Yukawa interactions $y_{A,V}$ with a scalar and a fermion at a common mass scale M in the loop, so that parametrically $\mu_\chi \sim Q|y_{A,V}|^2/M$ where Q is the electric charge of the mediators. The appearance of an EDM would then of course be tightly connected to CP violation in the new physics sector and $d_\chi \sim Q\mathrm{Im}[y_V y_A^*]/M$. Finally, AM and CR interactions may also arise radiatively; in the above example, a_χ, $b_\chi \sim Q|y_{A,V}|^2/M^2$, possibly be enhanced through a DM-mediator mass-degeneracy [17]. Indeed, a significant amount of attention has been directed to the phenomenology of those interactions, see also Refs. [18–22] besides the above mentioned works and references therein. In this work, we shall remain agnostic about the origin of the MDM, EDM, AM and CR of χ. While any embedding into a concrete setup likely implies further constraints on the existence of the effective values of μ_χ, d_χ, a_χ and b_χ, this way we remain model independent.

Much of the effort on the intensity frontier goes into the search of light, sub-GeV mass dark sector states. New particles can be produced in electron or positron beams on fixed targets, at e^+e^- colliders, in hadron beams from protons on fixed targets or in proton-proton collisions at LHC. Here, much attention has been devoted to the on shell or the s-channel resonant production of particles that either decay to electrons or muons inside the sensitive detector volume or escape or decay invisibly. A prominent example is the search for dark photons [23–26] in fixed target experiments, e.g., at APEX [27] or NA48/2 [28] and at e^+e^- colliders, e.g., at *BABAR* [29] just to name a few; for a recent comprehensive compilation see Ref. [30].

In this work we study the pair production of $\chi\bar{\chi}$ through the MDM, EDM, AM and CR interaction with photons in experiments involving *electrons* as projectiles. For dark sector experiments, there are three principal detection methods:

(1) search for missing momentum in e^+e^- colliders such as *BABAR* [31], Belle [32], Belle-II [33] and BESIII [34],
(2) search for missing energy in e^- fixed-target experiments such as NA64 [35] and the proposed LDMX detector [36],[1]
(3) direct search for χN or χe^- scattering of χ particles produced in e^- fixed-target experiments such as the previous mQ [40] detector and E137 at SLAC [41], as well as the proposed beam dump experiments at JLab (BDX) [42] or at the MESA accelerator [43].

We consider all three detection methods in turn, work out current constraints and estimate future sensitivity. As the production in fixed targets proceeds via the emission of off shell photons, we also present a detailed exposition of the underlying 2-to-4 scattering processes, thereby filling a gap in the existing literature on beyond Standard Model intensity frontier searches.

We then contrast these direct limits with predictions and constraints from SM precision observables and from limits originating from flavor physics. The experimental searches for dark states on the intensity frontier have in no little part been motivated by the observation that light new physics can induce a shift in the anomalous magnetic moment of the muon, see e.g., [44–47] among other works, and hence explain a long-standing discrepancy between the SM prediction and experiment [48]. We investigate this possibility in the light of dark-sector electromagnetic form factors and finally, we return to the possibility that χ is cosmologically long-lived and may constitute dark matter. In this case, further restrictions on the parameter space of

[1] In an analogous category, positron fixed-target experiments include PADME [37] and VEPP-3 [38,39].

χ from cosmological and astrophysical observations take hold—such as energy injection to the SM sector, altering the CMB or influencing structure formation, as well as a local dark matter abundance that could lead to direct and indirect detection signals.

The paper is organized as follows. In Sec. II we present the relativistic versions of the interaction operators for MDM, EDM, AM and CR. In Sec. III we present our cross section calculations on the production of $\chi\bar{\chi}$ in e^+e^- collisions as well as e^--scattering on a nuclear target with details relegated to Appendix A. In Sec. IV we then specialize to the various experiments, work out constraints and sensitivity projections and discuss other complementary probes. In Sec. V we discuss indirect probes of χ-particles and in Sec. VI we comment on the possibility that χ is DM and highlight the additional restrictions on a successful model of DM. In Sec. VII we present our conclusions and provide an outlook to further going works.

II. ELECTROMAGNETIC FORM FACTOR INTERACTIONS

We consider the following interaction terms in a Lagrangian of a Dirac fermion χ that interacts with the photon gauge field A_μ or its field strength tensor $F_{\mu\nu}$,

$$\text{millicharge}\,(\epsilon\mathrm{Q}):\quad +\epsilon e\bar{\chi}\gamma^\mu\chi A_\mu, \tag{1a}$$

$$\text{magnetic dipole}\,(\mathrm{MDM}):\quad +\frac{1}{2}\mu_\chi\bar{\chi}\sigma^{\mu\nu}\chi F_{\mu\nu}, \tag{1b}$$

$$\text{electric dipole}\,(\mathrm{EDM}):\quad +\frac{i}{2}d_\chi\bar{\chi}\sigma^{\mu\nu}\gamma^5\chi F_{\mu\nu}, \tag{1c}$$

$$\text{anapole moment}\,(\mathrm{AM}):\quad -a_\chi\bar{\chi}\gamma^\mu\gamma^5\chi\partial^\nu F_{\mu\nu}, \tag{1d}$$

$$\text{charge radius}\,(\mathrm{CR}):\quad +b_\chi\bar{\chi}\gamma^\mu\chi\partial^\nu F_{\mu\nu}. \tag{1e}$$

Here $e>0$ is the electric charge,[2] μ_χ and d_χ are the dimensionful coefficients of the mass-dimension-5 dipole interactions, and a_χ and b_χ are the dimensionful coefficients of the mass-dimension-6 anapole moment and charge radius interaction; as usual, $\sigma^{\mu\nu}=\frac{i}{2}[\gamma^\mu,\gamma^\nu]$. In what follows we shall measure the EDM and MDM moments in units of the Bohr magneton, $\mu_B \equiv e/(2m_e) = 1.93\times 10^{-11}\ e\,\mathrm{cm}$; m_e is the mass of the electron. All coupling strengths are real.

The interactions in Eq. (1) are assembled in the matrix element of the effective electromagnetic current of χ,

$$\langle\chi(p_f)|J^\mu_\chi(0)|\chi(p_i)\rangle = \bar{u}(p_f)\Gamma^\mu(q)u(p_i), \tag{2}$$

where $p_{i,f}$ and $q=p_i-p_f$ are four-momenta. For a neutral particle χ the vertex function reads,

$$\Gamma^\mu(q) = (q^2\gamma^\mu - q^\mu\not{q})[V(q^2)-A(q^2)\gamma^5] + i\sigma^{\mu\nu}q_\nu[M(q^2)+iD(q^2)\gamma^5]. \tag{3}$$

We regard the various moments as being generated at an energy scale that is well above the typical center-of-mass (CM) energies of the high-intensity beams. The coefficients in Eq. (1) are hence the static limits of the form factors above,

$$\mu_\chi = M(0),\qquad d_\chi = D(0),\qquad a_\chi = A(0),\qquad b_\chi = V(0).$$

A millicharged particle χ will have an additional form factor $Q(q^2)\gamma^\mu$ with $Q(0)=\epsilon e$. The next term in the q^2-expansion of $Q(q^2)$ is then the charge radius interaction and the equivalence with $V(0)$ above can be seen when the Dirac equation is applied for on shell χ, $\bar{u}(p_f)(q^2\gamma^\mu - q^\mu\not{q})u(p_i) = \bar{u}(p_f)q^2\gamma^\mu u(p_i)$. As should be clear from above, an electric charge of χ is not mandatory for χ to possess CR interactions, and we shall consider both interactions separately below. We note in passing that the Dirac and anapole form factors $V(q^2)$ and $A(q^2)$ are related to the so-called vector and axial vector charge radii as $\langle r_V^2\rangle = -6V(0)$ and $\langle r_A^2\rangle = -6A(0)$.

Finally, in addition to the operators listed above, at mass-dimension-7 there are the Rayleigh (or susceptibility) operators where scalar $\bar{\chi}\chi$ or pseudoscalar $\bar{\chi}\gamma^5\chi$ bilinears multiply either the CP-even or CP-odd squared field strength tensors $F_{\mu\nu}F^{\mu\nu}$ and $F_{\mu\nu}\tilde{F}^{\mu\nu}$. Such terms imply two-photon interactions with the χ-field and processes with a single photon in the final state proceed through a loop. In the processes arising from Eq. (1) that we shall consider in the paper, the latter interactions are then not only suppressed by the higher dimensionality of the coupling, but also by a loop factor. As the constraints on dim-6 operators already turn out to be weak, we shall not consider Rayleigh operators any further in this work.

III. PAIR PRODUCTION IN ELECTRON BEAMS

In this section we present the main expressions that are used to set bounds on new particles χ interacting through electromagnetic form factors. These involve the calculation of the $\chi\bar{\chi}$ pair production cross section, first, from e^+e^- annihilation accompanied by initial state radiation as shown in Fig. 1(a) and, second, from Bremsstrahlung in the scattering of electrons on nuclear targets as shown in Fig. 1(b). They are the dominant production modes in *BABAR* or Belle II and in NA64, LDMX, mQ or BDX, respectively. Finally, since mQ and BDX search for new particles via their elastic scattering within the detector, Fig. 1(c), we furthermore establish the nuclear and electron recoil cross sections in χ-scattering.

[2] The sign convention in (1a) is such that χ ($\bar{\chi}$) carries a fraction ϵ of the electron (positron) charge.

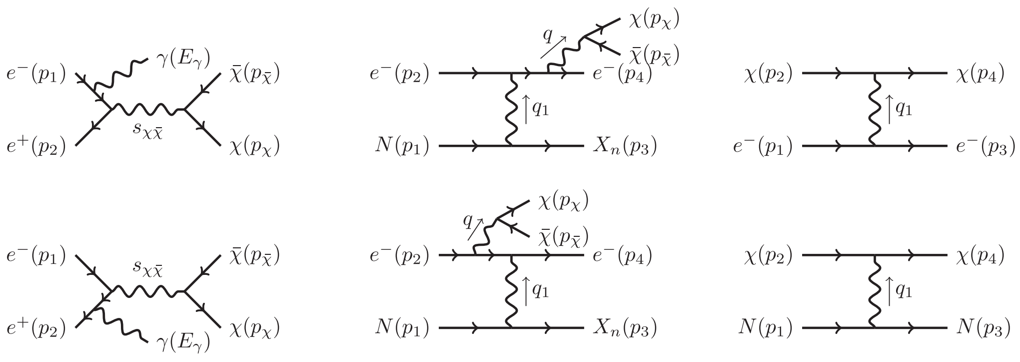

FIG. 1. Pair production of $\bar{\chi}\chi$ in (a) e^+e^- collisions and (b) in electron scattering on a target nucleus N. The mQ and BDX experiments search for (c) the elastic scattering of χ on electrons and nuclei. Momenta flow from left (bottom) to right (top).

A. Pair production at e^+e^- colliders

In B-factories such as *BABAR*, Belle, and Belle II, fermion pairs can be produced in e^+e^- collisions accompanied by initial state radiation (ISR). Production in association with final state radiation (FSR) is suppressed with respect to ISR by ϵ^2 for ϵQ and scales as $\mu_\chi^2 s/(4\pi\alpha) \sim (10^4\mu_\chi/\mu_B)^2$ for MDM and EDM. For the values of μ_χ and d_χ that are constrained through ISR by the various considered experiments, this gives a suppression of 10^{-1} and smaller for FSR with MDM and EDM interactions. For AM and CR, the FSR diagrams vanish identically at tree level. Therefore, we are allowed to neglect FSR and only consider $\chi\bar{\chi}$ production with associated ISR. Finally, monophoton resonant production through a putative process $\Upsilon(nS) \to \gamma\gamma^* \to \gamma\chi\bar{\chi}$ vanishes by Furry's theorem since $\Upsilon(nS)$ are C-odd states.

The ISR cross section approximately factorizes into the process without ISR, $e^+e^- \to \bar{\chi}\chi$, times the improved Altarelli-Parisi radiator function that takes into account all soft and collinear radiative corrections up to order m_e^2/s [49,50],

$$\frac{d\sigma_{e^+e^-\to\chi\bar{\chi}\gamma}}{dx_\gamma d\cos\theta_\gamma} = \sigma_{e^+e^-\to\chi\bar{\chi}}(s, s_{\chi\bar{\chi}})\mathcal{R}^{(\alpha)}(x_\gamma, \theta_\gamma, s) \tag{4}$$

with the radiator function

$$\mathcal{R}^{(\alpha)}(x_\gamma, \theta_\gamma, s) = \frac{\alpha}{\pi}\frac{1}{x_\gamma}\left[\frac{1+(1-x_\gamma)^2}{1+\frac{4m_e^2}{s}-\cos^2\theta_\gamma} - \frac{x_\gamma^2}{2}\right]. \tag{5}$$

Here, $x_\gamma = E_\gamma/\sqrt{s}$ is the energy fraction carried away by the ISR, $\sqrt{s} \simeq 10$ GeV and $\sqrt{s_{\chi\bar{\chi}}}$ are the CM energies of the e^+e^- and $\chi\bar{\chi}$ system, respectively, with $s_{\chi\bar{\chi}} = (1-x_\gamma)s$; θ_γ is the CM angle of the ISR photon. The χ-pair production cross section without ISR reads

$$\sigma_{e^+e^-\to\chi\bar{\chi}} = \frac{\alpha}{4}\frac{f(s_{\chi\bar{\chi}})}{s_{\chi\bar{\chi}}^2}\left(1+\frac{2m_e^2}{s}\right)\sqrt{\frac{s_{\chi\bar{\chi}}-4m_\chi^2}{s-4m_e^2}}. \tag{6}$$

Here, $f(s_{\chi\bar{\chi}})$ is the squared amplitude of $\gamma^* \to \chi\bar{\chi}$, integrated over the 2-body phase space of the fermion pair, as defined in (C7b). This factor will appear repeatedly and reads,

$$\epsilon\text{Q}:\ f(s_{\chi\bar{\chi}}) = \frac{4}{3}\epsilon^2 e^2 s_{\chi\bar{\chi}}\left(1+\frac{2m_\chi^2}{s_{\chi\bar{\chi}}}\right), \tag{7a}$$

$$\text{MDM}:\ f(s_{\chi\bar{\chi}}) = \frac{2}{3}\mu_\chi^2 s_{\chi\bar{\chi}}^2\left(1+\frac{8m_\chi^2}{s_{\chi\bar{\chi}}}\right), \tag{7b}$$

$$\text{EDM}:\ f(s_{\chi\bar{\chi}}) = \frac{2}{3}d_\chi^2 s_{\chi\bar{\chi}}^2\left(1-\frac{4m_\chi^2}{s_{\chi\bar{\chi}}}\right), \tag{7c}$$

$$\text{AM}:\ f(s_{\chi\bar{\chi}}) = \frac{4}{3}a_\chi^2 s_{\chi\bar{\chi}}^3\left(1-\frac{4m_\chi^2}{s_{\chi\bar{\chi}}}\right), \tag{7d}$$

$$\text{CR}:\ f(s_{\chi\bar{\chi}}) = \frac{4}{3}b_\chi^2 s_{\chi\bar{\chi}}^3\left(1+\frac{2m_\chi^2}{s_{\chi\bar{\chi}}}\right). \tag{7e}$$

Plugging Eq. (7) into Eq. (4), for $m_e \to 0$, we recover the expression in Ref. [51] for particles carrying ϵQ and the expressions in Ref. [52] for MDM and EDM.

In order to illustrate the difference between the various interactions, in Fig. 2 we show the differential cross sections with respect to the ISR energy for $m_\chi = 0$ (top) and $m_\chi = 3$ GeV (bottom). The different behaviors of the cross sections with respect to the fractional photon energy x_γ suggest, that stronger limits on ϵQ can be expected from high-energy monophoton searches, while for AM and CR the low energy region appears more prospective in

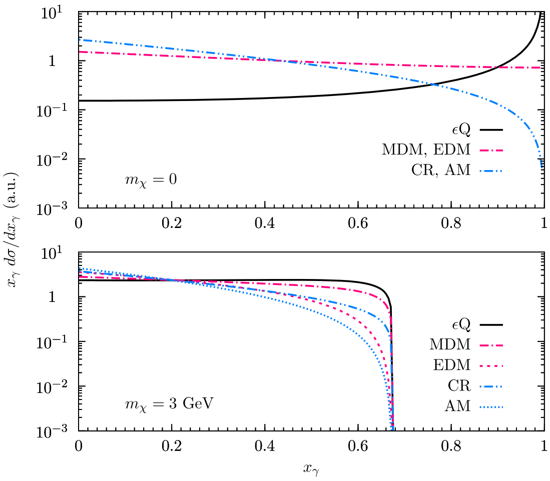

FIG. 2. Differential cross section for a CM energy of 10 GeV obtained from Eq. (4) by integrating over $\cos\theta_\gamma$ as a function of the ISR energy fraction, $x_\gamma = E_\gamma/\sqrt{s}$, multiplied by x_γ for ϵQ (black), MDM/EDM (pink) and CR/AM (blue). All curves are normalized to the same total cross section.

constraining these interactions (compare Fig. 4; to be discussed in more detail in Sec. IV). In the limit of $m_\chi \to 0$ the models with the same dimensionality of the interaction operators show the same behavior, i.e., for $\mu_\chi = d_\chi$ $(a_\chi = b_\chi)$ the cross sections for MDM and EDM (for AM and CR) as a function of x_γ are identical. Finally, we note in passing that in the presented numerical results we neglect the running of α since it is a few percent effect for energies up to 10 GeV.

B. Pair production at fixed target experiments

In the fixed target experiments we consider in this work, a pair of fermions is produced via an off shell photon emitted by an electron as it hits a nuclear target $(e^-N \to e^-N\gamma^* \to e^-N\chi\bar{\chi})$. The Feynman diagrams of the process are depicted in Fig. 1(b). In principle, also inelastic scatterings to an excited nuclear state N^* or to an all-inclusive final state X are possible. In the following we neglect such contributions, but present the general formalism to account for the latter in Appendixes A and B.

Note that we only consider the emission of the photon from the electron leg. The emission from the nuclear leg is parametrically smaller by a factor of $(Zm_e/m_N)^2 \sim 10^{-6}$ for coherent photon emission and receives a further suppression from the nuclear form factor for photon momenta above a few 100 MeV.[3] Finally, in order to properly cover the full kinematic range that is accessible to χ and $\bar{\chi}$ at a given CM energy, we compute the underlying 2-to-4 process exactly, without relying on approximations such as the Weizsäcker-Williams method.

It is still possible, however, to relate the 2-to-4 cross section to a 2-to-3 process with the emission of a vector boson of virtual squared mass $s_{\chi\bar{\chi}}$,

$$\frac{d\sigma_{2\to 4}}{ds_{\chi\bar{\chi}}} = \sigma_{2\to 3}(s_{\chi\bar{\chi}})\,\frac{f(s_{\chi\bar{\chi}})}{16\pi^2 s_{\chi\bar{\chi}}^2}\sqrt{1-\frac{4m_\chi^2}{s_{\chi\bar{\chi}}}}, \tag{8}$$

in which the directions of χ-particles have been integrated out in $f(s_{\chi\bar{\chi}})$.[4] Equation (8) is exact, and can in principle be generalized for higher differential cross sections that are not sensitive to the direction of χ or $\bar{\chi}$. Our actual calculations require higher differential cross sections than Eq. (8). For NA64 and LDMX the full 4-body phase space is presented in App. C [Eq. (C1)] and for mQ and BDX where the momentum of χ enters in the elastic detection channel it is presented in App. D [Eq. (D1)].

In principle, also pions and η-mesons (among other mesons) can be produced in this scattering process, which can subsequently decay into $\chi\bar{\chi}$ if kinematically allowed. However, while meson production dominates in fixed target experiments with a proton beam, it presents a subleading contribution for the electron beam experiments we consider. In addition, note that NA64 and LDMX should veto events that involve produced hadrons in the final state. For these reasons we neglect the contribution of hadronic production channels of $\chi\bar{\chi}$ to the event rate.

In Fig. 3 we show the inclusive $\chi\bar{\chi}$-production cross sections as a function of m_χ for several target materials and beam energies corresponding to the experiments discussed in Sec. IV. As expected from Eq. (7), the dimensionality of the operator determines the behavior of the cross section for $m_\chi^2 \ll s$. Since models with lower dimensional operators show a flatter dependence on $s_{\chi\bar{\chi}}$ in Eq. (7), there is no visible difference in the inclusive cross section for ϵQ at low masses between 4, 30 and 100 GeV beam energy in the top panel of Fig. 3, whereas for all other models, shown in the center and bottom panel, the cross section visibly rises with increasing beam energy. It is noteworthy that the cross section for an aluminium (Al) target is generally smaller than for tungsten (W) and lead (Pb) targets since the cross section scales with Z^2 and the charge of the Al nucleus is smaller by roughly a factor of 5–6. However, due to its smaller mass, the suppression at the kinematic edge is less pronounced in comparison to the heavier targets. The charge and mass differences between W and Pb are

[3]Photon emission from final-state light hadrons such as pions that accompany the primary scattering is suppressed by $(m_e/m_\pi)^2 \sim 10^{-5}$.

[4]In the calculation of $\sigma_{2\to 3}$ one may still make the replacement $\sum_{\rm pol}\epsilon_\mu\epsilon_\nu \to -g_{\mu\nu}$ in the polarization sum of the massive vector as the q^μ-dependent piece drops out by virtue of the Ward identity.

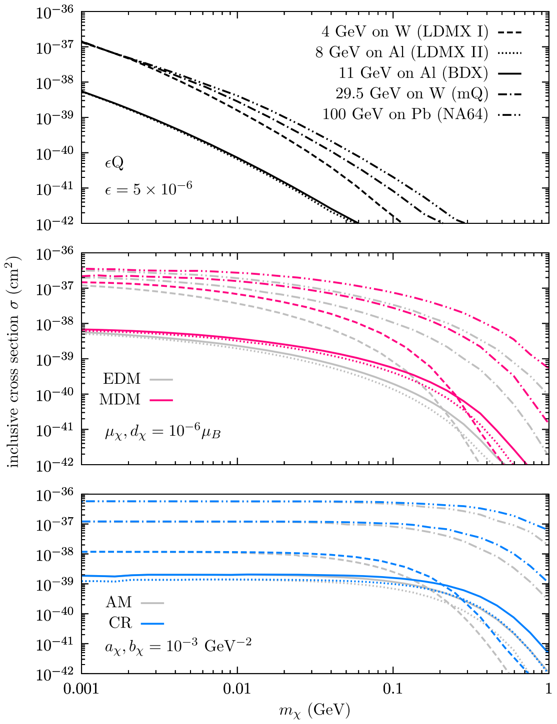

FIG. 3. Inclusive cross section of χ-pair production in e^--scattering on a fixed target, the process depicted in Fig. 1 (b). The beam energies and target nuclei correspond to the experiments discussed in this paper. In the limit of small DM mass, MDM and EDM in the central panel as well as CR and AM in the bottom panel yield identical cross sections. The mQ results agree with Ref. [53].

negligible in this case. Finally, while the cross section for millicharged particles rises with decreasing mass, it becomes independent of m_χ for MDM and EDM, and even quicker so for AM and CR. When m_χ increases towards the kinematic endpoint, the operators containing a factor of γ^5 yield velocity factors that result in a stronger suppression of the cross sections.

C. Detection via elastic scattering on nuclei

In mQ and BDX the produced fermions can directly be detected via elastic χ-nucleus and/or χ-electron scattering. In this case, the signal of χ particles would be a number of recoil events in the detector beyond the background, instead of missing momentum/energy. A presentation of the expressions of the recoil cross section $d\sigma/dE_R$ in the lab frame as a function of the recoil energy E_R and valid for relativistic χ-energies E_χ is relegated to App. E. The cross sections are functions of the nuclear mass (magnetic moment) m_N (μ_N) and the nuclear spin I_N. In the small-velocity limit, i.e., for $|\boldsymbol{p}_\chi| = m_\chi v$ and $E_\chi \simeq m_\chi + m_\chi v^2/2$ with $v \ll 1$, the expressions in Eq. (E2) are in agreement with the formulas found in Refs. [54,55]. Since the expressions are exact with respect to phase space, they apply to both χN and χe^- scatterings.

IV. INTENSITY FRONTIER SEARCHES WITH ELECTRON BEAMS

In this section we place constraints on the discussed fermion models with electromagnetic form factors from *BABAR*, NA64 and mQ and present projections for Belle II, LDMX and BDX. All limits in the presented plots are obtained at 90% confidence level (C.L.). The limits and projections for the models with dim-5 (dim-6) operators are shown in the summary plots in Fig. 7 (Fig. 8).[5]

A. *BABAR* and Belle 2

BABAR at SLAC [31] and Belle-II at SuperKEKB [33] are experiments at asymmetric e^+e^- colliders. Long-lived states χ that are produced through their (feeble) electromagnetic form factor interaction can escape from the detectors. The primary signature is hence the missing energy in $\chi\bar{\chi}$ production in association with a single photon (monophoton missing energy search). The main background processes are SM final states in which electrons or photons leave the detector undetected, i.e., $e^+e^- \to \gamma\not\gamma$, which produces a peak at $s_{\chi\bar{\chi}} = 0$ and $e^+e^- \to \gamma\not e^+\not e^-$ as well as $e^+e^- \to \gamma\not\gamma\not\gamma$ which constitute a continuum background that rises with $s_{\chi\bar{\chi}}$. The irreducible background $e^+e^- \to \gamma\nu\bar{\nu}$ is suppressed by m_Z^{-4} and can be neglected.

For deriving constraints from *BABAR*, we use the data of the analysis of monophoton events performed by the collaboration in a search for invisible decays of a light scalar at the $\Upsilon(3S)$ resonance [57,58].[6] The CM energy is thus 10.35 GeV. Two search regions with different trigger and cut efficiencies, a high photon energy region with 3.2 GeV $< E_\gamma <$ 5.5 GeV and low energy region with 2.2 GeV $< E_\gamma <$ 3.7 GeV in the CM frame, were presented. The high energy search uses the full data set of 28 fb^{-1} integrated luminosity and the low energy search a subsample of 19 fb^{-1}. The geometric cuts of the search regions are $-0.31 < \cos\theta_\gamma < 0.6$ (high energy) and $-0.46 < \cos\theta_\gamma < 0.46$ (low energy), where θ_γ is the photon angle in the CM frame with respect to the beam line as in Eq. (4).

[5]Even stronger (projected) bounds may be achievable from beam dump experiments with high-energy proton beams, as suggested by Ref. [56]. We leave such studies for a future work; see Sec. VII.

[6]In more recent [58], Boosted Decision Trees (BDT), trained on simulated massive dark photon signal events, were used for event selection. Our cases of main interest have different event shapes as shown in Fig. 4, and hence differ significantly from the training set used in Ref. [58]. For this reason, we use the smaller dataset [57] with cut-based event selection.

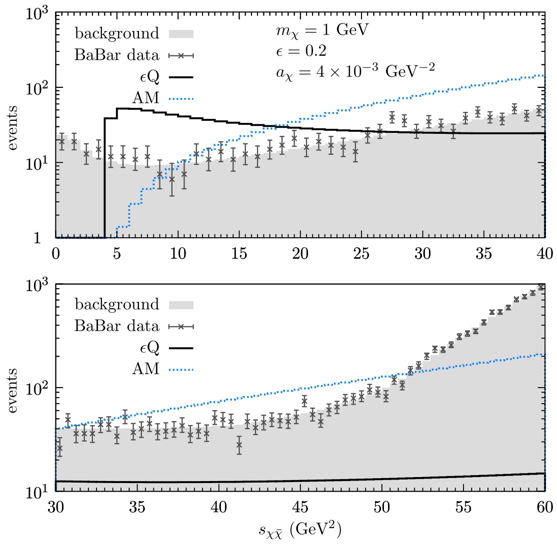

FIG. 4. High energy (3.2 GeV $< E_\gamma <$ 5.5 GeV) and low energy (2.2 GeV $< E_\gamma <$ 3.7 GeV) monophoton search region of *BABAR* in the top and bottom panels, respectively. The data points and background events taken from [57] are shown as a function of squared invariant missing mass and are binned per GeV^2 (top) and per half GeV^2 (bottom). Also shown are exemplary event shapes for ϵQ and AM interactions with $\epsilon = 0.2$ and $a_\chi = 4 \times 10^{-3}$ GeV^{-2} for $m_\chi = 1$ GeV in solid (black) and dotted (blue), respectively.

With the respective angular cuts applied, the number of signal events is given by

$$N_{\rm sig}^{(i)} = \epsilon_{\rm eff}\mathcal{L}\int_{{\rm bin}\ i}\frac{ds_{\chi\bar\chi}}{s}\int_{\cos\theta_\gamma^{\rm min}}^{\cos\theta_\gamma^{\rm max}} d\cos\theta_\gamma \frac{d\sigma_{e^+e^-\to\chi\bar\chi\gamma}}{dx_\gamma d\cos\theta_\gamma}, \qquad (9)$$

where $\epsilon_{\rm eff}$ is the total trigger and cut efficiency, $\mathcal{L}$ is the integrated luminosity. The boundaries of $s_{\chi\bar\chi}$ are given by the bins in Fig. 4, and the production cross section $d\sigma_{e^+e^-\to\chi\bar\chi\gamma}$ is given in Eq. (4). Following Ref. [59], in our analysis we apply a nongeometric cut $\epsilon_{\rm eff}$ of 30% (55%) in the high (low) energy region for *BABAR* and place conservative constraints on the models in Eq. (1) by requiring that the expected number of signal events does not exceed the observed number $N_{\rm obs}^{(i)}$ at 90% C.L. in any bin i. Concretely, we require $N_{\rm sig}^{(i)} < N_{\rm obs}^{(i)} + 1.28\sigma_{\rm obs}^{(i)}$, where $\sigma_{\rm obs}^{(i)}$ is given by the statistical and systematical uncertainties of $N_{\rm obs}^{(i)}$ added in quadrature.[7]

For the Belle II projections, we follow Ref. [59] and scale up the *BABAR* background from Ref. [57] (shown by the gray histogram in Fig. 4) to an integrated luminosity of 50 ab^{-1} with the CM energy of 10.57 GeV, employ a constant efficiency cut of 50% in both search regions and take identical geometric cuts for Belle II and *BABAR*. While the exact background subtraction in the monophoton search of Belle II needs to be provided by event generators [60], here we adopt the two projection-methods of Ref. [59]: first is a "statistics limited" projection, where we assume a full subtraction of the background yielding a limit that is only governed by statistical fluctuations. It comprises the best case scenario with the strongest ensuing limits on the new couplings. Second is a "systematics limited" projection, where we assume a 10% systematic uncertainty for the $\gamma/$ peak and a 20% uncertainty for the continuum backgrounds and exclude parameter regions where the signal exceeds the systematic plus statistical uncertainties at 90% C.L.. With good control over the backgrounds, the actual reach of Belle II should lie between those two projections.

In Fig. 4 we show exemplary event shapes as a function of $s_{\chi\bar\chi}$ at *BABAR* for ϵQ with $\epsilon = 0.2$ and for AM with $a_\chi = 4 \times 10^{-3}$ GeV^{-2}. As can be seen, the limit on millicharged particles is driven by the high monophoton energy search region (top panel of Fig. 4) while for particles carrying an anapole moment (and in analogy the other operators) the limits are set in the low monophoton energy search region as well as from the bins with lower photon energy in the high energy region. The ensuing constraints, as well as projected ones from Belle II, are shown as the parameter space of χ-mass and couplings in Fig. 7 for MDM and EDM and in Fig. 8 for CR and AM models.

For the ϵQ model, we find that in the kinematically unsuppressed region, $m_\chi \lesssim 1$ GeV, the *BABAR* data excludes $\epsilon \geq 6.4 \times 10^{-2}$ at 90% C.L. Moreover, the reach of the Belle II experiment is $\sim 2 \times 10^{-2}$ and $\sim 4 \times 10^{-3}$ for the systematics and statistics limited scenarios, respectively.

B. NA64 and LDMX

The NA64 experiment at the CERN SPS [35] and LDMX at SLAC [36] are current and proposed fixed target experiments using electron beams, where a $\chi\bar\chi$ pair can be produced via off shell photon emission. An active veto system together with cuts on the search region makes both experiments essentially background-free. Therefore, in the following we place limits on the operators in Eq. (1) by assuming zero background in the regions of interest.

In the NA64 experiment, an electron beam with $E_0 = 100$ GeV hits an electromagnetic calorimeter (ECAL) which is a matrix of 6×6 modules consisting of lead (Pb) and scandium (Sc) plates, each module having a size of approximately 40 radiation lengths (X_0), with $X_0 = 0.56$ cm for Pb. The radiation length of Sc is about one order of magnitude larger, so the scattering of electrons with Sc is subleading, and will not be considered here. In the initial part of the ECAL there is a preshower (PS)

[7] As is evident from Fig. 4, a signal will simultaneously be present at similar strength in many bins. It is hence safe to neglect the look-elsewhere effect.

detector of $4X_0$ in length with the same setup, functioning as target and detector simultaneously. Missing energy signals are required to have a starting point of the EM shower localized within the first few radiation lengths of the detector [61]. In our analysis, we conservatively take a thin target limit, with $L_{\rm target} = X_0$, meaning that the fermion pair is essentially produced within the first radiation length of the target material. After scattering, the final state electrons are detected in the main ECAL with a search region of $0.3\ \mathrm{GeV} < E_4 < 50\ \mathrm{GeV}$, where the lower boundary is due to the electron identification threshold in the PS detector and the upper boundary requires a missing energy larger than $0.5E_0$ [35]. We adopt a polar angular coverage of $\theta_4 < 0.23$ rad so that the final state electron should pass through the whole ECAL. The total cross section, however, is strongly forward-peaked and therefore the contribution of large angle scattering is negligible, meaning that a variation of $\theta_4^{\rm max}$ does not affect our limits.

The number of signal events in the thin target limit and with the geometric and angular cuts as specified above is given by

$$N_{\rm sig} = N_{\rm EOT}\frac{\rho_{\rm target}}{m_N}L_{\rm target}\int_{E_{\rm min}}^{E_{\rm max}} dE_4 \epsilon_{\rm eff}(E_4) \times \int_{\cos\theta_4^{\rm min}}^{\cos\theta_4^{\rm max}} d\cos\theta_4 \frac{d\sigma_{\rm prod}}{dE_4 d\cos\theta_4}, \tag{10}$$

where $d\sigma_{\rm prod}$ is the χ-pair production cross section, $e^- N \to e^- N\chi\bar{\chi}$, given by (C6), $N_{\rm EOT} = 4.3 \times 10^{10}$ is the number of electrons on target (EOT), $\rho_{\rm target}$ is the target density and m_N the target mass. The detector efficiency for NA64 only marginally depends on the electron energy, and we take it to be constant with $\epsilon_{\rm eff} = 0.5$. The constraints from NA64 on the interactions in Eq. (1) are then derived by requiring that parameters that generate more than 2.3 events in the detector are excluded.

The LDMX proposal consists of a silicon tracker system, an ECAL and a hadron calorimeter (HCAL). In our analysis we use the benchmark points of the proposed LDMX phase I with 4×10^{14} EOT at $E_0 = 4$ GeV, and phase II with 3.2×10^{15} EOT at $E_0 = 8$ GeV [36]. LDMX will use a tungsten (W) target ($X_0 = 0.35$ cm) with a thickness of $0.1X_0$ in phase I and an aluminium (Al) target ($X_0 = 8.9$ cm) with $0.4X_0$ in phase II. The first four track sensors with an area of 4 cm × 10 cm are located 7.5–52.5 mm behind the target along the beam line. We take a polar angular coverage in the forward direction of $\theta_4 < \pi/4$ and a search region for the final state electron energy of $50\ \mathrm{MeV} < E_4 < 0.3E_0$. While the actual signal efficiency varies mildly with the dark state mass and track requirements [36], a constant $\epsilon_{\rm eff} = 0.5$ is assumed here. In the end, the number of signal events is calculated according to Eq. (10), and the projected constraints from LDMX are derived analogously, requesting at least 2.3 events in the detector.

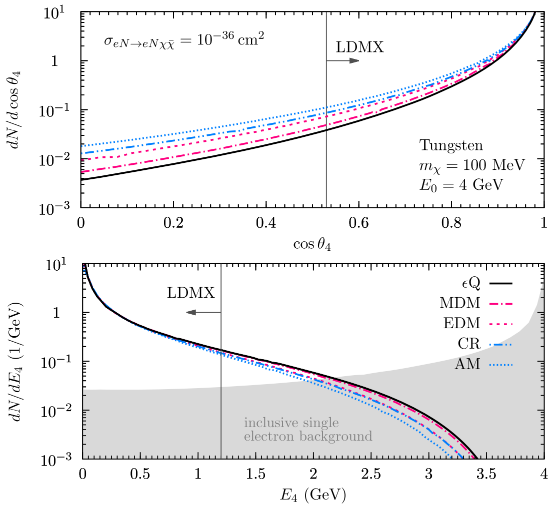

FIG. 5. Angular (top) and energy (bottom) distribution of the scattered electron in χ-pair production in e^--scattering on a tungsten target for $m_\chi = 100$ MeV and electron beam energy of 4 GeV, before imposing detector efficiency. In the bottom panel the inclusive single electron background taken from Ref. [36] is shown in gray.

In Fig. 5 we show the angular (top panel) and energy distributions (bottom panel) of the final state electrons for LDMX phase I obtained from Eq. (10). The event rates are rather similar for all models when normalized to the same total cross section; we normalize it to $\sigma = 10^{-36}$ cm^2 yielding approximately 1 predicted signal event in LDMX phase I. The signal is strongly forward peaked for $s_{\chi\bar{\chi}} \gg m_\chi^2$, but in the transverse direction and at the kinematic edge, the curves start to deviate slightly. We also show the geometric acceptance region of LDMX in the top panel of Fig. 5 and the energy cut in the bottom panel, indicating that LDMX is searching in a region in the (θ_4, E_4)-plane where the event shapes of all models are similar.

Both the current limits from NA64 and projections for the LDMX phases are shown in Fig. 7 for MDM and EDM and in Fig. 8 for CR and AM models. Whereas the NA64 limit is weaker than the limit derived from *BABAR* data, LDMX will significantly improve the sensitivity to μ_χ and d_χ but will be on par with *BABAR* for a_χ and b_χ. We note in passing that for the ϵQ model, our projections for LDMX agree with Ref. [36] and for NA64 are slightly weaker, by about a factor 2, than the limits presented in Ref. [62]. This is most likely due to a combination of a different assumption on detection efficiencies and the neglect of an energy threshold in the final state electron in Ref. [62].

C. mQ and BDX

In the mQ experiment at SLAC [40,53], $N_{\rm EOT} = 8.4 \times 10^{18}$ electrons with $E_0 = 29.5$ GeV energy were incident

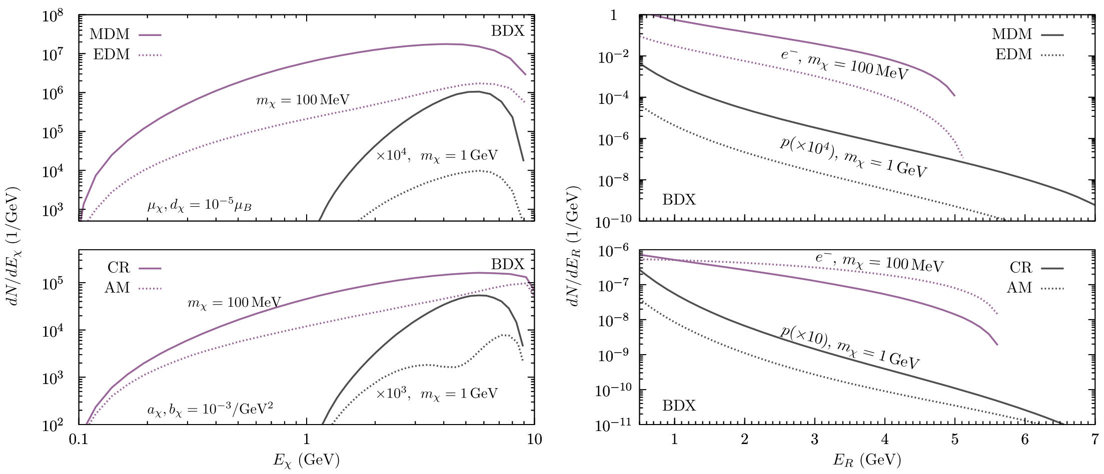

FIG. 6. Left: Energy differential total number dN_χ/dE_χ of χ-particles in the BDX detector as obtained from Eq. (11). The top (bottom) panel shows the mass dimension-5(6) interactions for $m_\chi = 100$ MeV and 1 GeV and coupling strengths as labeled. Right: Corresponding electron and proton recoil spectra dN_χ/dE_R as obtained from Eq. (12) for the same parameters.

on a W target of thickness $6X_0$. The produced dark particles are then searched for in their scattering off electrons and nuclei in the main detector, approximately 110 m down the beam line. The detector, made of plastic scintillators, has a polar angular coverage of $\theta_\chi < 2$ mrad, and a total path length of $L_{\rm det} = 131$ cm. The experiment found 207 recoil events above the estimated background, but below the estimated background uncertainty $\sigma_{\rm bkg} = \sqrt{N_{\rm bkg}} \simeq 382$, within the signal time window. While millicharged particles would mostly produce single photoelectron (PE) events, such assumption is not justified for the recoil spectra of the models considered in this work. Therefore, similarly to Ref. [63], we focus on nuclear/electron recoil events with a deposited energy larger than 0.1 MeV. Following Ref. [53], 90% C.L. exclusion limits can then be obtained by requiring the number of signal events induced by χ, $N_{\rm sig} < 207 + 1.28\sigma_{\rm bkg} \simeq 697$. Here we will not consider a further possible reduction of single-PE backgrounds [63]; they may strengthen our limits by a factor of 2–3.

The proposed BDX experiment at Jefferson Lab [42] will use an electron beam of $E_0 = 11$ GeV incident on an Al target that comprises 80 layers with thickness of 1–2 cm each. The χ particles produced in the bump pass through thick shields and reach an ECAL 20 m downstream. The ECAL, composed of CSI(Tl) crystals, will have an area of 50×55 cm^2 and a depth of $L_{\rm det} = 260$ cm, implying a polar angle coverage of $\theta_\chi \lesssim 12.5$ mrad. The BDX Collaboration has estimated that for $N_{\rm EOT} = 10^{22}$ the number of background events with deposited energy above 500 MeV is approximately 10, coming mostly from high energy neutrinos that scatter off electrons [64]. In the following, we conservatively take the uncertainty in the background estimation $\sigma_{\rm bkg} = N_{\rm bkg} = 10$, and assume a benchmark value for the projected number of observed events $N_{\rm obs} = 15$. It allows to set 90% C.L. limits on models studied here by requiring $N_{\rm sig} \leq 18$.

In both experiments, the energy differential expected number of particles χ that reach the detector is given by

$$\frac{dN_\chi}{dE_\chi} = N_{\rm EOT}\frac{\rho_{\rm target}}{m_N}X_0\int_{E_\chi}^{E_0} dE I(E)\frac{d\sigma_{\rm prod}(E)}{dE_\chi}, \qquad (11)$$

where the production cross section $d\sigma_{\rm prod}$ given by Eq. (D9) has been integrated over the angular coverage of the detector, and

$$I(E) = \frac{1 + (\frac{E_0 - E}{E_0})^{\frac{4t_0}{3}}(\frac{4t_0}{3}\ln(\frac{E_0-E}{E_0}) - 1)}{\frac{4}{3}(E_0 - E)\ln^2(\frac{E_0-E}{E_0})}$$

is the integrated energy distribution of electrons during its propagation in the target [25]. For the mQ experiment, $t_0 = L_{\rm target}/X_0 = 6$ ($X_0 = 0.35$ cm for W), and for BDX we take $t_0 = 15$ as fiducial value ($X_0 = 8.9$ cm for Al). Finally, m_N and $\rho_{\rm target}$ are the target mass and mass density, respectively. The energy spectra (11) are shown in Fig. 6 for several benchmark parameter values. One can observe that most of the χ particles entering the detector carry kinetic energies in the GeV-ballpark.

The total number of signal events in the downstream detectors that are produced in the scattering of χ on target i is then given by

$$N_{\rm sig}^{(i)} = N_T^{(i)}L_{\rm det}\int_{m_\chi}^{E_\chi^{\rm max}} dE_\chi \int_{E_R^{\rm th}}^{E_R^{\rm max}} dE_R \epsilon_{\rm eff}^{(i)}(E_R)\frac{dN_\chi}{dE_\chi}\frac{d\sigma_{\rm det}^{(i)}}{dE_R}, \qquad (12)$$

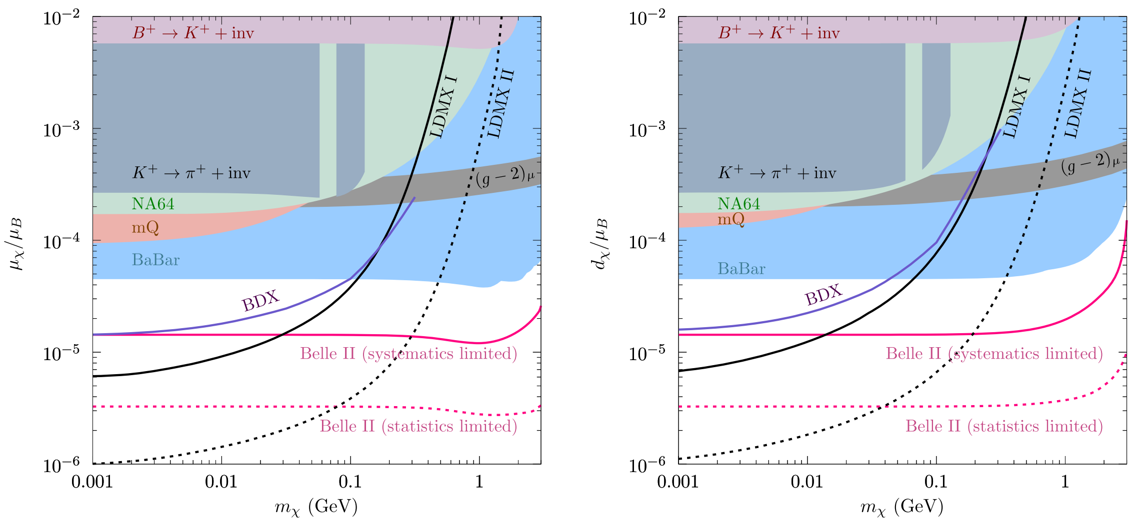

FIG. 7. Constraints (shaded regions) and projections (lines) on the electromagnetic form factors for fermions with an MDM (left) and an EDM (right).

where $\epsilon_{\rm eff}^{(i)}$ is the detection efficiency of an event with recoil energy E_R. $N_T^{(i)}$ is the target number density. For mQ, the signal is dominated by the scattering on e^- and by the (coherent) scattering on C atoms. Hence $i = e^-, C$ and we compute $N_T^{(i)}$ according to the chemical composition of the detector. For BDX, the detector is made of CsI, but given a threshold in deposited energy of $E_R^{\rm th} = 500$ MeV, we consider $i = p, e^-$ as targets. The corresponding detection cross sections $d\sigma_{\rm det}^{(i)}/dE_R$ are given by the elastic recoil cross sections found in App. E; the form-factors $F_{E,M}$ that are to be used for the respective targets i are provided in App. B. The energy of χ particles, E_χ, is limited by the electron beam energy, $E_\chi^{\rm max}$, as given in Eq. (D10). In turn, E_χ determines the maximal recoil energy of target i, $E_R^{\rm max}$, see Eq. (E3).

In the right panel of Fig. 6 we show the theoretical recoil spectra $dN^{(i)}/dE_R$ that are obtained from Eq. (12) by dropping the integration over E_R and before accounting for detection efficiencies, i.e., by setting $\epsilon_{\rm eff} = 1$ for the same values of parameters as in the left panel of Fig. 6. For $m_\chi \lesssim 1$ GeV the scattering on electron is most important for setting any limit on the interactions. Once $m_\chi \gtrsim 1$ GeV the maximum electron recoil energy $E_R^{\rm max}$ falls below the detector threshold $E_R^{\rm th}$ and any further sensitivity relies on recoil of protons (and, in principle, on neutrons). For completeness, we also note that for Fig. 6 we have neglected the momentum distribution of protons inside the target nucleus. The Fermi momentum of nucleons is $p_F \sim 250$ MeV and it will hence affect the shape of the proton recoil spectrum at energies $E_R < 1$ GeV, but be negligible for the bulk of the shown spectra.

For the value of the detection efficiency $\epsilon_{\rm eff}$, we use 0.5 for mQ [53]. Based on the simulations in Ref. [42], a numerical function of E_R has been adopted for electron recoils in BDX, giving $\epsilon_{\rm eff} \sim 5\%$ for $E_R = 0.5$ GeV and $\epsilon_{\rm eff} \sim 1\%$ for $E_R = 1.5$ GeV. However, there is currently no data available for proton recoils in BDX with $E_R \geq 0.5$ GeV, so we derive the BDX projections based on electron recoils only.

By requiring $N_{\rm sig}$, calculated from Eq. (12), to be below the values given above, the 90% C.L. (projected) limits on the electromagnetic factors of χ have been derived and are shown in Figs. 7 and 8. For $m_\chi \geq 0.5$ GeV and $E_0 = 11$ GeV, no incoming χ can deposit energy more than 0.5 GeV by its scattering off an electron. So that the high-m_χ end in the parameter space of Figs. 7–8 will not be constrained by electron recoils in BDX. In general, BDX will have stronger sensitivity than mQ to the models studied here. In contrast, the mQ experiment remains more sensitive to millicharged particles due to its low threshold in recoil energy.

The summary plots, Figs. 7 and 8, show that while the projections of BDX and LDMX for dim-5 interactions reach beyond Belle II for small m_χ, for dim-6 interactions they flatten out below ~0.1 GeV without surpassing Belle II in sensitivity. The difference of slopes of the BDX and LDMX curves in Figs. 7 and 8 is understood as follows: first, note that the χ-pair production rate receives significant contributions from the e-N forward scattering part which in turn is regulated by m_χ; the lower boundary of $s_{\chi\bar\chi}$ is $4m_\chi^2$. Second, as seen in Fig. 3, the m_χ-dependence of the production rate becomes weaker for higher mass-dimension interactions, since the $s_{\chi\bar\chi}$ factors in the emission pieces, Eqs. (7b)–(7e), tend to reduce the contribution of the forward

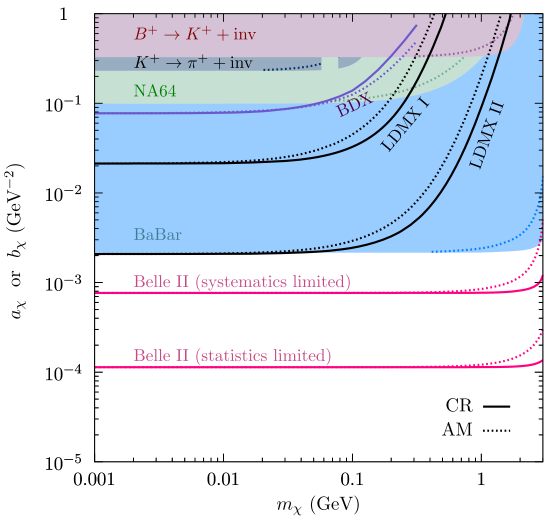

FIG. 8. Same as Fig. 7 for fermions with dim-6 operators. The solid (dotted) lines show the constraints and projections from the experiments for CR (AM) as labeled.

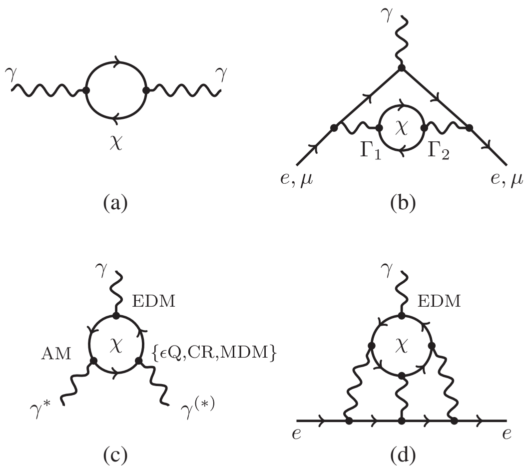

FIG. 9. Loop diagrams relevant in the discussion of SM corrections discussed in Sec. V. The vacuum polarization diagram (a) contributes to the running of α. The leading contribution to $g-2$ is from diagram (b), which we evaluate for $\Gamma_1 = \Gamma_2$. It can be shown that a similar diagram with $\Gamma_1 = \mathrm{EDM}$ and $\Gamma_1 \neq \Gamma_2$ does not contribute to an electric dipole moment of the electron. Diagram (c) shows an *a priori* nonvanishing χ-loop with three photons attached. Diagram (d) shows a 3-loop contribution to the electron electric dipole moment.

scattering part. Taken together, this explains the difference in slope. It is also for these reasons that the millicharged case (dim-4) [53] has an even bigger slope than the dim-5 ones.

V. SM PRECISION OBSERVABLES AND HIGH ENERGY SEARCHES

Focusing on a mass of χ below several GeV, SM precision observables and LEP measurements in general play an important role in constraining the existence of the various electromagnetic interactions. In the following we update bounds on EDM and MDM SM precision tests first obtained in Ref. [5], going beyond parametric estimates where possible, and provide new ones on CR and AM. In addition we compute the constraints from flavor physics, as well as from missing energy searches at LEP.

A. Running of α

In the electroweak theory, Fermi's constant G_F and the masses of W and Z bosons are related and receive calculable quantum corrections, summarized in the Δr parameter [65]. The SM prediction is $\Delta r_{\mathrm{SM}} = 0.03672 \pm 0.00019$ [66] and the observed value can be obtained from

$$\Delta r_{\mathrm{obs}} = 1 - \frac{A_0^2}{M_W^2 s_w^2} = 0.03492 \pm 0.00097, \qquad (13)$$

where $A_0 = (\pi\alpha/\sqrt{2}G_F)^{1/2}$ and $s_w^2 = 1 - M_W^2/M_Z^2$. For the actual number we have used the global averages of M_W, M_Z, and A_0 and their errors quoted in [66]. The range in which new physics can contribute is hence limited at 95% C.L. as[8]

$$-0.0038 < \Delta r_{\mathrm{new}} < 0.00018. \qquad (14)$$

Electromagnetic interactions of χ will contribute to Δr through the running of $\alpha(Q^2)$ they induce. Explicitly, $\Delta r_{\mathrm{new}} \simeq \Pi(-M_Z^2) - \Pi(0)$ where $\Pi(q^2)$ is the polarization function [Fig. 9(a)] at photon momentum $q^2 = -Q^2$. Details on the calculation of the photon vacuum polarization are found in App. F. Equation (14) then implies for MDM and EDM

$$|\mu_\chi| \mathrm{or} |d_\chi| < 3.2 \times 10^{-6} \mu_B, \qquad (15)$$

independent of m_χ, saturating the upper limit in Eq. (14) and improving the previously obtained limits in Ref. [5] by half an order of magnitude. In turn, for AM and CR we obtain

$$|a_\chi| \mathrm{or} |b_\chi| < 3.2 \times 10^{-5}\ \mathrm{GeV}^{-2}, \qquad (16)$$

saturating the lower limit in Eq. (14). The latter interactions hence contribute with opposite sign.

[8]The tension between measurement and observation is 1.8σ and any positive contribution to Δr_{new} is hence already tightly constrained.

The above limits are at or even stronger than the projected sensitivity from the various experiments considered above. As a quantum effect, they are, however, susceptible to a model dependence that a direct observation of a particle is not. If the theory contains additional states at a mass scale below M_Z or if χ carries more than one EM form factor, cancellations in $\Delta r_{\rm new}$ can occur. It is for this reason that we do not explicitly show those limits in Figs. 7 and 8. Finally, for completeness we also record a limit obtained from Eq. (14) on the positive contribution from ϵQ, $\epsilon \lesssim 0.1$, weakening for increasing χ-mass to $\epsilon \lesssim 0.3$ at $m_\chi = 10$ GeV.

B. Muon $g-2$

Here we consider the effect of the various interactions on the anomalous magnetic moment of the muon $a_\mu = \frac{1}{2}(g-2)_\mu$. There is a tantalizing long-standing discrepancy between the measured value [67] and prediction in the SM (see Ref. [48] for a summary),

$$\Delta a_\mu = a_\mu^{\rm exp} - a_\mu^{\rm SM} = (290 \pm 90) \times 10^{-11}, \qquad (17)$$

indicating a $3-4\sigma$ tension. Hence, any positive contribution at the level of 3×10^{-9} may solve the $(g-2)$ puzzle, and much anticipated upcoming experiments [68,69] will further weigh in on the anomaly in the near future.

In the current context, the lowest-order contribution to $g-2$ enters through the vacuum polarization diagram, Fig. 9(b) where χ is in the loop of the internal photon line. In QED, the 2-loop leptonic contribution is of course well known [70,71], readily evaluated by noting the correction from the vacuum polarization to the photon propagator, and one may in principle proceed in analogy using Eq. (F3), appropriately renormalized. A quicker way is to estimate the correction Δa_μ from χ by using the dispersion relation and optical theorem from the total cross section of χ-pair creation, $\sigma_{e^+e^-\to\chi\bar\chi}$, similar to what is done with hadronic contributions in SM,

$$\Delta a_\mu = \frac{1}{4\pi^3}\int_{4m_\chi^2} ds\,\sigma_{e^+e^-\to\chi\bar\chi}(s)K(s), \qquad (18)$$

where $K(s)/(\pi\alpha)$ is the contribution to the muon anomalous magnetic moment from a photon of mass $\sqrt{s}$,[9]

$$K(s) = \int_0^1 dx \frac{x^2(1-x)}{x^2 + \frac{s}{m_\mu^2}(1-x)}. \qquad (19)$$

The cross section $\sigma_{e^+e^-\to\chi\bar\chi}$ is given in Eq. (6) with $s = s_{\chi\bar\chi}$. The integral (18) has to be cut off such that the validity of the effective theory is respected. This yields a reasonable estimate for dim-5 operators, and we show the resulting 90% bands in Figs. 7. Since $K(s) \sim 1/s$, for dim-6 operators the energy dependence makes the same integral linearly sensitive on the chosen cutoff so that we do not show any region in Fig. 8. However, Eq. (18) is sufficient to convince oneself that both AM an CR only yield interesting contributions in an otherwise deeply excluded region; we leave a systematic study of this to a dedicated work.

C. Induced electric dipole moments

A sensitive and "background-free" probe of new physics are electric dipole moments of SM particles. Most recently, the ACME collaboration improved the limit on the electron EDM d_e by an order of magnitude [73],

$$|d_e| < 1.1 \times 10^{-29}\ e\,\text{cm}. \qquad (20)$$

Given the strong limit in Eq. (20), for simplicity, we restrict our attention to the electron EDM; for a general discussion of neutron and atomic EDMs cf. Ref. [9] and references therein.

Electron electric dipole moments may be generated by the loops of χ-particles. Since the interaction is T- and P-odd it can only be induced in a loop diagram with an odd number of insertions of EDM vertices of χ, as it is the only T-odd interaction among the ones we consider. Using dim-5 MDM and EDM operators, Ref. [5] then argued that such dipole moments appear at the 3-loop level with four photons attached to the χ-loop, as lower order diagrams vanish by virtue of Furry's theorem. The interaction d_e hence appears through a combination $d_\chi\mu_\chi^3$ and $d_\chi^3\mu_\chi$.

Furry's theorem relies on C-invariance of the considered interactions and moving to dim-6 operators, we observe that the AM interaction is C-odd. Thereby, a χ-loop with 3 photons that are attached through EDM, AM and one out of the set of interactions $\{\epsilon\text{Q}, \text{MDM}, \text{CR}\}$ as shown in Fig. 9(c) does not vanish *a priori*.[10] However, when attached to the electron line, this does not imply a 2-loop contribution to d_e as the resulting operator would be P-odd; we also verify the vanishing 2-loop contribution through explicit calculation using a projector onto d_e [75].

Hence, we conclude that d_e is only induced at the 3-loop level, an example of which is shown in Fig. 9(d). A parametric estimate of its size would then be,

$$d_e \sim e^3 m_e d_\chi \times (\text{mass})^{-1}, \qquad (21)$$

where the factor of m_e originates from the necessary helicity-flip on the electron line to which 3 photons are attached (e^3-factor). The factor $(\text{mass})^{-1}$ is built from the other interactions present in the diagram, saturated by

[9] $K(s)$ is thereby equivalent to the expression obtained in the context of dark photon contributions to $g-2$ [44,45,72].

[10] A way to see it is by following a proof for a generalized version of Furry's theorem [74]. Also note that the photons attached via AM and CR need to be virtual.

powers of m_χ or, possibly, m_e to obtain the correct dimension, such as $\epsilon^3 e^3/m_\chi$, $\mu_\chi^3 m_\chi^2$, $d_\chi^2 \mu_\chi m_\chi^2$, $b_\chi d_\chi^2 m_\chi^3$ and so on. We have omitted any loop factors $(16\pi)^{-2n}$ with $n = 3$ as we do not know if other large combinatorial factors are present.[11] Saturating the present limit (20) we infer that the suppression mass scale in Eq. (21) is at the level of $\sim 10^{13}$ GeV(d_χ/μ_B) or larger. For example, if the electron EDM then solely appears through the combination of dim-5 operators, such estimate points to a related inverse effective scale $(10^{-5} - 10^{-6})\mu_B\sqrt{\mathrm{GeV}/m_\chi}$, implying an important constraint on the presence on joint EDM and MDM interactions. A systematic study of this goes beyond the scope of this work, but similar limits on other combination of operators are readily evaluated from the above arguments.

D. Rare meson decays

Measurements and searches of the invisible decay width of various mesons place a constraint on light dark particles [77]. Strong constraints are in particular obtained from data on B^+ and K^+ decays. The decays $K^+ \to \pi^+\chi\bar{\chi}$ and $B^+ \to K^+\chi\bar{\chi}$ are closely related to the semileptonic decay with a charged lepton pair in the final state, $K^+ \to \pi^+ l^+ l^-$ and $B^+ \to K^+ l^+ l^-$, as both are accompanied by the emission of γ^* in the flavor changing $s \to d$ and $b \to s$ transitions. Hence, by evaluating explicitly the decay—details are found in App. G—we find

$$\frac{\Gamma(K^+ \to \pi^+\bar{\chi}\chi)}{\Gamma(K \to \pi e^+ e^-)} \simeq 1.9 \times 10^4 \left(\frac{\mu_\chi \,\mathrm{or}\, d_\chi}{\mu_B}\right)^2, \quad (22)$$

for the MDM and EDM interactions and

$$\frac{\Gamma(K^+ \to \pi^+\bar{\chi}\chi)}{\Gamma(K \to \pi e^+ e^-)} \simeq 2.6 \times 10^4 \left(\frac{a_\chi \,\mathrm{or}\, b_\chi}{\mathrm{TeV}^2}\right)^2. \quad (23)$$

With the experimental value $\mathrm{Br}(K \to \pi e^+ e^-) = (3.00 \pm 0.09) \times 10^{-7}$ [66] together with the strong constraint on the branching ratio $K^+ \to \pi^+ + \mathrm{inv} \lesssim 4 \times 10^{-10}$ [78,79] which is applicable in the pion momentum ranges 211 MeV $< p_\pi <$ 229 MeV and 140 MeV $< p_\pi <$ 199 MeV allows to set a constraint in the χ-mass range $m_\chi <$ 58 MeV and 76 MeV $< m_\chi <$ 130 MeV. We obtain, approximately,

$$|\mu_\chi| \mathrm{or} |d_\chi| \lesssim 3 \times 10^{-4} \mu_B, \quad (24)$$

$$|a_\chi| \mathrm{or} |b_\chi| \lesssim 0.2\ \mathrm{GeV}^{-2}, \quad (25)$$

and show the numerically obtained curves in Figs. 7 and 8. Equation (24) also shows that only MDM and EDM interactions are reasonably well constrained by rare K-decays.

To estimate a constraint on the electromagnetic interactions from a limit on $\mathrm{Br}(B^+ \to K^+ + \mathrm{inv}) < 7 \times 10^{-5}$ [80] one can proceed in a similar fashion and relate the branching ratio $\mathrm{Br}(B^+ \to K^+\chi\bar{\chi})$ to $\mathrm{Br}(B^+ \to K^+\mu^+\mu^-) = (4.41 \pm 0.23) \times 10^{-7}$ [66]. We obtain,

$$\frac{\Gamma(B^+ \to K^+\bar{\chi}\chi)}{\Gamma(B^+ \to K^+\mu^+\mu^-)} \simeq 4.8 \times 10^6 \left(\frac{\mu_\chi \,\mathrm{or}\, d_\chi}{\mu_B}\right)^2, \quad (26)$$

for the MDM and EDM interactions and

$$\frac{\Gamma(B^+ \to K^+\bar{\chi}\chi)}{\Gamma(B^+ \to K^+\mu^+\mu^-)} \simeq 1.6 \times 10^3 \left(\frac{a_\chi \,\mathrm{or}\, b_\chi}{\mathrm{GeV}^2}\right)^2. \quad (27)$$

From those numbers we limit the interactions away from the kinematic threshold as,

$$|\mu_\chi| \mathrm{or} |d_\chi| \lesssim 6 \times 10^{-3} \mu_B, \quad (28)$$

$$|a_\chi| \mathrm{or} |b_\chi| \lesssim 0.3\ \mathrm{GeV}^{-2}, \quad (29)$$

where the latter limit on CR/AM again implies a UV scale that would be well below the electroweak scale. The numerically obtained curves are again included in Figs. 7 and 8.

E. Invisible Z-width

A model-dependent constraint arises if χ has fundamental interactions with the hypercharge through similar operators as in Eq. (1), but with $F_{\mu\nu}$ replaced by the hypercharge field strength $F^Y_{\mu\nu}$ and A_μ replaced by the associated gauge boson B_μ. The Z-decay into $\chi\bar{\chi}$ is possible for $m_\chi < M_Z/2$ and the partial width is given by

$$\Gamma_{Z\to\chi\bar{\chi}} = \frac{s_w^2 f(M_Z^2)}{16\pi M_Z}\sqrt{1 - \frac{4m_\chi^2}{M_Z^2}}, \quad (30)$$

where the functions $f(M_Z^2)$ for the various operators are found in Eq. (7). The experimental measurement of the invisible with $\Gamma(Z \to \mathrm{inv})_{\mathrm{exp}} = 499.0 \pm 1.5$ MeV together with the SM prediction $\Gamma(Z \to \mathrm{inv})_{\mathrm{SM}} = 501.44 \pm 0.04$ MeV [66] limits any additional contribution to $\Gamma(Z \to \mathrm{inv})_{\mathrm{new}} < 0.56$ MeV at 95% C.L. In the kinematically unsuppressed region this implies,

$$|\mu_\chi^{(Y)}| \mathrm{or} |d_\chi^{(Y)}| < 1.7 \times 10^{-6} \mu_B, \quad (31a)$$

$$|a_\chi^{(Y)}| \mathrm{or} |b_\chi^{(Y)}| < 3.8 \times 10^{-6}\ \mathrm{GeV}^{-2}. \quad (31b)$$

[11] d_e induced by a possible EDM of the SM τ lepton, d_τ, at (finite) 3-loop level has explicitly been calculated in Ref. [76] with the result $d_e = a(m_e/m_\tau)d_\tau(\alpha/\pi)^3$, where a turned out to be a number close to unity. For MDM/EDM interactions of χ, Ref. [5] saturates the dimensions by powers of m_e and includes a double-logarithmic enhancement $\log^2(m_\chi/m_e)$.

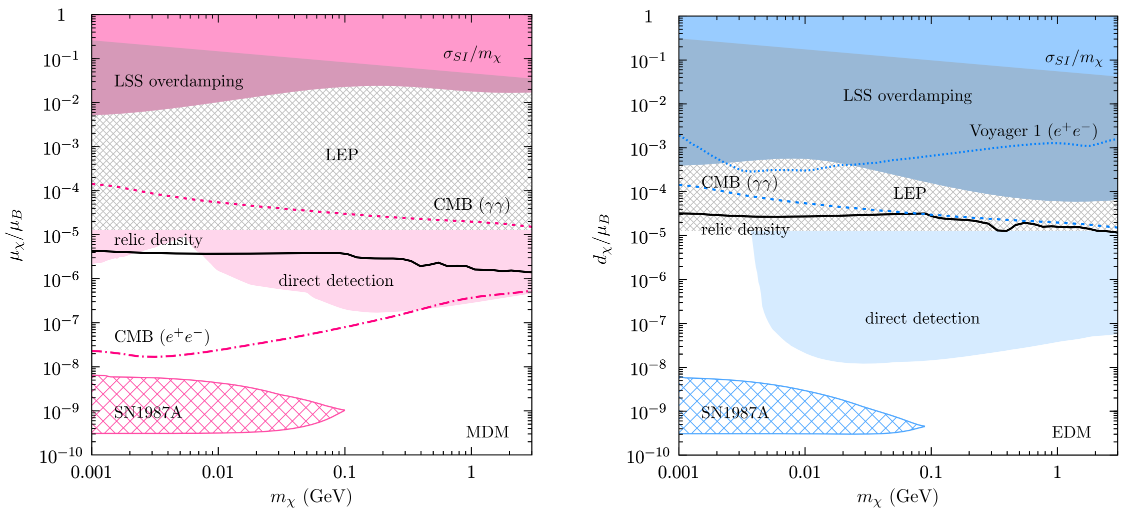

FIG. 10. Constraints on electromagnetic form factors for Dirac fermion DM with dim-5 operators from conventional direct/indirect/collider searches and cosmology. Bounds from indirect searches only apply to symmetric DM, while others are general. Parameters that generate the observed relic abundance via thermal freeze-out are illustrated by black lines.

F. Missing Energy at high-energy colliders

At high-energy colliders, sub-GeV particles χ can be produced kinematically unsuppressed, yielding limits on the couplings that are independent of m_χ. Among them, the strongest bounds on interactions studied here come from the LEP collider. Reference [52] has studied the L3 data with an integrated luminosity of 619/pb at CM energies $\sqrt{s} = 188.6$–209.2 GeV [81]. Using the monophoton channel, it was found that MDM and EDM models are constrained to

$$|\mu_\chi|\text{or}|d_\chi| < 1.3 \times 10^{-5}\mu_B. \tag{32}$$

The results can also be generalized to AM and CR interactions. Here we only adopt the high-energy single photon selection, which requires one photon with transverse momentum larger than $0.02\sqrt{s}$. Within the polar angular range $14° \leq \theta_\gamma \leq 166°$, in total 1898 events were reported while the SM expectations are 1905.1 events, mostly from $e^+e^- \to \nu\bar{\nu}\gamma(\gamma)$. Following Ref. [52], we use the eight data subsets with different kinematic regions of $\sqrt{s}$ studied in the single photon search in Ref. [81] and place 90% C.L. bounds on the couplings from the data subset that leads to the best constraints using the CLs method. We take a flat selection efficiency of 71% and a systematic background uncertainty of 1.1%, and obtain

$$|a_\chi|\text{or}|b_\chi| < 1.5 \times 10^{-5}\ \text{GeV}^{-2} \tag{33}$$

for the AM and CR models. Taking into account the low-energy selection would not significantly change these results. The limits are also shown in Figs. 10 and 11. While the bounds above are stronger than those derived from LHC

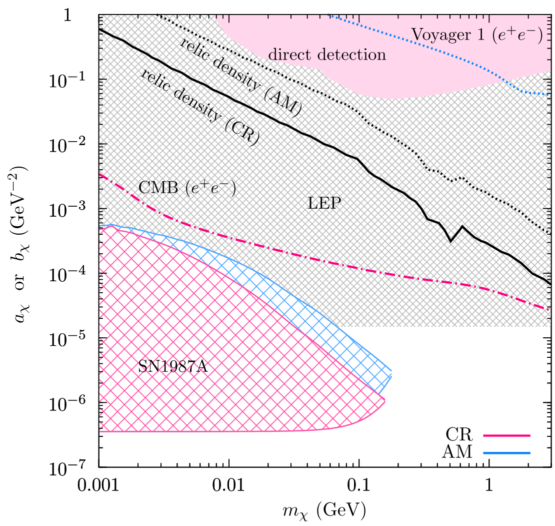

FIG. 11. Same as Fig. 10 for fermions with dim-6 operators. Constraints for AM are shown in blue and constraints for CR in pink. The LEP constraints are the same for both models.

data [82,83], future experiments, such as ILC and HL-LHC, may improve the sensitivity on these couplings by one to two orders of magnitude [84–86].

VI. χ DARK MATTER

If χ is long-lived on cosmological timescales, it may be DM. Additional laboratory, astrophysical, and cosmological limits then apply, which we discuss in this section.

A. Direct detection

Our primary interest is in the GeV and sub-GeV mass scale in m_χ. The elastic scattering cross sections on nuclei are given by the nonrelativistic expansion of Eq. (E2) in the incident energy of χ, $E_\chi \simeq m_\chi + m_\chi v^2/2$. In the case of the cross sections for EDM or MDM, the interaction of the dipole with the charge of the nucleus can be significantly enhanced by a small relative velocity. Direct detection experiments have put very stringent constraints on such models for m_χ above several GeV [87–89].

The sub-GeV region is better probed through DM-electron scattering as it allows to extend the conventional direct detection down to masses of $\sim$10 MeV [90,91], below which the halo DM kinetic energy falls below atomic ionization thresholds. First limits on even lower mass DM have been achieved by the use of semiconductor targets [92,93], by utilizing either a solar reflected velocity component [94] or a cosmic-ray accelerated component [95].

Limits on DM electron scattering are conventionally quoted in terms of a reference cross section [90]

$$\bar{\sigma}_e \equiv \frac{1}{16\pi(m_e + m_\chi)^2} \overline{|M_{\chi e}(q)|}^2_{q^2=\alpha^2 m_e^2}, \tag{34}$$

where $\overline{|M_{\chi e}(q)|}^2$ is the scattering amplitude on a free electron, evaluated at a typical atomic squared momentum transfer $q^2 = \alpha^2 m_e^2$; we list various $\overline{|M_{\chi e}(q)|}^2$ in Appendix E. The q-dependence of the actual ionization cross sections is moved into a DM-form factor and exclusion limits on $\bar{\sigma}_e$ have been derived for a constant form factor [94,96] and for one proportional to $1/q$ [91]. For MDM and CR, which correspond to constant form factors, we combine the bound from Ref. [96] based on the XENON10 data [97] and the bound in the low mass region by considering solar reflection [94] based on the XENON1T data [98]. For EDM, corresponding to a $1/q$ form factor, the XENON10 bound derived in Ref. [91] has been adopted here. These limits are shown in Figs. 10 and 11. For AM, the χ-electron scattering is velocity suppressed, and we estimate a relatively weak limit in the range $a_\chi \lesssim 0.1$–$10\ \mathrm{GeV}^{-2}$; we hence omit it in the figures below.

It should be noted that for the operators in Eq. (1) it is also possible that they induce transitions between mass-split (Majorana) states χ and χ^*. Once $\Delta m \equiv |m_{\chi^*} - m_\chi| \geq 100$ keV, such DM candidates can easily avoid any constraints from current direct detection experiments, see e.g., Refs. [54,99].

B. Dark radiation (N_{eff})

It is well known that (sub-)MeV mass particles, when they are thermally populated in the early Universe, will face severe limits from cosmology. χ particles with mass $m_\chi \lesssim$ few $\times$ MeV and couplings μ_χ, $d_\chi \geq 10^{-9}\mu_B$ or a_χ, $b_\chi \geq 5\times 10^{-5}\ \mathrm{GeV}^{-2}$ reach chemical equilibrium with the SM thermal bath once the early Universe's temperature exceeded $T_\gamma \sim m_\chi$. For example, the annihilation of χ into electron and photon pairs—if it continues after neutrino decoupling—heats the photon bath relative to the one of neutrinos, and hence modifies the effective number of neutrino species, N_{eff}, which in SM is given by $N_{\mathrm{eff}} = 3.045$ [100,101]. A general lower limit $m_\chi \gtrsim 7$–10 MeV has been derived for a Dirac fermion χ [102] based on the measurements by the Planck satellite, yielding $N_{\mathrm{eff}} = 3.15 \pm 0.23$ [2]; see also Refs. [103–105] for earlier work. Since the bound is subject to a model dependence when annihilation into other dark states (including neutrinos) is open, we do not show this bound explicitly in the figures below.

C. Kinetic decoupling

DM is required to kinetically decouple from the thermal bath after the photon temperature falls below 0.5 keV in order to avoid the overdamping of a large-scale structure (LSS) [106,107]. The kinetic decoupling temperature can be obtained by considering the transport scattering cross section between χ and target $i = e,\ p$,

$$\sigma_T^{\chi i} = \int (1-\cos\theta) \frac{d\sigma^{\chi i}}{d\Omega} d\Omega \simeq \sigma_0^{\chi i} v^n, \tag{35}$$

where θ is the CM scattering angle, and the cross section have been factored as a product of a constant $\sigma_0^{\chi i}$ and the nth power of the relative velocity v. The expressions for the various operators in leading order of v are listed in App. E. We find that $n = -2$ for EDM, $n = 0$ for MDM and CR, and $n = 2$ for AM. Then, assuming $T_\chi = T$ and demanding that the specific heating rate of DM particles derived in Ref. [108],

$$\sum_i \frac{2^{\frac{n+5}{2}}\Gamma(3+\frac{n}{2})}{\sqrt{\pi}} \frac{n_i m_i m_\chi}{(m_i + m_\chi)^2} \sigma_0^{\chi i} \left(\frac{T}{m_i} + \frac{T}{m_\chi}\right)^{\frac{n+1}{2}}, \tag{36}$$

be smaller than the Hubble rate, $H(T)$, from $T \sim 0.5$ keV to recombination, we obtain upper limits on the couplings. For dim-5 operators, they are shown as dark shaded regions labeled "LSS overdamping" in Fig. 10. As can be seen, the scaling of the cross section with v^{-2} makes the EDM case more stringently constrained. For fermions with dim-6 operators the bounds are too weak to be visible in Fig. 11. Our results on MDM and EDM agree with earlier studies [108,109].

The scattering processes tend to cool the gas in reverse. One can estimate the corresponding cooling rate using Eq. (36) by replacing n_i with $f_i n_\chi$, where f_i is the fraction of electron/proton particles involved in the interaction and n_χ gives the DM number density [110,111]. Therefore, cosmological 21 cm observations, such as recently reported by the EDGES experiment [112], may also constrain the couplings concerned here. Nevertheless, due to the minute free-electron fraction at redshift $z \sim 20$, $f_{e,p} \sim 10^{-4}$, the bounds will be much weaker than the ones from considering over-damping. Even for the EDM case with $n = -2$, in order to have the cooling rate comparable to the corresponding Hubble rate, one needs $d_\chi \sim \mu_B$ for $m_\chi = 10$ MeV.[12]

D. Self-scattering of χ

At low redshift, a strong self-interaction among light DM particles modifies the shape and density profile of DM halos, as well as the kinematics of colliding clusters. A fair amount of attention has been devoted to the study of millicharged DM, which exhibits a strong velocity dependence of the self-scattering cross section. For the models studied here, however, the corresponding interactions are not enhanced at low relative velocities, which can be seen explicitly the expression of the cross sections listed in App. H. Hence, we may directly use the constraint on the self-scattering cross section obtained from Bullet cluster observations, $\sigma_{\rm SI}/m_\chi \lesssim 1.25\ \mathrm{cm}^2/\mathrm{g}$ [114,115], to derive the bounds on MDM, EDM, CR and AM. Again, while the limits on CR and AM interactions are too weak to be shown, in Fig. 10 the ensuing constraints on MDM and EDM are shown by the shaded region labeled "$\sigma_{\rm SI}/m_\chi$." To be general, we do not take into account the scattering between χ and $\bar\chi$ particles, which, in any case, does not change our conclusion.

E. Supernova cooling

Light χ particles with $m_\chi \lesssim 400$ MeV can be produced in pairs inside supernovae (SN), and, if such particles escape from the core, it increases the SN cooling rate. In turn, if the coupling is only strong enough, the particles may reach thermal equilibrium, be trapped, and an energy loss argument does not immediately apply.

We estimate the region in parameter space where χ-particles affect the SN cooling as follows: if χ is thermalized within the SN core, a radius r_d can be estimated as the radius where the blackbody luminosity of χ equals the luminosity in neutrinos $L_\nu = 3 \times 10^{52}$ erg/s [116]. This is a maximum permissible luminosity if χ were to carry away this energy freely ("Raffelt criterion"). However, χ will typically be further deflected in elastic scatterings for $r > r_d$, engaging in a random walk before it reaches a free streaming radius that we take as $r_{\rm inf} = 50$ km. In order to estimate the efficiency of the trapping, as a rough criterion, we impose

$$\int_{r_d}^{r_{\rm inf}} dr \frac{\rho_p(r)}{m_p} \sigma_T^{\chi p} \le 2, \tag{37}$$

as an upper limit above which energy loss fails to be efficient; a similar argument has been used in Ref. [117] which we largely follow. We evaluate Eq. (37) by taking the SN numerical model of Ref. [118] with $T_\chi = T(r)$, and protons, with mass density $\rho_p(r)$, are assumed to be at rest as we focus on $m_\chi \ll m_p$. The value of r_d is then estimated from the SN model for each value of m_χ, and it ranges from 22 km for $m_\chi \sim$ MeV to 11.5 km for $m_\chi \sim 0.4$ GeV.

On the flip side, the lower boundary in couplings for energy loss to be efficient can be estimated by calculating the energy production rate of χ particles by electron-positron annihilation within the SN core,

$$\dot{Q} = \int \frac{d^3 p_{e^-} d^3 p_{e^+}}{(2\pi)^6} f_{e^-} f_{e^+} (\sigma_{e^- e^+ \to \chi\bar\chi} v) \sqrt{s}, \tag{38}$$

following Refs. [84,119,120].[13] The corresponding momentum distributions of electron and positron, f_{e^-} and f_{e^+}, as functions of the temperature and (opposite) chemical potentials for each r, are also given by the same SN model [118]. Setting the core size $r_{\rm core} = 10$ km, we derive the lower boundary by requiring

$$\int_0^{r_{\rm core}} d^3 r \dot{Q} \le L_\nu. \tag{39}$$

Both the lower and upper bounds discussed above are presented in Figs. 10 and 11. While these results are indicative of the relevant region in parameter space, a more detailed analysis may moderately but not qualitatively alter the results (e.g., Refs. [119,120]); we defer a more precise study of SN cooling to a dedicated future work.

In passing, we note that, besides SN, DM particles traversing the solar system may also be captured by the sun, affecting the stellar evolution. This has been studied in Refs. [55,121] for m_χ above 4 GeV. For lighter χ particles as we are concerned with in this work, any effect will be strongly suppressed due to immediate DM evaporation; see also Ref. [94].

F. Dark matter annihilation and indirect search

Here we consider the case that χ is a symmetric DM candidate, so that $\chi\bar\chi$ annihilation into light charged SM fermions and photons is operative both at CMB decoupling and at present day. The associated release of electromagnetic energy modifies the recombination history at high redshift and generates an excess in cosmic rays at low redshift.

For sub-GeV DM, the most stringent bounds typically come from CMB observations [122]. For MDM and CR DM particles, the annihilation to e^+e^- is s-wave, resulting in stringent limits on the relevant couplings. In contrast, for

[12]Note that the scattering cross section of χ with the dipole moment of hydrogen atoms always has $n \ge 0$, and thus is not velocity enhanced at low redshifts. This is different from the ϵQ case [113].

[13]For interactions studied here, the contribution from plasmon decay is either comparable or subleading and neglected for simplicity.

EDM and AM, where the annihilation cross sections to e^+e^- is p-wave and hence velocity suppressed, the leading bounds come from Voyager 1 data [123,124], and are relatively weaker. Moreover, CMB observations also strongly constrain the other annihilation channel, $\chi\bar{\chi} \to \gamma\gamma$. In contrast, gamma-ray telescope searches lead to bounds that are one to two orders of magnitude weaker in the sub-GeV region (see e.g., Ref. [125]), and are thus not shown in the figures. This channel is operative for MDM and EDM; for AM and CR, tree-level annihilation into physical photons vanishes identically. Here we will not further consider annihilation at loop-level (see e.g., Ref. [126]).

The bounds are summarized in Figs. 10 and 11. They show that MDM and CR, as symmetric DM candidates, are strongly constrained by the current observational data. Moreover, on-going and future experiments [112,127] have the potential to further improve the constraints on light DM annihilations soon.

VII. CONCLUSIONS AND OUTLOOK

In this paper, we consider the phenomenology of a new long-lived Dirac fermion χ in the MeV-GeV mass range and which interacts with the photon through mass-dimension-5 and -6 operators MDM, EDM and CR, AM, respectively, but is otherwise neutral. In a bottom-up approach, the existence of such states χ is constrained from intensity frontier and high energy collider experiments, from SM precision observables, from flavor physics, and, once the lifetime exceeds roughly one second, from cosmology and astrophysics. We have considered all these possibilities in turn and derived constraints on the dimensionful couplings. When not present in the current literature, we also derive analogous constraints on a potential millicharge of χ.

At intensity frontier experiments where these fermions can be produced in pairs, we focus on electron beams and show that the most stringent constraints on these models are currently set by monophoton searches at *BABAR* setting upper bounds on electric and magnetic dipole moments of $\sim 4 \times 10^{-5}\mu_B$ and on anapole moments and charge radius interactions of $\sim 2 \times 10^{-3}$ GeV^{-2}. Furthermore, we find that ongoing and future experiments, such as Belle II, LDMX and BDX, may extend the sensitivity by more than one order of magnitude. The projections for e^+e^--colliders discussed in this work are basically independent of the fermion mass m_χ across the whole MeV–GeV mass range, while the constraints from fixed target experiments exhibit a mass dependence that makes the interactions better testable in the low MeV-mass range. These results need to be compared to monophoton searches at high energy colliders. We find that LEP is superior in terms of present constraining power, but Belle-II and LDMX can improve the reach to smaller couplings in the dim-5 case. In the dim-6 case, however, due to the higher dimensionality of the coupling, we find that LEP remains the best probe for AM and CR interactions.

Next, we use a number of SM precision observables as an indirect test to constrain the parameter space further, albeit in a possibly more model dependent way than a direct observation can offer. For example, corrections to the vacuum polarization of the photon from the new interactions induce a running of the fine structure constant α, and we place a constraint on the respective new physics models that is even stronger than the bounds from accelerator experiments. However, we find that some of the operators contribute with a relative sign and cancellations are in principle possible. We also estimate the contribution to $(g-2)_\mu$ of the muon, concluding that the new interactions cannot contribute at the level of 3×10^{-9}—reflecting the current tension in this observable—without being in conflict with other direct searches, most notably with monophoton limits derived from *BABAR* data. In turn, relating $K^\pm \to \pi^\pm\chi\bar{\chi}$ and $B^\pm \to K^\pm\chi\bar{\chi}$ meson decays to analogous channels with missing energy we find that flavor observables yield only relatively weaker limits and are superseded by other intensity frontier searches. On the other hand, if χ also couples to the hypercharge field tensor with similar strength as to $F_{\mu\nu}$, the LEP observation on the invisible width of the Z-boson strongly constrains the whole parameter space which will be reachable by any of the future experiments discussed here. Clearly, the existence of such constraint hinges on the concrete UV realization that induces the studied dim-5 and dim-6 operators.

Finally, we have addressed the question on the possibility of χ being DM. If χ is to provide 100% of the DM abundance and has a mass below the GeV scale, direct detection constraints derived from DM-electron scattering are stronger than the limits derived from accelerators by 2 to 3 orders of magnitude for MDM and EDM. In contrast, we find that direct detection experiments have presently little sensitivity to AM and CR interactions when compared to other direct tests. In all cases, a combination of cosmological, astrophysical, direct detection and accelerator constraints rule out fermions with electromagnetic form factors making up 100% of the DM assuming a standard freeze-out scenario. If χ, however, only makes up a small fraction, $\lesssim 0.1\%$, of the DM abundance, one can evade the astrophysical constraints and will only be left with the accelerator and the supernova cooling constraints, which are independent of the DM relic density. For couplings smaller than μ_χ, $d_\chi \sim 10^{-9}\mu_B$ or a_χ, $b_\chi \sim 5 \times 10^{-5}$ GeV^{-2}, DM particles of MeV mass do not reach thermal equilibrium with the SM anymore, allowing for alternative production mechanisms in the early Universe and therefore in this region of parameter space fermions with EM form factors could still be DM without violating any constraints. Note that $\Delta N_{\rm eff}$ bounds also do not apply in this region of parameter space.

This work constitutes a systematic study of sub-GeV mass dark states carrying electromagnetic form factors.

Yet, many further avenues exist, which we are going to address in upcoming works:

First, we have focused on electron beams employed in intensity frontier searches. Once we consider protons as projectiles, a whole number of relevant experiments for similar analyses become available. Most notable are the proton beam dump facilities, such as E613 at Fermilab [128], SHIP at CERN's SPS [129] and the proposed MilliQan experiment at the LHC [130], as well as the neutrino detectors like MiniBooNE [131], DUNE [132], LSND [133] and CEνNS [134]. Studies of dark sectors along similar lines have already been performed in Refs. [56,135–137]. In order to systematically study χ-pair production from hadron beams, simulations are needed to generate event spectra because hadron physics cannot be neglected anymore. For example, in this set of experiments, contributions of the on shell production and subsequent decay of mesons π^0, $\eta \to \gamma\chi\bar{\chi}$ and $J/\psi, \Upsilon \to \chi\bar{\chi}$ will be non-negligible for the production of a $\chi\bar{\chi}$ pair when kinematically allowed. Working along the lines of our presented Appendixes for the 2-to-4 processes, a systematic write-up of the production process and derivation of the relevant kinematic quantities that feed into the computation of observables is in preparation, filling a gap in the existing literature.

Second, in this work we have considered a Dirac fermion χ for concreteness. A complex, but electrically neutral scalar particle ϕ can have dim-6 CR interactions. In addition, at the same mass dimension, a vector particle may carry electric and magnetic quadrupole moments. Finally, at mass-dimension 7, the Rayleigh or susceptibility operators alter the phenomenology: the elementary interaction involves two photons, so that either an additional loop-suppressing factor is present in signals with one external photon, or new signal topologies with two external photons need to be considered. We leave a systematic study of those possibilities for a future paper.

Third, in this paper we have chosen a bottom-up approach, leaving the UV physics that generates the dim-5 and dim-6 operators unspecified. Such UV completion will result in additional constraints, most prominently from high energy colliders, in particular when the value of the effective dimensionful coupling points towards generating physics that must be at or below the TeV-scale. Such program for electroweak-scale particles has recently been started in Ref. [22]. Given the relatively weak intensity frontier limits on dim-6 couplings, our considered parameter space is likely further constrained by the presence of additional particles carrying electromagnetic charge and/or hypercharge.

Fourth, a more systematic study of cosmological and astrophysical constraints can be performed. For example, the limits on supernova cooling are derived on simplifying assumptions, and a more detailed study incorporating finite temperature effects and a better simulation of the efficiency of trapping may alter the inferred regions in parameter space, albeit only moderately. Finally, we have shown that a χ particle that freezes-out at the appropriate relic DM density is already ruled out. On the other hand, once the couplings diminish, χ may freeze-in, and a detailed computation of its abundance as a function of mass and interaction strength as well as a discussion on its detectability is still outstanding.

Dark sector particles with mass below the GeV-scale that are perfectly electrically neutral may still interact with the photon through a number of higher-dimensional operators. The question how strong such coupling can be and "how dark is dark" is an experimental one. In this paper we have answered it utilizing currently available experimental observables and provided forecasts to clarify the detectability with the future experimental program that is coming online or is considered.

ACKNOWLEDGMENTS

We thank M. Battaglieri, A. Hoang, Z. Ligeti, M. Passera, A. Ritz for helpful discussions. The authors are supported by the New Frontiers program of the Austrian Academy of Sciences. L. S. is supported by the Austrian Science Fund FWF under the Doctoral Program W1252-N27 Particles and Interactions. We acknowledge the use of computer packages for algebraic [138,139] and numeric [140] evaluations.

APPENDIX A: MATRIX ELEMENTS FOR EMISSION

In this Appendix we provide the detailed calculation of the pair production of two long-lived particles χ through their electromagnetic form factors. From the interaction operators (1) we derive the Feynman rules $i\Gamma^\mu(q)$ with incoming photon four momentum q and

$$\epsilon\text{Q}:\ \Gamma^\mu(q) = +\epsilon e \gamma^\mu, \tag{A1a}$$

$$\text{MDM}:\ \Gamma^\mu(q) = +i\mu_\chi \sigma^{\mu\nu} q_\nu, \tag{A1b}$$

$$\text{EDM}:\ \Gamma^\mu(q) = -d_\chi \sigma^{\mu\nu} q_\nu \gamma^5, \tag{A1c}$$

$$\text{AM}:\ \Gamma^\mu(q) = -a_\chi [q^2\gamma^\mu - q^\mu \not{q}]\gamma^5, \tag{A1d}$$

$$\text{CR}:\ \Gamma^\mu(q) = +b_\chi [q^2\gamma^\mu - q^\mu \not{q}]. \tag{A1e}$$

Hermiticity of the electromagnetic current implies $\bar{\Gamma}^\mu(q) = \Gamma^\mu(-q)$ where $\bar{\Gamma} = \gamma^0\Gamma^\dagger\gamma^0$ is the Dirac adjoint.

We wish to compute the scattering cross section of e^- on a nucleus N with emission of a $\chi\bar{\chi}$ pair and into a potentially inclusive hadronic n-particle final state X_n,

$$N(p_1) + e^-(p_2) \to X_n(p_3) + e^-(p_4) + \chi(p_\chi) + \bar{\chi}(p_{\bar{\chi}}), \tag{A2}$$

where $p_3 = \sum_{i=1}^n p_{3,i}$ is the total inclusive four momentum of the recoiling target, potentially fragmented into n states. We introduce the momentum transfer variables

$$q \equiv p_\chi + p_{\bar\chi}, \qquad q_1 \equiv p_1 - p_3, \qquad q_2 \equiv p_2 - p_4, \tag{A3}$$

such that $q = q_1 + q_2$ which follows from overall energy-momentum conservation. Since q, q_1, q_2 are linearly dependent, we express the scattering by the six independent momenta p_1, p_2, q, q_1, q_2, p_χ and their scalar products.

The matrix elements for the processes depicted in Fig. 1(b) can split into the emission piece of the $\chi\bar\chi$-pair, $\mathcal{M}_\chi^\nu = \bar u(p_\chi)\Gamma^\nu(q)v(p_{\bar\chi})$, and the scattering piece on the nucleus, $\mathcal{M}_N$,

$$\mathcal{M}_{N,a}^\mu = \frac{e^2 g_{\rho\sigma}}{q_1^2[(p_4+q)^2 - m_e^2]} \times \langle p_3|J^\rho(0)|p_1\rangle \times [\bar u(p_4)\gamma^\mu(\not p_4 + \not q + m_e)\gamma^\sigma u(p_2)], \tag{A4a}$$

$$\mathcal{M}_{N,b}^\mu = \frac{e^2 g_{\rho\sigma}}{q_1^2[(p_2-q)^2 - m_e^2]} \times \langle p_3|J^\rho(0)|p_1\rangle \times [\bar u(p_4)\gamma^\sigma(\not p_2 - \not q + m_e)\gamma^\mu u(p_2)], \tag{A4b}$$

where $\langle p_3|J_\rho(0)|p_1\rangle = \langle J_\rho\rangle$ is the hadronic matrix element of the electromagnetic current. The overall matrix element for the emission is hence,

$$\mathcal{M} = \frac{1}{q^2}(\mathcal{M}_{N,a}^\mu + \mathcal{M}_{N,b}^\mu)(\mathcal{M}_\chi)_\mu, \tag{A5}$$

where we have dropped all gauge-dependent pieces as is manifest for when q gets dotted into the vertices (A5). In addition, the q_1 gauge-dependent part of the photon propagator in Eq. (A5) drops out when being dotted into the hadronic matrix element, $q_{1,\nu}\langle p_3|J^\nu(0)|p_1\rangle = 0$, so that we omitted those terms above as well.

The differential cross section for the process (A2) then reads,

$$d\sigma = \frac{1}{4E_1E_2|\boldsymbol{v}_1 - \boldsymbol{v}_2|}|\overline{\mathcal{M}}|^2 d\Phi, \tag{A6}$$

where $v_{1,2}$ are the velocities of the incoming particles and the total phase space

$$d\Phi = \prod_{i=1}^n \frac{d^3p_{3,i}}{(2\pi)^3 2E_{3,i}} \prod_{j=4}^6 \frac{d^3p_j}{(2\pi)^3 2E_j} \times (2\pi)^4\delta^{(4)}\left(p_1 + p_2 - \sum_{i=1}^n p_{3,i} - \sum_{j=4}^6 p_j\right). \tag{A7}$$

Here $p_{5,6} = p_{\bar\chi,\chi}$. One can further introduce to Eq. (A7) an integral with respect to $s_X = m_X^2 = p_3^2$ to obtain

$$d\Phi = 2ds_X d\Phi_4 \frac{1}{4\pi}\prod_{i=1}^n \frac{d^3p_{3,i}}{(2\pi)^3 2E_{3,i}}(2\pi)^4\delta^{(4)}\left(p_3 - \sum_{i=1}^n p_{3,i}\right), \tag{A8}$$

where $d\Phi_4$ is the 4-body phase space of p_j ($j = 3,4,5,6$)—which will explicitly be solved analytically in Appendixes C and D—and where the second line will be absorbed by the hadronic tensor $W_{\rho\sigma}$ defined below.

In the lab-frame where $|\boldsymbol{v}_1| = 0$, the cross section can be written as

$$d\sigma = \frac{(4\pi\alpha)^3}{2|\boldsymbol{p}_2|m_N q^4 q_1^4} L^{\rho\sigma,\mu\nu}\chi_{\mu\nu}(q)W_{\rho\sigma}(-q_1)ds_X d\Phi_4, \tag{A9}$$

where $\chi_{\mu\nu}$ is the χ emission piece. The electron scattering, averaged (summed) over the initial (final) spins is described by the terms

$$L^{\rho\sigma,\mu\nu} = \frac{L_a^{\rho\sigma,\mu\nu}}{[(p_4+q)^2 - m_e^2]^2} + \frac{L_b^{\rho\sigma,\mu\nu}}{[(p_2-q)^2 - m_e^2]^2} + \frac{2L_{ab}^{\rho\sigma,\mu\nu}}{[(p_4+q)^2 - m_e^2][(p_2-q)^2 - m_e^2]} \tag{A10}$$

with

$$L_a^{\rho\sigma,\mu\nu} = \frac{1}{2}\mathrm{Tr}[(\not p_4 + m_e)\gamma^\mu(\not p_4 + \not q + m_e) \times \gamma^\rho(\not p_2 + m_e)\gamma^\sigma(\not p_4 + \not q + m_e)\gamma^\nu], \tag{A11a}$$

$$L_b^{\rho\sigma,\mu\nu} = \frac{1}{2}\mathrm{Tr}[(\not p_2 + m_e)\gamma^\nu(\not p_2 - \not q + m_e) \times \gamma^\sigma(\not p_4 + m_e)\gamma^\rho(\not p_2 - \not q + m_e)\gamma^\mu], \tag{A11b}$$

$$L_{ab}^{\rho\sigma,\mu\nu} = \frac{1}{2}\mathrm{Tr}[(\not p_4 + m_e)\gamma^\mu(\not p_4 + \not q + m_e) \times \gamma^\rho(\not p_2 + m_e)\gamma^\nu(\not p_2 - \not q + m_e)\gamma^\sigma]. \tag{A11c}$$

The emission of the $\chi\bar\chi$ pair is captured in the final state spin-summed matrix element $\chi_{\mu\nu}$ given by,

$$\chi_{\mu\nu}(q) = \mathrm{Tr}[(\not p_\chi + m_\chi)\Gamma_\mu(q)(\not p_{\bar\chi} - m_\chi)\bar\Gamma_\nu(q)]. \tag{A12}$$

APPENDIX B: HADRONIC TENSOR AND FORM FACTORS

The response of the nuclear target is described by a hadronic tensor in Eq. (A9). In its general form, $W_{\sigma\rho}(-q_1)$ is given by,

$$W_{\sigma\rho}(-q_1) = \frac{1}{4\pi}\left(\frac{1}{2s+1}\sum_s\right)\sum_n \int \prod_{i=1}^{n} \frac{d^3\boldsymbol{p}'_{3,i}}{(2\pi)^3 2E_{p'_{3,i}}} \times (2\pi)^4 \delta^{(4)}\left(p_1 - q_1 - \sum_{i=1}^{n} p_{3,i}\right) \times \sum_{s'_{3,i}} \langle p_1, s|J^\dagger_\sigma(0)|X_n\rangle\langle X_n|J_\rho(0)|p_1, s\rangle = \frac{\sum_s \int d^4x e^{-iq_1\cdot x}\langle p_1, s|[J^\dagger_\sigma(x), J_\rho(0)]|p_1, s\rangle}{4\pi(2s+1)}, \tag{B1}$$

where the δ-function is from overall energy-momentum conservation and in this context guarantees that the fragments have the overall momentum p_3. The most general (parity conserving) form for Eq. (B1) is

$$W^{\rho\sigma} = \left[-g^{\rho\sigma} + \frac{q_1^\rho q_1^\sigma}{q_1^2}\right] W_1(q_1^2, s_X) + \left[p_1^\rho - \frac{p_1\cdot q_1}{q_1^2} q_1^\rho\right]\left[p_1^\sigma - \frac{p_1\cdot q_1}{q_1^2} q_1^\sigma\right] \frac{W_2(q_1^2, s_X)}{m_N^2}, \tag{B2}$$

where the form factors W_1 and W_2 are functions of q_1^2 and s_X.

In the elastic limit $s_X = m_N^2$ and $q_1^2 = 2(p_1\cdot q_1)$ and $W_{1,2}$ are only functions of q_1^2. For spin-1/2 fermions, they are related to the usual electric and magnetic form factors F_E and F_M via

$$W_1(q_1^2) = -q_1^2 F_M^2(q_1^2)\frac{\delta(s_X - m_N^2)}{2}, \tag{B3a}$$

$$W_2(q_1^2) = \frac{4m_N^2 F_E^2(q_1^2) - q_1^2 F_M^2(q_1^2)}{1 - q_1^2/(4m_N^2)} \frac{\delta(s_X - m_N^2)}{2}, \tag{B3b}$$

whereas for a scalar target they read,

$$W_1(q_1^2) = 0, \tag{B4a}$$

$$W_2(q_1^2) = 4m_N^2 F_E^2(q_1^2)\frac{\delta(s_X - m_N^2)}{2}. \tag{B4b}$$

When considering the scattering on protons p or neutrons n, the form factors can be taken in the dipole form [141],

$$F_E^p(t) = \frac{1}{(1 + t/0.71\ \mathrm{GeV}^2)^2}, \tag{B5a}$$

$$F_E^n(t) = -\frac{\mu_n t}{(4m_n^2 + 5.6t)} F_E^p(t), \tag{B5b}$$

and $F_M^{p,n} = \mu_{p,n} F_E^{p,n}$ where $t = -q_1^2$ and $\mu_{p,n}$ are the magnetic moments of proton and electron in units of the nuclear magneton $\mu_N = e/2m_p$, respectively; with $\mu_p = 2.79$ and $\mu_n = -1.91$.

For nuclear targets of charge Z, the electric form factor is given by

$$F_E(t) = Z \cdot \frac{a^2(Z)t}{1 + a(Z)^2 t}\frac{1}{1 + t/d(A)}, \tag{B6}$$

where A is the mass number and $a(Z) = 111Z^{1/3}/m_e$ and $d(A) = 0.164\ \mathrm{GeV}^2 A^{-2/3}$ [142,143]. The above expression includes a factor that accounts for the screening of Z by electrons such that $F_E(t) = 0$ for $t \to 0$. Finally, in our numeric evaluations we neglect the magnetic form factor for $Z \gg 1$, as it is generally subleading. We note in passing, that for heavy states χ, inelastic scattering may start to play a significant role [25].

APPENDIX C: 4-BODY PHASE SPACE FOR LDMX AND NA64

NA64 and LDMX measure the energy and momentum of the final state electron. Therefore we want to show the most important steps in our calculation of the covariant phase space for the elastic scattering process in Fig. 1(b) with $X_n = N$.

While a 4-body phase space has 12 degrees of freedom, 4 of them can be reduced by the momentum-energy conservation, and another one, the rotation along the axis of $\boldsymbol{p}_1 + \boldsymbol{p}_2$, is redundant. That is, only 7 of them are necessary to express the squared amplitude, and we obtain here:

$$\frac{d\Phi_4}{ds_{3\chi\bar\chi}dq_2^2} = \frac{|J|}{16(2\pi)^6}\frac{ds_{\chi\bar\chi}}{s_{\chi\bar\chi}} dq_1^2 \frac{\lambda^{1/2}(s_{\chi\bar\chi}, m_\chi^2, m_\chi^2)}{\lambda^{1/2}(s_{3\chi\bar\chi}, m_N^2, q_2^2)} \times du_{2q}\left|\frac{\partial\phi_3^{R3\chi\bar\chi}}{\partial u_{2q}}\right| \frac{d\Omega_\chi^{R\chi\bar\chi}}{4\pi}. \tag{C1}$$

The phase space can be described with the 5 independent Lorentz invariant integration variables $s_{3\chi\bar\chi} = (p_3 + p_\chi + p_{\bar\chi})^2$, $s_{\chi\bar\chi} = q^2 = (p_\chi + p_{\bar\chi})^2$ and $u_{2q} = p_2\cdot q$ as well as $q_1^2 = (p_1 - p_3)^2$ and $q_2^2 = (p_2 - p_4)^2$ with all momenta defined as in App. A. The other 2 degrees of freedom come from $\Omega_\chi^{R\chi\bar\chi}$, the solid angle of $\boldsymbol{p}_\chi$ in the CM frame of the $\chi\bar\chi$ pair (which will be integrated out). $\phi_3^{R3\chi\bar\chi}$ is the azimuthal angle of p_3 in the frame where $\boldsymbol{p}_3 + \boldsymbol{p}_\chi + \boldsymbol{p}_{\bar\chi} = 0$, $\lambda(a,b,c) = a^2 + b^2 + c^2 - 2(ab + ac + bc)$ is the triangle function. The Jacobian of the transformation from E_4 and $\cos\theta_4$ to the invariant variables $s_{3\chi\bar\chi}$ and q_2^2 is given by

$$\frac{\partial(E_4, \cos\theta_4)}{\partial(s_{3\chi\bar\chi}, q_2^2)} = \frac{|J|}{|\boldsymbol{p}_4|} \equiv \frac{\lambda^{-1/2}(s, m_N^2, m_e^2)}{2|\boldsymbol{p}_4|}. \tag{C2}$$

The integration boundaries for the invariant masses $s_{\chi\bar\chi}$ and $s_{3\chi\bar\chi}$ are

$$(m_N + 2m_\chi)^2 \le s_{3\chi\bar\chi} \le (\sqrt{s} - m_e)^2,$$
$$(2m_\chi)^2 \le s_{\chi\bar\chi} \le (\sqrt{s_{3\chi\bar\chi}} - m_N)^2. \tag{C3}$$

The integration boundaries of the t-channel variables q_1^2 and q_2^2 are

$$[q_1^2]^\pm = 2m_N^2 - \frac{(s_{3\chi\bar\chi} + m_N^2 - q_2^2)(s_{3\chi\bar\chi} + m_N^2 - s_{\chi\bar\chi})}{2s_{3\chi\bar\chi}} \mp \frac{\lambda^{1/2}(s_{3\chi\bar\chi}, m_N^2, q_2^2)\lambda^{1/2}(s_{3\chi\bar\chi}, m_N^2, s_{\chi\bar\chi})}{2s_{3\chi\bar\chi}}, \tag{C4a}$$

$$[q_2^2]^\pm = 2m_e^2 - \frac{(s + m_e^2 - m_N^2)(s + m_e^2 - s_{3\chi\bar\chi})}{2s} \mp \frac{\lambda^{1/2}(s, m_e^2, m_N^2)\lambda^{1/2}(s, m_e^2, s_{3\chi\bar\chi})}{2s}. \tag{C4b}$$

At last, the angular variable u_{2q} is given by

$$u_{2q} = \frac{(p_1 \cdot p_2)G_2(p_1, q_2; q_2, q)}{-\Delta_2(p_1, q_2)} - \frac{(q_2 \cdot p_2)G_2(p_1, q_2; p_1, q)}{-\Delta_2(p_1, q_2)} + \frac{\sqrt{\Delta_3(p_1, q_2, p_2)\Delta_3(p_1, q_2, q)}}{-\Delta_2(p_1, q_2)} \cos\phi_3^{R3\chi\bar\chi}, \tag{C5}$$

from which one can easily obtain the boundaries of u_{2q} with $\phi_3^{R3\chi\bar\chi} \in \{0, \pi\}$, as well as the expression of $|\frac{\partial\phi_3^{R3\chi\bar\chi}}{\partial u_{2q}}|$. In Eq. (C5), G_n is the Gram determinant of dimension n and Δ_n the respective Cayley determinant (or symmetric Gram determinant) [144]. The double differential cross section in the lab frame obviously follows from Eq. (C1) as

$$\frac{d\sigma}{dE_4 d\cos\theta_4} = \frac{|\boldsymbol{p}_4|}{4E_2 m_N |\boldsymbol{v}_2|} \int \frac{d\Phi_4}{ds_{3\chi\bar\chi} dq_2^2} \frac{1}{|J|} |\mathcal{M}|^2. \tag{C6}$$

For LDMX and NA64 where we are not interested in the direction of the χ pair, we can integrate out the part $\Omega_\chi^{R\chi\bar\chi}$ immediately, using the quantity defined below

$$X_{\mu\nu}(q) \equiv \int \frac{d\Omega_\chi^{R\chi\bar\chi}}{4\pi} \chi_{\mu\nu}(q) \tag{C7a}$$

$$= f(s_{\chi\bar\chi})\left(-g_{\mu\nu} + \frac{q_\mu q_\nu}{s_{\chi\bar\chi}}\right) \tag{C7b}$$

with $f(s_{\chi\bar\chi})$ found in the main text (7). This is because the rest of the squared amplitude is independent of $\Omega_\chi^{R\chi\bar\chi}$.

APPENDIX D: 4-BODY PHASE SPACE FOR mQ AND BDX

Since mQ and BDX ought to detect the produced dark fermions directly via elastic scattering on nuclei and electrons, we are interested in the direction of one of the fermions—denoted as θ_χ below—instead of the direction of the final state electron.

Note that there are seven independent Lorentz invariants for the full 4-body phase space. In this case, the phase space can be given by

$$\frac{d\Phi_4}{ds_{34\bar\chi} dt_{2\chi}} = ds_{4\bar\chi} dq_1^2 dt_{14} \frac{d\phi_3}{2\pi} \frac{d\phi_4}{2\pi} \frac{|J|}{(4\pi)^5} \times \lambda^{-1/2}(s_{34\bar\chi}^2, m_N^2, t_{2\chi})\lambda^{-1/2}(s_{4\bar\chi}^2, m_N^2, q_{23\chi}^2), \tag{D1}$$

where the Lorentz invariant integration variables are $s_{34\bar\chi} = (p_3 + p_4 + p_{\bar\chi})^2$, $t_{2\chi} = (p_2 - p_\chi)^2$, $s_{4\bar\chi} = (p_4 + p_{\bar\chi})^2$, $q_1^2 = (p_1 - p_3)^2$ and $t_{14} = (p_1 - p_4)^2$, as well as the 4-vector $q_{23\chi} = p_2 - p_3 - p_\chi$, with $q_{23\chi}^2 = m_N^2 + m_X^2 + s_{4\bar\chi} + t_{14} - s_{34\bar\chi} - q_1^2$. Here we fix the value of the effective mass of hadronic final states X_n, denoted as m_X. The other two independent Lorentz invariants are chosen to be $p_2 \cdot p_3$ and $p_3 \cdot p_4$, which can be calculated as

$$p_2 \cdot p_3 = \frac{(p_1 \cdot p_2)G_2(p_1, p_2 - p_\chi; p_2 - p_\chi, p_3)}{-\Delta_2(p_1, p_2 - p_\chi)} - \frac{(m_e^2 - p_2 \cdot p_\chi)G_2(p_1, p_2 - p_\chi; p_1, p_3)}{-\Delta_2(p_1, p_2 - p_\chi)} - \frac{\sqrt{\Delta_3(p_1, p_2 - p_\chi, p_2)\Delta_3(p_1, p_2 - p_\chi, p_3)}}{-\Delta_2(p_1, p_2 - p_\chi)} \cos\phi_3 \tag{D2}$$

and

$$p_3 \cdot p_4 = \frac{(p_1 \cdot p_3)G_2(p_1, q_{23\chi}; q_{23\chi}, p_4)}{-\Delta_2(p_1, q_{23\chi})} - \frac{(q_{23\chi} \cdot p_3)G_2(p_1, q_{23\chi}; p_1, p_4)}{-\Delta_2(p_1, q_{23\chi})} - \frac{\sqrt{\Delta_3(p_1, q_{23\chi}, p_3)\Delta_3(p_1, q_{23\chi}, p_4)}}{-\Delta_2(p_1, q_{23\chi})} \cos\phi_4, \tag{D3}$$

where ϕ_3 and ϕ_4 are the angle between the two planes defined by $(\boldsymbol{p}_2 - \boldsymbol{p}_\chi, \boldsymbol{p}_2)$ and $(\boldsymbol{p}_2 - \boldsymbol{p}_\chi, \boldsymbol{p}_3)$ in the frame where $\boldsymbol{p}_1 + \boldsymbol{p}_2 - \boldsymbol{p}_\chi = 0$, and the angle between the two planes defined by $(\boldsymbol{q}_{23\chi}, \boldsymbol{p}_3)$ and $(\boldsymbol{q}_{23\chi}, \boldsymbol{p}_4)$ in the frame where $\boldsymbol{p}_1 + \boldsymbol{q}_{23\chi} = 0$, respectively. Both scalar products are also functions of $s_{34\bar\chi}^2$, $t_{2\chi}$, $s_{4\bar\chi}^2$, q_1^2, and t_{14} defined above.

Note that the values of ϕ_3 and ϕ_4 remain the same after being transformed into the lab frame.

The integration ranges of $s_{34\bar{\chi}}$ are given by

$$(m_X + m_e + m_\chi)^2 \leq s_{34\bar{\chi}} \leq (\sqrt{s} - m_\chi)^2, \tag{D4}$$

and that of $t_{2\chi}$ are

$$[t_{2\chi}]^{\pm} = m_e^2 + m_\chi^2 - \frac{(s + m_e^2 - m_N^2)(s + m_\chi^2 - s_{34\bar{\chi}})}{2s} \mp \frac{\lambda^{1/2}(s, m_e^2, m_N^2)\lambda^{1/2}(s, m_\chi^2, s_{34\bar{\chi}})}{2s}. \tag{D5}$$

For $s_{4\bar{\chi}}$, we have

$$(m_4 + m_\chi)^2 \leq s_{4\bar{\chi}} \leq \left(\sqrt{s_{34\bar{\chi}}^2} - m_X\right)^2. \tag{D6}$$

And the upper and lower bounds of t_{13} are given by

$$[q_1^2]^{\pm} = m_N^2 - \frac{(s_{34\bar{\chi}} + m_N^2 - t_{2\chi})(s_{34\bar{\chi}} + m_X^2 - s_{4\bar{\chi}})}{2s_{34\bar{\chi}}} + m_X^2 \mp \frac{\lambda^{1/2}(s_{34\bar{\chi}}, m_N^2, t_{2\chi})\lambda^{1/2}(s_{34\bar{\chi}}, m_X^2, s_{4\bar{\chi}})}{2s_{34\bar{\chi}}}, \tag{D7}$$

and the upper and lower bounds of t_{14} are

$$[t_{14}]^{\pm} = m_N^2 - \frac{[s_{4\bar{\chi}} + m_N^2 - q_{23\chi}^2][q_{23\chi}^2 + m_e^2 - m_\chi^2]}{2s_{4\bar{\chi}}} + m_e^2 \mp \frac{\lambda^{1/2}(s_{4\bar{\chi}}, m_N^2, q_{23\chi}^2)\lambda^{1/2}(s_{4\bar{\chi}}, m_e^2, m_\chi^2)}{2s_{4\bar{\chi}}}. \tag{D8}$$

At last, the integration ranges of ϕ_3 and ϕ_4 are both from 0 to 2π.

Note that one Lorentz invariant needs to be given by the equation $\det[\mathcal{M}] = 0$, where the (i, j) entry of the 5×5 matrix $\mathcal{M}$ is the scalar product of p_i and p_j. This equality is due to the requirement that in four-dimensional space-time, any five 4-vectors cannot be linearly independent. We use this requirement to obtain the value of $(p_\chi \cdot p_{\bar{\chi}})$ from the seven Lorentz invariants above. Moreover, there are two solutions of $p_\chi \cdot p_{\bar{\chi}}$ from $\det[\mathcal{M}] = 0$. This can be understood in the frame where $\boldsymbol{p}_1 + \boldsymbol{q}_{23\chi} = 0$, as shown in Fig. 12. The two constraints derived from t_{14} and $p_3 \cdot p_4$, illustrated by the circles at the bottom of the two cones, cannot uniquely fix $\boldsymbol{p}_4$ (and thus $\boldsymbol{p}_{\bar{\chi}}$). Nevertheless, the degeneracy can be broken by fixing the rotation direction of ϕ_4, as can be seen from Fig. 12. Here we take one solution of $p_\chi \cdot p_{\bar{\chi}}$ for $\phi_4 \in [0, \pi)$ and the other for $\phi_4 \in [\pi, 2\pi)$. Other Lorentz invariants are not affected by $\phi_4 \leftrightarrow 2\pi - \phi_4$.

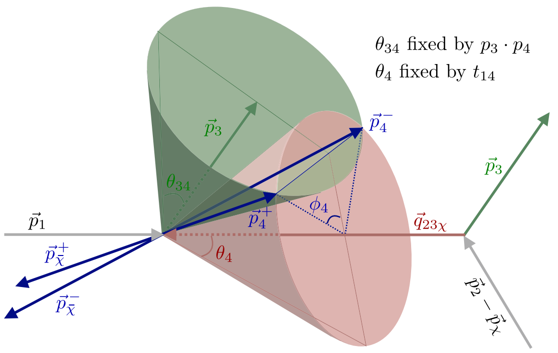

FIG. 12. Illustration of the solutions of $p_\chi \cdot p_{\bar{\chi}}$ to $\det[\mathcal{M}] = 0$ in the frame where $\boldsymbol{p}_1 + \boldsymbol{q}_{23\chi} = 0$. The direction of ϕ_4, the angle between the two planes defined by $(\boldsymbol{q}_{23\chi}, \boldsymbol{p}_3)$ and $(\boldsymbol{q}_{23\chi}, \boldsymbol{p}_4)$, breaks the degeneracy.

In the lab frame, we have

$$\frac{d\sigma}{dE_\chi d\cos\theta_\chi} = \frac{|\boldsymbol{p}_\chi|}{4E_2 m_N |\boldsymbol{v}_2|} \int \frac{d\Phi_4}{ds_{34\bar{\chi}} dt_{2\chi}} \frac{1}{|J|} |\mathcal{M}|^2, \tag{D9}$$

where in the limit of $m_e \to 0$ the available range of E_χ is

$$E_\chi \geq \frac{m_\chi(E_2 + m_N)}{\sqrt{m_N(2E_2 + m_N)}}, \tag{D10a}$$

$$E_\chi \leq \frac{(E_2 + m_N)}{2}\left(1 - \frac{m_X(2m_\chi + m_X)}{m_N(2E_2 + m_N)}\right) + \frac{E_2\sqrt{m_N(2E_2 + m_N) - (2m_\chi + m_X)^2}}{2m_N(2E_2 + m_N)} \times \sqrt{m_N(2E_2 + m_N) - m_X^2}, \tag{D10b}$$

and the corresponding range of $\cos\theta_\chi$ is

$$1 \geq \cos\theta_\chi \geq \max\left\{-1, \frac{E_\chi - m_N}{\sqrt{E_\chi^2 - m_\chi^2}} + \frac{m_N(2E_\chi - m_N) + m_X(2m_\chi + m_X)}{2E_2\sqrt{E_\chi^2 - m_\chi^2}}\right\}.$$

It is straightforward to also take into account the contribution of inelastic scattering between electron beam and the target by setting m_X, or equivalently s_X, variable, and by introducing the inelastic form factor of the target. Nevertheless, such a contribution is in general subleading, so following Refs. [42,53] we neglect it here and take $m_X = m_N$ to obtain our numerical results.

APPENDIX E: ELASTIC SCATTERING CROSS SECTIONS

Here, we present the full relativistic form of the differential recoil cross section of a nucleus with charge Z, electric and magnetic form factors F_E and F_M, mass m_N and spin I_N when scattering on a fermion χ with mass m_χ and energy E_χ,

$$\frac{d\sigma}{dE_R}=\frac{1}{A}\left[g_E(E_R)\alpha Z^2F_E^2(t)+g_M(E_R)\frac{\mu_N^2m_N^2}{\pi}\frac{I_N+1}{3I_N}F_M^2(t)\right], \tag{E1}$$

where $A=(E_\chi^2-m_\chi^2)(2m_N+E_R)$ and the functions $g_E(E_R)$ and $g_M(E_R)$ for all models are given by

$$\epsilon\mathrm{Q}:\ \frac{g_E}{\epsilon^2e^2}=\frac{1}{2E_R^2}(2E_\chi^2-m_NE_R-2E_\chi E_R)$$
$$\frac{g_M}{\epsilon^2e^2}=\frac{1}{4m_NE_R}(2E_\chi^2-2m_\chi^2+E_R^2)+\frac{1}{4m_N^2}(m_N^2-m_\chi^2-2m_NE_\chi), \tag{E2a}$$

$$\mathrm{MDM}:\ \frac{g_E}{\mu_\chi^2}=\frac{m_N}{2E_R}(4E_\chi^2-4m_\chi^2+E_R^2)-(m_\chi^2+2m_NE_\chi)$$
$$\frac{g_M}{\mu_\chi^2}=\frac{E_R}{2m_N}(m_\chi^2-m_N^2-2m_NE_\chi)+(E_\chi^2+m_\chi^2), \tag{E2b}$$

$$\mathrm{EDM}:\ \frac{g_E}{d_\chi^2}=\frac{m_N}{2E_R}(E_R-2E_\chi)^2$$
$$\frac{g_M}{d_\chi^2}=-\frac{E_R}{2m_N}(m_N^2+m_\chi^2+2m_NE_\chi)+(E_\chi^2-m_\chi^2), \tag{E2c}$$

$$\mathrm{AM}:\ \frac{g_E}{a_\chi^2}=-2m_NE_R(m_N^2+m_\chi^2+2m_NE_\chi)+4m_N^2(E_\chi^2-m_\chi^2)$$
$$\frac{g_M}{a_\chi^2}=m_NE_R(2E_\chi^2+2m_\chi^2+E_R^2)+E_R^2(m_N^2+m_\chi^2-2m_NE_\chi), \tag{E2d}$$

$$\mathrm{CR}:\ \frac{g_E}{b_\chi^2}=2m_N^2(2E_\chi^2-m_NE_R-2E_\chi E_R)$$
$$\frac{g_M}{b_\chi^2}=m_NE_R(2E_\chi^2-2m_\chi^2+E_R^2)+E_R^2(m_N^2-m_\chi^2-2m_NE_\chi). \tag{E2e}$$

where $t=2m_NE_R$; the form factors $F_{E,M}(t)$ are given in App. A. The expressions above also apply to χe^- scattering with $F_{E,M}=1$ and $Z=-1$ and for which the prefactors of the electric and magnetic pieces agree by setting $I_N=1/2$ and $\mu_N=\mu_B$. For millicharged particle scattering in the ultra relativistic limit, i.e., for $m_\chi\to 0$, we recover the Rosenbluth formula. Finally, the maximal recoil energy induced by χ carrying energy E_χ is given by

$$E_R^{\max}=\frac{2m_i(E_\chi^2-m_\chi^2)}{m_i(2E_\chi+m_i)+m_\chi^2}, \tag{E3}$$

where $m_i=m_N$ or m_e. Equivalently, the minimal value of E_χ to deposit energy E_R in the target at rest is

$$E_\chi^{\min}=\frac{E_R}{2}+\frac{1}{2}\sqrt{\left(2+\frac{E_R}{m_i}\right)(2m_\chi^2+E_Rm_i)}. \tag{E4}$$

For completeness, we also list the squared scattering amplitudes $\overline{|M_{\chi e}(q)|^2}$ on free electrons, averaged over initial states and summed over final states, as they go into the definition of a reference cross section $\bar{\sigma}_e$ (34) for estimating the direct detection limits. The leading terms are[14]

$$\mathrm{MDM}:\ \overline{|M_{\chi e}(q)|^2}=16\pi\mu_\chi^2\alpha m_\chi^2, \tag{E5a}$$

$$\mathrm{EDM}:\ \overline{|M_{\chi e}(q)|^2}=\frac{64\pi d_\chi^2\alpha m_e^2m_\chi^2}{q^2}, \tag{E5b}$$

$$\mathrm{AM}:\ \overline{|M_{\chi e}(q)|^2}=16\pi a_\chi^2\alpha m_\chi^2q^2, \tag{E5c}$$

$$\mathrm{CR}:\ \overline{|M_{\chi e}(q)|^2}=64\pi b_\chi^2\alpha m_e^2m_\chi^2. \tag{E5d}$$

Finally, in the limit of small velocities the transport cross sections $\sigma_T^{\chi i}$ as they are used in (35) read,

$$\mathrm{MDM}:\ \sigma_T^{\chi i}=\frac{\mu_\chi{}^2\alpha[(2m_im_\chi+2m_i^2+m_\chi^2)F_E^2+2m_\chi^2F_M^2]}{(m_i+m_\chi)^2}, \tag{E6a}$$

$$\mathrm{EDM}:\ \sigma_T^{\chi i}=\frac{2d_\chi^2\alpha F_E^2}{v^2}, \tag{E6b}$$

$$\mathrm{AM}:\ \sigma_T^{\chi i}=\frac{4a_\chi^2\alpha m_i^2m_\chi^2[(m_i+m_\chi)^2F_E^2+4m_\chi^2F_M^2]v^2}{3(m_i+m_\chi)^4}, \tag{E6c}$$

$$\mathrm{CR}:\ \sigma_T^{\chi i}=\frac{4b_\chi^2\alpha m_i^2m_\chi^2F_E^2}{(m_i+m_\chi)^2}. \tag{E6d}$$

[14]For detectable electron recoils the typical momentum transfer is $q^2\sim\alpha^2m_e^2\gg m_e^2v^2$, so that we have neglected terms that scale as $m_e^2v^2/q^2$.

Here the momentum transfer of interest is, on average, at the same order as the temperature T. Hence we use $F_E = 1$ and $F_M = -2.79$ for the proton, neglecting the dependence on t, as we are interested in $T = O(\mathrm{keV})$ in this context.

APPENDIX F: PHOTON VACUUM POLARIZATION

Virtual χ-loops contribute to the photon self-energy at four-momentum q^2,

$$i\Pi_{\mu\nu}(q) = i(q^2 g_{\mu\nu} - q_\mu q_\nu)\Pi(q^2). \tag{F1}$$

The polarization function $\Pi(q^2)$ for the operators considered in this paper is given by

$$\Pi(q^2) = \int_0^1 dx A(x, q^2) L_0. \tag{F2}$$

In dimensional regularization the space-time dimension is written as $d = 4 - \epsilon$ and $L_0 = 2/\epsilon + \log(\tilde{\mu}/\Delta)$ with $\Delta = m_\chi^2 - (1-x)xq^2$ and $\tilde{\mu} = 4\pi e^{-\gamma_E}\mu$ where μ is the renormalization scale; $\gamma_E = 0.577\ldots$ is the Euler-Mascheroni constant. For the function $A(x, q^2)$ we find

$$\epsilon\mathrm{Q:}\quad -\frac{2\epsilon^2\alpha}{\pi}(1-x)x, \tag{F3a}$$

$$\mathrm{MDM:}\quad -\frac{\mu_\chi^2}{4\pi^2}[q^2(1-x)x + m_\chi^2], \tag{F3b}$$

$$\mathrm{EDM:}\quad -\frac{d_\chi^2}{4\pi^2}[q^2(1-x)x - m_\chi^2], \tag{F3c}$$

$$\mathrm{AM:}\quad -\frac{a_\chi^2}{2\pi^2}q^2[q^2(1-x)x - m_\chi^2], \tag{F3d}$$

$$\mathrm{CR:}\quad -\frac{b_\chi^2}{2\pi^2}q^4(1-x)x. \tag{F3e}$$

Keeping the finite correction, in the limit of $|q^2|/m_\chi^2 \ll 1$ we find for the difference $\Pi(q^2) - \Pi(0)$,[15]

$$\epsilon\mathrm{Q:}\quad -\frac{\epsilon^2\alpha}{15\pi}\frac{q^2}{m_\chi^2}, \tag{F4a}$$

$$\mathrm{MDM:}\quad -\frac{\mu_\chi^2}{24\pi^2}q^2\left[1 + \log\left(\frac{\tilde{\mu}^2}{m_\chi^2}\right)\right], \tag{F4b}$$

$$\mathrm{EDM:}\quad +\frac{d_\chi^2}{24\pi^2}q^2\left[1 - \log\left(\frac{\tilde{\mu}^2}{m_\chi^2}\right)\right], \tag{F4c}$$

$$\mathrm{AM:}\quad +\frac{a_\chi^2}{2\pi^2}q^2 m_\chi^2 \log\left(\frac{\tilde{\mu}^2}{m_\chi^2}\right), \tag{F4d}$$

$$\mathrm{CR:}\quad -\frac{b_\chi^2}{12\pi^2}q^4 \log\left(\frac{\tilde{\mu}^2}{m_\chi^2}\right). \tag{F4e}$$

In deriving the limit on the running of α in the main text, we set $\tilde{\mu} = 1$ TeV and use the full (finite) forms (F3) that are also valid for $|q^2| \gg m_\chi$. Also note that the finite part of $\Pi(0) = 0$ for AM and CR and hence those operators do not contribute to a constant shift in the fine structure constant.

APPENDIX G: MESON DECAYS

The decay $K^+ \to \pi^+\chi\bar{\chi}$ is closely related to the process of K-decay with emission of a charged lepton pair $K^+ \to \pi^+ l^+ l^-$ as both are accompanied by the emission of γ^* in the $s \to d$ transition. The decay width reads,

$$\Gamma_{K^+\to\pi^+\bar{\chi}\chi} = \frac{G_F^2\alpha m_K^3}{4(4\pi)^6}\int_{4m_\chi^2}^{(m_K-m_\pi)^2} ds_{\chi\bar{\chi}}\frac{f(s_{\chi\bar{\chi}})}{s_{\chi\bar{\chi}}} \times\sqrt{1-\frac{4m_\chi^2}{s_{\chi\bar{\chi}}}}\lambda^{3/2}\left(1,\frac{m_\pi^2}{m_K^2},\frac{s_{\chi\bar{\chi}}}{m_K^2}\right)|f_V(s_{\chi\bar{\chi}})|^2 \tag{G1}$$

and the model dependence for the various interactions we consider is entirely captured in the factor $f(s_{\chi\bar{\chi}})$, found in Eq. (7). For the kaon form factor f_V we use [145],

$$f_V(q^2) = -0.578 - 0.779(q^2/m_K^2). \tag{G2}$$

The decay $B^+ \to K^+\chi\bar{\chi}$ is treated analogously, with the obvious replacement of masses in Eq. (G1) and using instead the form factor [146],

$$f_V(q^2) = \frac{0.161}{1 - q^2/(5.41\ \mathrm{GeV})^2} + \frac{0.198}{[1 - q^2/(5.41\ \mathrm{GeV})^2]^2}. \tag{G3}$$

APPENDIX H: ANNIHILATION AND SELF-INTERACTION CROSS SECTIONS

Here we collect, for completeness, all $2 \to 2$ annihilation and self-scattering cross sections in the nonrelativistic velocity expansion.[16] Annihilation into charged lepton pairs l^+l^- is given by

[15]We are at variance with the MDM and EDM expressions obtained in Ref. [5] which are, however, numerically of little relevance.

[16]In the calculation of the relic density of χ-states, we use the full expression as a function of CM-energy $\sqrt{s}$ and follow Ref. [147] for the thermal average and in the solution of the Boltzmann equation.

$$\sigma_{\chi\bar{\chi}\to l^+l^-} v = B\frac{\alpha}{m_\chi^2}\left(1+\frac{m_l^2}{2m_\chi^2}\right)\sqrt{1-\frac{m_l^2}{m_\chi^2}}, \tag{H1}$$

where the factor B reads

$$\epsilon\text{Q}:\ \pi\epsilon^2\alpha, \tag{H2a}$$

$$\text{MDM}:\ \mu_\chi^2 m_\chi^2, \tag{H2b}$$

$$\text{EDM}:\ \frac{1}{12}d_\chi^2 m_\chi^2 v^2, \tag{H2c}$$

$$\text{AM}:\ \frac{2}{3}a_\chi^2 m_\chi^4 v^2, \tag{H2d}$$

$$\text{CR}:\ 4b_\chi^2 m_\chi^4. \tag{H2e}$$

Since we are interested in DM masses below few GeV and hence freeze-out below (or at) the QCD phase-transition, we relate the annihilation of hadronic final states to the experimentally measured R-ratio,

$$\sigma_{\chi\bar{\chi}\to\text{had}}(s) = \sigma_{\chi\bar{\chi}\to\mu^+\mu^-}(s)\times R(\sqrt{s}), \tag{H3}$$

and we use the tabulated data from Ref. [66].[17] The annihilation to photon-pairs is given by

$$\sigma_{\chi\bar{\chi}\to\gamma\gamma} v = C/m_\chi^2 \tag{H4}$$

with $C=\pi\epsilon^4\alpha^2$ (ϵQ), $\mu_\chi^4 m_\chi^4/4\pi$ (MDM), $d_\chi^4 m_\chi^4/4\pi$ (EDM). The cross section is identically zero for CR and AM.

Finally, for the self-scattering process $\chi\chi\to\chi\chi$, we adopt the viscosity cross section [150], defined as

$$\sigma_{\text{SI}}^{\chi\chi} = \frac{1}{2}\int_{-1}^{1} d\cos\theta(1-\cos^2\theta)\frac{d\sigma}{d\cos\theta}, \tag{H5}$$

which, to leading order in the relative velocity, is

$$\text{MDM}:\ \sigma_{\text{SI}}^{\chi\chi} = \frac{\mu_\chi^4 m_\chi^2}{2\pi}, \tag{H6a}$$

$$\text{EDM}:\ \sigma_{\text{SI}}^{\chi\chi} = \frac{d_\chi^4 m_\chi^2}{4\pi}, \tag{H6b}$$

$$\text{AM}:\ \sigma_{\text{SI}}^{\chi\chi} = \frac{2a_\chi^4 m_\chi^6 v^4}{15\pi}, \tag{H6c}$$

$$\text{CR}:\ \sigma_{\text{SI}}^{\chi\chi} = \frac{b_\chi^4 m_\chi^6 v^4}{30\pi}, \tag{H6d}$$

where we do not show the self-scattering cross section for millicharged particles here, since it is formally divergent and depends on a cutoff of the interaction range, see Refs. [151–154]. For particle-antiparticle scattering $\chi\bar{\chi}\to\chi\bar{\chi}$, we adopt the transport cross section, defined as

$$\sigma_{\text{SI}}^{\chi\bar{\chi}} = \int_{-1}^{1} d\cos\theta(1-\cos\theta)\frac{d\sigma}{d\cos\theta}, \tag{H7}$$

which, to leading order in the relative velocity, is

$$\text{MDM}:\ \sigma_{\text{SI}}^{\chi\bar{\chi}} = \frac{7\mu_\chi^4 m_\chi^2}{4\pi}, \tag{H8a}$$

$$\text{EDM}:\ \sigma_{\text{SI}}^{\chi\bar{\chi}} = \frac{d_\chi^4 m_\chi^2}{4\pi}, \tag{H8b}$$

$$\text{AM}:\ \sigma_{\text{SI}}^{\chi\bar{\chi}} = \frac{a_\chi^4 m_\chi^6 v^4}{2\pi}, \tag{H8c}$$

$$\text{CR}:\ \sigma_{\text{SI}}^{\chi\bar{\chi}} = \frac{12b_\chi^4 m_\chi^6}{\pi}. \tag{H8d}$$

[17] The data starts at $\sqrt{s}=0.3$ GeV, somewhat above the dipion threshold. The intermediate regime can be accounted for by using the cross section data $e^+e^-\to\pi^+\pi^-$ [148,149]. We neglect this complication as it is of minor importance for our purposes.

[1] G. Hinshaw *et al.* (WMAP Collaboration), Astrophys. J. Suppl. Ser. **208**, 19 (2013).
[2] P. A. R. Ade *et al.* (Planck Collaboration), Astron. Astrophys. **594**, A13 (2016).
[3] G. Bertone, D. Hooper, and J. Silk, Phys. Rep. **405**, 279 (2005).
[4] M. Pospelov and T. ter Veldhuis, Phys. Lett. B **480**, 181 (2000).
[5] K. Sigurdson, M. Doran, A. Kurylov, R. R. Caldwell, and M. Kamionkowski, Phys. Rev. D **70**, 083501 (2004); **73**, 089903 (2006).
[6] C. M. Ho and R. J. Scherrer, Phys. Lett. B **722**, 341 (2013).
[7] R. Essig *et al.*, in *Proceedings, 2013 Community Summer Study on the Future of U.S. Particle Physics: Snowmass on the Mississippi (CSS2013): Minneapolis, MN, USA, 2013*

(SLAC National Accelerator Laboratory, 2013), http://www.slac.stanford.edu/econf/C1307292/.
[8] M. Battaglieri *et al.*, arXiv:1707.04591.
[9] M. Pospelov and A. Ritz, Ann. Phys. (Amsterdam) **318**, 119 (2005).
[10] I. B. Zel'Dovich, Sov. J. Exp. Theor. Phys. **6**, 1184 (1958).
[11] C. S. Wood, S. C. Bennett, D. Cho, B. P. Masterson, J. L. Roberts, C. E. Tanner, and C. E. Wieman, Science **275**, 1759 (1997).
[12] C. Giunti and A. Studenikin, Rev. Mod. Phys. **87**, 531 (2015).
[13] J. Bagnasco, M. Dine, and S. D. Thomas, Phys. Lett. B **320**, 99 (1994).
[14] R. Foadi, M. T. Frandsen, and F. Sannino, Phys. Rev. D **80**, 037702 (2009).
[15] O. Antipin, M. Redi, A. Strumia, and E. Vigiani, J. High Energy Phys. 07 (2015) 039.
[16] S. Raby and G. West, Phys. Lett. B **194**, 557 (1987).
[17] M. Pospelov and A. Ritz, Phys. Rev. D **78**, 055003 (2008).
[18] D. Schmidt, T. Schwetz, and T. Toma, Phys. Rev. D **85**, 073009 (2012).
[19] J. Kopp, L. Michaels, and J. Smirnov, J. Cosmol. Astropart. Phys. 04 (2014) 022.
[20] A. Ibarra and S. Wild, J. Cosmol. Astropart. Phys. 05 (2015) 047.
[21] P. Sandick, K. Sinha, and F. Teng, J. High Energy Phys. 10 (2016) 018.
[22] B. J. Kavanagh, P. Panci, and R. Ziegler, arXiv:1810.00033.
[23] R. Essig, P. Schuster, and N. Toro, Phys. Rev. D **80**, 015003 (2009).
[24] M. Reece and L.-T. Wang, J. High Energy Phys. 07 (2009) 051.
[25] J. D. Bjorken, R. Essig, P. Schuster, and N. Toro, Phys. Rev. D **80**, 075018 (2009).
[26] B. Batell, M. Pospelov, and A. Ritz, Phys. Rev. D **80**, 095024 (2009).
[27] S. Abrahamyan *et al.* (APEX Collaboration), Phys. Rev. Lett. **107**, 191804 (2011).
[28] J. R. Batley *et al.* (NA48/2 Collaboration), Phys. Lett. B **746**, 178 (2015).
[29] J. P. Lees *et al.* (*BABAR* Collaboration), Phys. Rev. Lett. **113**, 201801 (2014).
[30] J. Alexander *et al.*, arXiv:1608.08632.
[31] B. Aubert *et al.* (*BABAR* Collaboration), Nucl. Instrum. Methods Phys. Res., Sect. A **479**, 1 (2002).
[32] A. Abashian *et al.*, Nucl. Instrum. Methods Phys. Res., Sect. A **479**, 117 (2002).
[33] T. Abe *et al.* (Belle-II Collaboration), arXiv:1011.0352.
[34] M. Ablikim *et al.* (BESIII Collaboration), Nucl. Instrum. Methods Phys. Res., Sect. A **614**, 345 (2010).
[35] D. Banerjee *et al.* (NA64 Collaboration), Phys. Rev. D **97**, 072002 (2018).
[36] T. Åkesson *et al.* (LDMX Collaboration), arXiv:1808.05219.
[37] M. Raggi and V. Kozhuharov, Adv. High Energy Phys. **2014**, 959802 (2014).
[38] B. Wojtsekhowski, AIP Conf. Proc. **1160**, 149 (2009).
[39] B. Wojtsekhowski, D. Nikolenko, and I. Rachek, arXiv:1207.5089.
[40] A. A. Prinz *et al.*, Phys. Rev. Lett. **81**, 1175 (1998).
[41] J. D. Bjorken, S. Ecklund, W. R. Nelson, A. Abashian, C. Church, B. Lu, L. W. Mo, T. A. Nunamaker, and P. Rassmann, Phys. Rev. D **38**, 3375 (1988).
[42] M. Battaglieri *et al.* (BDX Collaboration), arXiv:1607.01390.
[43] L. Doria, P. Achenbach, M. Christmann, A. Denig, P. Gülker, and H. Merkel, in *13th Conference on the Intersections of Particle and Nuclear Physics (CIPANP 2018) Palm Springs, California, USA, 2018* (SLAC National Accelerator Laboratory, 2018), http://inspirehep.net/record/1655149?ln=en.
[44] S. N. Gninenko and N. V. Krasnikov, Phys. Lett. B **513**, 119 (2001).
[45] M. Pospelov, Phys. Rev. D **80**, 095002 (2009).
[46] C.-Y. Chen, H. Davoudiasl, W. J. Marciano, and C. Zhang, Phys. Rev. D **93**, 035006 (2016).
[47] B. Batell, N. Lange, D. McKeen, M. Pospelov, and A. Ritz, Phys. Rev. D **95**, 075003 (2017).
[48] F. Jegerlehner and A. Nyffeler, Phys. Rep. **477**, 1 (2009).
[49] O. Nicrosini and L. Trentadue, Phys. Lett. B **231**, 487 (1989).
[50] G. Montagna, O. Nicrosini, F. Piccinini, and L. Trentadue, Nucl. Phys. **B452**, 161 (1995).
[51] S. Y. Choi, T. Han, J. Kalinowski, K. Rolbiecki, and X. Wang, Phys. Rev. D **92**, 095006 (2015).
[52] J.-F. Fortin and T. M. P. Tait, Phys. Rev. D **85**, 063506 (2012).
[53] A. A. Prinz, The search for millicharged particles at SLAC, Ph. D. thesis, Stanford University, 2001.
[54] S. Chang, N. Weiner, and I. Yavin, Phys. Rev. D **82**, 125011 (2010).
[55] B. Geytenbeek, S. Rao, P. Scott, A. Serenelli, A. C. Vincent, M. White, and A. G. Williams, J. Cosmol. Astropart. Phys. 03 (2017) 029.
[56] S. Mohanty and S. Rao, arXiv:1506.06462.
[57] B. Aubert *et al.* (*BABAR* Collaboration), in *Proceedings, 34th International Conference on High Energy Physics (ICHEP 2008): Philadelphia, Pennsylvania, 2008* (SLAC National Accelerator Laboratory, 2008), http://www.slac.stanford.edu/econf/C080730/.
[58] J. P. Lees *et al.* (*BABAR* Collaboration), Phys. Rev. Lett. **119**, 131804 (2017).
[59] R. Essig, J. Mardon, M. Papucci, T. Volansky, and Y.-M. Zhong, J. High Energy Phys. 11 (2013) 167.
[60] E. Kou *et al.* (Belle II Collaboration), arXiv:1808.10567.
[61] S. N. Gninenko, N. V. Krasnikov, M. M. Kirsanov, and D. V. Kirpichnikov, Phys. Rev. D **94**, 095025 (2016).
[62] S. N. Gninenko, D. V. Kirpichnikov, and N. V. Krasnikov, arXiv:1810.06856.
[63] M. D. Diamond and P. Schuster, Phys. Rev. Lett. **111**, 221803 (2013).
[64] M. Battaglieri *et al.* (BDX Collaboration), arXiv:1712.01518.
[65] A. Sirlin, Phys. Rev. D **22**, 971 (1980).
[66] M. Tanabashi *et al.* (Particle Data Group), Phys. Rev. D **98**, 030001 (2018).
[67] G. W. Bennett *et al.* (Muon g-2 Collaboration), Phys. Rev. D **73**, 072003 (2006).
[68] J. Grange *et al.* (Muon g-2 Collaboration), arXiv:1501.06858.
[69] N. Saito (J-PARC g-'2/EDM Collaboration), AIP Conf. Proc. **1467**, 45 (2012).
[70] A. Petermann, Helv. Phys. Acta **30**, 407 (1957).

[71] C. M. Sommerfield, Phys. Rev. **107**, 328 (1957).
[72] C. Boehm and P. Fayet, Nucl. Phys. **B683**, 219 (2004).
[73] V. Andreev *et al.* (ACME Collaboration), Nature (London) **562**, 355 (2018).
[74] K. Nishijima, Prog. Theor. Phys. **6**, 614 (1951).
[75] A. Czarnecki and B. Krause, Acta Phys. Pol. B **28**, 829 (1997).
[76] A. G. Grozin, I. B. Khriplovich, and A. S. Rudenko, Nucl. Phys. **B821**, 285 (2009).
[77] C. Bird, P. Jackson, R. V. Kowalewski, and M. Pospelov, Phys. Rev. Lett. **93**, 201803 (2004).
[78] V. V. Anisimovsky *et al.* (E949 Collaboration), Phys. Rev. Lett. **93**, 031801 (2004).
[79] A. V. Artamonov *et al.* (BNL-E949 Collaboration), Phys. Rev. D **79**, 092004 (2009).
[80] B. Aubert *et al.* (*BABAR* Collaboration), in *38th Rencontres de Moriond on Electroweak Interactions and Unified Theories Les Arcs, France, 2003* (2003).
[81] P. Achard *et al.* (L3 Collaboration), Phys. Lett. B **587**, 16 (2004).
[82] V. Barger, W.-Y. Keung, D. Marfatia, and P.-Y. Tseng, Phys. Lett. B **717**, 219 (2012).
[83] Y. Gao, C. M. Ho, and R. J. Scherrer, Phys. Rev. D **89**, 045006 (2014).
[84] K. Kadota and J. Silk, Phys. Rev. D **89**, 103528 (2014).
[85] R. Primulando, E. Salvioni, and Y. Tsai, J. High Energy Phys. 07 (2015) 031.
[86] A. Alves, A. C. O. Santos, and K. Sinha, Phys. Rev. D **97**, 055023 (2018).
[87] T. Banks, J.-F. Fortin, and S. Thomas, arXiv:1007.5515.
[88] E. Del Nobile, C. Kouvaris, P. Panci, F. Sannino, and J. Virkajarvi, J. Cosmol. Astropart. Phys. 08 (2012) 010.
[89] E. Del Nobile, G. B. Gelmini, P. Gondolo, and J.-H. Huh, J. Cosmol. Astropart. Phys. 06 (2014) 002.
[90] R. Essig, J. Mardon, and T. Volansky, Phys. Rev. D **85**, 076007 (2012).
[91] R. Essig, A. Manalaysay, J. Mardon, P. Sorensen, and T. Volansky, Phys. Rev. Lett. **109**, 021301 (2012).
[92] R. Essig, M. Fernandez-Serra, J. Mardon, A. Soto, T. Volansky, and T.-T. Yu, J. High Energy Phys. 05 (2016) 046.
[93] M. Crisler, R. Essig, J. Estrada, G. Fernandez, J. Tiffenberg, M. S. Haro, T. Volansky, and T.-T. Yu (SENSEI Collaboration), Phys. Rev. Lett. **121**, 061803 (2018).
[94] H. An, M. Pospelov, J. Pradler, and A. Ritz, Phys. Rev. Lett. **120**, 141801 (2018).
[95] T. Bringmann and M. Pospelov, arXiv:1810.10543.
[96] R. Essig, T. Volansky, and T.-T. Yu, Phys. Rev. D **96**, 043017 (2017).
[97] J. Angle *et al.* (XENON10 Collaboration), Phys. Rev. Lett. **107**, 051301 (2011); **110**, 249901(E) (2013).
[98] E. Aprile *et al.* (XENON Collaboration), Phys. Rev. Lett. **119**, 181301 (2017).
[99] E. Masso, S. Mohanty, and S. Rao, Phys. Rev. D **80**, 036009 (2009).
[100] G. Mangano, G. Miele, S. Pastor, and M. Peloso, Phys. Lett. B **534**, 8 (2002).
[101] P. F. de Salas and S. Pastor, J. Cosmol. Astropart. Phys. 07 (2016) 051.
[102] J. H. Heo and C. S. Kim, J. Korean Phys. Soc. **68**, 715 (2016).
[103] C. Boehm, M. J. Dolan, and C. McCabe, J. Cosmol. Astropart. Phys. 08 (2013) 041.
[104] K. M. Nollett and G. Steigman, Phys. Rev. D **89**, 083508 (2014).
[105] K. M. Nollett and G. Steigman, Phys. Rev. D **91**, 083505 (2015).
[106] C. Boehm and R. Schaeffer, Astron. Astrophys. **438**, 419 (2005).
[107] T. Bringmann and S. Hofmann, J. Cosmol. Astropart. Phys. 04 (2007) 016; 03 (2016) E02.
[108] C. Dvorkin, K. Blum, and M. Kamionkowski, Phys. Rev. D **89**, 023519 (2014).
[109] P. Gondolo and K. Kadota, J. Cosmol. Astropart. Phys. 06 (2016) 012.
[110] H. Tashiro, K. Kadota, and J. Silk, Phys. Rev. D **90**, 083522 (2014).
[111] J. B. Muñoz, E. D. Kovetz, and Y. Ali-Haïmoud, Phys. Rev. D **92**, 083528 (2015).
[112] J. D. Bowman, A. E. E. Rogers, R. A. Monsalve, T. J. Mozdzen, and N. Mahesh, Nature (London) **555**, 67 (2018).
[113] R. Barkana, N. J. Outmezguine, D. Redigolo, and T. Volansky, Phys. Rev. D **98**, 103005 (2018).
[114] S. W. Randall, M. Markevitch, D. Clowe, A. H. Gonzalez, and M. Bradac, Astrophys. J. **679**, 1173 (2008).
[115] A. Robertson, R. Massey, and V. Eke, Mon. Not. R. Astron. Soc. **465**, 569 (2017).
[116] G. G. Raffelt, *Stars as Laboratories for Fundamental Physics* (University of Chicago Press, Chicago, 1996).
[117] J. H. Chang, R. Essig, and S. D. McDermott, J. High Energy Phys. 09 (2018) 051.
[118] T. Fischer, S. Chakraborty, M. Giannotti, A. Mirizzi, A. Payez, and A. Ringwald, Phys. Rev. D **94**, 085012 (2016).
[119] H. K. Dreiner, C. Hanhart, U. Langenfeld, and D. R. Phillips, Phys. Rev. D **68**, 055004 (2003).
[120] G. Magill, R. Plestid, M. Pospelov, and Y.-D. Tsai, Phys. Rev. D **98**, 115015 (2018).
[121] I. Lopes, K. Kadota, and J. Silk, Astrophys. J. Lett. **780**, L15 (2014).
[122] H. Liu, T. R. Slatyer, and J. Zavala, Phys. Rev. D **94**, 063507 (2016).
[123] M. Boudaud, J. Lavalle, and P. Salati, Phys. Rev. Lett. **119**, 021103 (2017).
[124] M. Boudaud, T. Lacroix, M. Stref, and J. Lavalle, arXiv:1810.01680.
[125] K. K. Boddy and J. Kumar, Phys. Rev. D **92**, 023533 (2015).
[126] D. C. Latimer, Phys. Rev. D **95**, 095023 (2017).
[127] R. Bartels, D. Gaggero, and C. Weniger, J. Cosmol. Astropart. Phys. 05 (2017) 001.
[128] R. Ball *et al.*, Proceedings: Mini-Conference and Workshop on Neutrino Mass, Telemark, Wisconsin, 1980, **C801002**, 172 (1980).
[129] M. Anelli *et al.* (SHiP Collaboration), arXiv:1504.04956.
[130] A. Haas, C. S. Hill, E. Izaguirre, and I. Yavin, Phys. Lett. B **746**, 117 (2015).
[131] A. A. Aguilar-Arevalo *et al.* (MiniBooNE Collaboration), Phys. Rev. Lett. **121**, 221801 (2018).

[132] R. Acciarri *et al.* (DUNE Collaboration), arXiv:1512.06148.
[133] C. Athanassopoulos *et al.* (LSND Collaboration), Nucl. Instrum. Methods Phys. Res., Sect. A **388**, 149 (1997).
[134] D. Akimov *et al.* (COHERENT Collaboration), Science **357**, 1123 (2017).
[135] D. E. Soper, M. Spannowsky, C. J. Wallace, and T. M. P. Tait, Phys. Rev. D **90**, 115005 (2014).
[136] G. Magill, R. Plestid, M. Pospelov, and Y.-D. Tsai, arXiv:1806.03310.
[137] M. Sher and J. Stevens, Phys. Lett. B **777**, 246 (2018).
[138] R. Mertig, M. Bohm, and A. Denner, Comput. Phys. Commun. **64**, 345 (1991).
[139] V. Shtabovenko, R. Mertig, and F. Orellana, Comput. Phys. Commun. **207**, 432 (2016).
[140] T. Hahn, Comput. Phys. Commun. **168**, 78 (2005).
[141] C. F. Perdrisat, V. Punjabi, and M. Vanderhaeghen, Prog. Part. Nucl. Phys. **59**, 694 (2007).
[142] K. J. Kim and Y.-S. Tsai, Phys. Rev. D **8**, 3109 (1973).
[143] Y.-S. Tsai, Rev. Mod. Phys. **46**, 815 (1974); **49**, 421 (1977).
[144] E. Byckling and K. Kajantie, Nucl. Phys. **B9**, 568 (1969).
[145] J. R. Batley *et al.* (NA48/2 Collaboration), Phys. Lett. B **677**, 246 (2009).
[146] P. Ball and R. Zwicky, Phys. Rev. D **71**, 014015 (2005).
[147] P. Gondolo and G. Gelmini, Nucl. Phys. **B360**, 145 (1991).
[148] V. V. Ezhela, S. B. Lugovsky, and O. V. Zenin, arXiv:hep-ph/0312114.
[149] M. Davier, S. Eidelman, A. Hocker, and Z. Zhang, Eur. Phys. J. C **27**, 497 (2003).
[150] S. Tulin, H.-B. Yu, and K. M. Zurek, Phys. Rev. D **87**, 115007 (2013).
[151] L. Ackerman, M. R. Buckley, S. M. Carroll, and M. Kamionkowski, Phys. Rev. D **79**, 023519 (2009).
[152] J. L. Feng, M. Kaplinghat, H. Tu, and H.-B. Yu, J. Cosmol. Astropart. Phys. 07 (2009) 004,
[153] S. D. McDermott, H.-B. Yu, and K. M. Zurek, Phys. Rev. D **83**, 063509 (2011).
[154] P. Agrawal, F.-Y. Cyr-Racine, L. Randall, and J. Scholtz, J. Cosmol. Astropart. Phys. 05 (2017) 022.

Stellar probes of dark sector-photon interactions

Xiaoyong Chu,* Jui-Lin Kuo,† Josef Pradler,‡ and Lukas Semmelrock§

Institute of High Energy Physics, Austrian Academy of Sciences,
Nikolsdorfergasse 18, 1050 Vienna, Austria

(Received 12 August 2019; published 3 October 2019)

Electromagnetically neutral dark sector particles may directly couple to the photon through higher dimensional effective operators. Considering the electric and magnetic dipole moment, anapole moment, and charge radius interactions, we derive constraints from the stellar energy loss in the Sun, horizontal branch and red giant stars, as well as from cooling of the proto-neutron star of SN1987A. We provide the exact formula for in-medium photon-mediated pair production to leading order in the dark coupling and compute the energy loss rates explicitly for the most important processes, including a careful discussion on resonances and potential double counting between the processes. Stringent limits for dark states with masses below 3 keV (40 MeV) arise from red giant stars (SN1987A), implying an effective lower mass-scale of approximately 10^9 GeV (10^7 GeV) for mass-dimension five and 100 GeV (2.5 TeV) for mass-dimension six operators as long as dark states stream freely; for the proto-neutron star, the trapping of dark states is also evaluated. Together with direct limits previously derived by us in Chu *et al.* (2018), this provides the first comprehensive overview of the viability of effective electromagnetic dark-state interactions below the GeV mass-scale.

DOI: 10.1103/PhysRevD.100.083002

I. INTRODUCTION

The prospect that new physics might be hiding under our noses in the form of light dark states that have been in kinematic reach for decades is most intriguing if not seemingly preposterous. In fact, cases exist where new interactions are of comparable strength to the ones encountered in the Standard Model (SM), while being compatible with all to-date searches. The direct test of such physics, i.e., new particles and interactions below the GeV-scale has become a major field in recent years [1,2] and provides a complementary direction to the beyond-SM searches at the energy frontier.

Whereas the GeV-mass scale might comprise somewhat of a "blind-spot" that allows for the existence of new physics with appreciable interactions to the SM, once the mass enters the keV-regime the landscape changes fundamentally. Astrophysical constraints on long-lived dark states that are derived from stellar cooling arguments [3] are typically so severe that the cases for laboratory detection drastically diminish. Of course, the observable signatures of dark states depend on the nature of the coupling to the SM. For example, a new force can be mediated by new scalar or vector particles. Benchmark models are then derived based on minimality of the SM extension and on the dimensionality of the interaction operator, and within this framework the interplay between cosmological and astrophysical implications and direct tests is fleshed out.

A prominent example is the vector portal, where the low-energy phenomenology is determined by the kinetic mixing strength ϵ of the "dark photon" V with the SM photon [4]. If the mass of V, m_V, originates from a Higgs mechanism, implying an additional scalar particle in the vicinity of m_V, stellar cooling constraints obliterate any prospects of probing such a model below the keV-region, as limits on millicharged particles apply. However, a decoupling of stellar constraints as $\epsilon^2 m_V^2$ [5] when m_V arises from a Stuckelberg mechanism, opens the opportunity to explore a vast parameter region through direct, laboratory searches, in particular if V is the dark matter (DM); see, e.g., [6–11,11–20].

In this work we will consider—from the low-energy effective theory point of view—an even more minimal possibility than the dark photon, namely, that the SM photon is the new physics mediator. Beyond carrying a millicharge, DM may also interact *directly* with the photon through a number of higher dimensional operators that encapsulate magnetic or electric dipole moment

*xiaoyong.chu@oeaw.ac.at
†jui-lin.kuo@oeaw.ac.at
‡josef.pradler@oeaw.ac.at
§lukas.semmelrock@oeaw.ac.at

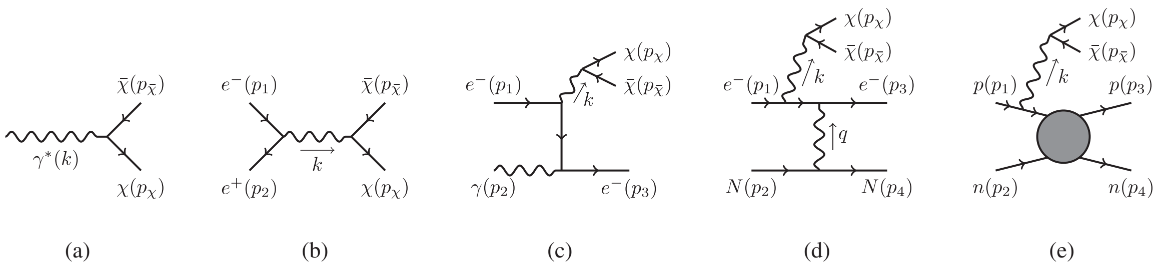

FIG. 1. Shown are the pair production processes of $\chi\bar{\chi}$ that are calculated in this paper, namely, (a) plasmon decay, (b) e^+e^- annihilation, (c) $2 \to 3$ Compton scattering, (d) electron bremsstrahlung and (e) nucleon bremsstrahlung; for (c)–(d) we only show one of two relevant diagrams. The four momentum of the $\chi\bar{\chi}$-producing photon is denoted by k throughout the paper.

interactions (MDM or EDM), an anapole moment (AM) or a charge radius interaction (CR). These possibilities were originally considered in [21–23] with further studies on the phenomenology found in [24–29]. Motivated by the intense efforts to search for sub-GeV dark sector states [1,2], the topic of form-factor interactions was recently revisited in detail by some of us [30].

In [30] we focused on the prospects of detecting electromagnetic (EM) form factor interactions of a dark sector Dirac particle χ with mass at or below the GeV-scale. The direct production of pairs $\chi\bar{\chi}$ was constrained with data from *BABAR* [31], NA64 [32] and mQ [33] and future improvements in sensitivity were derived for Belle-II [34], LDMX [35] and BDX [36]. The direct sensitivity was then compared with indirect probes such as electroweak precision tests, flavor physics constraints, as well as with results from LEP and LHC. It was found that, owing to the higher dimensionality of the operators, high energy probes provide superior sensitivity. The conclusions are independent of the lifetime of χ, as long as its stability is guaranteed while traversing terrestrial detectors.

In contrast, if χ is long-lived, additional constraints from cosmology, astrophysics, and direct DM searches apply, and in [30] we have considered the most important ones that are crucial in the MeV-GeV mass bracket of χ. However, once we allow the χ-mass to drop into the keV-region, additional constraints from the production of $\chi\bar{\chi}$-pairs in stars become important [3]. In this work we complement our previous results derived in [30] with astrophysical limits that apply once the dark state is stable on a macroscopic time scale, without necessarily demanding that sub-MeV χ particles make up the DM. We derive the limits from stellar cooling that arise from red giant (RG), horizontal branch (HB) stars, and the Sun, and revisit our calculation of the supernova bound, taking into account all major production channels.

Concretely, we are considering the following fundamental dark state emission processes, highlighting in brackets the stellar system(s) for which the process is most relevant,

$$\text{Plasmon decay:} \quad \gamma_{\mathrm{T,L}} \to \chi\bar{\chi} \quad (\text{all}), \tag{1}$$

$$\text{Annihilation:} \quad e^+e^- \to \chi\bar{\chi} \quad (\text{SN}), \tag{2}$$

$$\begin{aligned} \text{Bremsstrahlung:} \quad & e^-N \to e^-N\chi\bar{\chi} \quad (\text{RG, HB, Sun}), \\ & NN \to NN\chi\bar{\chi} \quad (\text{SN}), \end{aligned} \tag{3}$$

$$\text{Compton scattering:} \quad e^-\gamma_{\mathrm{T,L}} \to e^-\chi\bar{\chi} \quad (\text{all}). \tag{4}$$

The respective processes are decay of in-medium longitudinal (L) and transverse (T) modes of thermal photons $\gamma_{\mathrm{T,L}}$ which we will simply refer to as "plasmons", electron-positron annihilation, electron bremsstrahlung on protons and nuclei, nucleon-nucleon bremsstrahlung and Compton scattering with the emission of a $\chi\bar{\chi}$-pair. Exemplary respective diagrams are shown in Fig. 1.

The paper is organized as follows: in Sec. II we first set the stage by listing the effective operators that mediate χ-photon interactions. Section III gives a brief account on stellar energy loss arguments. Our calculations on χ particle emission are presented in Sec. IV. The ensuing constraints are then collected in Sec. V before concluding in Sec. VI. Several Appendixes provide details on the calculations and are referenced in the main text.

II. ELECTROMAGNETIC FORM FACTOR INTERACTIONS

A Dirac fermion χ may have a number of interactions with the photon gauge field A_μ or its field strength tensor $F_{\mu\nu}$. At mass dimension-5 the interaction terms of the Lagrangian are given by

$$\mathcal{L}_\chi^{\text{dim-5}} = \frac{1}{2}\mu_\chi\bar{\chi}\sigma^{\mu\nu}\chi F_{\mu\nu} + \frac{i}{2}d_\chi\bar{\chi}\sigma^{\mu\nu}\gamma^5\chi F_{\mu\nu}, \tag{5}$$

where μ_χ and d_χ are the MDM and EDM coupling which may be measured in units of the Bohr magneton, $\mu_B \equiv e/(2m_e) = 1.93\times10^{-11}\ e\,\mathrm{cm}$; m_e is the mass of the electron and $\sigma^{\mu\nu} = \frac{i}{2}[\gamma^\mu,\gamma^\nu]$. At mass dimension-6 we have

$$\mathcal{L}_\chi^{\text{dim-6}} = -a_\chi \bar{\chi}\gamma^\mu\gamma^5\chi\partial^\nu F_{\mu\nu} + b_\chi \bar{\chi}\gamma^\mu\chi\partial^\nu F_{\mu\nu}, \quad \text{(6a)}$$

where a_χ and b_χ are the AM and CR coefficients. All coupling strengths in Eqs. (5) and (6) are real. At mass-dimension-7 the interactions involve two photons at the vertex and hence require a dedicated treatment. For this reason we restrict our study to dim-5 and dim-6 operators.

The effective interactions in Eqs. (5) and (6) may, e.g., arise from the compositeness of χ [37–39] or perturbatively, from a UV completion that contains electrically charged states [40]. In the latter case, MDM and EDM moments are e.g., generated by loop-induced axial or vector Yukawa interactions $y_{A,V}$ of χ with additional scalars and fermions. Parametrically, one expects $\mu_\chi \sim Q|y_{A,V}|^2/M$ and $d_\chi \sim Q\mathrm{Im}[y_V y_A^*]/M$ where Q is the electric charge of the mediator and M is some common mass-scale of these new states. In turn, the strength of AM and CR interactions may be expected as a_χ, $b_\chi \sim Q|y_{A,V}|^2/M^2$. It should be noted, however, that these estimates may be significantly enhanced by the lightness and/or mass-degeneracy of the spectrum of states [41]; a systematic study on EDMs induced by CP violation from light dark sectors was recently performed in [42]. In what follows, we treat the interactions (5) and (6) independent of their embedding.

For the Feynman-diagrammatic computation, one assembles the interactions into the matrix element of the effective EM current of χ,

$$\langle \chi(p_f)|J_\chi^\mu(0)|\chi(p_i)\rangle = \bar{u}(p_f)\Gamma_\chi^\mu(q)u(p_i),$$

where $p_{i,f}$ and $q = p_i - p_f$ are four-momenta. For a neutral particle χ the vertex functions reads

$$\Gamma_\chi^\mu(q) = i\sigma^{\mu\nu}q_\nu(\mu_\chi + id_\chi\gamma^5) + (q^2\gamma^\mu - q^\mu \not{q})(b_\chi - a_\chi\gamma^5).$$

Here we regard the various moments as being generated at an energy scale well above the energies involved in the stellar production; they are hence q-independent.

III. STELLAR OBSERVABLES

In this section we review the arguments on stellar energy loss. Active stars such as RG, HB, or the Sun are systems of negative heat capacity: if energy is lost, either through photon emission or through new, anomalous processes, the decrease of total energy causes the gravitational energy to become more negative. By virtue of the virial theorem, the average kinetic energy and thereby the photon temperature increases. The system heats up leading to a faster consumption of its nuclear fuel while the overall stellar structure remains largely unchanged. In contrast, dead stars such as white dwarfs or the proto-neutron star formed in core-collapse SN are supported by degeneracy pressure and stellar energy loss implies a cooling of the system. Constraints are then derived based on an observationally inferred cooling curve.

A. RG and HB stars

In globular clusters (GCs), the population of stars on the red giant branch vs horizontal branch is directly related to the lifetime of stars in the respective phases. Their observationally inferred number ratio agrees with standard predictions to within 10%. Anomalous energy losses shorten the helium-burning lifetime in HB stars, creating an imbalance in the number of HB vs RG stars. This constrains the luminosity in non-standard channels to be less than approximately 10% of the standard helium-burning luminosity of the HB core [3],

$$\int_{\text{core}} dV\,\dot{Q} < 10\% \times L_{\text{HB}} \quad (\text{HB}). \quad (7)$$

Following [3], L_{HB} will be taken as 20 $L_\odot$ for a 0.5 $M_\odot$ core below. The values of the Solar mass and luminosity are $M_\odot = 1.99 \times 10^{33}$ g and $L_\odot = 3.83 \times 10^{33}$ erg/s, respectively. The computation of the anomalous energy loss rate per unit volume and time, $\dot{Q}$, will be the subject of the next section.

A constraint for RG stars may be derived from an agreement between predicted and observationally inferred core masses prior to helium ignition. Energy loss delays the latter and the core mass keeps increasing as the hydrogen burning "ashes" fall onto the degenerate He core. Preventing an increase in core mass by no more than 5% yields the constraint [3],

$$\dot{Q} < 10\ \text{erg/g/s} \times \rho \quad (\text{RG}). \quad (8)$$

Here, $\dot{Q}$ is to be evaluated at an average density of $\rho = 2 \times 10^5\ \text{g/cm}^3$ and a temperature of $T = 10^8\ \text{K} \simeq 8.6$ keV, slightly higher than that of HB stars.

The criterion (8) on energy loss can be improved utilizing high precision photometric observations of GCs. For example, considering the brightness of the tip of the RG branch, [43] has provided a detailed error budget, and new limits on neutrino dipole moments from GC M5 were derived based on predictions of absolute brightness in the presence of anomalous energy loss that are obtained with dedicated stellar evolutionary codes. It was found, however, that previously derived limits based on (8) remain largely intact, as there appears to be a slight preference for anomalous energy loss channels [43]. In the following, for our purposes it will hence be entirely sufficient to employ the simple condition (8) to arrive at constraints on the EM form factors.

B. Sun

Solar neutrino fluxes are a direct measure of the nuclear fusion rates inside the Sun. For example, not only the ^{8}B neutrino flux is very well measured but also the sensitive dependence of the responsible reaction on the temperature provides an excellent handle for constraining anomalous energy losses. The ensuing constraint is then phrased in terms of the total Solar photon luminosity [44,45], as

$$\int_{\mathrm{Sun}} dV\,\dot{Q} < 10\% \times L_\odot \quad (\mathrm{Sun}). \tag{9}$$

It is important to note that (9) is basically insensitive to the long-standing "solar opacity problem": the measured ^{8}B neutrino flux is situated in the overlap region of the nominal error ranges between the discrepant high- and low-metallicity determinations of the Solar chemical composition [8]; see the respective Refs. [46,47]. Hence, (9) suffices as a criterion, awaiting further developments on Solar opacity determinations.

C. Supernova

New particles that are emitted from the proto-neutron star and that stream freely may quench the electroweak rates of neutrino emission during the cooling phase. The involved processes and their dynamics are highly complex. However, an approximate but very useful criterion to constrain additional energy loss is the condition that the total luminosity due to nonstandard processes should not exceed the neutrino luminosity at one second after core bounce [3],

$$\int_{\mathrm{core}} dV\,\dot{Q} < L_\nu = 3\times 10^{52}\ \mathrm{erg}/s \quad (\mathrm{SN}). \tag{10}$$

The applicability of the bounds above are contingent on that the SN1987A was a neutrino-driven SN explosion[1] and that the produced particles are able to escape the dense environment of the SN remnant, assumed to be a proto-neutron star (PNS). Below, we will account for this so-called "trapping-limit" in the case of SN. For all other systems introduced above, trapping is either irrelevant or happens in a parameter region that is excluded otherwise.

IV. PRODUCTION CROSS SECTIONS AND ENERGY LOSS RATES

In this section we first provide the general formula for $\chi\bar{\chi}$ pair production in the thermal bath, before breaking it down into the most relevant pieces that dominate the in-medium production cross sections and, thereby, the stellar cooling rates.

[1]For an alternative explosion mechanism where the SN1987A bounds would not apply, see [48,49].

A. Exact formula for $\chi\bar{\chi}$ pair production

In thermal field theory, the production rate of a decoupled fermion per volume per time may be obtained from its relation to the imaginary part of its self-energy in medium [50] via

$$\dot{N}_\chi = -\int \frac{d^3\vec{p}_\chi}{(2\pi)^3}\frac{1}{(e^{E_\chi/T}+1)}\frac{\mathrm{Im}\Pi_\chi(E_\chi,\vec{p}_\chi)}{E_\chi}, \tag{11}$$

where $\mathrm{Im}\Pi_\chi(E_\chi,\vec{p}_\chi) = \bar{u}(p_\chi)\Sigma(E_\chi,\vec{p}_\chi)u(p_\chi)$ is the discontinuity of the thermal self-energy of χ, $\Sigma(E_\chi,\vec{p}_\chi)$; $u(p_\chi)$ and $\bar{u}(p_\chi)$ are free particle spinors with four-momentum $p_\chi = (E_\chi,\vec{p}_\chi)$. To lowest order in the dark coupling, $\Sigma(E_\chi,\vec{p}_\chi)$ is found from the one-loop diagram with a dressed photon propagator attached to the χ fermion line. A general exposition on calculating discontinuities in the thermal plasma is found in [50,51].

Below, in Eq. (13), we are using a different formulation, and the equivalence may be appreciated in the following way: when cutting the self-energy diagram for χ, the optical theorem implies that the production rate may also be obtained by computing all graphs where a photon γ^* of four-momentum $k = p_\chi + p_{\bar{\chi}}$ emerges from a SM current and is being dotted into the dark current of the $\chi\bar{\chi}$ pair. The SM-process that leads to the creation of γ^* is in turn related to the imaginary part of the photon self-energy in the medium, $\mathrm{Im}\Pi_{\mu\nu}$, where

$$\Pi^{\mu\rho} = (\epsilon^\mu_{\mathrm{T},1}\epsilon^\rho_{\mathrm{T},1} + \epsilon^\mu_{\mathrm{T},2}\epsilon^\rho_{\mathrm{T},2})\Pi_\mathrm{T} + \epsilon^\mu_\mathrm{L}\epsilon^\rho_\mathrm{L}\Pi_\mathrm{L}. \tag{12}$$

Here $\epsilon_{\mathrm{T,L}}$ are the transverse and longitudinal photon polarization vectors and $\Pi_{\mathrm{L,T}}(k)$ is thermal photon self-energy for the respective polarization; explicit expressions are given in Appendix A. Identifying the leading contributions to $\mathrm{Im}\Pi_{\mathrm{L,T}}(k)$ in various mediums then allows us to account for the dominant χ pair production channels.

The exact differential production rate per volume of $\chi\bar{\chi}$ pairs via a photon of 4-momentum $k = (\omega,\vec{k})$ emerging from *any* SM process to lowest order in the dark current can be obtained by borrowing the results from dilepton production in hot matter; see e.g., [52,53]. Adopted to our purposes (see Appendix B) it reads

$$\frac{d\dot{N}_\chi}{ds_{\chi\bar{\chi}}} = -\sum_{i=\mathrm{T,L}} g_i \int \frac{d^3\vec{k}}{(2\pi)^3}\frac{1}{(e^{\omega/T}-1)}\frac{\mathrm{Im}\Pi_i(\omega,\vec{k})}{\omega} \times \frac{f(s_{\chi\bar{\chi}})}{16\pi^2|s_{\chi\bar{\chi}}-\Pi_i|^2}\sqrt{1-\frac{4m_\chi^2}{s_{\chi\bar{\chi}}}}, \tag{13}$$

where $s_{\chi\bar{\chi}} = k^2$ is the invariant mass of the χ-pair and the internal degrees of freedom (d.o.f.) of two polarization modes are $g_\mathrm{T} = 2$, $g_\mathrm{L} = 1$. The differences in the various interaction possibilities are entirely captured in a factor that

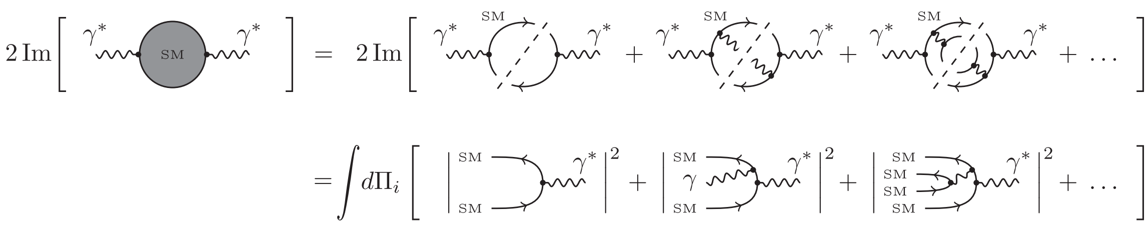

FIG. 2. Optical theorem relating the imaginary part of the photon self energy to the sum of all SM processes that create an off shell photon γ^*. The first equality shows the leading individual contributions to the self-energy. When the latter loop-diagrams are cut, they correspond to the scattering processes shown in the second line, where $d\Pi_i$ symbolizes the phase space integral of all external particles, except γ^*. When the scattering diagrams are deformed in a way such that two SM particles are in the initial state, the processes correspond to annihilation, Compton scattering and bremsstrahlung (from left to right). Any diagrams with χ particles involved yield contributions to the production rate (13) that are of higher order in the dark coupling.

will repeatedly appear and that was obtained in our preceding work [30],

$$\text{MDM}: \; f(s_{\chi\bar{\chi}}) = \frac{2}{3}\mu_\chi^2 s_{\chi\bar{\chi}}^2 \left(1 + \frac{8m_\chi^2}{s_{\chi\bar{\chi}}}\right), \tag{14a}$$

$$\text{EDM}: \; f(s_{\chi\bar{\chi}}) = \frac{2}{3}d_\chi^2 s_{\chi\bar{\chi}}^2 \left(1 - \frac{4m_\chi^2}{s_{\chi\bar{\chi}}}\right), \tag{14b}$$

$$\text{AM}: \; f(s_{\chi\bar{\chi}}) = \frac{4}{3}a_\chi^2 s_{\chi\bar{\chi}}^3 \left(1 - \frac{4m_\chi^2}{s_{\chi\bar{\chi}}}\right), \tag{14c}$$

$$\text{CR}: \; f(s_{\chi\bar{\chi}}) = \frac{4}{3}b_\chi^2 s_{\chi\bar{\chi}}^3 \left(1 + \frac{2m_\chi^2}{s_{\chi\bar{\chi}}}\right). \tag{14d}$$

Equation (13) is the general expression of the weakly coupled χ pair-production rate from the thermal medium; details are found in Appendix B.

The contribution to $\chi\bar{\chi}$ production to leading order in α is given by the *pole* in (13), i.e., for $s_{\chi\bar{\chi}} = \mathrm{Re}\Pi_{\mathrm{L,T}}$. When this condition is met, (13) reduces to the decay rate of thermal photons $\gamma_{\mathrm{L,T}} \to \chi\bar{\chi}$. Hence, resonant $\chi\bar{\chi}$ production is fully accounted for by $\gamma_{\mathrm{L,T}}$ decay. The decay itself becomes possible by virtue of the in-medium (squared) mass of $\gamma_{\mathrm{L,T}}$: it is given by $\mathrm{Re}\Pi_{\mathrm{L,T}}(\omega_{\mathrm{L,T}}, \vec{k})$, where $\omega_{\mathrm{L,T}}$ denotes the solution of $\omega(|\vec{k}|)$ of the corresponding longitudinal and transverse dispersion relations $\omega^2 - |\vec{k}|^2 - \mathrm{Re}\Pi_{\mathrm{L,T}}(\omega, \vec{k}) = 0$. Plasmon decay is discussed in the following subsection, and explicitly calculated in (B7)–(B9) in Appendix B. The expressions for $\mathrm{Re}\Pi_{\mathrm{L,T}}$ and finite-temperature dispersion relations are found in (A5)–(A6).

Production *off-the-pole* to Eq. (13) can be elucidated by studying the contributions to $\mathrm{Im}\Pi$ using the optical theorem, illustrated in Fig. 2. The left-hand side shows the fully dressed vacuum polarization of an off shell photon γ^*, found by considering loop-diagrams of increasing order in α illustrated in the first equality. When those loop diagrams are cut, their imaginary parts are given by the tree-level production processes for γ^* shown in the last equality. The leading α contribution to $\mathrm{Im}\Pi$ is then given by the electron one-loop diagram. Although it is well known that on shell plasmon decay $\gamma_{\mathrm{L,T}} \to e^+e^-$ remains forbidden at finite temperature [54], an electron loop still contributes to $\mathrm{Im}\Pi$ in the off shell case. The associated process is then e^+e^- annihilation to $\chi\bar{\chi}$, i.e., process (2b).

The second and third diagrams in the last line of Fig. 2 are related to $\chi\bar{\chi}$ production in Compton scattering and bremsstrahlung. Here, it is important to note that $s_{\chi\bar{\chi}} = \mathrm{Re}\Pi_{\mathrm{L,T}}$ can also be met in the photon propagator that produces the χ-pair with invariant squared mass $s_{\chi\bar{\chi}}$. However, including such resonances would amount to double-counting. As we have seen above, the pole contributions are already captured by plasmon decay.[2] In our calculations, we explicitly avoid this situation by setting $\Pi_{\mathrm{L,T}} \to 0$ in the propagator if the resonance is kinematically allowed for the photon that directly couples to the dark current. We have numerically verified that our results remain otherwise unaffected by neglecting the thermal shift in the photon propagator.

Finally, there is also a potential double counting between Compton scattering and bremsstrahlung processes, which happens when in the bremsstrahlung process the photon exchanged between two initial particles carries 4-momentum q [see Fig. 1(d)] that satisfies the dispersion relation $q^2 - \mathrm{Re}\Pi_L(q^0, \vec{q}) = 0$, leading to the exchange of an on shell longitudinal plasmon. The process then becomes equivalent to Compton scattering $e/N + \gamma_L \to e/N + \chi + \bar{\chi}$. This has been reported for axion production processes, where the contribution of latter is mostly covered by that of bremsstrahlung [57]. To avoid such double-counting, we take the static approximation ($q^0 = 0$) for the thermal mass

[2]A heuristic argument on such double counting was also given in the context of neutrino pair emission in Sec. 2.5 of [55]. It furthermore appears to us, that double counting may have occurred in [56] where a potentially resonant bremsstrahlung process was added to the plasmon decay contribution.

of the photon exchanged in bremsstrahlung processes, which is a valid limit as the nucleon mass is large. As $q^2 < 0$ and $\Pi_L(q^0 = 0, \vec{q})$ is always positive, the exchanged photon can not become on shell in bremsstrahlung processes, thus double counting is avoided (see Sec. IV D for more details).

B. $\gamma_{\mathrm{T,L}}$ decay

The on shell process of photon decay to $\chi\bar{\chi}$ [Fig. 1(a)] becomes possible in the medium and has an important analogy in the literature, the plasmon decay to neutrinos. Since the dispersion relation for transverse and longitudinal thermal photons are distinct, it is again helpful to separate the two polarizations in the calculation. Explicitly, we obtain for the decay rate per d.o.f.,

$$\Gamma_{\mathrm{T,L}} = \frac{1}{16\pi} Z_{\mathrm{T,L}} \sqrt{1 - \frac{4m_\chi^2}{\omega_{\mathrm{T,L}}^2 - |\vec{k}|^2}} \frac{f(\omega_{\mathrm{T,L}}^2 - |\vec{k}|^2)}{\omega_{\mathrm{T,L}}}, \quad (15)$$

where $\omega_{\mathrm{T,L}} = \omega_{\mathrm{T,L}}(|\vec{k}|)$ for each polarization mode, as defined above. Details on the definition of the wave function renormalization factors $Z_{\mathrm{T,L}}$ and the calculation are again given in Appendix B. In the limit of $m_\chi \to 0$, the decay widths for MDM agree with the well-known formulas for plasmon decay to a neutrino pair [3].

For the plasmon decay processes, the energy loss rate can be expressed as [3]

$$\dot{Q}_{\mathrm{decay,T}} = \frac{2}{2\pi^2} \int_0^\infty d|\vec{k}| \frac{|\vec{k}|^2 \Gamma_{\mathrm{T}} \omega_{\mathrm{T}}}{e^{\omega_{\mathrm{T}}/T} - 1} \Theta(\omega_{\mathrm{T}}^2 - |\vec{k}|^2 - 4m_\chi^2),$$
$$\dot{Q}_{\mathrm{decay,L}} = \frac{1}{2\pi^2} \int_0^{k_{\mathrm{max}}} d|\vec{k}| \frac{|\vec{k}|^2 \Gamma_{\mathrm{L}} \omega_{\mathrm{L}}}{e^{\omega_{\mathrm{L}}/T} - 1} \Theta(\omega_{\mathrm{L}}^2 - |\vec{k}|^2 - 4m_\chi^2). \quad (16)$$

The expression for k_{max} is given in Eq. (A7). For a nonrelativistic medium (HB, RG, Sun), the dispersion relation crosses the light cone at $|\vec{k}| = k_{\mathrm{max}}$, signaling the damping of longitudinal modes (*i.e.*, Landau damping); for a relativistic plasma (SN) $k_{\mathrm{max}} \to \infty$. The relative factor of 2 between the expressions reflects the counting of polarization d.o.f. Finally, the last factor is a kinematic restriction on the phase space, $\omega_{\mathrm{T,L}}^2 - |\vec{k}|^2 \geq 4m_\chi^2$. For transverse mode thermal photons, the integral becomes bounded from below since $\omega_{\mathrm{T}}^2 - |\vec{k}|^2$ increases as $|\vec{k}|$ increases according to the dispersion relation. For the longitudinal case, the integral is additionally bounded from above since the trend in $\omega_{\mathrm{L}}^2 - |\vec{k}|^2$ with respect to $|\vec{k}|$ is reversed.

C. e^+e^- annihilation

The degenerate plasma of the PNS core with temperature $T \gg m_e$ contains a population of e^+, allowing for dark state pair-production through e^+e^- annihilation [Fig. 1(b)]. The calculation for the pair production cross section is detailed in Appendix B.

In terms of the invariant $s = (p_1 + p_2)^2$ and the sum/difference of incoming $e^\mp$ energies $E_{1,2}$ in the frame of the thermal bath, i.e., $E_\pm \equiv E_1 \pm E_2$, the corresponding cross section mediated by the transverse polarization part of the propagator reads

$$\sigma_{\mathrm{T}} = \frac{\alpha[sE_-^2 + (4m_e^2 + s)(E_+^2 - s)]}{8\sqrt{s(s - 4m_e^2)}(E_+^2 - s)(s - \Pi_T)^2} \sqrt{1 - \frac{4m_\chi^2}{s}} f(s). \quad (17)$$

For the longitudinal part we obtain

$$\sigma_{\mathrm{L}} = \frac{\alpha[s(E_+^2 - E_-^2 - s)]}{8\sqrt{s(s - 4m_e^2)}(E_+^2 - s)(s - \Pi_L)^2} \sqrt{1 - \frac{4m_\chi^2}{s}} f(s). \quad (18)$$

Note that there is no interference term between the two. Furthermore, the sum of both cross sections, $\sigma_{\mathrm{T}} + \sigma_{\mathrm{L}}$, becomes Lorentz invariant in the limit of $\Pi_{\mathrm{T,L}} \to 0$.[3]

Before using (17) and (18) in the calculation of the energy loss rate, a comment on the analytic structure is in order. Although it appears that the process may be significantly enhanced when $s = \mathrm{Re}\Pi_{\mathrm{T,L}}$, this condition is never met: for the same reason that the decay of thermal photons into an electron-positron pair ($\gamma_{\mathrm{T,L}} \to e^+e^-$) is forbidden [54], the finite-temperature corrections to m_e prevent the process (2) from going on shell. It is for this reason that we have explicitly evaluated the thermal electron mass for the employed radial profile of the PNS; see Appendix A. In other words, we use a thermal electron mass in SN, and use the zero-temperature electron mass in HB, RG and Sun, where e^+e^- annihilation is of little relevance. The values of chemical potential μ_e are self-consistently adjusted to match the numerical PNS profiles from the literature (see below).

The energy loss rate of e^+e^- annihilation is found by weighing the emission process by the total radiated final state energy $E_3 + E_4 = E_1 + E_2$ and by the probability of finding the initial states with the respective energies E_1 and E_2,

$$\dot{Q}_{\mathrm{ann}} = \int d\Pi_{i=1,2,3,4} (2\pi)^4 \delta^4(p_1 + p_2 - p_3 - p_4) \times g_{e^-} g_{e^+} f_{e^-} f_{e^+} \frac{1}{4} \sum_{\mathrm{spins}} |\mathcal{M}_{\mathrm{ann}}|^2 (E_1 + E_2). \quad (19)$$

[3]We use a definition of the cross section for which the Møller velocity instead of the relative velocity $|\vec{v}_1 - \vec{v}_2|$ appears. At zero temperature, this makes the cross section a Lorentz invariant quantity; see the discussion in [58].

Here, $f_{e^\pm}$ are the phase-space distributions of $e^\pm$, with internal d.o.f. $g_{e^\pm} = 2$, and $|\mathcal{M}_{\rm ann}|^2$ is the squared matrix element for e^+e^- annihilation into the dark state pair. In (19) a Pauli-blocking factor induced by χ and $\bar\chi$ is neglected; we have verified that this does not affect the derived constraints. Finally, $d\Pi_i = \prod_i d^3\vec{p}_i(2\pi)^{-3}(2E_i)^{-1}$ is the Lorentz invariant phase space element.

The energy loss rate can be written in terms of the cross sections $\sigma_{\rm T,L}$. Borrowing from the discussion on phase space in [59], we find explicitly

$$\dot{Q}_{\rm ann} = \int_{4m_{\rm th}^2}^{\infty} ds \int_{\sqrt{s}}^{\infty} dE_+ \int_{-\sqrt{(1-4m_e^2/s)(E_+^2-s)}}^{\sqrt{(1-4m_e^2/s)(E_+^2-s)}} dE_- \times \frac{1}{64\pi^4} g_{e^-} g_{e^+} f_{e^-} f_{e^+} E_+ \sqrt{s(s-4m_e^2)}\sigma_{\rm T,L}. \tag{20}$$

The distribution functions f_{e^-} and f_{e^+} read

$$f_{e^\mp} = \frac{1}{e^{(E_+ \pm E_- \mp 2\mu_e)/2T} + 1}. \tag{21}$$

Here, μ_e is the chemical potential of electrons and T is the temperature. The threshold mass $m_{\rm th}$ is equal to $\max\{m_e, m_\chi\}$.

D. Compton scattering

For $2\to 3$ Compton scattering ($e^-/N + \gamma_{\rm T,L} \to e^-/N + \chi + \bar\chi$) with an initial $\gamma_{\rm T,L}$ [Fig. 1(c)], we calculate the differential cross section via

$$\frac{d\sigma_{2\to 3}}{ds_{\chi\bar\chi}} = \sigma_{2\to 2}(s_{\chi\bar\chi}) \frac{f(s_{\chi\bar\chi})}{16\pi^2 s_{\chi\bar\chi}^2} \sqrt{1 - \frac{4m_\chi^2}{s_{\chi\bar\chi}}}. \tag{22}$$

Here, $\sigma_{2\to 2}(s_{\chi\bar\chi})$ is the cross section of the two-body Compton scattering with the final-state photon having a mass $\sqrt{s_{\chi\bar\chi}}$. We are only required to consider the process on electrons, $e^- + \gamma_{\rm T,L} \to e^- + \chi + \bar\chi$, as Compton scattering on protons is strongly suppressed. Following the treatment in [55] and our discussion above, we neglect the thermal mass of the final state photon in $\sigma_{2\to 2}$ to avoid any potential double counting with $\gamma_{\rm T,L}$ decay. For the initial state photon in the integration of energy loss rate, Eq. (23) below, the thermal mass is properly taken in account through the dispersion relation (A6).

Furthermore, note that there is no double counting between the Compton process and bremsstrahlung either in our treatment. A double counting would appear if the t-channel photon exchange in bremsstrahlung, with 4-momentum q [see Fig. 1(d)], goes on resonance. This is in principle possible for the longitudinal mode, since $\Pi_{\rm L}$ in the propagator could become negative once the dispersion relation of $\gamma_{\rm L}$ crosses the light cone. Nevertheless, in the electron bremsstrahlung process discussed below—most relevant for RG, HB and the Sun—the proton recoil and hence the energy exchange are extremely small. Therefore, the propagator can be taken in the static limit (energy exchange $q^0 \to 0$). This limit amounts to Debye screening, characterized by $\Pi_{\rm L}(q^0 \to 0, |\vec{q}|)$. Since the screening scale is always positive, a resonance is never met. Therefore, we include the contribution from $e^- + \gamma_{\rm L} \to e^- + \chi + \bar\chi$ to capture the t-channel resonance contribution of electron bremsstrahlung, although it is less important than plasmon decay.

The energy loss rate from Compton scattering is calculated in a similar way as (19), but here $E_{\rm loss}$ is given by the energy carried by the virtual photon in the medium frame,

$$\dot{Q}_{\rm Compton} = \int d\Pi_{i=1,2} 4E_1E_2\sigma_{2\to 3}^{\rm T,L} v_M g_{e^-} g_{\rm T,L} f_1 f_2 \times (1-f_3)E_{\rm loss}, \tag{23}$$

where $f_{1,2,3}$ are the distribution functions of the incoming electron, $\gamma_{\rm T,L}$ and outgoing electron, respectively, with $g_{e^-} = g_{\rm T} = 2$ and $g_{\rm L} = 1$ the internal d.o.f. for the incoming electron and $\gamma_{\rm T,L}$. Pauli blocking is accounted for by including the factor $(1-f_3)$. The energy loss $E_{\rm loss} = E_{\bar\chi} + E_\chi$ can be expressed in terms of variables defined in the medium frame. Moreover, for RG, HB and the Sun, the relativistic corrections induced by transforming from the center-of-mass (CM) frame to the medium frame are very small and are neglected for simplicity.

E. e^-N bremsstrahlung

In this subsection we consider dark state pair production from bremsstrahlung of electrons on protons or other nuclei [Fig. 1(d)]. Similar to the Compton scattering above, we also relate the $2\to 4$ cross section to a $2\to 3$ process of $eN \to eN + \gamma^*_{T,L}$ in which the emitted photon, $\gamma^*_{T,L}$, has an invariant mass $\sqrt{s_{\chi\bar\chi}}$,

$$\frac{d\sigma_{2\to 4}}{ds_{\chi\bar\chi}} = \sigma_{2\to 3}(s_{\chi\bar\chi}) \frac{f(s_{\chi\bar\chi})}{16\pi^2 s_{\chi\bar\chi}^2} \sqrt{1 - \frac{4m_\chi^2}{s_{\chi\bar\chi}}}. \tag{24}$$

In the following we shall only consider photon-emission from electrons, as the emission from the nuclear leg is suppressed by a factor of $(Zm_e/m_N)^2 \ll 1$ where Z and m_N are the charge and mass of the nucleon/nucleus. Furthermore, ordinary electron-electron bremsstrahlung is a quadrupole emission process and correspondingly smaller in practice. We therefore also neglect such production channel.

The eN process is sensitive to the details of in-medium corrections. To this end, recall that the t-channel photon exchange in Fig. 1(d) has a well-known Coulomb divergence in the limit of vanishing momentum-transfer. This issue is mitigated by two factors: first, the divergence is not met kinematically as long as $m_\chi \neq 0$ since a minimum momentum transfer is necessary to create the final state pair. Second, the medium itself regulates the process through the Debye screening of bare charges characterized by a momentum scale k_D. The latter appears as the static limit of $\Pi_L(q^0 \to 0, \vec{q})$ and for a classical plasma reads

$$k_D^2 = \frac{4\pi\alpha n_e}{T} + \text{ion-contributions}. \tag{25}$$

For the numerical results, we have calculated $\sigma_{2\to3}$ in (24) using the propagator (A4), neglecting, for simplicity, ion contributions. We separate the squared amplitude into transverse and longitudinal parts and include the static limits of $\Pi_{T,L}$ in the respective propagators. For the longitudinal part, the zero-temperature propagator q^{-2} is replaced by $(q^2 - k_D^2)^{-1}$. In contrast, there is no magnetic screening in the static limit $[\Pi_T(q^0 \to 0, |\vec{q}|) = 0]$; hence there is no thermal screening for the propagator of the transverse mode. We find that in the nonrelativistic limit the contribution of the longitudinal mode dominates.

To avoid any double counting between this process and the $\gamma_{T,L}$ decay, we need to subtract the contribution when the virtual photon that directly couples to χ goes on shell. As stated above, this is achieved by setting $\Pi_{T,L}$ in the corresponding propagator to zero. Since this should overestimate the production rate at $s_{\chi\bar{\chi}} \le \Pi_{T,L}$, we have also tested an opposite option of choosing $\Pi_{T,L} \to -\Pi_{T,L}(E_\chi + E_{\bar{\chi}})$ to avoid the singularity, which underestimates the production rate. We find that both prescriptions lead to same results at the percent level, which justifies our simplification of taking $\Pi_{T,L} \equiv 0$ for the photon that directly couples to χ.

For dark state pair production in e^- bremsstrahlung on protons and nuclei, the energy loss rate is expressed as

$$\dot{Q}_{\text{brem}} = \int d\Pi_{i=1,2} 4E_1E_2\sigma_{2\to4} v_M g_1 g_2 f_1 f_2 (1 - f_3) E_{\text{loss}}, \tag{26}$$

where $f_{1,2,3}$ are the distribution functions of the incoming electron, proton/nucleus and outgoing electron, with $g_{1,2}$ the internal d.o.f. for the incoming particles. We have neglected the Pauli blocking factor for final-state protons/nuclei as it plays little role. The Møller velocity $v_M = F/(E_1E_2)$ is given in terms of the flux factor F found in (B19). The energy carried-away by the dark states is $E_{\text{loss}} = E_{\bar{\chi}} + E_\chi$ and its expression in the medium frame is introduced in Appendix B.

Making the approximation that protons and other nuclei are at rest, their phase-space integral gives $\int d\Pi_2 f_2 = n_N/(2m_N g_2)$, where n_N is the number density of the protons/nuclei. Hence we arrive at

$$\dot{Q}_{\text{brem}} = \int_{m_e+2m_\chi}^{\infty} dE_1 \frac{2n_N E_1 E_2 v_M}{(2\pi)^2 m_N} |\vec{p}_1| g_1 f_1 \sigma_{2\to4} (1 - f_3) E_{\text{loss}}, \tag{27}$$

with $|\vec{p}_1| = \sqrt{E_1^2 - m_e^2}$ and where $\sigma_{2\to4}$ is obtained from integrating (24) over appropriate boundaries (see Appendix B 5). Generically, bremsstrahlung is less effective when pair annihilation or plasmon decay are open as production channels, but it can be dominant at low temperatures where the latter processes are kinematically suppressed.

Before ending this subsection, it is worth commenting on the so-called soft photon approximation, which states that in the limit that the emitted photon energy is small compared to the available kinetic energy (i.e., $\omega \ll E_{\text{kin}}$), the process of $eN \to eN + \gamma^*_{T,L}$ factorizes into a product of elastic scattering times a factor describing the additional emission of $\gamma^*_{T,L}$. While this approximation works well for the emission of a massless photon, it breaks down if the off shell photon's *effective* mass is large, $\sqrt{s_{\chi\bar{\chi}}} \sim E_{\text{kin}}$. Overall, we find that the soft photon approximation describes the $2 \to 4$ process well for small m_χ in the nonrelativistic limit. However, for $2m_\chi \sim E_{\text{kin}}$ or for relativistic initial states the approximation fails, and it is ultimately related to the UV-sensitivity of the cross section (see Appendix C for details). Even though calculations simplify considerably in the soft photon limit, it cannot be applied for the whole m_χ-range in electron bremsstrahlung, and we therefore calculate $\sigma_{2\to4}$ exactly, relegating details of the calculation to Appendix B. However, we will use the soft photon approximation in its region of validity to estimate the energy loss from nucleon bremsstrahlung in the next subsection.

F. Nucleon bremsstrahlung

Proton and nuclear bremsstrahlungs are strongly suppressed in low-temperature environments due to the negligible thermal velocities of the initial states. However, in the interior of a PNS, the typical nucleon velocity is $v \lesssim 1/3$ and NN-bremsstrahlung contributes to the total energy loss.

The photon that pair-creates the dark states is emitted from the proton-leg in proton-proton (pp) and neutron-proton (np) scattering. Radiating off the neutron-leg through the neutron magnetic dipole moment is suppressed. In addition, since pp-scattering is associated with quadrupole radiation, it is suppressed with respect np scattering by a factor v^2 [60]. Therefore, we only consider np-scattering in the following. The interaction of protons and neutrons is mostly mediated by pions whose mass is of the order of the average momentum transfer in elastic collisions in PNS, allowing for a separation of the phase space into an elastic and an emission piece (see Appendix C for details). The energy loss rate in the nonrelativistic, nondegenerate limit[4] is then given by [60]

[4]The corrections to Eq. (28) due to matter degeneracy in PNS are estimated in Ref. [60] to be small (≈30%) compared to the corrections neglected in the soft-photon approximation, which are up to a factor of 3 as mentioned in Appendix C.

$$\dot{Q}_{np} = \frac{n_n n_p}{\sqrt{\pi}(m_n T)^{3/2}} \int_{2m_\chi}^{\infty} dE_{\rm kin} E_{\rm kin}^2 e^{-\frac{E_{\rm kin}}{T}} \int_{4m_\chi^2}^{E_{\rm kin}^2} ds_{\chi\bar{\chi}} \times \sqrt{1 - \frac{4m_\chi^2}{s_{\chi\bar{\chi}}}} \frac{f(s_{\chi\bar{\chi}})}{16\pi^2 s_{\chi\bar{\chi}}^2} \sigma_{np}^T(E_{\rm kin}) \mathcal{I}_\omega(s_{\chi\bar{\chi}}), \tag{28}$$

where n_n and n_p are the neutron and proton number densities, m_n is the average nucleon mass and $E_{\rm kin}$ the available kinetic center of mass energy. For the elastic np-scattering transport cross section σ_{np}^T we use the numerical data from Fig. 3 in Ref. [60] for $E_{\rm kin} \gtrsim 1$ MeV and Fig. 2 in Ref. [61] for smaller energies; the emission piece $\mathcal{I}_\omega$ is given by Eq. (C8).

The energy loss rates from nucleon bremsstrahlung are comparable with the rates from plasmon decay and are depicted for $m_\chi = 1$ MeV as a function of the PNS radius in Fig. 4.

V. CONSTRAINTS ON THE EFFECTIVE COUPLING

After calculating the energy loss rates induced by those relevant processes in each stellar environment (e.g., see Figs. 3–4), we apply the luminosity criteria introduced in Sec. III to obtain the upper bounds on the EM form-factors of light dark states.

A. Limits from RG, HB, and the Sun

In this subsection, we derive the constraints coming from HB and RG stars utilizing the above calculated anomalous energy loss rates. For HB, we consider a representative star of 0.8 $M_\odot$ and utilize the stellar profiles for density, temperature and chemical partition between hydrogen and helium from [3,62], reproduced in Fig. 7 in Appendix A. The luminosity of its helium-burning core is $L_{\rm HB} = 20\ L_\odot$ to which (7) is then applied. For RG we use the prescription detailed below (8): a 0.5 $M_\odot$ helium core with a constant density of $\rho = 2 \times 10^5$ g/cm^3 and a temperature $T = 10^8$ K.

For the Sun, we use the standard Solar model BP05(OP) [63] to calculate the total power radiated into $\chi\bar{\chi}$ which in turn is constrained from (9). For bremsstrahlung we take the contribution of electron scattering on H, ^{4}He and other less abundant nuclei (^{3}He, C, N, and O). For simplicity, we assume all targets are in a fully ionized state. We find numerically that the contribution from the second class of elements contribute 10% of the total energy loss rate from bremsstrahlung, as the coherent enhancement from atomic charge number Z somewhat compensates for their scarcity in number.

The energy loss rates as a function of fractional stellar radius for HB (Sun) for all operators considered in (5) and (6) are shown in the left (right) panel of Fig. 3 for $m_\chi = 10$ eV and $\mu_\chi(\text{or } d_\chi) = 10^{-6}\ \mu_B$ and $a_\chi(\text{or } b_\chi) = 0.1\ \text{GeV}^{-2}$. MDM and EDM as well as AM and CR lines essentially yield identical results. This is owed to the fact that production proceeds in the kinematically unsuppressed region $T \gg m_\chi$ for which the energy loss rates match; the γ^5 factor discriminating the interactions of same mass-dimension only plays a role when χ particles become nonrelativistic, hence

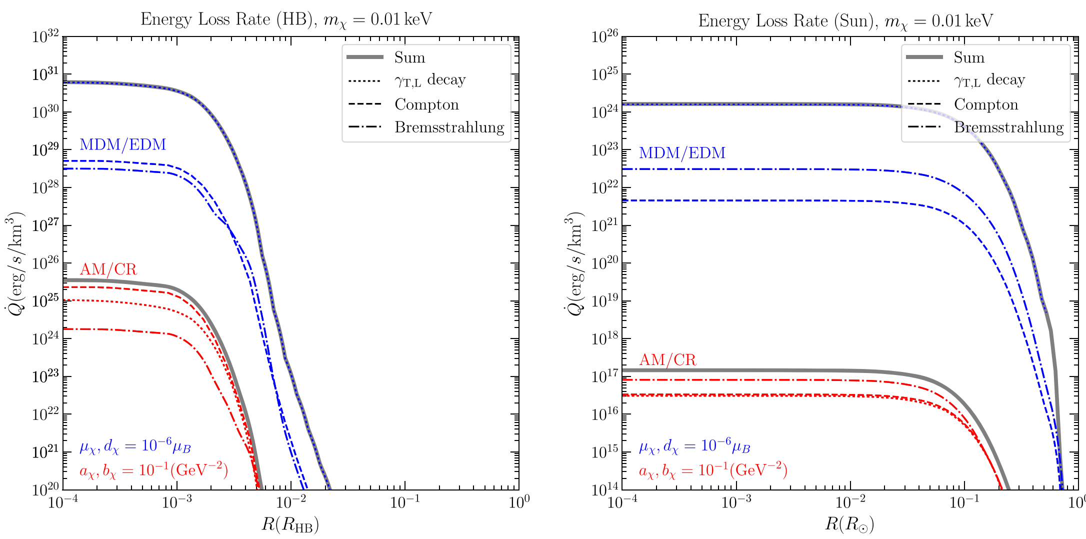

FIG. 3. *Left*: Energy loss rates as a function of fractional stellar radius from $\gamma_{\rm T,L}$ decay (dotted lines), Compton production (dashed lines) and electron bremsstrahlung (dash-dotted lines) for $m_\chi = 0.01$ keV and $\mu_\chi(\text{or } d_\chi) = 10^{-6}\ \mu_B$ and $a_\chi(\text{or } b_\chi) = 0.1/\text{GeV}^2$ in the representative HB star we consider. The sum of all processes is shown by the thick gray line, which for MDM/EDM interactions practically coincides with plasmon decay. *Right*: The same processes as in the left panel but for the Sun.

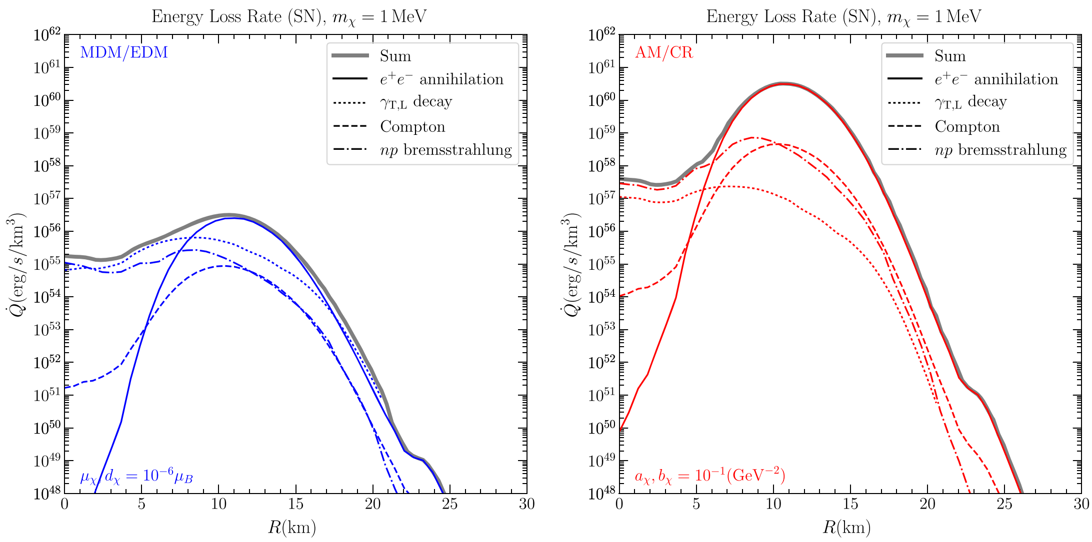

FIG. 4. *Left*: Energy loss rates inside PNS for MDM/EDM interactions with $\mu_\chi(\text{or } d_\chi) = 10^{-6}\ \mu_B$ and $m_\chi = 1$ MeV are shown for all computed processes, namely, e^+e^- annihilation (thin solid line), $\gamma_{\rm T,L}$ photon decay (dotted line), Compton production (dashed line) and np bremsstrahlung (dash-dotted line). The sum of all contributions is the thick solid line. *Right*: The same processes as in the left panel but for AM/CR interactions with $a_\chi(\text{ or } b_\chi) = 0.1/\mathrm{GeV}^2$.

close to kinematic end points. As can be seen, for dimension-5 operators the decay process (dotted lines) dominates over bremsstrahlung (dash-dotted lines) and Compton scattering (dashed lines) processes in both HB and the Sun. For dimension-6 operators, the contribution of Compton scattering is comparable to that of decay processes in HB while in the Sun all three processes are of comparable importance.

Applying the criteria for the maximum allowable energy loss of Sec. III, we obtain the excluded shaded regions in Figs. 5 and 6 as labeled. The strongest limits are provided by RG stars. They have a higher core temperature, $T = 8.6$ keV, compared to HB stars or the Sun, favoring an emission process that is UV-biased because of the considered higher-dimensional operators. In the low mass region, for $2m_\chi < \omega_p$, the limits are governed by $\gamma_{\rm T,L}$ decays, and become independent of χ mass quickly. Once the decay process is kinematically forbidden, the limits become determined by the bremsstrahlung and Compton scattering processes. As can be seen, the critical values of m_χ where this happens for RG, HB, and the Sun are reflective of the differing core-plasma frequencies (A3) of the respective systems. Furthermore, the mass-dimension 5 constraints on MDM and EDM are practically identical; differences only appear in the kinematic endpoint region.

B. Limits from SN1987A

Limits on χ-photon interactions from SN1987A have previously been estimated in our earlier paper [30], largely following the approach of [56], and considering e^+e^- annihilation but with plasmon decay neglected. Here we revisit these constraints in light of a more detailed calculation. Dark state pairs with mass $m_\chi \lesssim 400$ MeV can be efficiently produced inside PNS, predominantly through e^+e^- annihilation as positrons are thermally supported. Nevertheless, we will consider all processes in Fig. 1 except for electron bremsstrahlung as it is significantly weaker than the others; see Fig. 4 for one example with $m_\chi = 1$ MeV.

When the particles stream freely after production and are hence able to escape from the PNS core, the limit (10) applies. We set the size of the PNS core to be $r_{\rm core} = 15$ km and model the PNS from which $\chi\bar{\chi}$ pairs are emitted using the simulation results of a 18 $M_\odot$ progenitor in [64] (see Fig. 7 in Appendix A). Notice that such simulation results are based on an artificial neutrino-driven explosion method and should be taken with a grain of salt. We adopt the total energy density $\rho(r)$, temperature $T(r)$ and electron abundance $Y_e(r)$ profiles at 1s after the core bounce. The number density of baryons can be computed as $n_b(r) \simeq \rho(r)/m_p$ and the number density of electrons can be written as $n_e(r) \simeq n_b(r)Y_e(r)$. Other quantities such as chemical potential of electrons $\mu_e(r)$, plasma frequency $\omega_p(r)$ and effective electron mass $m_e^{\rm eff}(r)$ are derived from $n_e(r)$ and $T(r)$. $m_e^{\rm eff}(r)$ is recursively solved at each radius using Eq. (A20); see Appendix A for details. In the calculations that relate to the anomalous emission, m_e is understood to be $m_e^{\rm eff}$.

The result is shown by the lower boundary of the region labeled SN1987A in Figs. 5 and 6. Compared to our previous result in [30] where only e^+e^- annihilation was

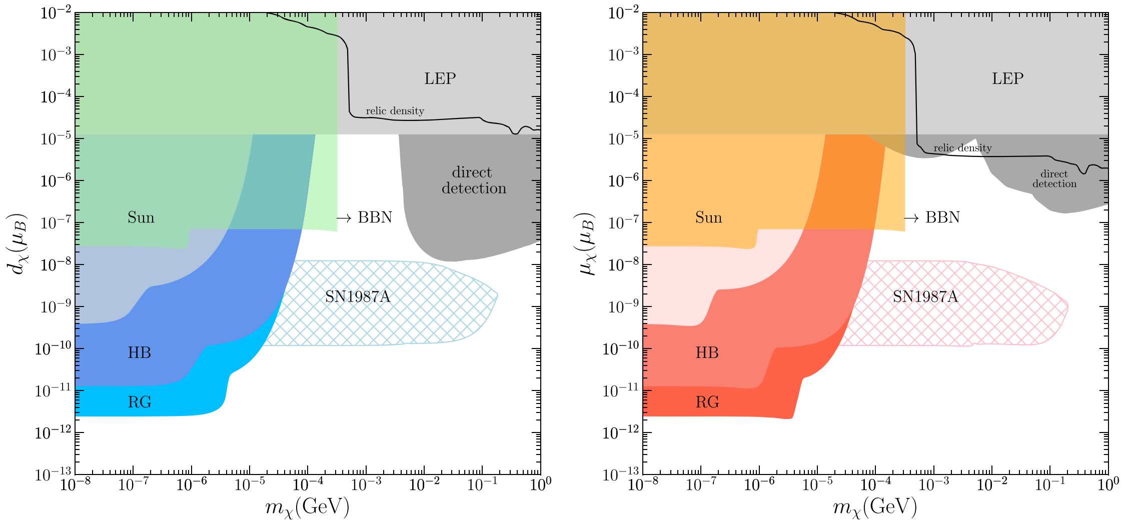

FIG. 5. Summary of constraints on the EM form factors for dim-5 operators, i.e., EDM (left) and MDM (right). Colored exclusions are derived in this work. Direct detection (only applying to dark matter) and LEP bounds are taken from our previous work [30]. On the solid black line the thermal freeze-out abundance matches the DM density.

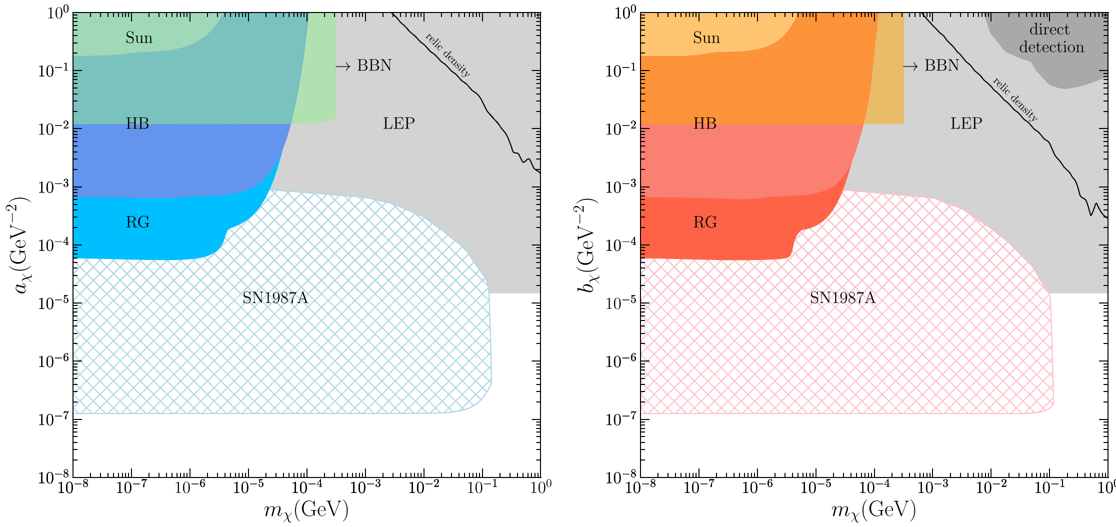

FIG. 6. Summary of constraints on the EM form factors for dim-6 operators, i.e., AM (left) and CR (right); labels are the same as in Fig. 5.

taken into account, the constraint for MDM and EDM is improved. This is traced back to the fact that the energy loss rate of $\gamma_{\mathrm{T,L}}$, nucleon-bremsstrahlung and Compton scattering for MDM and EDM are comparable to e^+e^- annihilation into a $\chi\bar{\chi}$ pair. For AM and CR, however, the results from [30] remain largely unchanged, as $\gamma_{\mathrm{T,L}}$ decay, nucleon-bremsstrahlung and Compton scattering are less efficient.

Once the effective coupling becomes large enough, the produced χ particles will eventually come into thermal equilibrium with SM particles. Here we follow [65,66] to divide the radial region into an inner "energy sphere" of radius r_{ES}, within which light dark particles are thermalized, and an outer diffusion zone, where the χ luminosity gets attenuated by a transmission coefficient S_{ES}. Both quantities are obtained from the energy-exchange and

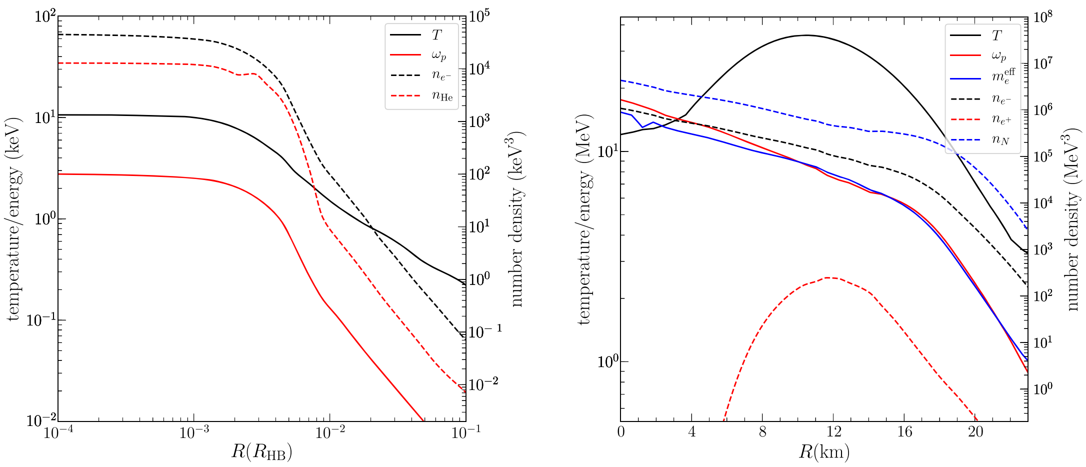

FIG. 7. Reproduced profiles of a representative 0.8 $M_\odot$ HB star [62] (left) and of a PNS of a 18 $M_\odot$ progenitor [64] (right) that are adopted in our work. In each panel, the left vertical axis corresponds to the values of temperature and plasma frequency (solid lines) at each radius, in units of keV(HB) or MeV(PNS), and the right vertical axis gives the number densities (dashed lines) of each particle species, in keV^3(HB) or MeV^3(PNS). For SN, the effective electron mass m_e^{eff} is also displayed.

momentum-exchange mean-free-paths, i.e., $\lambda_E(r)$ and $\lambda_M(r)$, of the χ particle in the medium [65],

$$\int_{r_{\mathrm{ES}}}^{r_{\mathrm{inf}}} \frac{dr}{\sqrt{\lambda_E(r)\lambda_M(r)}} = \frac{2}{3}, \tag{29}$$

and

$$S_{\mathrm{ES}} = \frac{1}{1+\frac{3}{4}\int_{r_{\mathrm{ES}}}^{r_{\mathrm{inf}}} \frac{dr}{\lambda_M(r)}}, \tag{30}$$

where r_{inf} is set to be 35 km, beyond which χ particles free-stream.

In the PNS environment of interest here, the energy-exchange mean-free-path is mostly governed by e-χ elastic scattering. We estimate it at each radius r through

$$\lambda_E(r) = \frac{\langle n_\chi v_\chi \rangle}{\langle n_e n_\chi \int d\cos\theta \frac{d\sigma_{e\chi}}{d\cos\theta} v_M \frac{|\Delta E|}{T}\rangle}. \tag{31}$$

Here, $\langle \ldots \rangle$ denotes a thermal average over all participating particles; n_e and n_χ are the number densities of electrons and χ particles which are all assumed to be in equilibrium. $d\sigma_{e\chi}/d\cos\theta$ is the differential cross section of e-χ elastic scattering. The energy-exchange in the scattering, $|\Delta E|$, is a function of the scattering angle θ in the rest frame of the medium. Although not explicitly written in the expression, we take the Pauli blocking factor for the final state electron into account.

Meanwhile, the momentum-exchange mean-free-path $\lambda_M(r)$ turns out to be dominated by χ-nucleon scattering,

$$\lambda_M(r) = \frac{\langle n_\chi v_\chi \rangle}{\sum_{i=n,p}\langle n_i n_\chi \int d\cos\theta \frac{d\sigma_{i\chi}}{d\cos\theta} v_M (1-\cos\theta)\rangle}, \tag{32}$$

where n_i is the number density of neutrons (n) and protons (p), provided by the PNS model [64]. The differential scattering cross section with χ is denoted as $d\sigma_{i\chi}/d\cos\theta$. In obtaining our numerical results, we have neglected the nucleon velocities in the medium frame for simplicity.

As we assume that χ stay in chemical equilibrium at r_{ES}, its blackbody luminosity $L_\chi(r_{\mathrm{ES}})$ is described by

$$L_\chi(r_{\mathrm{ES}}) = \frac{g_\chi r_{\mathrm{ES}}^2}{2\pi} \int d|\vec{p}_\chi| \frac{|\vec{p}_\chi|^3}{e^{\sqrt{|\vec{p}_\chi|^2+m_\chi^2}/T(r_{\mathrm{ES}})}+1}, \tag{33}$$

where $g_\chi = 4$. These χ particles are emitted towards the exterior from the energy sphere, but they continue to scatter elastically with the medium inside the diffusion zone. The χ flux-attenuation during its propagation from r_{ES} to r_{inf} can be estimated via

$$L_{\mathrm{inf}} = L_\chi(r_{\mathrm{ES}}) S_{\mathrm{ES}} \tag{34}$$

in the diffusion limit [65]. That is, such attenuation only relies on the momentum-transfer cross section. Requiring $L_{\mathrm{inf}} \le L_\nu$ then leads to upper boundaries of SN exclusion limits shown in Figs. 5 and 6. We note in passing, that the location of the upper boundaries is still conservative, as additional "freeze-in" χ-production for $r > r_{\mathrm{ES}}$ has been neglected. With respect to our previous work [30], where the transmission ratio S_{ES} was in practice taken as a simple unit-step function, the upper limits are improved by up to a factor of 2.

C. Related works

Stellar bounds on the EM properties of light dark states have been studied in the literature, mostly in the context of EM properties of eV-scale (SM) neutrinos; see [67,68] and references therein. In these studies, the mass of neutrino is essentially zero. Therefore, in the limit $m_\chi \to 0$ our results can be compared with previously derived constraints on neutrino EM interactions.

For instance, based on similar energy loss arguments, bounds on the neutrino MDM have been obtained by calculating the plasmon decay process, from RG as $\mu_\nu \leq (2-4)\times 10^{-12}\ \mu_B$ [69–71], from HB as $\mu_\nu \leq (1-3)\times 10^{-11}\ \mu_B$ [72,73], from the Sun as $\mu_\nu \leq 4\times 10^{-10}\ \mu_B$ [74]. Indeed, all these bounds are in essential agreements with our newly derived ones once the limit $m_\chi \to 0$ is taken.

For higher-dimensional operators, [75] estimated the anomalous energy loss rate in PNS through electron pair annihilation into light right-handed neutrinos, limiting its charge radius to be below $3.7\times 10^{-34}\ \mathrm{cm}^2$, that is $9.5\times 10^{-7}\ \mathrm{GeV}^{-2}$, about 7 times weaker than the one presented above. This is partially due to the fact that [75] assumed an 1 order of magnitude larger luminosity as the maximum permissible energy loss.

D. Cosmological constraints

Light dark states may lead to extra radiation in the early Universe, and thus its coupling to the SM bath is constrained by both the predictions from big bang nucleosynthesis (BBN) and the observed cosmic microwave background (CMB). On the one hand, for the mass region considered here the CMB bounds depend on how it annihilates/decays. On the other hand, primordial abundance measurements of D and ^{4}He suggest that extra relativistic d.o.f. need to be less than that of one chiral fermion during the nucleosynthesis (see e.g., [76–78]). Thus here we require that the Dirac fermion χ is thermally diminished at $T \sim 100$ keV, either due to a feeble EM form-factor coupling or by a Boltzmann-suppression induced by its mass.

The relevant bounds are also given in Figs. 5 and 6. They only constrain the parameter region with $m_\chi \ll 1$ MeV. In the same figures, we also show the line which corresponds to the thermal freeze-out scenario which generates the observed dark matter abundance, although such scenario has been excluded by various constraints for this model; see our previous work [30]. The dominant annihilation channel is into two photons at $m_\chi < m_e$ and into a pair of electrons at $m_\chi \geq m_e$, which explains the sharp decrease of the relic density curve at $m_\chi \sim m_e$ seen in Fig. 5.

VI. CONCLUSIONS

In this paper we explore the sensitivity of stellar systems to neutral dark states that share higher-dimensional interactions with the SM photon. To this end we choose a Dirac fermion χ that is coupled to mass dimension 5 MDM and EDM operators with respective dimensionful coefficients μ_χ and d_χ and mass dimension 6 AM and CR operators with respective coefficients a_χ and b_χ. We consider anomalous energy losses from the interior of RG and HB stars, of the Sun, and of the PNS core of SN1987A. Together with previously derived direct, indirect, and cosmological limits by us in [30], this work adds astrophysical constraints to draw a first comprehensive overview of light dark states with masses (well) below the GeV-scale and EM moment interactions.

The thermal environments of stellar interiors significantly affect (or enable) production processes of $\chi\bar{\chi}$ pairs. Before breaking it down to individual contributions, we establish the exact formula, Eq. (13), for the pair-production rate in leading order of the dark coupling. The expression factorizes into a piece that represents the probability to produce an off shell photon γ^* from a SM current, and a piece that describes the production of the $\chi\bar{\chi}$ pair from that photon. The former is proportional to the imaginary parts of the longitudinal and transverse thermal photon self energies $\mathrm{Im}\Pi_{\mathrm{L,T}}$. The latter are model-dependent but otherwise universal factors that represent the choice of interaction, Eq. (14). The optical theorem then allows us to identify all major production processes by studying the contributions to $\mathrm{Im}\Pi_{\mathrm{L,T}}$. The approach also allows us to clarify the role of thermal resonances in these processes, i.e., the kinematic situation when the pair-producing photon goes on shell, $k^2 = \mathrm{Re}\Pi_{\mathrm{L,T}}$. We find that resonant production is entirely captured by the decay of transverse and longitudinal thermal photons or "plasmons", $\gamma_{\mathrm{T,L}} \to \chi\bar{\chi}$.

We compute the rates of χ-pair production and its ensuing energy loss from plasmon decay and Compton production for all systems. In addition, we evaluate eN bremsstrahlung for RG, HB and the Sun, and e^+e^- annihilation and NN bremsstrahlung for SN1978A. For MDM and EDM interactions, plasmon decay dominates in HB and RG stars and in the Sun. For the interactions of increased mass dimension, AM and CR, the Compton (bremsstrahlung) production dominates in HB and RG (Sun). In PNS core, e^+e^- annihilation dominates the anomalous energy loss for $r \gtrsim 7$ km. In the most inner region the population of positrons becomes extremely Boltzmann suppressed by a decrease in temperature, and plasmon decay and np bremsstrahlung take over as the most important production channels. For all processes we have taken into account all important finite-temperature effects. Furthermore, in the evaluation of rates, we explicitly avoid any double counting between plasmon decay and an on shell emitted photon in bremsstrahlung and between Compton production and an on shell exchanged t-channel photon in bremsstrahlung.

The rates when integrated over stellar radius then become subject to the observationally inferred limits on anomalous energy loss. The resulting restrictions on the parameter space are found in Figs. 5 and 6. In the kinematically unrestricted regime $m_\chi \lesssim 1$ keV, the stellar limits are dominated by RG with μ_χ, $d_\chi \leq 2\times 10^{-12}\ \mu_B$ and a_χ, $b_\chi \leq 6\times 10^{-5}$ GeV^{-2}. All interactions are additionally constrained from SN1987A, in the windows $10^{-10}\ \mu_B \leq \mu_\chi$, $d_\chi \leq 10^{-8}\ \mu_B$ and 10^{-7} GeV$^{-2} \leq a_\chi$, $b_\chi \leq 10^{-3}$ GeV^{-2} for $m_\chi \lesssim 10$ MeV. The SN constraining region is bounded from above by the trapping of χ particles, which we evaluate in some detail. The presented astrophysical constraints add to a program that we have started in [30] and that aims at charting out the experimental and observational sensitivity to effective dark state-photon interactions. The stellar constraints on anomalous energy loss derived in this work yield the most important limits on the existence of effective dark sector-photon interactions for χ-particles below the MeV-scale.

ACKNOWLEDGMENTS

The authors are supported by the New Frontiers program of the Austrian Academy of Sciences. J.-L. K and L. S. are supported by the Austrian Science Fund FWF under the Doctoral Program No. W1252-N27 Particles and Interactions. We acknowledge the use of computer packages for algebraic calculations [79,80].

APPENDIX A: PHOTONS IN A THERMAL MEDIUM

The processes depicted in Fig. 1 are fundamentally affected (or enabled) by the in-medium modified photon dispersion. Here we collect the central results that go into the computation of the energy loss rates (our convention largely follows [3]). The central quantity measuring the strength of the medium-effect is the plasma frequency ω_p, obtained through

$$\omega_p^2 = \frac{4\alpha}{\pi}\int_0^\infty dp\,\frac{p^2}{E}\left(1-\frac{1}{3}v^2\right)(f_{e^-}+f_{e^+}), \tag{A1}$$

where $v = p/E$ is the velocity of electrons or positrons, and f_{e^-} and f_{e^+} are their respective Fermi-Dirac distributions, $f_{e^\pm} = [e^{(E\pm\mu_e)/T}+1]^{-1}$.

Equation (A1) takes on the following analytic forms in the classical, degenerate and relativistic limit respectively:

$$\omega_p^2 \simeq \begin{cases} \frac{4\pi\alpha n_e}{m_e}\left(1-\frac{5}{2}\frac{T}{m_e}\right) & \text{classical} \\ \frac{4\pi\alpha n_e}{E_F} = \frac{4\alpha}{3\pi}p_F^2 v_F & \text{degenerate}, \\ \frac{4\alpha}{3\pi}\left(\mu_e^2+\frac{1}{3}\pi^2T^2\right) & \text{relativistic} \end{cases} \tag{A2}$$

where α is the fine-structure constant, n_e is the number density of electrons, $p_F = (3\pi^2 n_e)^{1/3}$ is the Fermi momentum, $E_F = \sqrt{m_e^2+p_F^2}$ is the Fermi energy and $v_F = p_F/E_F$ is the Fermi velocity. Here "classical" refers to a nonrelativistic ($T \ll m_e$) and nondegenerate ($T \gg \mu_e - m_e$) plasma.

The PNS core of a SN is both in a relativistic and degenerate regime, and we find that the relativistic limit above yields a better fit to the general form of ω_p in (A1) than the degenerate limit; the latter exhibits a 10% deviation. The core of a RG star is nonrelativistic but degenerate whereas HB stars and the Sun are well described by the classical limit. In our numerical calculations, we adopt ω_p computed from Eq. (A1), avoiding any ambiguities of taking limiting cases. Representative values of ω_p at the cores of all stellar objects are summarized as

$$\omega_p \sim \begin{cases} 0.3\text{ keV} & \text{Sun's core} \\ 2.6\text{ keV} & \text{HB's core} \\ 8.6\text{ keV} & \text{RG's core} \\ 17.6\text{ MeV} & \text{SN's core} \end{cases}. \tag{A3}$$

The computation of most of the processes requires the in-medium photon propagator. Picking Coulomb gauge, for a photon carrying 4-momentum $k = (\omega, \vec{k})$, the latter divides into longitudinal (L) and transverse (T) parts [81],

$$D_{00} = \frac{k^2}{|\vec{k}|^2(k^2-\Pi_{\rm L})}g_{00},$$
$$D_{ij} = \frac{1}{k^2-\Pi_{\rm T}}\left(\delta_{ij}-\frac{k_ik_j}{|\vec{k}|^2}\right), \tag{A4}$$

where k_i is the Cartesian component of the photon three-momentum (magnitude $|\vec{k}|$). Using [81] and adopting the conventions of [3,5], the real part of the polarization functions $\Pi_{\rm T,L}$ in the rest frame of the (isotropic) thermal bath reads

$${\rm Re}\Pi_{\rm T} = \frac{3\omega^2}{2v_*^2|\vec{k}|^2}\omega_p^2\left[1-\frac{\omega^2-v_*^2|\vec{k}|^2}{2\omega v_*|\vec{k}|}\ln\frac{\omega+v_*|\vec{k}|}{\omega-v_*|\vec{k}|}\right],$$
$${\rm Re}\Pi_{\rm L} = 3\omega_p^2\left(\frac{\omega^2-|\vec{k}|^2}{v_*^2|\vec{k}|^2}\right)\left[\frac{\omega}{2v_*|\vec{k}|}\ln\frac{\omega+v_*|\vec{k}|}{\omega-v_*|\vec{k}|}-1\right]. \tag{A5}$$

The full expressions for the dispersion relations $k^2 - \Pi_{\rm L,T} = 0$ then relate the energies of an on shell photon, $\omega_{\rm T,L}$, to its momentum $\vec{k}$ to order α [81], via

$$\omega_\mathrm{T}^2 = |\vec{k}|^2 + \omega_p^2 \frac{3\omega_\mathrm{T}^2}{2v_*^2|\vec{k}|^2}\left[1 - \frac{\omega_\mathrm{T}^2 - v_*^2|\vec{k}|^2}{2\omega_\mathrm{T} v_*|\vec{k}|}\ln\frac{\omega_\mathrm{T} + v_*|\vec{k}|}{\omega_\mathrm{T} - v_*|\vec{k}|}\right],$$
$$\omega_\mathrm{L}^2 = \omega_p^2 \frac{3\omega_\mathrm{L}^2}{v_*^2|\vec{k}|^2}\left[\frac{\omega_\mathrm{L}}{2v_*|\vec{k}|}\ln\frac{\omega_\mathrm{L} + v_*|\vec{k}|}{\omega_\mathrm{L} - v_*|\vec{k}|} - 1\right]. \tag{A6}$$

Equations (A6) are also valid to order $|\vec{k}|^2$ at small $|\vec{k}|$ for all temperatures and electron number densities. Throughout the paper, we always use $\omega_{\mathrm{T,L}}$, as functions of $|\vec{k}|$, to denote the energy of an on shell thermal photon, which satisfies Eqs. (A6), and use ω for off shell photons.

Longitudinal photons are populated up to a wave number k_max, beyond which the longitudinal dispersion relation crosses the light cone and L-modes become damped, with

$$k_\mathrm{max} = \left[\frac{3}{v_*^2}\left(\frac{1}{2v_*}\ln\frac{1+v_*}{1-v_*} - 1\right)\right]^{1/2}\omega_p, \tag{A7}$$

and in the relativistic limit $k_\mathrm{max} \to \infty$. In these equations, the mobility of charges is captured by the typical velocity of electrons, $v_* \equiv \omega_1/\omega_p$, where

$$\omega_1^2 = \frac{4\alpha}{\pi}\int_0^\infty dp\,\frac{p^2}{E}\left(\frac{5}{3}v^2 - v^4\right)(f_{e^-} + f_{e^+}). \tag{A8}$$

In the three limits mentioned previously, v_* can be approximated as

$$v_* \simeq \begin{cases} \sqrt{5T/m_e} & \text{classical} \\ v_F & \text{degenerate}\,. \\ 1 & \text{relativistic} \end{cases} \tag{A9}$$

Finally, as alluded to in the main text, the processes we consider are nonresonant in the photon exchange and $\mathrm{Im}\Pi_{\mathrm{T,L}}$ can be neglected throughout.

In turn, the computation of in-medium photon decay, i.e., the process (1a), requires the description of external in-medium photon states. For propagation in the z-direction, i.e., $k_x = k_y = 0$, the transverse and longitudinal polarization vectors are given by

$$\epsilon_\mathrm{T}^\mu = (0,1(0),0(1),0), \qquad \epsilon_\mathrm{L}^\mu = \frac{1}{\sqrt{\omega_L^2 - |\vec{k}|^2}}(|\vec{k}|,0,0,\omega_L). \tag{A10a}$$

In all cases $\epsilon^\mu\epsilon_\mu = -1$ and $\epsilon^\mu k_\mu = 0$.

Furthermore, the in-medium coupling of the photon to the EM current is modified by the vertex renormalization constants $Z_{\mathrm{T,L}} \equiv (1 - \partial\Pi_{\mathrm{T,L}}/\partial\omega_{\mathrm{T,L}}^2)^{-1}$. For the convention adopted here, they are equivalent to the ones given in [3]

$$Z_\mathrm{T} = \frac{2\omega_\mathrm{T}^2(\omega_\mathrm{T}^2 - v_*^2|\vec{k}|^2)}{3\omega_p^2\omega_\mathrm{T}^2 + (\omega_\mathrm{T}^2 + |\vec{k}|^2)(\omega_\mathrm{T}^2 - v_*^2|\vec{k}|^2) - 2\omega_\mathrm{T}^2(\omega_\mathrm{T}^2 - |\vec{k}|^2)},$$
$$Z_\mathrm{L} = \frac{2(\omega_\mathrm{L}^2 - v_*^2|\vec{k}|^2)}{3\omega_p^2 - (\omega_\mathrm{L}^2 - v_*^2|\vec{k}|^2)}\frac{\omega_L^2}{\omega_L^2 - |\vec{k}|^2}. \tag{A11}$$

These factors are attached to each zero-temperature vertex factor involving an external photon state. For internal photons, this effect is already accounted for in the momentum-dependent self-energy $\Pi_{\mathrm{T,L}}(\omega,\vec{k})$.

For thermal corrections to the electron mass which is relevant for PNS, we closely follow [82]. For an electron with a general 4-momentum $p = (E,\vec{p})$ in a neutral medium where the positron number density is negligible, we first introduce the four functions below,

$$A_e = \frac{-\alpha}{4\pi|\vec{p}|}\int_0^\infty dq\,\frac{qf_{e^-}(q)}{\sqrt{q^2+m_e^2}}[4|\vec{p}|q - (p^2 + m_e^2)L_2], \tag{A12}$$

$$C_e = \frac{\alpha m_e}{\pi|\vec{p}|}\int_0^\infty dq\,\frac{qf_{e^-}(q)}{\sqrt{q^2+m_e^2}}(-L_2), \tag{A13}$$

$$A_\gamma = \frac{-\alpha}{4\pi|\vec{p}|}\int_0^\infty dq f_\gamma(q)[8|\vec{p}|q + (p^2 + m_e^2)(L_3 - L_4)], \tag{A14}$$

$$C_\gamma = \frac{\alpha m_e}{\pi|\vec{p}|}\int_0^\infty dq f_\gamma(q)(L_3 - L_4), \tag{A15}$$

where q here is the absolute value of the 3-momentum of medium particles (electron, photon) that is integrated over and $L_{1,2,3,4}$ are functions of q in terms of

$$L_1(q) = \ln\left[\frac{2(E\sqrt{q^2+m_e^2} + |\vec{p}|q) - p^2 - m_e^2}{2(E\sqrt{q^2+m_e^2} - |\vec{p}|q) - p^2 - m_e^2}\right], \tag{A16}$$

$$L_2(q) = \ln\left[\frac{2(E\sqrt{q^2+m_e^2} + |\vec{p}|q) + p^2 + m_e^2}{2(E\sqrt{q^2+m_e^2} - |\vec{p}|q) + p^2 + m_e^2}\right], \tag{A17}$$

$$L_3(q) = \ln\left[\frac{2(Eq + |\vec{p}|q) + p^2 - m_e^2}{2(Eq - |\vec{p}|q) + p^2 - m_e^2}\right], \tag{A18}$$

$$L_4(q) = \ln\left[\frac{2(Eq + |\vec{p}|q) - p^2 + m_e^2}{2(Eq - |\vec{p}|q) - p^2 + m_e^2}\right]. \tag{A19}$$

Here m_e is the zero-temperature mass of electron, 0.511 MeV, while $f_\gamma(p)$ and $f_{e^-}(p)$ give the thermal momentum distribution functions of photon and electron (per d.o.f.). We have set $f_{e^+}(p) = 0$ in the above equations. In the end, we take the approximation made in [83] to obtain that

$$m_e^{\rm eff}(p) = \sqrt{m_e^2 - 2(A_\gamma + A_e) - 2m_e(C_\gamma + C_e)}. \quad \text{(A20)}$$

We have neglected thermal corrections to χ states. In the phenomenologically relevant regime, their coupling to the thermal bath is very weak.

Finally, we have reproduced the profiles of the HB model from [62], and PNS model from [64], adopted in this work, as shown in Fig. 7, where neutrality and $\mu_{e^-} + \mu_{e^+} = 0$ at each radius have been taken for granted for the PNS profile.

APPENDIX B: DECAY RATE AND CROSS SECTION CALCULATIONS

In this Appendix we collect some further details that enter the calculation of the $\chi\bar{\chi}$ production cross sections found in Sec. IV.

1. Full expression of χ-pair production rate

For any process that produces a $\chi\bar{\chi}$ pair through a photon propagator of 4-momentum $k = (\omega, \vec{k})$, its spin-summed squared matrix element can be written in terms of

$$\sum_{\rm spins} |\mathcal{M}|^2 = D_{\mu\nu}(k) D^*_{\rho\sigma}(k) \mathcal{T}^{\mu\rho}_{\rm SM} \mathcal{T}^{\nu\sigma}_\chi, \quad \text{(B1)}$$

where the in-medium photon propagator $D^{\mu\nu}$ is given by (A4), while $\mathcal{T}^{\mu\rho}_{\rm SM}$ and $\mathcal{T}^{\nu\sigma}_\chi$ represent the corresponding squared matrix elements of the SM current, i.e., $\mathrm{SM} \to \gamma^*(k)(+\mathrm{SM}')$, and the dark current, i.e., $\gamma^*(k) \to \chi(p_\chi) + \bar{\chi}(p_{\bar{\chi}})$, of which the latter is given by

$$\mathcal{T}^{\nu\sigma}_\chi = \mathrm{Tr}[(\not{p}_\chi + m_\chi)\Gamma^\nu(k)(\not{p}_{\bar{\chi}} - m_\chi)\Gamma^\sigma(-k)]. \quad \text{(B2)}$$

The vertex factors $\Gamma^\nu(k)$ are derived from the Lagrangians (5) and (6) through the usual prescription of obtaining Feynman rules; see [30] for the explicit expressions. Generalizing Eq. (5.156) of [53] yields an expression for the exact $\chi\bar{\chi}$ differential production rate per volume,

$$\frac{d\dot{N}_\chi}{d^4k} = \frac{1}{(2\pi)^4} D_{\mu\nu}(k) D^*_{\rho\sigma}(k) \left(\frac{2\mathrm{Im}\Pi^{\mu\rho}(k)}{e^{\omega/T} - 1}\right) I^{\nu\sigma}_\chi, \quad \text{(B3)}$$

where $\mathrm{Im}\Pi^{\mu\rho}$ is the imaginary part of the thermal photon self-energy induced by all possible SM currents. In the medium it is decomposed into longitudinal and transverse components, $\mathrm{Im}\Pi_{L,T}$, as shown in Eq. (12) in the main text. The factor $I^{\nu\sigma}$ is the 2-body final state integrated over its phase space,

$$I^{\nu\sigma}_\chi = \int d\Pi_{i=\chi,\bar{\chi}} (2\pi)^4 \delta^4(k - p_\chi - p_{\bar{\chi}}) \mathcal{T}^{\nu\sigma}_\chi, \quad \text{(B4)}$$

where $d\Pi_i = \prod_i d^3\vec{p}_i (2\pi)^{-3}(2E_i)^{-1}$, as mentioned in the main text. The integration can be executed in an arbitrary frame, and in particular in the rest frame of the thermal bath by adopting Lenard's formula [84], generalized to massive final states. We find

$$\int d\Pi_{i=\chi,\bar{\chi}} (2\pi)^4 \delta^4(k - p_\chi - p_{\bar{\chi}}) p^\mu_\chi p^\nu_{\bar{\chi}} = \frac{1}{96\pi}(Ak^2 g^{\mu\nu} + 2Bk^\mu k^\nu), \quad \text{(B5)}$$

where the coefficients A and B are given by

$$A = \left(1 - \frac{4m_\chi^2}{s_{\chi\bar{\chi}}}\right)^{3/2}, \qquad B = \sqrt{1 - \frac{4m_\chi^2}{s_{\chi\bar{\chi}}}}\left(1 + \frac{2m_\chi^2}{s_{\chi\bar{\chi}}}\right),$$

with $s_{\chi\bar{\chi}} = k^2$. In terms of the functions $f(s_{\chi\bar{\chi}})$ defined in (14), the factor $I^{\nu\sigma}$ is then explicitly given by

$$I^{\nu\sigma} = \frac{1}{8\pi}\sqrt{1 - \frac{4m_\chi^2}{s_{\chi\bar{\chi}}}} f(s_{\chi\bar{\chi}}) \left(-g^{\nu\sigma} + \frac{k^\nu k^\sigma}{s_{\chi\bar{\chi}}}\right). \quad \text{(B6)}$$

Putting all of the above together, we obtain the differential production rate per volume (13) found in the main text which we repeat here for convenience,

$$\frac{d\dot{N}_\chi}{d^4k} = \frac{1}{64\pi^5}\left[-\frac{\mathrm{Im}\Pi_{\rm L}(k)}{|s_{\chi\bar{\chi}} - \Pi_{\rm L}|^2} - \frac{2\mathrm{Im}\Pi_{\rm T}(k)}{|s_{\chi\bar{\chi}} - \Pi_{\rm T}|^2}\right] \times f_B(\omega) f(s_{\chi\bar{\chi}}) \sqrt{1 - \frac{4m_\chi^2}{s_{\chi\bar{\chi}}}}, \quad \text{(B7)}$$

where $f_B(\omega) = (e^{\omega/T} - 1)^{-1}$ is the Bose-Einstein momentum distribution of thermal bosons. During the derivation we have used that

$$-g^{\nu\sigma} + \frac{k^\nu k^\sigma}{s_{\chi\bar{\chi}}} = \epsilon^\nu_{\rm T,1}\epsilon^\sigma_{\rm T,1} + \epsilon^\nu_{\rm T,2}\epsilon^\sigma_{\rm T,2} + \epsilon^\nu_{\rm L}\epsilon^\sigma_{\rm L}.$$

2. Leading contributions to $\mathrm{Im}\Pi_{T,L}$

We now demonstrate that (13) or, equivalently, (B3) contain the leading production mechanisms considered in this paper. In particular we clarify the role of resonances, and that they are accounted for by the process $\gamma_{\rm T,L} \to \chi\bar{\chi}$. To this end, we isolate the pole contribution to the total production rate, i.e., the case $s_{\chi\bar{\chi}} = \mathrm{Re}\Pi_{\rm L,T}$. To this end, we adopt the narrow width approximation,

$$\lim_{\mathrm{Im}\Pi_{\rm L,T} \to 0} \frac{-\mathrm{Im}\Pi_{\rm L,T}(k)}{\pi |s_{\chi\bar{\chi}} - \Pi_{\rm L,T}|^2} = \delta(s_{\chi\bar{\chi}} - \mathrm{Re}\Pi_{\rm L,T}), \quad \text{(B8)}$$

where $\mathrm{Im}\Pi_{\rm L,T} < 0$. Then noting that $\mathrm{Re}\Pi_{\rm L,T}$ is also a function of $s_{\chi\bar{\chi}}$ and writing $d^4k = d^3\vec{k}\, ds_{\chi\bar{\chi}}/(2\omega)$ yield

$$\dot{N}_\chi^{\mathrm{T,L}} = g_{\mathrm{T,L}} \int \frac{d^3\vec{k}}{(2\pi)^3} f_B(\omega_{\mathrm{T,L}}) \times \left[\frac{Z_{\mathrm{T,L}} f(\mathrm{Re}\Pi_{\mathrm{T,L}})}{16\pi\omega_{\mathrm{T,L}}} \sqrt{1 - \frac{4m_\chi^2}{\mathrm{Re}\Pi_{\mathrm{T,L}}}} \right], \qquad (\mathrm{B9})$$

where $g_\mathrm{T} = 2$ and $g_\mathrm{L} = 1$, counting the d.o.f. of the photon modes. Now both $\omega_{\mathrm{T,L}}$ and $\mathrm{Re}\Pi_{\mathrm{L,T}}$ need to satisfy the photon dispersion relation with a 3-momentum $\vec{k}$ due to the δ-function above. As will be calculated below and given explicitly in (15), the term in the parentheses is exactly the decay rate of $\gamma_{\mathrm{L,T}}$ into χ pairs.

In a next step we further verify that the contribution of the one electron loop (OEL) to $\mathrm{Im}\Pi_{\mu\rho}$ induces the production rate of χ from electron pair annihilation,[5] the process (2b). In this case, it is easier to start with (B3), where according to the in-medium optical theorem (see Fig. 2) we may write

$$2\mathrm{Im}\Pi^{\mu\rho}|_{\mathrm{OEL}} = \int d\Pi_{i=1,2} \mathcal{T}_e^{\mu\rho}(1 - f_{e^-} - f_{e^+}) \times (2\pi)^4\delta^4(k - p_1 - p_2), \qquad (\mathrm{B10})$$

where $\mathcal{T}_e^{\mu\rho} = \mathcal{M}^\mu_{\gamma^*\to e^+e^-}\mathcal{M}^\rho_{e^+e^-\to\gamma^*}$, and $f_{e^\mp}$ gives the momentum distribution function of $e^-(p_1)$, $e^+(p_2)$ per d.o.f. as defined above. Moreover, terms that are kinetically forbidden for $k^2 > 0$ have been neglected [50]. The presence of $(1 - f_{e^-} - f_{e^+})$ is due to quantum statistics, and would disappear for classical particles. Substituting this expression into (B3) gives

$$\left.\frac{d\dot{N}_\chi}{d^4k}\right|_{\mathrm{OEL}} = \int d\Pi_{i=1,2,\chi,\bar\chi} |\mathcal{M}_{\mathrm{ann}}|^2 (1 - f_{e^-} - f_{e^+}) f_B(\omega) \times (2\pi)^4\delta^4(k - p_1 - p_2)\delta^4(k - p_\chi - p_{\bar\chi}). \qquad (\mathrm{B11})$$

Then for the Fermi-Dirac distribution function $f_{e^\pm}$ and the Bose-Einstein distribution $f_B(\omega)$ with the energy conservation $E_1 + E_2 = \omega$, there exists the relation

$$\left(\frac{f_{e^-}}{1 - f_{e^-}}\right)\left(\frac{f_{e^+}}{1 - f_{e^+}}\right) = \frac{f_B(\omega)}{1 + f_B(\omega)} \qquad (\mathrm{B12})$$

allowing us to rewrite the number production rate per volume above as

$$\dot{N}_\chi|_{\mathrm{OEL}} = \int d\Pi_{i=1,2,\chi,\bar\chi} |\mathcal{M}_{\mathrm{ann}}|^2 f_{e^-} f_{e^+} \times (2\pi)^4\delta^4(p_1 + p_2 - p_\chi - p_{\bar\chi}), \qquad (\mathrm{B13})$$

after integrating over d^4k on both sides. The last expression transforms precisely to the corresponding energy loss rate (19), once both the energy-loss factor $(E_1 + E_2)$ and fermionic d.o.f. $f_{e^\pm}$ are taken in account.

3. $\gamma_{T,L}$ decay to dark states

In the following Appendixes we calculate the leading processes in the usual Feynman-diagrammatic approach using tree-level perturbation theory augmented by the thermal corrections outlined in Appendix A. The decay of a transverse or longitudinal photon of 4-momentum k to a pair of dark states $\bar\chi(p_{\bar\chi}) + \chi(p_\chi)$ is described by the spin-summed squared matrix element,

$$\sum_{\mathrm{spins}} |\mathcal{M}_{\mathrm{T,L}}|^2 = Z_{\mathrm{T,L}}\epsilon_\mu(k)\epsilon^*_\nu(k)\mathcal{T}_\chi^{\mu\nu}, \qquad (\mathrm{B14})$$

where $Z_{\mathrm{T,L}}$ is the vertex renormalization factor in (A11), ϵ_μ is the photon polarization vector and $\mathcal{T}_\chi^{\mu\nu}$ is given in (B2). The decay rate is given by the phase-space integral,

$$\Gamma_{\mathrm{T,L}} = \int d\Pi_{i=\chi,\bar\chi}(2\pi)^4\delta^4(k - p_\chi - p_{\bar\chi}) \frac{1}{2\omega_{\mathrm{T,L}}} \sum_{\mathrm{spins}} |\mathcal{M}_{\mathrm{T,L}}|^2, \qquad (\mathrm{B15})$$

where $\omega_{\mathrm{T,L}}$ is the energy of the external transverse or longitudinal photon. It is useful to employ (B5). In terms of $I^{\nu\sigma}$ defined in (B6), we can write the decay rate as

$$\Gamma_{\mathrm{T,L}} = \frac{1}{2\omega_{\mathrm{T,L}}} Z_{\mathrm{T,L}}\epsilon_\mu(k)\epsilon^*_\nu(k) I^{\mu\nu}. \qquad (\mathrm{B16})$$

The explicit expression, given by (15) in the main text, is then found by using the expressions (A10) for the polarization vectors when the initial state propagates in positive z-direction, i.e., for $k^\mu = (\omega, 0, 0, k)$; note that the term proportional to $k^\mu k^\nu$ in $I^{\mu\nu}$ does not contribute due to the Ward identity.

4. e^+e^- annihilation to dark states

Here we consider the process $e^-(p_1) + e^+(p_2) \to \chi(p_\chi) + \bar\chi(p_{\bar\chi})$. By setting $p_i = (E_i, \vec{p}_i)$ and $k = p_1 + p_2$, one can define the cross sections[6] in terms of the squared matrix element for annihilation $|\mathcal{M}_{\mathrm{ann}}|^2$,

$$\sigma = \int \frac{d\Pi_{i=\chi,\bar\chi}}{4E_1E_2v_M}(2\pi)^4\delta^4(k - p_\chi - p_{\bar\chi})\frac{1}{4}\sum_{\mathrm{spins}}|\mathcal{M}_{\mathrm{ann}}|^2 = \frac{\pi\alpha}{4E_1E_2v_M} D_{\mu\nu}D^*_{\rho\sigma}\mathcal{T}_e^{\mu\rho}I_\chi^{\nu\sigma}, \qquad (\mathrm{B17})$$

[5]The contribution of the two and three electron loops to $\mathrm{Im}\Pi_{\mu\rho}$ correspond to Compton scattering and bremsstrahlung, respectively.

[6]We emphasize that this leads to a Lorentz-invariant total cross section up to the thermal mass of photons, which is convenient for the phase space integral.

where $\mathcal{T}_e^{\mu\rho}$ reads

$$\mathcal{T}_e^{\mu\rho} = -2(sg^{\mu\rho} - 2p_1^\mu p_2^\rho - 2p_1^\rho p_2^\mu), \tag{B18}$$

and $I_\chi^{\nu\sigma}$ is given in (B6); here $s = k^2$. Furthermore, v_M is the Møller velocity defined as $v_M = F/(E_1 E_2)$ and the flux factor F is given by

$$F = [(p_1 \cdot p_2)^2 - m_e^4]^{1/2} = \frac{1}{2}\sqrt{s(s - 4m_e^2)}. \tag{B19}$$

Contracting the Lorentz indices then yields

$$\sigma = \sigma_T + \sigma_L, \tag{B20}$$

where the interference term vanishes in the Coulomb gauge, as can also be seen from (13), and the cross section for each polarization mode is given as Eqs. (17) and (18) in the main text.

5. $e^- N$ bremsstrahlung production of dark states

The $2 \to 3$ amplitude squared $|\mathcal{M}_{2\to3}|^2$ can be split into three parts as

$$\sum_{\text{spins}} \frac{|\mathcal{M}_{2\to3}|^2}{(4\pi\alpha)^2 g_1 g_2} = D^{\rho\beta}(q) D^{\sigma\gamma*}(q) W_{\rho\sigma} L_{\beta\gamma}^{\mu\nu} \epsilon_\mu^*(k) \epsilon_\nu(k), \tag{B21}$$

where $q = p_2 - p_4$ is the momentum transfer between the initial states, $L_{\beta\gamma}^{\mu\nu}$ stands for the leptonic part, $W_{\rho\sigma}$ is the hadronic tensor and $\epsilon_\nu(k)$ is the polarization vector of the emitted photon of virtual mass $s_{\chi\bar{\chi}} = k^2$. Detailed forms for $L_{\beta\gamma}^{\mu\nu}$ and $W_{\rho\sigma}$ are given in the Appendix A of our previous work [30].

The $2 \to 3$ cross section reads

$$\sigma_{2\to3} = \frac{1}{4 g_1 g_2 E_1 E_2 v_M} \int d\Pi_{i=3,4,k} \sum_{\text{spins}} |\mathcal{M}_{2\to3}|^2, \tag{B22}$$

where v_M is the Møller velocity, as defined in the main text. The phase space integrations, when written in terms of Lorentz invariants reads

$$\sigma_{2\to3} = \frac{1}{32(2\pi)^4 E_1 E_2 v_M} \int ds_4 \int dt_1 \frac{1}{\sqrt{\lambda(s_4, m_p^2, t_1)}} \times \int dt_2 \int dp_{1k} \left|\frac{\partial\phi_4^{R4k}}{\partial p_{1k}}\right| \frac{1}{g_1 g_2} \sum_{\text{spins}} |\mathcal{M}_{2\to3}|^2. \tag{B23}$$

Here, $s = (p_1 + p_2)^2$, $t_1 \equiv (p_1 - p_3)^2$, $t_2 \equiv (p_2 - p_4)^2 = q^2$, $s_4 \equiv (p_4 + k)^2$, $p_{1k} = p_1 \cdot k$ and ϕ_4^{R4k} is the azimuthal angle between p_4 and k in their center of mass frame; $\lambda(a^2, b^2, c^2)$ is the Källén function. The Jacobian $|\partial\phi_4^{R4k}/\partial p_{1k}|$ transforms the variable ϕ_4^{R4k} to the Lorentz invariant variable p_{1k}.

The integration boundary of s_4 is given by

$$(m_N + \sqrt{s_{\chi\bar{\chi}}})^2 \le s_4 \le (\sqrt{s} - m_e)^2, \tag{B24}$$

and the boundaries of t_1 and t_2 are given by

$$\begin{aligned} t_1^\pm &= 2m_e^2 - \frac{1}{2s}[(s + m_e^2 - m_N^2)(s + m_e^2 - s_4) \\ &\quad \mp \lambda(s, m_e^2, m_N^2)^{1/2} \lambda(s, m_e^2, s_4)^{1/2}], \\ t_2^\pm &= 2m_N^2 - \frac{1}{2s_4}[(s_4 + m_N^2 - t_1)(s_4 + m_N^2 - s_{\chi\bar{\chi}}) \\ &\quad \mp \lambda(s_4, m_N^2, t_1)^{1/2} \lambda(s_4, m_N^2, s_{\chi\bar{\chi}})^{1/2}]. \end{aligned} \tag{B25}$$

The physical region for p_{1k} is expressed by $n \times n$ asymmetric and symmetric Gram determinants, G_n and Δ_n. It reads

$$\begin{aligned} p_{1k}^\pm = &\frac{(p_1 \cdot p_2) G_2(p_2, \sqrt{t_1}; \sqrt{t_1}, k)}{-\Delta_2(p_2, \sqrt{t_1})} \\ &- \frac{(\sqrt{t_1} \cdot p_1) G_2(p_2, \sqrt{t_1}; p_2, k)}{-\Delta_2(p_2, \sqrt{t_1})} \\ &\pm \frac{\sqrt{\Delta_3(p_2, \sqrt{t_1}, p_1) \Delta_3(p_2, \sqrt{t_1}, k)}}{-\Delta_2(p_2, \sqrt{t_1})}, \end{aligned} \tag{B26}$$

and the Jacobian $|\partial\phi_4^{R4k}/\partial p_{1k}|$ reads

$$\left|\frac{\partial\phi_4^{R4k}}{\partial p_{1k}}\right| = -\frac{\sqrt{-\Delta_2(p_2, \sqrt{t_1})}}{\sqrt{-\Delta_4(p_2, \sqrt{t_1}, p_1, k)}}. \tag{B27}$$

Putting everything together, the full $2 \to 4$ cross section is given by

$$\sigma_{2\to4} = \int ds_{\chi\bar{\chi}} \sigma_{2\to3}(s_{\chi\bar{\chi}}) \frac{f(s_{\chi\bar{\chi}})}{16\pi^2 s_{\chi\bar{\chi}}^2} \sqrt{1 - \frac{4m_\chi^2}{s_{\chi\bar{\chi}}}}. \tag{B28}$$

The integration boundaries of $s_{\chi\bar{\chi}}$ are given by

$$4m_\chi^2 \le s_{\chi\bar{\chi}} \le (\sqrt{s} - m_e - m_N)^2. \tag{B29}$$

APPENDIX C: SOFT-PHOTON APPROXIMATION FOR BREMSSTRAHLUNG

Here we discuss the soft-photon approximation for bremsstrahlung, its regime of validity and explain where it fails in calculating the $2 \to 4$ cross section. In the soft limit, that is, if the emitted photon energy is small compared to the available kinetic energy $\omega \ll E_{\text{kin}}$, the

$2 \to 3$ cross section can be factorized into an elastic scattering and an emission part,[7]

$$d\sigma_{2\to3}^{\rm soft} = d\sigma_{2\to2}\int \frac{d^3k}{(2\pi)^3 2\omega} 4\pi\alpha \left| \frac{p_3\cdot\epsilon^*}{p_3\cdot k} - \frac{p_1\cdot\epsilon^*}{p_1\cdot k}\right|^2, \quad \text{(C1)}$$

where $\omega^2 = |\vec{k}|^2 + s_{\chi\bar{\chi}}$ and ϵ_μ is the polarization vector of the emitted photon. In this approximation, a simple form of the differential $2 \to 3$ cross section can be obtained in the nonrelativistic and ultrarelativistic limit respectively [85],

$$\omega\frac{d\sigma_{2\to3}^{\rm soft}}{d\omega} = \begin{cases} \frac{16}{3}\frac{\alpha^3}{\mu^2 v^2}\ln\left[\frac{1+\sqrt{1-\omega/E_{\rm kin}}}{1-\sqrt{1-\omega/E_{\rm kin}}}\right] \\ \frac{4\alpha^3}{\mu^2}\frac{E'}{E}\left(\frac{E}{E'}+\frac{E'}{E}-\frac{2}{3}\right)\left(\ln\frac{E^2E'}{\mu^2\omega}-\frac{1}{2}\right), \end{cases} \quad \text{(C2)}$$

where μ is the reduced mass, v is the relative velocity and E (E') is the initial (final) total CM energy of the colliding particles. Even though in deriving the expression in Eq. (C2) we have assumed $\sqrt{s_{\chi\bar{\chi}}} \ll E_{\rm kin}$ and $\omega \ll E_{\rm kin}$, integrating (C2) over ω in the region,

$$\sqrt{s_{\chi\bar{\chi}}} < \omega < E_{\rm kin} \quad \text{(C3)}$$

still gives a very good approximation to the full cross section. Obviously, the approximation breaks down if $\sqrt{s_{\chi\bar{\chi}}} \sim E_{\rm kin}$ where the integration region of ω gets very small and the integral is dominated by large emission energies.

To obtain the $2 \to 4$ cross section from the $2 \to 3$ cross section in Eq. (24), $\sigma_{2\to3}^{\rm soft}$ gets multiplied by the factors in Eq. (14) corresponding to the EM form factor interactions. This leads to the following parametric dependence on $s_{\chi\bar{\chi}}$:

$$d\sigma_{2\to4}^{\rm soft} \propto \begin{cases} d\sigma_{2\to3}^{\rm soft} ds_{\chi\bar{\chi}}/s_{\chi\bar{\chi}} & \text{(dim-4)}, \\ d\sigma_{2\to3}^{\rm soft} ds_{\chi\bar{\chi}} & \text{(dim-5)}, \\ d\sigma_{2\to3}^{\rm soft} ds_{\chi\bar{\chi}} s_{\chi\bar{\chi}} & \text{(dim-6)}, \end{cases} \quad \text{(C4)}$$

that is, for dim-4 operators, like millicharged states, the $2 \to 4$ cross section is dominated by small $s_{\chi\bar{\chi}}$, whereas for higher dimensional operators, the expression is UV biased. Hence, the main contribution to the integral comes from $s_{\chi\bar{\chi}}$-values for which the soft approximation breaks down as one probes the kinematic end point region. It turns out that in the nonrelativistic regime and for $m_\chi + m_{\bar{\chi}} \ll E_{\rm kin}$, using Eq. (C2) reproduces the exact $2 \to 4$ cross section up to a factor 2 or 3. However, for relativistic particles, the error at $\sqrt{s_{\chi\bar{\chi}}} \sim E_{\rm kin}$ gets larger. Due to the $s_{\chi\bar{\chi}}$-dependence in Eq. (C4), this still results in a decent description of millicharged $\chi\bar{\chi}$ emission, but produces errors of several orders of magnitude in the relativistic regime for the EM form factors considered in this paper.

Equation (C1) can be further simplified by separating the phase space. This is possible, if the elastic scattering cross section is insensitive to an angular cutoff in the forward or backward direction, e.g., if the interaction is mediated by a massive particle such as the pion in np scattering.[8] Then,

$$\sigma_{2\to3}^{\rm soft} = \sigma_{2\to2}^{\rm T}\mathcal{I}(s_{\chi\bar{\chi}}), \quad \text{(C5)}$$

where $\sigma_{2\to2}^{\rm T}$ is the transport cross section,

$$\sigma_{2\to2}^{\rm T} = \int_{-1}^{1} d\cos\theta \frac{d\sigma_{2\to2}}{d\cos\theta}(1-\cos\theta), \quad \text{(C6)}$$

and the emission piece $\mathcal{I}(s_{\chi\bar{\chi}})$ is obtained by executing the integral in Eq. (C1),

$$\begin{aligned}\mathcal{I}(s_{\chi\bar{\chi}}) &= \frac{1}{1-\cos\theta}\int \frac{d^3k}{(2\pi)^3 2\omega}4\pi\alpha\left|\frac{p_3\cdot\epsilon^*}{p_3\cdot k} - \frac{p_1\cdot\epsilon^*}{p_1\cdot k}\right|^2 \\ &= \frac{\alpha}{3\pi}\int_{\sqrt{s_{\chi\bar{\chi}}}}^{E_{\rm kin}} d\omega \frac{\sqrt{\omega^2 - s_{\chi\bar{\chi}}}(s_{\chi\bar{\chi}}/2+\omega^2)}{\omega^4}. \end{aligned} \quad \text{(C7)}$$

In the first line, we have divided by $(1-\cos\theta)$ to cancel the θ-dependent part in the emission piece, which we have absorbed into the elastic cross section. In Sec. IV F we make use of this factorization in calculating the energy loss rate for neutron-proton scattering in PNS. For that, the integral in Eq. (C7) is weighted with ω to obtain

$$\begin{aligned}\mathcal{I}_\omega(s_{\chi\bar{\chi}}) &= \frac{\alpha}{3\pi}\int_{\sqrt{s_{\chi\bar{\chi}}}}^{E_{\rm kin}} d\omega \frac{\sqrt{\omega^2 - s_{\chi\bar{\chi}}}(s_{\chi\bar{\chi}}/2+\omega^2)}{\omega^3} \\ &= \frac{\alpha E_{\rm kin}}{3\pi}[\sqrt{1-x^2}(4-x^2) - 3x\arccos(x)] \end{aligned} \quad \text{(C8)}$$

with $x = \sqrt{s_{\chi\bar{\chi}}}/E_{\rm kin}$, which is in agreement with the findings of Ref. [60].

[7]The emission part here describes the emission off one of the particles. If both particles can emit photons, the emission part has to be adjusted correspondingly.

[8]For ep scattering, on the other hand, the phase space separation is not possible, since the elastic cross section is forward divergent. In these cases, 3-body kinematics is required.

[1] R. Essig *et al.*, in *Proceedings, 2013 Community Summer Study on the Future of U.S. Particle Physics: Snowmass on the Mississippi (CSS2013): Minneapolis, MN, USA* (SLAC National Accelerator Laboratory, 2013).
[2] M. Battaglieri *et al.*, arXiv:1707.04591.
[3] G. G. Raffelt, *Stars as Laboratories for Fundamental Physics* (University of Chicago Press, 1996).
[4] B. Holdom, Phys. Lett. **166B**, 196 (1986).
[5] H. An, M. Pospelov, and J. Pradler, Phys. Lett. B **725**, 190 (2013).
[6] M. Pospelov, A. Ritz, and M. B. Voloshin, Phys. Rev. D **78**, 115012 (2008).
[7] J. Redondo and M. Postma, J. Cosmol. Astropart. Phys. 02 (2009) 005.
[8] J. Redondo and G. Raffelt, J. Cosmol. Astropart. Phys. 08 (2013) 034.
[9] H. An, M. Pospelov, and J. Pradler, Phys. Rev. Lett. **111**, 041302 (2013).
[10] H. An, M. Pospelov, J. Pradler, and A. Ritz, Phys. Lett. B **747**, 331 (2015).
[11] S. Chaudhuri, P. W. Graham, K. Irwin, J. Mardon, S. Rajendran, and Y. Zhao, Phys. Rev. D **92**, 075012 (2015).
[12] S. Dubovsky and G. Hernandez-Chifflet, J. Cosmol. Astropart. Phys. 12 (2015) 054.
[13] A. Aguilar-Arevalo *et al.* (DAMIC Collaboration), Phys. Rev. Lett. **118**, 141803 (2017).
[14] E. Hardy and R. Lasenby, J. High Energy Phys. 02 (2017) 033.
[15] R. Essig, T. Volansky, and T.-T. Yu, Phys. Rev. D **96**, 043017 (2017).
[16] M. Baryakhtar, R. Lasenby, and M. Teo, Phys. Rev. D **96**, 035019 (2017).
[17] V. Cardoso, P. Pani, and T.-T. Yu, Phys. Rev. D **95**, 124056 (2017).
[18] M. Baryakhtar, J. Huang, and R. Lasenby, Phys. Rev. D **98**, 035006 (2018).
[19] V. Cardoso, o. J. C. Dias, G. S. Hartnett, M. Middleton, P. Pani, and J. E. Santos, J. Cosmol. Astropart. Phys. 03 (2018) 043.
[20] A. Pierce, K. Riles, and Y. Zhao, Phys. Rev. Lett. **121**, 061102 (2018).
[21] M. Pospelov and T. ter Veldhuis, Phys. Lett. B **480**, 181 (2000).
[22] K. Sigurdson, M. Doran, A. Kurylov, R. R. Caldwell, and M. Kamionkowski, Phys. Rev. D **70**, 083501 (2004); **73**, 089903(E) (2006).
[23] C. M. Ho and R. J. Scherrer, Phys. Lett. B **722**, 341 (2013).
[24] D. Schmidt, T. Schwetz, and T. Toma, Phys. Rev. D **85**, 073009 (2012).
[25] J. Kopp, L. Michaels, and J. Smirnov, J. Cosmol. Astropart. Phys. 04 (2014) 022.
[26] A. Ibarra and S. Wild, J. Cosmol. Astropart. Phys. 05 (2015) 047.
[27] P. Sandick, K. Sinha, and F. Teng, J. High Energy Phys. 10 (2016) 018.
[28] B. J. Kavanagh, P. Panci, and R. Ziegler, J. High Energy Phys. 04 (2019) 089.
[29] T. Trickle, Z. Zhang, and K. M. Zurek, arXiv:1905.13744.
[30] X. Chu, J. Pradler, and L. Semmelrock, Phys. Rev. D **99**, 015040 (2019).
[31] B. Aubert *et al.* (*BABAR* Collaboration), Nucl. Instrum. Methods Phys. Res., Sect. A **479**, 1 (2002).
[32] D. Banerjee *et al.* (NA64 Collaboration), Phys. Rev. D **97**, 072002 (2018).
[33] A. A. Prinz *et al.*, Phys. Rev. Lett. **81**, 1175 (1998).
[34] T. Abe *et al.* (Belle-II Collaboration), arXiv:1011.0352.
[35] T. Åkesson *et al.* (LDMX Collaboration), arXiv:1808.05219.
[36] M. Battaglieri *et al.* (BDX Collaboration), arXiv:1607.01390.
[37] J. Bagnasco, M. Dine, and S. D. Thomas, Phys. Lett. B **320**, 99 (1994).
[38] R. Foadi, M. T. Frandsen, and F. Sannino, Phys. Rev. D **80**, 037702 (2009).
[39] O. Antipin, M. Redi, A. Strumia, and E. Vigiani, J. High Energy Phys. 07 (2015) 039.
[40] S. Raby and G. West, Phys. Lett. B **194**, 557 (1987).
[41] M. Pospelov and A. Ritz, Phys. Rev. D **78**, 055003 (2008).
[42] S. Okawa, M. Pospelov, and A. Ritz, arXiv:1905.05219.
[43] N. Viaux, M. Catelan, P. B. Stetson, G. Raffelt, J. Redondo, A. A. R. Valcarce, and A. Weiss, Phys. Rev. Lett. **111**, 231301 (2013).
[44] J. A. Frieman, S. Dimopoulos, and M. S. Turner, Phys. Rev. D **36**, 2201 (1987).
[45] G. G. Raffelt and G. D. Starkman, Phys. Rev. D **40**, 942 (1989).
[46] N. Grevesse and A. J. Sauval, Space Sci. Rev. **85**, 161 (1998).
[47] M. Asplund, N. Grevesse, A. J. Sauval, and P. Scott, Annu. Rev. Astron. Astrophys. **47**, 481 (2009).
[48] K. Blum and D. Kushnir, Astrophys. J. **828**, 31 (2016).
[49] N. Bar, K. Blum, and G. D'amico, arXiv:1907.05020.
[50] H. A. Weldon, Phys. Rev. D **28**, 2007 (1983).
[51] M. E. Carrington, H. Defu, and R. Kobes, Phys. Rev. D **67**, 025021 (2003).
[52] J. Alam, S. Sarkar, P. Roy, T. Hatsuda, and B. Sinha, Ann. Phys. (N.Y.) **286**, 159 (2000).
[53] M. L. Bellac, *Thermal Field Theory*, Cambridge Monographs on Mathematical Physics (Cambridge University Press, Cambridge, England, 2011).
[54] E. Braaten, Phys. Rev. Lett. **66**, 1655 (1991).
[55] E. Vitagliano, J. Redondo, and G. Raffelt, J. Cosmol. Astropart. Phys. 12 (2017) 010.
[56] J. H. Chang, R. Essig, and S. D. McDermott, J. High Energy Phys. 09 (2018) 051.
[57] G. G. Raffelt, Phys. Rev. D **37**, 1356 (1988).
[58] P. Gondolo and G. Gelmini, Nucl. Phys. **B360**, 145 (1991).
[59] J. Edsjo and P. Gondolo, Phys. Rev. D **56**, 1879 (1997).
[60] E. Rrapaj and S. Reddy, Phys. Rev. C **94**, 045805 (2016).
[61] D. A. Brown *et al.*, Nucl. Data Sheets **148**, 1 (2018).
[62] D. Dearborn, G. Raffelt, P. Salati, J. Silk, and A. Bouquet, Astrophys. J. **354**, 568 (1990).
[63] J. N. Bahcall, A. M. Serenelli, and S. Basu, Astrophys. J. **621**, L85 (2005).
[64] T. Fischer, S. Chakraborty, M. Giannotti, A. Mirizzi, A. Payez, and A. Ringwald, Phys. Rev. D **94**, 085012 (2016).
[65] G. G. Raffelt, Astrophys. J. **561**, 890 (2001).
[66] M. T. Keil, G. G. Raffelt, and H.-T. Janka, Astrophys. J. **590**, 971 (2003).
[67] C. Giunti and A. Studenikin, Rev. Mod. Phys. **87**, 531 (2015).
[68] M. Tanabashi *et al.* (Particle Data Group), Phys. Rev. D **98**, 030001 (2018).

[69] G. G. Raffelt, Phys. Rev. Lett. **64**, 2856 (1990).
[70] N. Viaux, M. Catelan, P. B. Stetson, G. Raffelt, J. Redondo, A. A. R. Valcarce, and A. Weiss, Astron. Astrophys. **558**, A12 (2013).
[71] S. Arceo-Díaz, K. P. Schröder, K. Zuber, and D. Jack, Astropart. Phys. **70**, 1 (2015).
[72] M. Fukugita and S. Yazaki, Phys. Rev. D **36**, 3817 (1987).
[73] G. G. Raffelt and D. S. P. Dearborn, Phys. Rev. D **37**, 549 (1988).
[74] G. G. Raffelt, Phys. Rep. **320**, 319 (1999).
[75] J. A. Grifols and E. Masso, Phys. Rev. D **40**, 3819 (1989).
[76] G. Steigman, J. Cosmol. Astropart. Phys. 04 (2010) 029.
[77] G. Mangano and P. D. Serpico, Phys. Lett. B **701**, 296 (2011).
[78] J. Hamann, S. Hannestad, G. G. Raffelt, and Y. Y. Y. Wong, J. Cosmol. Astropart. Phys. 09 (2011) 034.
[79] R. Mertig, M. Bohm, and A. Denner, Comput. Phys. Commun. **64**, 345 (1991).
[80] V. Shtabovenko, R. Mertig, and F. Orellana, Comput. Phys. Commun. **207**, 432 (2016).
[81] E. Braaten and D. Segel, Phys. Rev. D **48**, 1478 (1993).
[82] S. J. Hardy, Astron. Astrophys. **342**, 614 (1999).
[83] J. F. Donoghue and B. R. Holstein, Phys. Rev. D **28**, 340 (1983); **29**, 3004(E) (1984).
[84] A. Lenard, Phys. Rev. **90**, 968 (1953).
[85] V. Berestetskii, E. Lifshitz, and L. Pitaevskii, *Quantum Electrodynamics*, Course of Theoretical Physics (Butterworth-Heinemann, United Kingdom, 2012).

CHAPTER 4

Photon Emission

Exact Theory of Non-relativistic Electron-Electron Bremsstrahlung

Josef Pradler and Lukas Semmelrock

Submitted to (28.07.2020): The Astrophysical Journal

Preprint version: arXiv:2007.06592 [hep-ph]

Exact Theory of Non-relativistic Electron-Electron Bremsstrahlung

Josef Pradler* and Lukas Semmelrock†
Institute of High Energy Physics, Austrian Academy of Sciences, Nikolsdorfergasse 18, 1050 Vienna, Austria

The quantum mechanical treatment of quadrupole radiation due to bremsstrahlung exact to all orders in the Coulomb interaction of two colliding unpolarized non-relativistic charged spin-1/2 particles is presented. We calculate the elements of the quadrupole tensor, and present analytical solutions for the double differential photon emission cross section of identical and non-identical particles. Contact is made to Born-level and quasi-classical results in the respective kinematic limits and effective energy loss rates are obtained. A generally valid formula for soft-photon emission is established and an approximate formula across the entire kinematic regime is constructed. The results apply to bremsstrahlung emission in the scattering of pairs of electrons and are hence relevant in the study of astrophysical phenomena. A definition of a Gaunt factor is proposed which should facilitate broad applicability of the results.

I. INTRODUCTION

The emission of a photon in the scattering of two electrically charged particles is one of the most fundamental processes of quantum electrodynamics, and bremsstrahlung *per se* is an important phenomenon in many branches of physics. The exact treatment of bremsstrahlung in a Coulomb potential, as seen in the collision of two charged particles, is a difficult endeavour since it involves the evaluation and integration of hypergeometric functions as part of the positive energy solutions of the respective Schrödinger equation. While for many applications treating the wave functions as plane waves and solving the problem to first order in perturbation theory is of sufficient accuracy, say for scattering of fast electrons on protons or light ions, there is a significant kinematic regime where such approximation fails. It is perhaps surprising to note that a complete description of electron-electron bremsstrahlung scattering to leading order in the electrons' non-relativistic velocity and exact in their Coulomb interaction is seemingly absent in the literature today.

For the scattering of two particles with different charge-to-mass ratios, the leading contribution to bremsstrahlung is dipole radiation. The classical electrodynamics calculation was given in 1923 by Kramers [1]. The first quantum mechanical calculations were done independently by Oppenheimer [2] and Sugiura [3] in 1929 as well as two years later by Sommerfeld [4], and results were obtained in the Born approximation. The full non-relativistic quantum mechanical solution for dipole bremsstrahlung was first found by Sommerfeld and Maue [5] in 1935 closing the gap between the Born and the classical limit. A few years later, Elwert [6] found an approximate solution for dipole bremsstrahlung by multiplying the Born cross section by the ratio of probabilities for finding the two initial and final particles, respectively, at the same position. This factor is always greater than unity for attractive and less than unity for repulsive interactions. Thus, the Elwert approximation extends the range of validity of the Born approximation in an easy way. There is, however, still an entire kinematic range where the Elwert approximation fails and the full result must be used. In quest of a generally valid formula for soft photon emission, Weinberg most recently revisited [7] the process of dipole radiation in an application of his soft photon theorem [8].

In case the two scattering particles have the same charge-to-mass ratio, their combined dipole moment vanishes and the leading order contribution to bremsstrahlung is quadrupole radiation. The first calculation of quadrupole bremsstrahlung for spin-1/2 particles in the Born approximation was done by Fedyushin [9] in 1952, and later extended to arbitrary spin by Gould in [10]; see also [11]. The Elwert prescription was applied to electron-electron bremsstrahlung in [12], and there is a body of literature that is concerned with various aspects of the elementary process of electron-electron bremsstrahlung such as the evaulation of Gaunt factors for astrophysical purposes or differential particle distributions as they are relevant in laboratory measurements; we refer the reader to the textbook discussions [13, 14] and references therein. However, while the exact quantum mechanical formulation of dipole bremsstrahlung has found its entry in advanced textbooks on quantum electrodynamics [15–17], the corresponding result for quadrupole bremsstrahlung has not yet been presented in a complete manner.

In this paper, we bring this topic to a closure by calculating the exact differential cross section for quadrupole bremsstrahlung in the non-relativistic approximation and provide its analytical form. Contact is then made to all relevant kinematic regimes, *i.e.*, the Born, classical and soft-photon regimes where our findings can be compared with results from the literature, primarily in connection with the process of electron-electron bremsstrahlung. For the sake of better generality, we shall consider the collision of two particles with arbitrary charge-to-mass ratios Z_1e/m_1 and Z_2e/m_2 where $e > 0$ is the unit of electromagnetic charge. Results are then easily specialized to the case of colliding electrons e^- and/or positrons e^+ of

* josef.pradler@oeaw.ac.at
† lukas.semmelrock@oeaw.ac.at

mass $m_{1,2} = m_e$ and charges $Z(e^{\pm}) = \pm 1$, respectively.

The paper is organized as follows: in Sec. II we introduce the formulæ for the matrix elements and cross sections and in Sec. III we briefly review dipole emission in a Coulomb potential. In Sec. IV we then derive the double differential cross sections in photon energy and scattering angle for quadrupole emission. In Sec. V we relate our results to asymptotic expressions in the Born and classical regime, and in Sec. VI we study the regime of soft photon emission. In Sec. VII we show numerical results on the effective energy loss, and in Sec. VIII we propose a definition of a Gaunt factor for electron-electron scattering. We conclude in Sec. IX and several appendices provide further details on the calculations.

Throughout the paper we will use rationalized natural units where $\hbar = c = 1$ and $\alpha = e^2/(4\pi) \simeq 1/137$.

II. MATRIX ELEMENTS AND CROSS SECTIONS

The S-matrix element for the emission of a photon of energy ω, three-momentum $\mathbf{q}$ and helicity λ with transverse polarization vector $\boldsymbol{\epsilon}^*_{\mathbf{q},\lambda}$ in Coulomb gauge in the collision of non-relativistic particles with charges $Z_n e$, masses m_n, momenta $\mathbf{p}_n$ and respective coordinates $\mathbf{x}_n$ is given by [18],

$$\begin{aligned} S_{f\gamma,i} &= 2\pi\, i\, \delta(E_i - E_f - \omega) \\ &\times \frac{\boldsymbol{\epsilon}^*_{\mathbf{q},\lambda}}{\sqrt{2\omega}} \cdot \sum_n \frac{Z_n e}{m_n} \langle \Psi_f | e^{-i\mathbf{q}\cdot\mathbf{x}_n} \mathbf{p}_n | \Psi_i \rangle. \end{aligned} \tag{1}$$

As for our premise of providing a result of quadrupolar photon emission that is exact to all orders in the Coulomb interaction of two colliding particles, we take the inital (final) states $|\Psi_{i(f)}\rangle$ to be the positive energy solutions of the Hamiltonian

$$H_0 = \frac{\mathbf{p}_1^2}{2m_1} + \frac{\mathbf{p}_2^2}{2m_2} + \frac{Z_1 Z_2 \alpha}{|\mathbf{x}_1 - \mathbf{x}_2|}, \tag{2}$$

such that $H_0|\Psi_{i,f}\rangle = E_{i,f}|\Psi_{i,f}\rangle$. The motion of the center-of-mass (CM) can be separated as usual, $\langle \mathbf{x}|\Psi_i\rangle = e^{i\mathbf{P}\cdot\mathbf{X}}\chi_{\mathbf{p}_i}(\mathbf{r})$ where $\mathbf{P} = \mathbf{p}_1 + \mathbf{p}_2$ and $\mathbf{X} = (\mu/m_2)\mathbf{x}_1 + (\mu/m_1)\mathbf{x}_2$ are CM momentum and coordinate, respectively, and $\mathbf{r} = \mathbf{x}_1 - \mathbf{x}_2$ and $\mathbf{p}_i = \mu(\mathbf{p}_1/m_1 - \mathbf{p}_2/m_2)$ are the respective particles' relative position and initial relative momenta; $\mu = m_1 m_2/(m_1+m_2)$ is the reduced mass. The separation yields an overall momentum-conserving delta function $(2\pi)^3\delta^{(3)}(\mathbf{P} - \mathbf{p}_3 - \mathbf{p}_4 - \mathbf{q})$ where $\mathbf{p}_{3,4}$ are the final state momenta with relative momentum $\mathbf{p}_f = \mu(\mathbf{p}_3/m_1 - \mathbf{p}_4/m_2)$. From the above matrix element, and in the CM frame $\mathbf{P} = 0$, we are hence left to evaluate

$$\mathbf{M}_I = e\frac{A_I}{\mu} \int d^3\mathbf{r}\, \chi^*_{\mathbf{p}_f}(\mathbf{r}) \mathcal{O}_I(-i\nabla_{\mathbf{r}}) \chi_{\mathbf{p}_i}(\mathbf{r}). \tag{3}$$

The operator $\mathcal{O}_I$ originates from the expansion of the exponentials $e^{-i\mathbf{q}\cdot\mathbf{r}_n}$ where $\mathbf{r}_n = \mathbf{x}_n - \mathbf{X}$ and the dipole and quadrupole emission cases assemble themselves through the respective leading and next-to-leading order terms,

$$\text{dipole:} \quad \mathcal{O}_D = 1,\ A_D = \mu\left(\frac{Z_1}{m_1} - \frac{Z_2}{m_2}\right), \tag{4}$$

$$\text{quadrupole:} \quad \mathcal{O}_Q = -i\mathbf{q}\cdot\mathbf{r},\ A_Q = \mu^2\left(\frac{Z_1}{m_1^2} + \frac{Z_2}{m_2^2}\right). \tag{5}$$

As is evident, if two particles have the same charge-to-mass ratio, $Z_1/m_1 = Z_2/m_2$, their mutual dipole moment vanishes and the leading order contribution to bremsstrahlung becomes quadrupole radiation. Hence, for the special cases of scattering of electrons/positrons with their counterparts we have $|A_D^{(e^\pm e^\pm)}| = 0$, $|A_D^{(e^- e^+)}| = 1$, $|A_Q^{(e^\pm e^\pm)}| = 1/2$, $|A_Q^{(e^- e^+)}| = 0$.

The wave functions $\chi_{\mathbf{p}_{i,f}}$ for the relative motion of the particles that are to be used in (3) are (linear combinations of) the Coulomb wave functions of appropriate asymptotic behavior [19],

$$\chi^{(+)}_{\mathbf{p}_i}(\mathbf{r}) = \Gamma(1 - i\nu_i)\ e^{\frac{\pi}{2}\nu_i} e^{i\mathbf{p}_i\cdot\mathbf{r}}\ {}_1F_1\Big(i\nu_i, 1; i\zeta_i^-\Big), \tag{6a}$$

$$\chi^{(-)}_{\mathbf{p}_f}(\mathbf{r}) = \Gamma(1 + i\nu_f)\ e^{\frac{\pi}{2}\nu_f} e^{i\mathbf{p}_f\cdot\mathbf{r}}\ {}_1F_1\Big(-i\nu_f, 1; -i\zeta_f^+\Big), \tag{6b}$$

where ${}_1F_1$ is the confluent hypergeometric function [20]. The magnitudes of the relative three-momenta and position are denoted by $p_{i,f} \equiv |\mathbf{p}_{i,f}|$ and $r \equiv |\mathbf{r}|$, respectively, and $\zeta^\pm_{i,f} = p_{i,f} r \pm \mathbf{p}_{i,f}\cdot\mathbf{r}$. The relative velocities—small parameters in this problem—are denoted by $v_{i,f} = p_{i,f}/\mu$. Note that we define the Sommerfeld parameters $\nu_{i,f}$ such that they carry the sign of the interaction,

$$\nu_{i,f} \equiv -Z_1 Z_2 \frac{\alpha}{v_{i,f}}, \tag{7}$$

i.e., $\nu_{i,f} > 0$ for attractive interactions ($Z_1Z_2 < 0$) and $\nu_{i,f} < 0$ for repulsive interactions ($Z_1Z_2 > 0$). The wave functions are normalized as $\int d^3\mathbf{r}\, \chi^*_{\mathbf{p}}(\mathbf{r})\chi_{\mathbf{p}'}(\mathbf{r}) = (2\pi)^3\delta^{(3)}(\mathbf{p} - \mathbf{p}')$ and the asymptotic forms of $\chi^{(+)}$ and $\chi^{(-)}$ at spatial infinity comprise a (Coulomb-distorted) plane wave plus an outgoing and incoming spherical wave, respectively.

The parameters $|\nu_{i,f}|$ can be viewed as the ratio of the magnitude of the potential energy of the colliding particle pair, $|Z_1Z_2|\alpha/r$, at a separation r that equals the de Broglie wavelength of the relative motion, $1/(\mu v_{i,f})$, to the respective kinetic energies $\mu v_{i,f}^2/2$. This highlights the role ν_i and ν_f play in delineating the various kinematic regimes,

$$|\nu_{i,f}| \ll 1 \quad \text{Born regime}, \tag{8}$$

$$|\nu_{i,f}| \gg 1 \quad \text{classical regime}. \tag{9}$$

In the Born regime, the electrostatic interaction energy of the two colliding charges before and after the collision remains small compared to the respective kinetic energies. The process then becomes treatable by replacing $\chi_{\mathbf{p}_{i,f}}$ with plane waves. In turn, in the opposite limit the particles' motion is quasi-classical and the process becomes describable in terms of formulæ derived from classical electrodynamics; note that $|\nu_f| \geq |\nu_i|$ out of kinematic reasons. Below we shall study those limits and see how the known results follow from the full quantum mechanical formula.

The matrix element $\mathcal{M}$, defined through $S_{f\gamma,i} = (2\pi)^4\delta(E_i - E_f - \omega)\delta^{(3)}(\mathbf{P} - \mathbf{p}_3 - \mathbf{p}_4 - \mathbf{q})\mathcal{M}$, when squared, summed over the two photon polarizations, and averaged over the direction of the outgoing photon is given by

$$\langle|\mathcal{M}_I|^2\rangle_{\hat{\mathbf{q}}} = \frac{1}{4\pi}\int d\Omega_{\mathbf{q}} \sum_\lambda \left|\frac{\boldsymbol{\epsilon}^*_{\mathbf{q},\lambda}}{\sqrt{2\omega}} \cdot \mathbf{M}_I\right|^2 . \tag{10}$$

The energy-differential cross section for dipole ($I = D$) or quadrupole ($I = Q$) emission is then given by

$$\omega\frac{d\sigma_I}{d\omega} = \frac{\mu^2\omega^3}{4\pi^3}\sqrt{1 - \frac{2\omega}{\mu v_i^2}}\int d\cos\theta\, \langle|\mathcal{M}_I|^2\rangle_{\hat{\mathbf{q}}} . \tag{11}$$

where $\cos\theta = \mathbf{p}_i \cdot \mathbf{p}_f/(p_i p_f)$ is the cosine of the CM scattering angle of the colliding particle pair. The boundaries of the $d\cos\theta$ integration are $(-1, 1)$ for non-identical particles and $(0, 1)$ for identical particles.

III. DIPOLE EMISSION

In order to prepare for the quadrupole case and to set some of the notation, in this section we review the calculation of the dipole transition integral. By defining $\nu_{i,f}$ as we did in Eq. (7), we can treat the case of an attractive Coulomb interaction $Z_1Z_2 < 0$ and a repulsive Coulomb interaction $Z_1Z_2 > 0$ simultaneously. The wave functions $\chi_{\mathbf{p}_i}(\mathbf{r})$ and $\chi_{\mathbf{p}_f}(\mathbf{r})$ to be used in (3) are the ones of (6) [17],

$$\mathbf{M}_D = e\frac{A_D}{\mu}B_iB_f \lim_{\lambda\to 0}\Big[ip_i\nabla_{\mathbf{p}_i}J_1^D(\lambda, \mathbf{k}, \mathbf{p}_i, \mathbf{p}_f) + \mathbf{p}_i J_2^D(\lambda, \mathbf{k}, \mathbf{p}_i, \mathbf{p}_f)\Big] , \tag{12}$$

with $B_{i,f} = e^{-\pi\nu_{i,f}/2}\Gamma\left(1 - i\nu_{i,f}\right)$ and using the abbreviation ${}_1F_1\left(i\zeta_{i(f)}\right) \equiv {}_1F_1\left(i\nu_{i(f)}, 1, i\zeta_{i(f)}\right)$, J_1^D and J_2^D are given by

$$J_1^D(\lambda, \mathbf{k}, \mathbf{p}_i, \mathbf{p}_f) = \int d^3\mathbf{r}\, \frac{e^{i\mathbf{k}\cdot\mathbf{r} - \lambda r}}{r}\, {}_1F_1(i\zeta_f^+)\, {}_1F_1(i\zeta_i^-) , \tag{13a}$$

$$J_2^D(\lambda, \mathbf{k}, \mathbf{p}_i, \mathbf{p}_f) = \int d^3\mathbf{r}\, e^{i\mathbf{k}\cdot\mathbf{r} - \lambda r}\, {}_1F_1(i\zeta_f^+)\, {}_1F_1(i\zeta_i^-) . \tag{13b}$$

The solution to the first integral has been given by Nordsieck [21], which we shall denote by $\mathcal{I}_N$, *i.e.*, $J_1^D = \mathcal{I}_N$,

$$\mathcal{I}_N(\lambda, \mathbf{k}, \mathbf{p}_i, \mathbf{p}_f) = \frac{2\pi}{\eta_1}e^{-\pi\nu_i}\left(\frac{\eta_1}{\eta_3}\right)^{i\nu_i}\left(\frac{\eta_3 + \eta_4}{\eta_3}\right)^{-i\nu_f} \times {}_2F_1\left(1 - i\nu_i, i\nu_f, 1, \frac{\eta_1\eta_4 - \eta_2\eta_3}{\eta_1(\eta_3 + \eta_4)}\right) , \tag{14}$$

with $\eta_1 = (k^2 + \lambda^2)/2$, $\eta_2 = \mathbf{p}_f \cdot \mathbf{k} - i\lambda p_f$, $\eta_3 = \mathbf{p}_i \cdot \mathbf{k} + i\lambda p_i - \eta_1$ and $\eta_4 = p_i p_f + \mathbf{p}_i \cdot \mathbf{p}_f - \eta_2$. The integral J_2^D vanishes due to the orthogonality of the Coulomb wave functions; this is also manifest in the integrated form by noting that $J_2^D = -\partial_\lambda J_1^D$ and $\lim_{\lambda\to 0}\partial_\lambda\mathcal{I}_N = 0$. Setting $\mathbf{k} = \mathbf{p}_i - \mathbf{p}_f$ and using the properties of the hypergeometric functions, ${}_2F_1\left(a, b; c; z\right) = (1 - z)^{-b}\,{}_2F_1\left(b, 1 - a; c; z/(z - 1)\right)$ and ${}_2F_1\left(a, b; c; z\right) = {}_2F_1\left(b, a; c; z\right)$ one finds that the dipole transition amplitude is

$$\mathbf{M}_D = \frac{-i8\pi eA_DB_iB_fe^{-\pi\nu_i}}{\mu(p_i - p_f)^2(p_i + p_f)^2}\left[\frac{p_i - p_f}{p_i + p_f}(1 - z)\right]^{i(\nu_i + \nu_f) - 1} \times \left[i\nu_ip_iF\left(z\right)\mathbf{k} - (1 - z)\left(p_f\mathbf{p}_i - p_i\mathbf{p}_f\right)F'(z)\right] ,$$

with $z = -2(p_ip_f - \mathbf{p}_i \cdot \mathbf{p}_f)/(p_i - p_f)^2$ and where we have introduced the shorthand notation

$$F(z) \equiv {}_2F_1(i\nu_f, i\nu_i; 1; z), \tag{15}$$

$$F'(z) \equiv \frac{\partial}{\partial z}\,{}_2F_1(i\nu_f, i\nu_i; 1; z), \tag{16}$$

to be used extensively below. The squared integral is therefore [17]

$$|\mathbf{M}_D|^2 = \frac{16\pi\alpha^3Z_1^2Z_2^2A_D^2S_iS_f}{(p_i + p_f)^2(p_i - p_f)^4}\left[\frac{|F\left(z\right)|^2}{1 - z} - \frac{z|F'(z)|^2}{\nu_i\nu_f} + i\frac{\nu_i + \nu_f}{2\nu_i\nu_f}\frac{z}{1 - z}\Big(F\left(z\right)F'^*(z) - F^*\left(z\right)F'(z)\Big)\right], \tag{17}$$

where the Sommerfeld factors $S_{i,f}$ characterize the action of the Coulomb field near the origin,

$$S_i = e^{-2\pi\nu_i}|\chi^{(+)}_{\mathbf{p}_i}(0)|^2 = \frac{2\pi\nu_i}{e^{2\pi\nu_i} - 1}, \tag{18}$$

$$S_f = |\chi^{(-)}_{\mathbf{p}_f}(0)|^2 = \frac{-2\pi\nu_f}{e^{-2\pi\nu_f} - 1}. \tag{19}$$

The differential cross section with respect to the emitted energy ω is given by effecting the angular integral in (17), which can be written as $d\cos\theta = (p_i - p_f)^2/(2p_ip_f)\,dz$. In the dipole case, one can then use the hypergeometric differential equation to substitute the expression in the square brackets of (17) by a total derivative in z to get the differential cross section for an attractive interaction [17]

$$\omega\frac{d\sigma_D}{d\omega} = \frac{16}{3}\frac{\alpha^3Z_1^2Z_2^2A_D^2}{\mu^2v_i^2}S_iS_f\,\frac{1}{\nu_i\nu_f}\frac{\xi}{4}\frac{d}{d\xi}\left|F(\xi)\right|^2 , \tag{20}$$

with $\xi = \min(z) = -4p_i p_f/\left(p_i - p_f\right)^2$. Note that $\nu_{i,f}$, arguments in the Sommerfeld factors $S_{i,f}$ and parameters in the hypergeometric function F, are positive for attractive interactions and negative for repulsive interactions. Equation (20) is therefore applicable to both cases.

IV. QUADRUPOLE EMISSION

If two particles have the same charge-to-mass ratio, their combined dipole moment vanishes and the leading order contribution to bremsstrahlung is quadrupole radiation. The quantum mechanical calculation for the collision of two non-relativistic electrons to first order in perturbation theory was presented in [9]; for textbook discussions see [16, 17]. We now proceed to the calculation that is complete to all orders in the Coulomb interaction of the scattering particles. We additionally recover the previous results [9] in a dedicated Born-level quantum field theory calculation that is presented in App. B.

We start this section by considering the scattering of a distinguishable particle pair. In this case, $A_D \neq 0$, dipole radiation dominates (unless $A_D \ll A_Q$ because of some accidental cancellation), and quadrupole radiation is the first correction in a velocity expansion of the cross section. In a second part, we then consider the scattering of identical particles, such as two electrons, for which $A_D = 0$ and quadrupole radiation will become the leading process.

The calculations below will be framed in terms of a quadrupole tensor $\boldsymbol{\mathcal{Q}} = (Q^{ab})$ that is defined through the expression (3) for the matrix element $\mathbf{M}_Q = (M_Q^b)$,

$$M_Q^b = -\frac{A_Q}{\mu}\, q^a Q^{ab}. \tag{21}$$

The Cartesian components of $\boldsymbol{\mathcal{Q}}$ are then given by the tensor[1]

$$Q^{ab} = e\int d^3\mathbf{r}\, \chi^*_{\mathbf{p}_f}(\mathbf{r}) r^a \partial^b \chi_{\mathbf{p}_i}(\mathbf{r}), \tag{22}$$

where ∂^b is the derivative with respect to the b-th Cartesian component of $\mathbf{r}$, *i.e.* r^b. The tensor is symmetric in its indices, $Q^{ab} = Q^{ba}$, which is related to the fact that the two-particle system (without explicit magnetic moment interaction[2]) has vanishing magnetic dipole moment, see *e.g.* [22].

[1] Throughout this paper, Cartesian coordinates are given by upper indices $a, b, \ldots$ to discern them from the lower indices i and f labeling in and out states; the Einstein summation convention is used for upper indices.

[2] The relative unimportance of bremsstrahlung induced by the particles' intrinsic magnetic moments $\mu_n \sim e_n/m_n$ is discussed in [10].

The squared matrix element (10) can be then written in terms of the quadrupole tensor as

$$\begin{aligned}\langle|\mathcal{M}_I|^2\rangle_{\hat{\mathbf{q}}} &= \frac{\omega A_Q^2}{2\mu^2}\left\langle \sum_\lambda \hat{q}^a\hat{q}^c(\epsilon^*_{\mathbf{q},\lambda})^b\epsilon^d_{\mathbf{q},\lambda}\right\rangle_{\hat{\mathbf{q}}}(Q^*)^{ab}Q^{cd} \\ &= \frac{\omega A_Q^2}{30\mu^2}\left[3|Q^{ab}|^2 - |Q^{aa}|^2\right], \end{aligned}\tag{23}$$

with $|Q^{ab}|^2 \equiv (Q^*)^{ab}Q^{ba} = \mathrm{Tr}(\boldsymbol{\mathcal{Q}}^\dagger\boldsymbol{\mathcal{Q}})$ and $|Q^{aa}|^2 \equiv (Q^*)^{aa}Q^{bb} = |\,\mathrm{Tr}(\boldsymbol{\mathcal{Q}})|^2$. In the second equality we have used for the angular average

$$\begin{aligned}\left\langle \sum_\lambda \hat{q}^a\hat{q}^c\epsilon^{*b}\epsilon^d\right\rangle_{\hat{\mathbf{q}}} =& \frac{3}{30}\left(\delta^{ac}\delta^{bd} + \delta^{bc}\delta^{ad} - \frac{2}{3}\delta^{ab}\delta^{cd}\right) \\ &+ \frac{5}{30}\left(\delta^{ac}\delta^{bd} - \delta^{bc}\delta^{ad}\right). \end{aligned}\tag{24}$$

At this point the quadrupolar E2 nature of the emission becomes manifest: because of the symmetry in Q^{ab}, the contraction with the second bracket vanishes and only the symmetric combination in a and b and in c and d survives. The term corresponding to magnetic dipole emission M1 is therefore not present.

An important aspect in the calculation of $\boldsymbol{\mathcal{Q}}$ is that for identical spin-1/2 particles, the overall wave function is anti-symmetric under particle exchange. The non-relativistic absence of an interaction that involves the spin-coordinate of the particles implies, that the spin only enters in the counting of spatially symmetric and anti-symmetric states. If the particles are in the spin singlet ($\uparrow\downarrow$) state, the wave-function is spatially symmetric and vice versa for the three spin triplet ($\uparrow\uparrow$) states. The wave functions $\chi_{\mathbf{p}_{i,f}}$ to be used are then,

$$\chi^{\uparrow\downarrow}_{\mathbf{p}_i}(\mathbf{r}) = \frac{1}{\sqrt{2}}\left(\chi^{(+)}_{\mathbf{p}_i}(\mathbf{r}) + \chi^{(+)}_{\mathbf{p}_i}(-\mathbf{r})\right), \tag{25a}$$

$$\chi^{\uparrow\uparrow}_{\mathbf{p}_i}(\mathbf{r}) = \frac{1}{\sqrt{2}}\left(\chi^{(+)}_{\mathbf{p}_i}(\mathbf{r}) - \chi^{(+)}_{\mathbf{p}_i}(-\mathbf{r})\right), \tag{25b}$$

with analogous linear combinations $\chi^{\uparrow\downarrow}_{\mathbf{p}_f}(\mathbf{r})$ and $\chi^{\uparrow\uparrow}_{\mathbf{p}_f}(\mathbf{r})$ made from $\chi^{(-)}_{\mathbf{p}_f}$. For the scattering of identical particles, there are hence more overlap integrals of hypergeometric functions to consider.

A. Scattering of non-identical particles

If the scattered particles are distinguishable, the wave functions $\chi_{\mathbf{p}_i}(\mathbf{r})$ and $\chi_{\mathbf{p}_f}(\mathbf{r})$ to be used in (22) are the ones of (6). Following the notation for the dipole case, we replace the scalar functions $J^D_{1,2}$ with vector-valued functions $\mathbf{J}^Q_{1,2}$, given by

$$\begin{aligned}\mathbf{J}^Q_1(\lambda,\mathbf{k},\mathbf{p}_i,\mathbf{p}_f) &= \int d^3\mathbf{r}\,\frac{\mathbf{r}}{r}e^{i\mathbf{k}\cdot\mathbf{r}-\lambda r}{}_1F_1(i\zeta_f^+){}_1F_1(i\zeta_i^-) \\ &= -i\nabla_{\mathbf{k}}\mathcal{I}_N(\lambda,\mathbf{k},\mathbf{p}_i,\mathbf{p}_f), \end{aligned}\tag{26a}$$

$$\mathbf{J}_2^Q(\lambda,\mathbf{k},\mathbf{p}_i,\mathbf{p}_f)=\int d^3\mathbf{r}\;\mathbf{r}\,e^{i\mathbf{k}\cdot\mathbf{r}-\lambda r}{}_1F_1(i\zeta_f^+){}_1F_1(i\zeta_i^-)$$
$$=i\frac{\partial}{\partial\lambda}\nabla_{\mathbf{k}}\mathcal{I}_N(\lambda,\mathbf{k},\mathbf{p}_i,\mathbf{p}_f). \tag{26b}$$

We hence make the important observation, that the integrals are expressible as derivatives of the Nordsieck integral $\mathcal{I}_N$ given by Eq. (14). Because of this, we are in the position of assembling an analytical solution. Also note that unlike in the dipole case, $\mathbf{J}_2^Q$ does not identically vanish. From the definitions (26a) and (26b), it follows that the quadrupole tensor $\boldsymbol{\mathcal{Q}}$ with Cartesian components Q^{ab} can be written as

$$Q^{ab}=e\,B_iB_f\lim_{\lambda\to0}\frac{\partial}{\partial k^a}\left[ip_i\frac{\partial}{\partial p_i^b}-p_i^b\frac{\partial}{\partial\lambda}\right]\mathcal{I}_N(\lambda,\mathbf{k},\mathbf{p}_i,\mathbf{p}_f)\,, \tag{27}$$

where $\mathbf{p}_i$, $\mathbf{p}_f$, $\mathbf{k}$ are treated as separate variables in the partial derivatives of $\mathcal{I}_N$. After taking the derivatives, we set $\mathbf{k}=\mathbf{p}_i-\mathbf{p}_f$. The elements of the quadrupole tensor can then be split into the following symmetric combinations,

$$Q^{ab}=f_0\bigg[\Big(f_1\hat p_i^a\hat p_i^b+f_2\hat p_f^a\hat p_f^b+f_3(\hat p_i^a\hat p_f^b+\hat p_i^b\hat p_f^a)\Big)F(z)$$
$$+\Big(f_4\hat p_i^a\hat p_i^b+f_5\hat p_f^a\hat p_f^b+f_6(\hat p_i^a\hat p_f^b+\hat p_i^b\hat p_f^a)\Big)F'(z)\bigg], \tag{28}$$

where the various $\hat p_{i,f}^a$ are the Cartesian components of the unit vectors $\hat{\mathbf{p}}_{i,f}=\mathbf{p}_{i,f}/p_{i,f}$. The prefactors f_0 to f_6 are

$$f_0=\frac{1}{p_i^3}\frac{e\,B_iB_f\;16\pi e^{-\pi\nu_i}}{(1-y)^3(1+y)^4}\left[\frac{1-y}{1+y}\,(1-z)\right]^{i\left(\nu_i+\nu_f\right)-2}, \tag{29a}$$
$$f_1=\nu_i\Big[-2+(1-y)z\Big]$$
$$+i\frac{\nu_i^2}{zy}\Big[2y^2+2y(2-y)z+(1-y)^2z^2\Big]\,, \tag{29b}$$
$$f_2=\nu_i\Big[-2y^3-y^2(1-y)z\Big]$$
$$+i\frac{\nu_i^2}{zy}\Big[2y^2+2y^2(2y-1)z+y^2(1-y)^2z^2\Big]\,, \tag{29c}$$
$$f_3=\nu_i\Big[y(1+y)\Big]+i\frac{\nu_i^2}{zy}\Big[-2y^2-y(1+y^2)z\Big]\,, \tag{29d}$$
$$f_4=\nu_i(1-z)\Big[-y(3-y)-(1-y)^2z\Big]$$
$$+i\frac{(1-z)^2}{z}\Big[2y^2-y(1-y)z\Big]\,, \tag{29e}$$
$$f_5=\nu_i(1-z)\Big[y(1-3y)-y(1-y)^2z\Big]$$
$$+i\frac{(1-z)^2}{z}\Big[2y^2+y^2(1-y)z\Big]\,, \tag{29f}$$
$$f_6=\nu_i(1-z)\Big[y(1+y)\Big]-i\frac{(1-z)^2}{z}2y^2\,. \tag{29g}$$

with $y=p_f/p_i$ and the definitions of z as in Sec. III above.

At this point, we can calculate $|Q^{ab}|^2=\mathrm{Tr}(\boldsymbol{\mathcal{Q}}^\dagger\boldsymbol{\mathcal{Q}})$ and $|Q^{aa}|^2=|\,\mathrm{Tr}(\boldsymbol{\mathcal{Q}})|^2$ with $\left(\hat{\mathbf{p}}_i\cdot\hat{\mathbf{p}}_f\right)=\cos\theta=1+z(1-y)^2/(2y)$, both of which can be written in the form

$$|Q^{\alpha\beta}|^2=G_0\bigg[\left(A_{\hat\alpha\hat\beta}+C_{\hat\alpha\hat\beta}\frac{d}{dz}\right)|F(z)|^2+B_{\hat\alpha\hat\beta}\left|F'(z)\right|^2$$
$$+iD_{\hat\alpha\hat\beta}\left(F\left(z\right)F'^*(z)-F^*\left(z\right)F'(z)\right)\bigg]. \tag{30}$$

The hats on $\hat\alpha\hat\beta=\hat a\hat a$ or $\hat a\hat b$ are labels of the coefficients A to D and not Cartesian components that would need to be summed over. The prefactor reads

$$G_0=\frac{64\pi\alpha^3Z_1^2Z_2^2S_iS_f}{\mu^6v_i^8\,(1+y)^4(1-y)^6}\,. \tag{31}$$

The coefficients A to D for $|Q^{aa}|^2$ are given by

$$A_{\hat a\hat a}=\frac{4(y+1)^2}{(z-1)^2},\;\;B_{\hat a\hat a}=\frac{9y^2}{\nu_i^2},\;\;D_{\hat a\hat a}=\frac{6y(y+1)}{\nu_i(z-1)}\,, \tag{32a}$$

and $C_{\hat a\hat a}=0$. For $|Q^{ab}|^2$ we find

$$A_{\hat a\hat b}=\frac{\nu_i^2}{2(z-1)^2}\Bigg\{\left[\frac{(y-1)^4}{y^2}-\frac{(y-1)^2}{\nu_i^2}\right]z^2$$
$$+\frac{4}{y}\left[2(1-y)^2-\frac{y^2}{\nu_i^2}\right]z+8\left[2+\frac{(y+1)^2}{\nu_i^2}\right]\Bigg\}, \tag{33a}$$

$$B_{\hat a\hat b}=\frac{1}{2y}\Bigg\{\frac{z}{(z-1)}\Big[(y-1)^2z+4y\Big]^2$$
$$+\frac{y^2}{\nu_i^2}\Big[10y-2\left(1+y^2\right)z-(1-y)^2z^2\Big]\Bigg\}, \tag{33b}$$

$$C_{\hat a\hat b}=\frac{(1-y)^4}{2y(z-1)^2}\left[z+\frac{4y}{(1-y)^2}\right]\left[z^2+\frac{y(1+3z)}{(1-y)^2}\right], \tag{33c}$$

$$D_{\hat a\hat b}=-\frac{(1+y)}{4\nu_iy^2(1-z)^2}\Bigg\{\Big[y^2-\nu_i^2(y-1)^2\Big]$$
$$\times(y-1)^2z^3+\Big[4y^3-8\nu_i^2(y-1)^2y\Big]z^2$$
$$-4y^2\Big[4\nu_i^2+(y+4)y+1\Big]z+8y^3\Bigg\}. \tag{33d}$$

The double differential cross section in the incoming particles' scattering angle θ and the emitted energy ω can then be obtained by plugging (30) into (11) using the respective expressions for the quadrupole transition amplitude given by (23),

$$\left.\frac{\omega\, d\sigma_Q}{d\omega\, d\cos\theta}\right|_{\text{non-id.}} = \frac{8}{15}\frac{\alpha^3 Z_1^2 Z_2^2 A_Q^2}{\mu^2}\frac{y}{(1-y)^2} S_i S_f \left[\left(A + C\frac{d}{dz}\right)|F(z)|^2 + B\left|F'(z)\right|^2 + 2D\,\mathrm{Im}\left[F^*(z)\,F'(z)\right]\right], \quad (34)$$

where $A = 3A_{\hat{a}\hat{b}} - A_{\hat{a}\hat{a}}$ and the same for B, C and D. Again, the expression for the cross section is valid for attractive and repulsive interactions with ν_i changing sign going from the former to the latter. Equation (34) is our first main result.

B. Scattering of identical particles

To calculate the scattering of identical particles—such as in electron-electron scattering—we have to use the spatially (anti-)symmetrized wave functions (25). In the following, we treat the symmetric and antisymmetric case separately,

$$Q^{ab}_{\uparrow\downarrow} = e\int d^3\mathbf{r}\, (\chi^{\uparrow\downarrow}_{\mathbf{p}_f})^*\, r^a\partial^b\, \chi^{\uparrow\downarrow}_{\mathbf{p}_i}, \quad (35a)$$

$$Q^{ab}_{\uparrow\uparrow} = e\int d^3\mathbf{r}\, (\chi^{\uparrow\uparrow}_{\mathbf{p}_f})^*\, r^a\partial^b\, \chi^{\uparrow\uparrow}_{\mathbf{p}_i}. \quad (35b)$$

The squared amplitude will then be given by

$$|\mathcal{Q}^{\alpha\beta}|^2 = \frac{1}{4}\left(|\mathcal{Q}^{\alpha\beta}_{\uparrow\downarrow}|^2 + 3|\mathcal{Q}^{\alpha\beta}_{\uparrow\uparrow}|^2\right) \qquad \alpha\beta = aa,\, ab, \quad (36)$$

where the factor 1/4 is from the spin average of the four possible (singlet and triplet) spin configurations of the colliding unpolarized spin-1/2 particles. The four relevant integrals are

$$Q^{ab}_1 = e\int d^3\mathbf{r}\, \left[\chi^{(-)}_{\mathbf{p}_f}(\mathbf{r})\right]^* r^a\partial^b\, \chi^{(+)}_{\mathbf{p}_i}(\mathbf{r})$$
$$= e\,B_iB_f\frac{\partial}{\partial k^a}\left[ip_i\frac{\partial}{\partial p_i^b} - p_i^b\frac{\partial}{\partial\lambda}\right]\mathcal{I}_N(\lambda,\mathbf{k},\mathbf{p}_i,\mathbf{p}_f), \quad (37a)$$

$$Q^{ab}_2 = e\int d^3\mathbf{r}\, \left[\chi^{(-)}_{\mathbf{p}_f}(-\mathbf{r})\right]^* r^a\partial^b\, \chi^{(+)}_{\mathbf{p}_i}(\mathbf{r})$$
$$= e\,B_iB_f\frac{\partial}{\partial l^a}\left[ip_i\frac{\partial}{\partial p_i^b} - p_i^b\frac{\partial}{\partial\lambda}\right]\mathcal{I}_N(\lambda,\mathbf{l},\mathbf{p}_i,-\mathbf{p}_f), \quad (37b)$$

$$Q^{ab}_3 = e\int d^3\mathbf{r}\, \left[\chi^{(-)}_{\mathbf{p}_f}(-\mathbf{r})\right]^* r^a\partial^b\, \chi^{(+)}_{\mathbf{p}_i}(-\mathbf{r}) = Q^{ab}_1, \quad (37c)$$

$$Q^{ab}_4 = e\int d^3\mathbf{r}\, \left[\chi^{(-)}_{\mathbf{p}_f}(\mathbf{r})\right]^* r^a\partial^b\, \chi^{(+)}_{\mathbf{p}_i}(-\mathbf{r}) = Q^{ab}_2, \quad (37d)$$

with $\boldsymbol{\mathcal{Q}}_{\uparrow\downarrow} = (\boldsymbol{\mathcal{Q}}_1 + \boldsymbol{\mathcal{Q}}_2 + \boldsymbol{\mathcal{Q}}_3 + \boldsymbol{\mathcal{Q}}_4)/2$ and $\boldsymbol{\mathcal{Q}}_{\uparrow\uparrow} = (\boldsymbol{\mathcal{Q}}_1 - \boldsymbol{\mathcal{Q}}_2 + \boldsymbol{\mathcal{Q}}_3 - \boldsymbol{\mathcal{Q}}_4)/2$, where $\mathbf{k} = \mathbf{p}_i - \mathbf{p}_f$ (as before) and $\mathbf{l} \equiv \mathbf{p}_i + \mathbf{p}_f$ are treated as independent from $\mathbf{p}_i$ and $\mathbf{p}_f$ until after taking the derivative; furthermore $\lim_{\lambda\to 0}\mathcal{I}_N(\lambda,-\mathbf{k},-\mathbf{p}_i,-\mathbf{p}_f) = \lim_{\lambda\to 0}\mathcal{I}_N(\lambda,\mathbf{k},\mathbf{p}_i,\mathbf{p}_f)$ holds. We can see that $\boldsymbol{\mathcal{Q}}_1 = \boldsymbol{\mathcal{Q}}_3$ and $\boldsymbol{\mathcal{Q}}_2 = \boldsymbol{\mathcal{Q}}_4$ which gives

$$|Q^{\alpha\beta}|^2 = |Q^{\alpha\beta}_1|^2 + |Q^{\alpha\beta}_2|^2 - \frac{1}{2}|I^{\alpha\beta}|^2, \quad (38)$$

with $\alpha\beta = ab$ or aa as before. Here, $|Q^{\alpha\beta}_1|^2$ is nothing else than the squared quadrupole tensor (30) of Sec. IV A. It can be easily shown that $|Q^{\alpha\beta}_2|^2$ can be obtained from $|Q^{\alpha\beta}_1|^2$ by replacing $\cos\theta \to -\cos\theta$, which is identical to the transformation $z \to \tilde{z} = -z - 4y/(1-y)^2$. For the interference term in (38), we can use the expression (28) for the quadrupole tensors $\boldsymbol{\mathcal{Q}}_1$ and $\boldsymbol{\mathcal{Q}}_2$ with $\boldsymbol{\mathcal{Q}}_1 \equiv \boldsymbol{\mathcal{Q}}_1(z)$ and $\boldsymbol{\mathcal{Q}}_2 \equiv \boldsymbol{\mathcal{Q}}_2(\tilde{z})$. The result for the interference term $|I^{\alpha\beta}|^2$ is rather lengthy which we therefore relegate to App. A. In the limit $\nu_i \to 0$, the expressions obtained by plugging (A2) and (A3) into the three terms in (38) agree with the expressions obtained from the t-channel, u-channel, and interference terms of the tree level diagrams in a Born-level calculation. The double differential cross section for two identical particles with mass $m_{1,2} = m$ and charge $Z_{1,2} = Z$ so that $A_Q = 1/2$ reads,

$$\left.\frac{\omega d\sigma_Q}{d\omega d\cos\theta}\right|_{\text{ident.}} = \frac{8}{15}\frac{\alpha^3 Z^4}{m^2}\frac{y}{(1-y)^2} S_i S_f \Bigg[\left(A + C\frac{d}{dz}\right)|F(z)|^2 + B\left|F'(z)\right|^2 + 2D\mathrm{Im}\left[F^*(z)F'(z)\right] + \left(\tilde{A} + \tilde{C}\frac{d}{d\tilde{z}}\right)|F(\tilde{z})|^2$$
$$+ \tilde{B}\left|F'(\tilde{z})\right|^2 + 2\tilde{D}\mathrm{Im}\left[F^*(\tilde{z})F'(\tilde{z})\right] - A^+\mathrm{Re}\left[F^*(z)F(\tilde{z})\right] - A^-\mathrm{Im}\left[F^*(z)F(\tilde{z})\right] - B^+\mathrm{Re}\left[F'^*(z)F'(\tilde{z})\right] -$$
$$B^-\mathrm{Im}\left[F'^*(z)F'(\tilde{z})\right] - C^+\mathrm{Re}\left[F^*(z)F'(\tilde{z})\right] - C^-\mathrm{Im}\left[F^*(z)F'(\tilde{z})\right] - D^+\mathrm{Re}\left[F'^*(z)F(\tilde{z})\right] - D^-\mathrm{Im}\left[F'^*(z)F(\tilde{z})\right]\Bigg]. \quad (39)$$

where, as in Eq. (34), $A = 3A_{\hat{a}\hat{b}} - A_{\hat{a}\hat{a}}$, $A^\pm = 3A^\pm_{\hat{a}\hat{b}} - A^\pm_{\hat{a}\hat{a}}$, $\tilde{A} = A(z \to \tilde{z})$ and the same for the other coefficients

$B,\ C,\ D$ and $\tilde{B},\ \tilde{C},\ \tilde{D}$, as well as $B^{\pm},\ C^{\pm},\ D^{\pm}$. This is our second main result, and it is the exact expression for bremsstrahlung emission in the scattering of a non-relativistic electron pair. Note that in the scattering of identical particles, the latter only share repulsive Coulomb interactions.

V. BORN AND QUASI-CLASSICAL LIMITS

The expressions presented in the previous section are valid for bremsstrahlung in the presence of Coulomb interactions for general values of the Sommerfeld parameters $\nu_{i,f}$. Hence, they contain both, the Born and the quasi-classical limit. In the following, we shall discuss how the limiting expressions, as they are often found in the literature, appear from the exact results above; dedicated Born and classical calculations of the cross sections are additionally presented in the appendices.

A. Born Limit

The Born regime is characterized by $|\nu_{i,f}| \ll 1$. In this limit, the hypergeometric function and its derivative can be written in closed form as [20]

$$F(z) \approx 1\,, \quad F'(z) \approx \frac{\nu_i^2}{y}\frac{\ln(1-z)}{z} \quad (|\nu_i| \ll 1). \tag{40a}$$

In the same limit, the Sommerfeld factors go to unity, $S_{i,f} \to 1$. It is then straight-forward to obtain the Born expressions, which we shall record in the following.

For dipole emission, and denoting by $x \equiv 2\omega/\mu v_i^2$ the fraction of kinetic CM energy that is carried away by the emitted photon, the energy differential cross section reads

$$\omega\,\frac{d\sigma_D}{d\omega}\bigg|_{\text{Born}} = \frac{16}{3}\frac{\alpha^3 Z_1^2 Z_2^2 A_D^2}{\mu^2 v_i^2}\ln\left(\frac{1+\sqrt{1-x}}{1-\sqrt{1-x}}\right). \tag{41}$$

For quadrupole emission, the corresponding cross section for non-identical particles is obtained from (34) by taking the limits (40) and by integrating over $\cos\theta$,

$$\omega\,\frac{d\sigma_Q}{d\omega}\bigg|_{\substack{\text{Born}\\ \text{non-id.}}} = \frac{8}{15}\frac{\alpha^3 Z_1^2 Z_2^2 A_Q^2}{\mu^2}\Bigg[10\sqrt{1-x} + 3(2-x)\ln\left(\frac{1+\sqrt{1-x}}{1-\sqrt{1-x}}\right)\Bigg]. \tag{42}$$

For identical particles, such as in e^-e^- scattering, with mass $m_{1,2}=m$ and charge $Z_{1,2}=Z$ one finds in agreement with literature [9],

$$\omega\,\frac{d\sigma_Q}{d\omega}\bigg|_{\substack{\text{Born}\\ \text{ident.}}} = \frac{4}{15}\frac{\alpha^3 Z^4}{m^2}\sqrt{1-x}\Bigg[17-\frac{3x^2}{(2-x)^2} + \frac{12(2-x)^4-7(2-x)^2x^2-3x^4}{2\,(2-x)^3\sqrt{1-x}}\ln\left(\frac{1+\sqrt{1-x}}{1-\sqrt{1-x}}\right)\Bigg]. \tag{43}$$

We have verified that we obtain the cross sections above also by integrating the squared matrix elements presented in App. B, which were obtained from a tree-level quantum field theory calculation for $|Z_1|/m_1 = |Z_2|/m_2$. The Born cross sections (41)–(43) are shown as dash double-dotted gray lines in Figs. 1 and 2.

In the Elwert prescription [6] mentioned in the introduction, the Born cross sections are multiplied by a ratio of the Sommerfeld factors S_i and S_f, defined in Eq. (18) and which also multiply the exact expressions (20), (34) and (39).[3] The Elwert cross section is then given by,

$$\omega\,\frac{d\sigma_I}{d\omega}\bigg|_{\text{Elwert}} = e^{-2\pi\nu_i}\frac{S_f}{S_i}\omega\,\frac{d\sigma_I}{d\omega}\bigg|_{\text{Born}}. \tag{44}$$

Note that the prefactor $e^{-2\pi\nu_i}S_f/S_i$ is always greater than unity for attractive and less than unity for repulsive interactions. Results based on the prescription (44) are shown by the dashed red lines in all figures. In Figs. 1 and 2, one can see that the Elwert cross section deviates from the differential Born cross section towards the kinematic endpoint, *i.e.* for $x \to 1$. In the soft photon region, both expressions give the same result.

B. Quasi-classical Limit

Classical results from quantum mechanics are obtained by taking the limit $\hbar \to 0$. Let us hence, momentarily, reinstate the factors of $\hbar$ in the Sommerfeld parameter and in the fraction of CM energy carried away by the photon,

$$\nu_{i,f} = \frac{Z_1 Z_2 \alpha}{\hbar v_{i,f}}, \quad x = \frac{\hbar 2\omega}{\mu v_i^2}. \tag{45}$$

For $|\nu_i| \gg 1$ it is then said that the particles move on classical trajectories and both, $|\nu_i| \to \infty$ and $|\nu_f| = |\nu_i|/\sqrt{1-x} \to \infty$ when $\hbar \to 0$. Taking the classical limit therefore requires the limiting behaviour of the hypergeometric functions $F(z) = {}_2F_1(i\nu_f, i\nu_i; 1; z)$ and its derivative $F'(z)$ for two large imaginary parameters $\pm i|\nu_{i,f}|$; the positive sign is for attractive and the negative sign for repulsive interactions.

In turn, the limit $x \to 0$ when $\hbar \to 0$ is the long-wavelength (soft photon) limit, implying vanishing recoil of the emitting particle pair. We point out that also $|z|$, the argument of F, F', becomes large and $z \to -\infty$ for

[3] An extensive physical reasoning why the correction factor involves the *ratio* of wave-functions at the origin, $|\chi^{(-)}_{\mathbf{p}_f}(0)|^2/|\chi^{(+)}_{\mathbf{p}_i}(0)|^2$, can be found in [13].

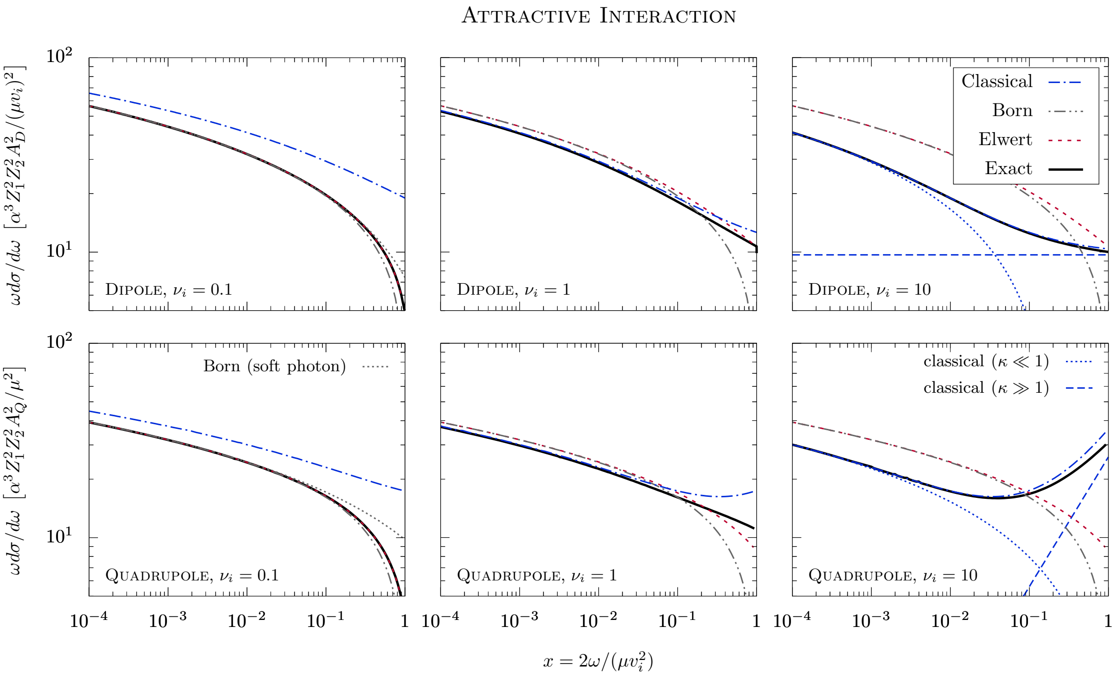

Figure 1. Differential cross section in ω for attractive interactions $Z_1 Z_2 < 0$ for dipole (top) and quadrupole (bottom) emission for three different values of $\nu_i = \{0.1, 1, 10\}$ (increasing from left to right). The exact result [Eq. (20) for dipole emission and angle-integrated Eq. (34) for quadrupole emission] is shown in solid black. The Born limits (41) and (42) are given by the dash double-dotted gray lines and the rigorous classical limit [Eq. (C10) for dipole and Eq. (C11) integrated over ϵ for quadrupole emission] is shown by the dash-dotted blue lines. The classical asymptotic expressions (52) and (53) are shown by the long-dashed blue thin lines and the classical soft photon limit (59) and (65) are given by the thin dotted blue lines in the right panels. In the left panels, the Born soft-photon limits (58) and (63) are shown by thin dotted gray lines. The Elwert approximation is shown in dashed red.

$x \to 0$. The asymptotic expansion of the hypergeometric functions hence depends on which of its arguments $|\nu_{i,f}|$ or $|z|$ grows quicker in magnitude. To this end, note that the product of x and ν_i is independent of $\hbar$,

$$\kappa \equiv \frac{|\nu_i| x}{2} = \frac{|Z_1 Z_2| \alpha \omega}{\mu v_i^3}, \tag{46}$$

so that the value of κ becomes the parameter delineating the possible asymptotic limits [17]. In the following, we will treat the case $\kappa \gg 1$ observing that it remains compatible with the quasi-classicality condition $x \ll 1$. For the attractive case, such limit in the hypergeometric functions can be calculated with the saddle-point method. A discussion of it can be found in Sommerfeld's book [15], which we also follow. A discussion of the case $\kappa \ll 1$ will be relegated to Sec. VI.

We start with attractive interactions, $Z_1 Z_2 < 0$, and note that for taking the limit $\nu_{i,f} \gg 1$, the contour integral representation of the hypergeometric functions can be used to rewrite $F(z)$ and $F'(z)$ in the form

$$F^{(\prime)}(z) = \frac{e^{-\pi\nu_i}}{2\pi i} \oint_{0^-}^{1^+} du\, \overset{(\sim)}{g}(u)\, e^{\nu_f f(u)}, \tag{47a}$$

$$f(u) = i \ln\left[\frac{u^y}{(1-u)^y (1-uz)}\right], \tag{47b}$$

with $g(u) = 1/u$ for F and $\tilde{g}(u) = i\nu_f/(1-uz)$ for F'. The contour in (47a) circles the singular points $u = 0$ and $u = 1$ in positive direction. The saddle points are situated at

$$u_0 = \frac{1-y}{2}\left(1 + i\cot\frac{\theta}{2}\right). \tag{48}$$

We can then expand around u_0, taking into account the second and third order in the expansion of $f(u)$ yielding for $\nu_i \gg 1$,

$$F(z) \approx -\frac{e^{-\pi\nu_i + \nu_f f(u_0)}}{2\pi i u_0 \nu_f^{1/3}}\left[\mathcal{I}_1 - \frac{\mathcal{I}_2}{u_0 \nu_f^{1/3}}\right], \tag{49a}$$

$$F'(z) \approx -\frac{\nu_f e^{-\pi\nu_i + \nu_f f(u_0)}}{2\pi(1-zu_0)\nu_f^{1/3}}\left[\mathcal{I}_1 + \frac{z\,\mathcal{I}_2}{(1-zu_0)\nu_f^{1/3}}\right], \tag{49b}$$

where the first integral is the leading order expansion in $\overset{(\sim)}{g}(u)$ around the saddle point and the second integral is

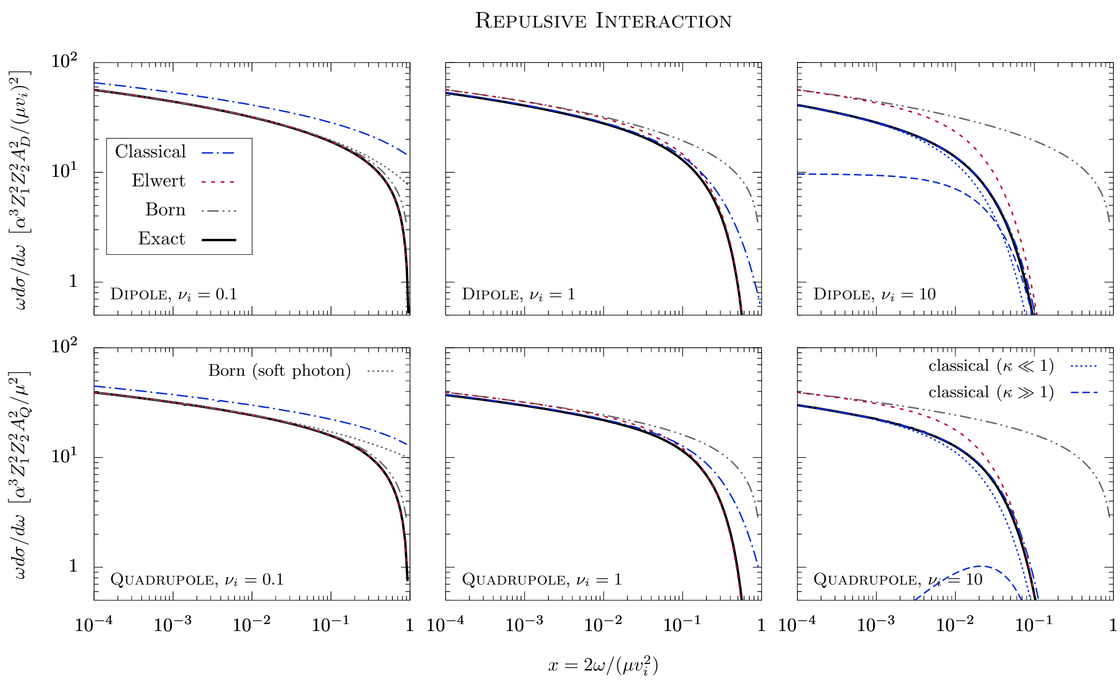

Figure 2. Same as Fig. 1 but for repulsive interactions.

the next to leading order expansion. The integrals can be identified as the integral representations of the modified Bessel functions

$$\mathcal{I}_1 = \int_{-\infty}^{\infty} dx e^{-ax^2+ibx^3} = \frac{2}{3\sqrt{3}}\frac{a}{b} e^{\frac{2}{27}\frac{a^3}{b^2}} K_{1/3}\left(\frac{2}{27}\frac{a^3}{b^2}\right), \quad (50)$$

$$\begin{aligned}\mathcal{I}_2 &= \int_{-\infty}^{\infty} dx x e^{-ax^2+ibx^3} \\ &= \frac{2i}{9\sqrt{3}}\frac{a^2}{b^2} e^{\frac{2}{27}\frac{a^3}{b^2}} \left[K_{1/3}\left(\frac{2}{27}\frac{a^3}{b^2}\right) - K_{2/3}\left(\frac{2}{27}\frac{a^3}{b^2}\right)\right],\end{aligned} \quad (51)$$

with $a = -\nu_f^{1/3} f''(u_0)/2$, $b = -i f'''(u_0)/6$. Plugging (49) into (20) implies evaluating $\mathcal{I}_1$ and $\mathcal{I}_2$ at $\theta = \pi$, which yields in agreement with [17]

$$\omega \frac{d\sigma_D}{d\omega}\bigg|_{\text{classical}} = \frac{16\pi}{3\sqrt{3}} \frac{\alpha^3 Z_1^2 Z_2^2 A_D^2}{\mu^2 v_i^2} \quad (Z_1 Z_2 < 0,\ \kappa \gg 1). \quad (52)$$

This expression is generally used in the definition of a Gaunt factor for dipole radiation, see Sec. VIII, and it is related to Kramers' original result [1] on the inverse process, namely, the classical rate for photon absorption. For repulsive interactions, $Z_1 Z_2 > 0$, Eq. (52) gets multiplied with an overall factor $\exp(-2\pi\kappa)$.

For quadrupole bremsstrahlung, we only possess closed solutions for the double differential cross section in ω and $\cos\theta$, *i.e.* (34) and (39). Therefore, we have to keep the θ-dependence in $\mathcal{I}_1$ and $\mathcal{I}_2$ and integrate to get the differential cross section in ω. For the solution in an attractive potential, it can be shown that for $\nu_i \to \infty$, the double differential cross section goes to zero for all values of θ except for $\theta = \pi$. A tedious calculation, which involves expanding $\mathcal{I}_1$ and $\mathcal{I}_2$ around $\theta = \pi$ up to fourth order and integrating the result over θ, yields for quadrupole radiation,

$$\omega \frac{d\sigma_Q}{d\omega}\bigg|_{\text{classical}} = \frac{32\pi^{3/2}}{3^{7/6}\Gamma(1/6)} \frac{\alpha^3 Z_1^2 Z_2^2 A_Q^2}{\mu^2} \left(\frac{\alpha |Z_1 Z_2| \omega}{\mu v_i^3}\right)^{2/3} \quad (Z_1 Z_2 < 0,\ \kappa \gg 1). \quad (53)$$

Again, the repulsive case, $Z_1 Z_2 > 0$, is obtained by multiplying the right hand side by $\exp(-2\pi\kappa)$. It is worth noting at this point, that the cross sections for scattering of identical and non-identical particles yield the same classical limit (53) as they should.[4]

Appendix C presents the classical calculations for energy loss. For dipole radiation, the result for $d\sigma/d\omega$ is integrable to Hankel functions for arbitrary κ . When an expansion is made for $\kappa \gg 1$ and the classical velocity is identified with v_i, Eq. (52) follows.[5] For the classi-

[4] $\Gamma(1/6) \approx 5.5663$ can be related to a complete elliptic integral of the first kind, but no simple relation to resolve $\Gamma(1/6)$ exists.

[5] The classical calculation does not resolve the difference between v_i and v_f so that the agreement is in that sense accidental [17].

cal treatise of quadrupole radiation, we are able to cast the result on $d\sigma/d\omega$ as an integral over Airy functions, as shown in App. C 3, which can be solved analytically and yields Eq. (53) to leading order for $\kappa \gg 1$ after the classical velocity is again identified with v_i. The asymptotic forms can be seen in the right panels of Figs. 1 and 2 where the thin dashed blue lines show the "hard photon" ($\kappa \gg 1$) expressions (52) and (53). In addition, the blue dash-dotted lines are the full classical results for general κ derived in App. C.

VI. SOFT-PHOTON LIMIT

In this section, we finally comment on the case of soft photon emission, *i.e.*, the limit $x \ll 1$. It is long known [23] that in the soft-photon limit the double-differential emission cross section can be written as the product of elastic scattering cross section $d\sigma/d\cos\theta|_{\mathbf{v}_i\to\mathbf{v}_f}$ and an overall factor $\mathcal{A}_I$ describing the emission (see *e.g.* [17]),

$$\omega \frac{d\sigma_I}{d\omega d\cos\theta}\bigg|_{\text{soft}} = \mathcal{A}_I \times \frac{d\sigma}{d\cos\theta}\bigg|_{\mathbf{v}_i\to\mathbf{v}_f}. \tag{54}$$

$\mathcal{A}_I$ is assembled from the soft emission factors $\propto e_n(p_n\cdot\epsilon^*)/(p_n\cdot q)$ that multiply the individual amplitudes where a photon with four-momentum $q = (\omega, \mathbf{q})$ and polarization vector ϵ^* is attached to an external leg with four-momentum p_n and charge e_n. For the polarization-summed squared matrix element this implies,

$$\mathcal{A}_I = -\frac{\omega^2}{(2\pi)^2}\sum_{m,n}\eta_m\eta_n\, e_m e_n \frac{p_m\cdot p_n}{(p_m\cdot q)(p_n\cdot q)}. \tag{55}$$

Here, the sum runs over all initial (final) states with $\eta = \pm 1$. The analytic structure of (55) is independent of the spin of the emitting particles [24] and underlies the theorem implying the cancellation of infrared divergences in quantum electrodynamics, and along analogous lines, with a modified version of (55), the cancellation of infrared divergences in the emission of soft gravitons [8].

In the dipole case, it is then straight-forward to show that in the non-relativistic expansion, $\mathcal{A}_D$ becomes the squared difference of initial and final state velocity,

$$\mathcal{A}_D(\omega,\cos\theta) = \frac{2\alpha A_D^2}{3\pi}|\mathbf{v}_i - \mathbf{v}_f|^2, \tag{56}$$

and which is to be multiplied by the Rutherford cross section

$$\frac{d\sigma}{d\cos\theta}\bigg|_{\mathbf{v}_i\to\mathbf{v}_f} = \frac{8\pi\alpha^2 Z_1^2 Z_2^2}{\mu^2}\frac{1}{|\mathbf{v}_i - \mathbf{v}_f|^4}. \tag{57}$$

It is important to note that (57) is *exact* in the Coulomb interaction of the scattering particles and also coincides with the Born result.

Integrating the product (56) with (57) over the scattering angle yields to leading order in x the Born cross section (41) after the latter is expanded in x as well[6],

$$\omega\, \frac{d\sigma_D}{d\omega}\bigg|^{\text{soft}}_{\text{Born}} = \frac{16}{3}\frac{\alpha^3 Z_1^2 Z_2^2 A_D^2}{\mu^2 v_i^2}\ln\left(\frac{2\mu v_i^2}{\omega}\right). \tag{58}$$

Since the result is a direct consequence of his soft-photon theorem [8] and *per se* an exact result in the limit $x\to 0$, Weinberg recently investigated the validity of (58) away from $|\nu_i| \ll 1$ and observed that when the scattering approaches the forward direction in (57), the requirement on the smallness of x becomes increasingly stringent for (58) to hold [7]. A formula was therefore suggested that splits the angular integration into two regimes, where in the forward direction, for $\theta < \theta_c$, a correction factor $\pi^2\nu_i^2/\sinh^2\pi\nu_i$ is applied to the product of (56) and (57). The factor was obtained from an asymptotic analysis, and although not explicitly stated in [7], it is just the product of Sommerfeld factors $S_i S_f$ as they appear in the exact formula (20) in the limit $x\to 0$. In this treatment, θ_c is a critical angle that can be determined from matching onto the classical limit ($|\nu_i| \gg 1$) for soft photon emission ($\kappa \ll 1$) [22],[7]

$$\omega\frac{d\sigma_D}{d\omega}\bigg|^{\text{soft}}_{\text{classical}} = \frac{16}{3}\frac{\alpha^3 Z_1^2 Z_2^2 A_D^2}{\mu^2 v_i^2}\ln\left(\frac{2\mu v_i^3\, e^{-\gamma}}{\alpha|Z_1 Z_2|\omega}\right), \tag{59}$$

where $\gamma \approx 0.5772$ is the Euler-Mascheroni constant. Such formulation has the benefit of providing an approximate formula for *soft* dipole bremsstrahlung for arbitrary ν_i. Note that (59) is also obtained by expanding the classical expression (C10) for small κ.

If we now turn to the case of quadrupole emission, the elastic Coulomb scattering cross section for identical particles of charge Z and mass m reads [17]

$$\frac{d\sigma}{d\cos\theta}\bigg|^{\text{ident.}}_{\mathbf{v}_i\to\mathbf{v}_f} = \frac{32\pi\alpha^2 Z^4}{m^2}\left[\frac{1}{|\mathbf{v}_i - \mathbf{v}_f|^4} + \frac{1}{|\mathbf{v}_i + \mathbf{v}_f|^4} - \frac{1}{|\mathbf{v}_i + \mathbf{v}_f|^2|\mathbf{v}_i - \mathbf{v}_f|^2}\cos\left(\nu_i\ln\frac{|\mathbf{v}_i - \mathbf{v}_f|^2}{|\mathbf{v}_i + \mathbf{v}_f|^2}\right)\right]. \tag{60}$$

[6] In fact, the full Born cross section could be obtained when we use $v_f = v_i\sqrt{1-x}$ and multiply the factorized differential cross section with v_f/v_i before integrating over the scattering angle; this factor usually appears as a phase space factor in the definition of the cross section but is unity for elastic scattering in the CM frame. The agreement is somewhat accidental and beyond the accuracy of the factorization. It has to do with the fact that for non-relativistic bremsstrahlung the emitted momentum $|\mathbf{q}| \le \mu v_i^2/2$ is negligible with respect to the typical exchanged momentum $|\mathbf{k}| \sim \mu v_i$.

[7] The θ_c dependence drops out in the Born limit, and using the asymptotic classical result for the matching such that θ_c becomes independent of ν_i makes the relation to the exact result approximate; in actual physical applications Debye screening needs to be accounted for when $\omega \lesssim \omega_p$ where ω_p is the plasma frequency.

Since the formula is exact in the Coulomb interaction of the scattering particles, it is natural to attempt to establish an analytical formula for soft photon emission that is valid for arbitrary ν_i by following Weinberg's treatment for dipole radiation [7]. For this, however, there are two obstacles to overcome: one is related to the complicated analytical structure of the cosine-term in (60) and another is related to the fact, that a naive application of the factorization (54) yields a prohibitive requirement on the smallness of x. The rest of this section will be concerned with showing how we can overcome these two obstacles, and we start with the latter. The final formula is presented in (64).

For quadrupole radiation, it turns out that although using (55) for the multiplying factor $\mathcal{A}_Q$ yields the correct asymptotic behavior for $x \to 0$, its range of applicability will be exceedingly small. A better result can be obtained by correcting for the fact that different momenta (by an amount $\pm q$) are exchanged in the individual diagrams that mediate the Coulomb interaction; in the Born limit, this is best seen from the diagrams of Fig. 5. Correcting each term in (55) for the actual exchanged momentum k_m in the emission from an external leg of momentum p_m by multiplying it with the factor $k^4_{\text{elastic}}/(k_m^2 k_n^2)$, where k_{elastic} denotes the exchanged momentum for $q \to 0$, yields

$$\begin{aligned}\mathcal{A}_Q^{\text{corr}} &= \frac{2\alpha A_Q^2}{15\pi}\left[4v_i^4 + 4v_f^4 - v_i^2 v_f^2\left(5 + 3\cos^2\theta\right)\right], \\ &= \frac{2\alpha v_i^4 A_Q^2}{15\pi}\left[3(1-\cos^2\theta) - 3x(1-\cos^2\theta) + 4x^2\right].\end{aligned} \tag{61}$$

The difference with respect to using (55) is in the quadratic term $4x^2$ which would otherwise have read x^2.

The importance of using (61) over an emission factor obtained from (55) is exemplified when considering the Born regime $|\nu_i| \ll 1$ for which one may take the cosine in the last term of (60) to unity. Integrating the product of (60) with (61) over the scattering angle one then obtains to leading order in x,

$$\omega \left.\frac{d\sigma_Q}{d\omega}\right|^{\text{soft}}_{\substack{\text{Born}\\ \text{ident.}}} = \frac{4}{15}\frac{\alpha^3 Z^4}{m^2}\left[17 + 12\ln\left(\frac{2\mu v_i^2}{\omega}\right)\right]. \tag{62}$$

This expression now not only agrees in the leading logarithmic term with the result that is obtained from the Born cross section (43) after an expansion in x has been performed, but also in the constant coefficient 17. For example, while for dipole radiation the Born cross sections (41) and (58) agree to better than one part in 10^3 for $x = 10^{-2}$, the cross section obtained from (55) for quadrupole radiation would deviate by 25% from (43) and the error would drop to 10^{-3} only at an unreasonable exponentially smaller value $x = 10^{-1000}$. Using instead (61) the agreement between (62) and (43) is as good as for dipole radiation. Similar conclusions hold for non-idential particles, and for completeness we record the

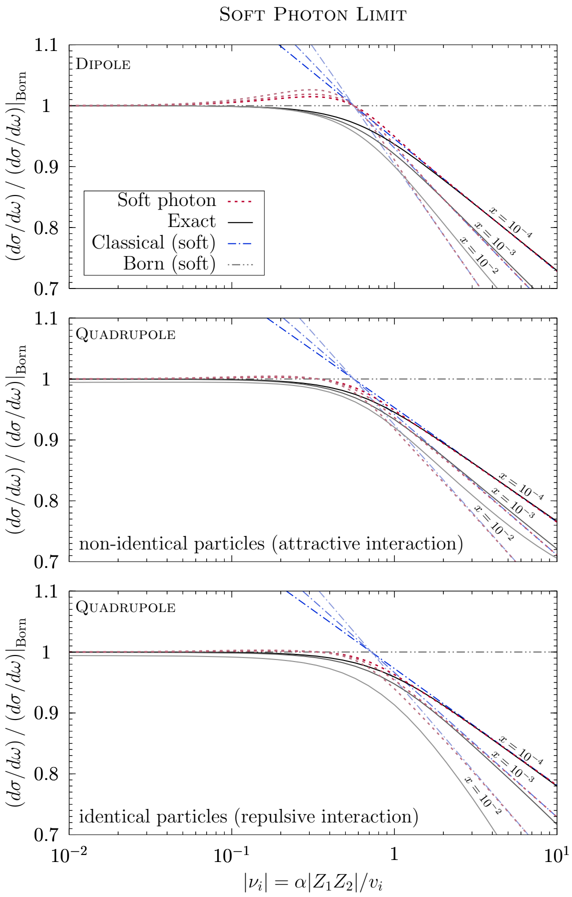

Figure 3. Differential cross section $\omega\, d\sigma/d\omega$ evaluated at $x = 10^{-4}, 10^{-3}, 10^{-2}$ (darker to lighter lines) as a function of ν_i for dipole emission (top) and quadrupole emission for attractive interactions (center) and for identical particles (bottom). The general soft photon cross sections, *i.e.*, (37) in [7] and (64) of this work, with θ_c matched to the soft classical limit, are shown by the dashed red lines. They are compared to the classical limits (59) and (65) for $\kappa \ll 1$ in dash-dotted blue, the Born limits (58), (63) and (62) in dash double-dotted gray and the exact results (20) and angle-integrated (34) and (39) in black.

soft-photon limit of the quadrupole emission cross section for non-identical particles which is obtained by integrating the Rutherford cross section (57) with (61) and which in leading order in x reads,

$$\omega \left.\frac{d\sigma_Q}{d\omega}\right|^{\text{soft}}_{\substack{\text{Born}\\ \text{non-id.}}} = \frac{16}{15}\frac{\alpha^3 Z_1^2 Z_2^2 A_Q^2}{\mu^2}\left[5 + 3\ln\left(\frac{2\mu v_i^2}{\omega}\right)\right]. \tag{63}$$

Equipped with the appropriate factors (60) and (61), an analysis like the one performed for dipole radiation by Weinberg in [7] and as mentioned above may now be performed for the quadrupole case. The remaining difficulty is that the cosine-term in (60) cannot be integrated analytically. In the limit $|\nu_i| \ll 1$ this term goes to unity while in the limit $|\nu_i| \gg 1$ it oscillates quickly so that the interference term vanishes in the integral over θ, and as one expects from the classical limit where the concept of identical particles is not present. We overcome the problem caused by the cosine-term by making the replacement $\cos(\dots) \to \xi = 1(0)$ in the interference term of (60) for identical (non-identical) particles. When we then split the θ-integral in the manner of Ref. [7], it turns out that the interference term for identical particles will still vanish in the classical limit as it should due to the introduced factor $S_i S_f|_{x\to 0} \to 0$ for $|\nu_i| \to \infty$; for non-identical particles it vanishes trivially because $\xi = 0$. Conversely, this prescription also retains the correct form in the Born limit, and hence yields an analytical formula for the soft cross section that has the correct asymptotic forms for $|\nu_i| \ll 1$ and $|\nu_i| \gg 1$ and becomes a reasonable approximation for intermediate values of ν_i,

$$\omega \frac{d\sigma_Q}{d\omega}\bigg|_{\text{soft}} = \frac{8}{15}\frac{\alpha^3 Z_1^2 Z_2^2 A_Q^2}{\mu^2}\left\{13 - \frac{6+3\xi}{\zeta^2+1} + 6\ln\left(\frac{2\mu v_i^2}{\omega\zeta}\right) + S_i S_f\big|_{x=0}\left[\frac{6+3\xi}{\zeta^2+1} - \frac{6+3\xi}{2} + 6\ln\zeta\right]\right\}, \tag{64}$$

with $\zeta \equiv \sqrt{(1+\cos\theta_c)/(1-\cos\theta_c)}$. In the Born limit, $|\nu_i| \ll 1$, we have $S_i S_f\big|_{x=0} \to 1$, the ζ dependence in (64) drops out, and we retrieve (62) or (63), respectively, depending on the value of ξ. In the classical limit, $|\nu_i| \gg 1$, we get $S_i S_f\big|_{x=0} \to 0$ and we can identify $\zeta = |\nu_i| e^{\gamma+1/2} \gg 1$ by matching onto the classical result for soft photon emission ($\kappa \ll 1$),

$$\omega \frac{d\sigma_Q}{d\omega}\bigg|_{\text{classical}}^{\text{soft}} = \frac{8}{15}\frac{\alpha^3 Z_1^2 Z_2^2 A_Q^2}{\mu^2}\left[10 + 6\ln\left(\frac{2\mu v_i^3\, e^{-\gamma}}{\alpha|Z_1 Z_2|\omega}\right)\right], \tag{65}$$

which we obtain by expanding the classical expression (C11) for small κ. Note that in the classical limit the ξ dependence in (64) becomes negligible as it should. The above equations are valid for attractive and repulsive interactions since the factor $\exp(-2\pi\kappa)$ that gets usually multiplied to the classical cross sections going from $Z_1 Z_2 > 0$ to $Z_1 Z_2 < 0$ goes to unity in the soft photon limit $\kappa \ll 1$. Finally we note that one can in fact improve on (64) to extend the validity to larger values of x. A formula for this is presented in App. D.

The behavior of (64) between the Born and classical limits—with ζ fixed as outlined above—is shown in the middle and bottom panel of Fig. 3 for three values of x. As can be seen, the soft cross section (64) is a good approximation up to values of $x = 10^{-2}$ in the Born limit, while in the classical limit there are clearly visible deviations from the exact result due to the stricter condition $\kappa \ll 1$ for the classical result that is used in the matching. For comparison, the result of Ref. [7] for dipole radiation with fixed ζ is shown in the top panel of Fig. 3. The soft limits are also shown by the thin dotted gray (blue) lines in the left (right) panels of Figs. 1 and 2 for the Born (classical) limit.

VII. EFFECTIVE ENERGY LOSS

Since the exact expressions for multipole radiation obtained in Sections III and IV are rather complicated and sometimes numerically challenging to evaluate, it is of interest to show how the exact solutions behave in between the Born and the classical regimes. We investigate this by comparing the effective energy loss or "effective retardation", *i.e.*, the energy-weighted integral over the emission cross section $d\sigma/d\omega$ up to the kinematic endpoint,

$$\varepsilon^*\sigma_I(v_i) = \int_0^{\frac{\mu v_i^2}{2}} d\omega\, \omega \frac{d\sigma_I}{d\omega}\,, \tag{66}$$

and which is a quantity of general interest.[8]

In the Born limit, the effective energy loss including dipole and quadrupole radiation for non-identical particles is obtained by integrating (41) and (42),

$$\varepsilon^*\sigma(v_i)\big|_{\substack{\text{Born}\\ \text{non-id.}}} = \frac{\alpha^3 Z_1^2 Z_2^2}{\mu}\left[\frac{16}{3}A_D^2 + \frac{40}{9}A_Q^2\, v_i^2\right]. \tag{67}$$

The result is valid for both, attractive and repulsive interactions as the Born limit does not distinguish these cases. For identical particles only quadrupole radiation exists, $A_D = 0$, $A_Q = 1/2$. Writing $Z_{1,2} = Z$, $m_{1,2} = m$, and $\mu = m/2$ one obtains from integrating (43),

$$\varepsilon^*\sigma_Q(v_i)\big|_{\substack{\text{Born}\\ \text{ident.}}} = \frac{\alpha^3 Z^4}{m}\frac{5}{36}(44 - 3\pi^2)v_i^2\,. \tag{68}$$

[8] For example, the luminosity in a non-relativistic Maxwellian gas of such colliding particles with number densities $n_{1,2}$ and common temperature T can be computed from the CM frame expression through [25] $l_I = \frac{n_1 n_2}{(1+\delta_{12})}\sqrt{\frac{2}{\pi}}\left(\frac{\mu}{T}\right)^{3/2}\int dv_i v_i^3 e^{-\mu v_i^2/2T}\varepsilon^*\sigma_I(v_i)$. Another example is the energy loss of electrons in the passage of a gas of heavy ions, for which $-dE/dx \simeq n_I \varepsilon^*\sigma(v_i)$ where n_I is the number density of scattering centers.

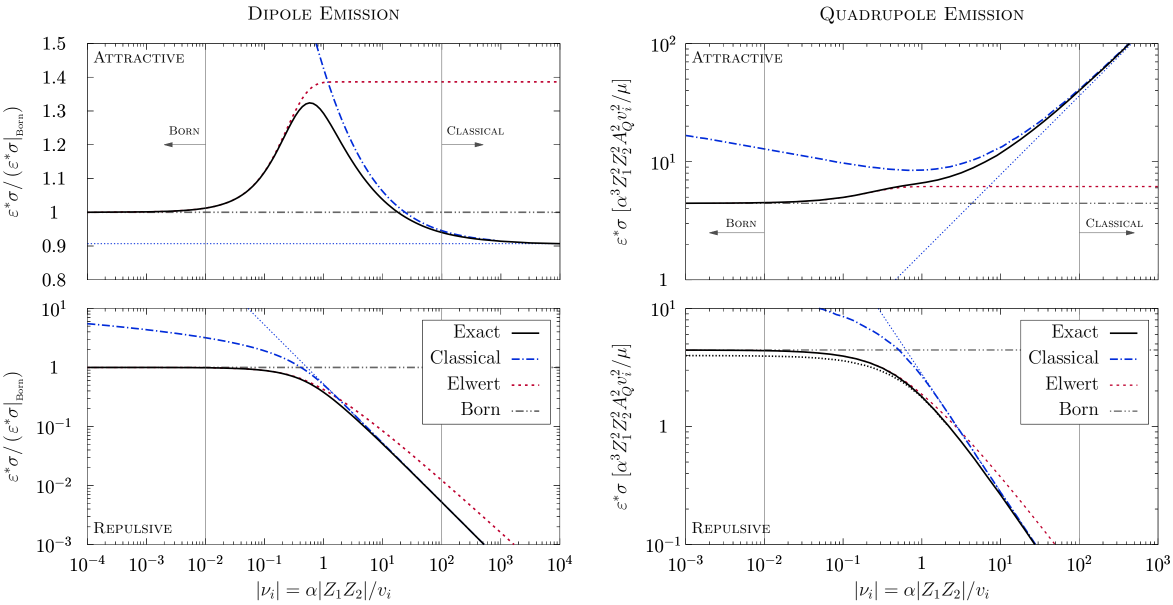

Figure 4. *Left panel:* Effective energy loss from dipole emission, normalized to the Born result [first term of Eq. (67) (dash double-dotted gray line)] as a function of ν_i for an attractive (top) and a repulsive (bottom) interaction. The full non-relativistic quantum mechanical result from Eq. (20) is shown in solid black. The rigorous classical limit from Eq. (C10) containing the Hankel functions is shown in dash-dotted blue, while the asymptotic expressions, *i.e.* the dipole terms in Eqs. (69) and (70), are shown by the thin dotted blue line. The Elwert approximation is shown in dashed red. *Right panel:* Effective energy loss from quadrupole emission as a function of ν_i for an attractive (top) and a repulsive (bottom) interaction. The exact result for non-identical particles from Eq. (34) is shown in solid black. The rigorous classical limit from Eq. (C11) containing the Hankel functions is shown in dash-dotted blue, while the asymptotic expressions, *i.e.* the quadrupole terms in Eqs. (69) and (70), are shown by the thin dotted blue line. The Elwert approximation is shown in dashed red. For comparison, the effective energy loss for identical particles is shown in dotted black for the exact calculation obtained from Eq. (39).

As expected, in the Born limit quadrupole emission is suppressed by a factor v_i^2 with respect to dipole emission.

Turning now to the classical expressions, from (52) and (53) the effective energy loss for attractive interactions in the classical limit up to quadrupole order reads,

$$\varepsilon^*\sigma(v_i)\big|_{\substack{\text{asympt.}\\ \text{classical}}} = \frac{\alpha^3 Z_1^2 Z_2^2}{\mu}\left[\frac{8\pi}{3\sqrt{3}}A_D^2 + \frac{8\pi^{3/2}2^{1/3}}{3^{1/6}5\Gamma(1/6)} \times |\alpha Z_1 Z_2|^{2/3} A_Q^2\, v_i^{4/3}\right] \quad (Z_1Z_2 < 0). \tag{69}$$

For repulsive interactions, the energy loss receives equally important contributions from the kinematic regimes $\kappa \gg 1$ and from $\kappa \ll 1$. Hence, using only the $\kappa \gg 1$ limit in Sec. V B would underestimate the result. However, the effective energy loss can be calculated directly from the classical theory using Eq. (C1) and rewriting the time integral to a line integral along the particles' relative distance from infinity to the distance of closest approach and back to infinity (see *e.g.* [22]). One then arrives at

$$\varepsilon^*\sigma(v_i)\big|_{\substack{\text{asympt.}\\ \text{classical}}} = \frac{8\pi}{9}\frac{\alpha^2 Z_1 Z_2}{\mu}\left[A_D^2 v_i + A_Q^2\, v_i^3\right] \quad (Z_1Z_2 > 0)\,. \tag{70}$$

Note that in the attractive case, the dipole term is of the same order in v_i in the Born and in the classical limit while the quadrupole term is only suppressed by a factor $v_i^{4/3}$ w.r.t. the dipole term in the classical limit as opposed to a factor v_i^2 in the Born limit. In the repulsive case, the quadrupole term is suppressed by a factor v_i^2 w.r.t. the dipole term but the classical effective energy loss shows an overall suppression of $v_i/(\alpha Z_1 Z_2)$ w.r.t. the Born limit; hence the single powers of $Z_{1,2}$ in (70).

We point out again that while the Born approximation distinguishes between identical and non-identical particles, this concept is not present in the classical calculation. On the other hand, the classical approximation distinguishes between attractive and repulsive potentials while—as is well known—the Born approximation does not. The exact calculation presented in Sec. IV captures all of these aspects and interpolates smoothly between the Born and classical limit.

In Fig. 4 we show the full effective energy loss calculation as obtained from Eqs. (34) and (39) and compare it with the expressions listed above. In addition, we also investigate here the energy loss based on the Elwert prescription (44). As can be seen, $\varepsilon^*\sigma(v_i)\big|_{\rm Born}$ is numerically within a few percent of the effective energy loss calculated from the exact cross sections for $|\nu_i| \lesssim 10^{-2}$. The Elwert prescription extends the range of validity of $\varepsilon^*\sigma(v_i)\big|_{\rm Born}$ to $|\nu_i| \lesssim 0.5$. The reason is that the ratio of Sommerfeld factors, which get multiplied onto the Born cross section account for the larger (smaller) probability of finding the colliding particles at same position due to the attractive (repulsive) Coulomb interaction and therefore increases (decreases) the cross section accordingly, as detailed in Sec. V A. For $|\nu_i| \gtrsim 10$ the exact energy loss is well described by the classical approximation derived in App. C in terms of Hankel functions (shown as blue dash-dotted lines), whose leading order terms in the expansion $|\nu_i| \gg 1$, Eqs. (69) and (70), are shown as blue dotted lines. For attractive interactions, the classical approximation asymptotes to Eq. (69) for $|\nu_i| \gtrsim 10^3$ while for repulsive interactions, it already reaches its asymptotic form of Eq. (70) at $|\nu_i| \gtrsim 1$.

While the energy loss in dipole emission for $Z_1Z_2 < 0$ only deviates from the Born approximation by a maximum $\sim 30\%$ at a given ν_i, the energy loss in quadrupole emission can deviate from the Born approximation by several orders of magnitude since the classical and Born limit show different scalings with velocity. Note, however, that even though quadrupole radiation in an attractive potential gets enhanced with respect to the Born approximation for large ν_i while dipole radiation does not, the former can never become larger than the latter since it is additionally suppressed by v_i^2 as can be seen in Eq. (69). To this end, note that the units on the y-axes on the right panel of Fig. 4 carry an additional v_i^2 factor, and the energy loss for attractive interactions in the quadrupole case does not grow without bounds as $\nu_i \to \infty$, but rather vanishes instead.

VIII. ELECTRON-ELECTRON GAUNT FACTOR

The net rate of photon absorption in free-free transitions and its inverse process, bremsstrahlung, is of ample importance in the understanding of opacity and emissivity of astrophysical environments. In the scattering of electrons on ions of charge Z (dipole case) it has become traditional to express the exact rates as a product of the classical electrodynamics result by Kramers [1] and a "free-free Gaunt factor" $g_{\rm ff}$. In terms of the bremsstrahlung cross section, with (52) specialized to $Z_1 = Z$ $Z_2 = -1$, $\mu \simeq m_e$,

$$\frac{d\sigma_D}{d\omega} = \frac{16\pi}{3\sqrt{3}}\frac{\alpha^3 Z^2}{m_e^2 v_i^2} \times g_{\rm ff}(\omega, v_i). \tag{71}$$

Because of the numerical demanding nature of evaluating hypergeometric functions, Gaunt factors are being tabulated. The classic compilation is [26] with literature that continues into the most recent past [27, 28]; for soft-photon emission an improved Gaunt factor was recently proposed in [7] as discussed in Sec. VI.

Having gathered insight into the exact non-relativistic bremsstrahlung cross section in all kinematic regimes, we are now in a position to make an informed proposal for a Gaunt factor for electron-electron bremsstrahlung, $g_{ee}(\omega, v)$. Given the complexity of the result, there are down-sides with any simple definition. For example, staying with historical convention and defining the Gaunt factor through the classical result, one notes that for quadrupole emission in a repulsive potential there are important contributions—as exemplified in the study of effective energy loss in the previous section—from both, "soft" and "hard" photons, defined through $\kappa \ll 1$ and $\kappa \gg 1$ with κ of Eq. (46), respectively. One could then define the Gaunt factor as the multiplicative factor that brings the *sum* of classical hard and soft cross sections for quadrupole radiation (53) and (65) into agreement with the full result. However, this has the unpalatable property that there is no easy analytical limiting expression for g_{ee}.

The kinematic region of largest practical interest is the Born regime. The reason is that for $Z = 1$ Coulomb corrections remain comparably smaller than for electron-ion interactions. For example, considering the case of a hot galaxy cluster gas with a ballpark temperature of $T \simeq 10\,\rm keV$ and a typical electron velocity of $v \sim \sqrt{2T/m_e} \simeq 0.2$ implies $|\nu_i| \simeq 0.04$, well in the validity regime of the Born cross section. In addition, as we have observed above, the Elwert prescription extends the validity to larger $|\nu_i|$, and we propose a definition of the Gaunt factor that is based on the latter,

$$\frac{d\sigma_Q}{d\omega} = \frac{\nu_f}{\nu_i}\frac{1-e^{-2\pi\nu_i}}{1-e^{-2\pi\nu_f}}\left.\frac{d\sigma_Q}{d\omega}\right|_{\substack{\rm Born\\ \rm ident.}} \times g_{ee}(\omega, v), \tag{72}$$

where $d\sigma_Q/d\omega\big|_{\substack{\rm Born\\ \rm ident.}}$ is given through (43). The Elwert factor is important to capture the spectrum for hard photons, and for $|\nu_i| \gtrsim 0.1$ it is required to yield the appropriate suppression in the effective energy loss. In the Born regime, for $|\nu_i| \ll 1$, it then follows that $g_{ee} \to 1$ and $g_{ee} < 1$ otherwise; deviations from unity are most important for $|\nu_i| \gtrsim 1$. Lastly, we note that a tabulation of g_{ee} together with its thermally averaged version over a large kinematic regime remains a challenging task as it requires a precise evaluation and integration of F and F' for large parameters and argument. This will be presented elsewhere [29].[9]

[9] A previous compilation exists [30], where a quadrupole Gaunt factor was defined as a multiplicative factor of the dipole cross section. In lieu of a full result, the tabulation could only be based on the Elwert prescription and results are hence not accurate for $\nu_i \gg 1$. A thermally averaged version of the Born cross section (43) for a Maxwellian gas has been given in [12].

IX. CONCLUSIONS

In this work we present the full quantum mechanical treatment for the quadrupolar single-photon emission which is exact in the low energy scattering of two electrically charged spin-1/2 particles. The double differential cross sections in the center-of-mass scattering angle θ and photon energy ω is presented in Eq. (34) for non-identical and in Eq. (39) for identical particles. The latter formula applies to the important case of the scattering of a pair of electrons for which quadrupole radiation is the leading energy loss process.

For dipole radiation, the result can be cast into the rather short form (20) by making use of the differential equation for the hypergeometric function. This is not possible anymore for the quadrupole case. The analytic structure of the result is considerably more complex. Its building blocks are the elements of a tensor of Coulomb transition matrix elements, Eq. (22), and we are able to obtain the elements in closed form by making use of an integral formula for confluent hypergeometric functions that was established by Nordsieck, see (27) and (14).

The results apply to all non-relativistic kinematic regimes and yield the correct Born and quasi-classical limits for $|\nu_i| \ll 1$ and $|\nu_i| \gg 1$, respectively. We show how these limits are derived from the full expressions and compare them to the Born-level and classical treatments, that we present in additional calculations. Making contact in these asymptotic regimes, gives credence to the correctness of our results.

We then study the kinematic regime of soft photon emission where the emitted photon energy is much smaller than the available center-of-mass energy. Here one may tap into the soft-photon theorems that imply the factorization of the cross section into the elastic cross section, multiplied by an emission piece. Weinberg recently showed how a formula for soft photon emission may be constructed for arbitrary ν_i for the case of dipole radiation. With some modifications, we are able to carry these ideas over to the case of quadrupole emission, and Eq. (64) gives the soft photon cross section that applies in both, the Born and the classical regime. Taking this approach further, we also show how an approximate formula valid for arbitrary ν_i and accross the kinematic range of x can be constructed for repulsive potentials in (D1).

Equipped with all this knowledge on the quadrupole bremsstrahlung process, in a final section we then propose an adequate form for a Gaunt factor for electron-electron scattering which is based on practical demand. A numerical tabulation over a large kinematic regime will be presented in an upcoming work [29]. The emission of photons in the Coulomb collision of unpolarized free particles is perhaps *the* fundamental process in the interaction of light with matter. This work closes a seeming gap in the literature, by laying out the exact theory for quadrupole radiation in the non-relativistic limit and by studying its consequences in all relevant kinematic regimes.

Acknowledgements: The authors are supported by the New Frontiers program of the Austrian Academy of Sciences. LS is supported by the Austrian Science Fund FWF under the Doctoral Program W1252-N27 Particles and Interactions. We acknowledge the use of computer packages for algebraic calculations [31, 32].

Note added: In the final stages of preparing this paper, we became aware of Refs. [33] and [34] which calculated the elements of the quadrupole tensor in a Coulomb field for gravitational and electromagnetic bremsstrahlung, respectively. The results appear to have gone unnoticed in the Western literature, see *e.g.* [13] claiming the absence of such calculation (p. 236). We disagree—by individually different amounts—with all real coefficients of F and two of the three imaginary coefficients of F' listed in Eq. (17) of [34]. We have also studied the cross section that can be deduced from Eq. (17) of [34] numerically and find that it generally yields wrong results and asymptotes to the correct Born and classical limits only in a limited region of parameter space. The authors start from a different ansatz—Eqs. (1) and (2) in [33]—to establish the elements of the quadrupole tensor from the Nordsieck integral. Using their starting point, we recover our coefficients (29) for the quadrupole tensor. From this we must conclude that the result of [34] contains errors; English and Russian version of [34] are consistent in their critical equation. Despite those discrepancies, we agree in the deduced asymptotic expression for the classic limit for $\kappa \gg 1$, Eq. (53) in this work. In either case, our work presents the problem of non-relativistic quadrupole emission for all relevant kinematic regimes in a self-complete manner and goes well beyond the brief expositions of those previous works.

Appendix A: Interference term in the full result

The interference term $|I^{\alpha\beta}|^2$ in (38) is composed as $|I^{\alpha\beta}|^2 = Q_1^{*\alpha\beta} Q_2^{\gamma\delta} + Q_2^{*\alpha\beta} Q_1^{\gamma\delta}$ where $\alpha\beta = \gamma\delta = ab$ or $\alpha\beta = aa$ and $\gamma\delta = bb$, respectively. We find

$$\begin{aligned}\frac{1}{2}|I^{\alpha\beta}|^2 = G_0 \Big\{ & A^+_{\hat\alpha\hat\beta} \operatorname{Re}\left[F^*(z)F(\tilde z)\right] + A^-_{\hat\alpha\hat\beta} \operatorname{Im}\left[F^*(z)F(\tilde z)\right] \\ & + B^+_{\hat\alpha\hat\beta} \operatorname{Re}\left[F'^*(z)F'(\tilde z)\right] + B^-_{\hat\alpha\hat\beta} \operatorname{Im}\left[F'^*(z)F'(\tilde z)\right] \\ & + C^+_{\hat\alpha\hat\beta} \operatorname{Re}\left[F^*(z)F'(\tilde z)\right] + C^-_{\hat\alpha\hat\beta} \operatorname{Im}\left[F^*(z)F'(\tilde z)\right] \\ & + D^+_{\hat\alpha\hat\beta} \operatorname{Re}\left[F'^*(z)F(\tilde z)\right] + D^-_{\hat\alpha\hat\beta} \operatorname{Im}\left[F'^*(z)F(\tilde z)\right] \Big\}\end{aligned} \tag{A1}$$

where G_0 is given by Eq. (31). For $|Q^{aa}|^2$ the coefficients read

$$\begin{aligned} A^+_{\hat a\hat a} &= \frac{4(y+1)^2}{(1-z)(1-\tilde z)}\,, \qquad B^+_{\hat a\hat a} = \frac{9y^2}{\nu_i^2}\,, \\ C^-_{\hat a\hat a} &= \frac{6y(y+1)}{\nu_i(z-1)}\,, \qquad D^-_{\hat a\hat a} = -\frac{6y(y+1)}{\nu_i(\tilde z-1)}\,, \end{aligned} \tag{A2}$$

with $A^-_{\hat a\hat a} = B^-_{\hat a\hat a} = C^+_{\hat a\hat a} = D^+_{\hat a\hat a} = 0$. For $|Q^{ab}|^2$ one gets the lengthy expressions

$$A^+_{\hat a\hat b}=\frac{4\left(y^8+1\right)-2y^2\left(y^4+1\right)\left(1+7\cos^2\theta\right)+4y^4\left(1+2\cos^4\theta+3\cos^2\theta\right)}{(1-y)^6(1-z)^2(1-\tilde z)^2}+\frac{2\left(1-\cos^2\theta\right)\left[y^4+2y^2\left(2\cos^2\theta-3\right)+1\right]}{(1-y)^4(1-z)^2(1-\tilde z)^2}\nu_i^2,$$

$$A^-_{\hat a\hat b}=-\frac{4\nu_i(y+1)^3\cos\theta}{(y-1)^2(1-z)^2(1-\tilde z)^2},\quad B^+_{\hat a\hat b}=\frac{y^2\left[3y^2-2y\left(2+\cos^2\theta\right)+3\right]}{(1-y)^2\nu_i^2}-\frac{8y^3\left(1-\cos^2\theta\right)^2}{(1-y)^4(1-z)(1-\tilde z)},\quad B^-_{\hat a\hat b}=\frac{4y^3(1+y)\cos\theta\left(1-\cos^2\theta\right)}{(1-y)^4(1-z)(1-\tilde z)\nu_i},$$

$$C^+_{\hat a\hat b}=\frac{y(1+\cos\theta)\left[y^4-6y^2+8y^2\cos^3\theta-4\left(y^3+y^2+y\right)\cos^2\theta+4\left(-y^4+y^3+2y^2+y-1\right)\cos\theta+1\right]}{(1-y)^4(1-z)^2(1-\tilde z)},$$

$$C^-_{\hat a\hat b}=\frac{2y\left[(1-y)y\left(2y^3+y+2\right)-2\right]-2y(y+1)\left[y\left((y-3)^2y-6\right)+1\right]\cos\theta+2y^2(y+1)[y(2y-3)+2]\cos^2\theta-2y^3(y+1)\cos^3\theta}{(1-y)^4(1-z)^2\nu_i}$$
$$+\frac{2y(y+1)(\cos\theta-1)(1+\cos\theta)^2\left[y\left(y-4+2\cos\theta\right)+1\right]}{(1-y)^4(1-z)^2(1-\tilde z)}\nu_i,$$

$$D^+_{\hat a\hat b}=\frac{y\left(1-6y^2+y^4\right)+y\left[(y-2)y\left(y(3y+2)+2\right)+3\right]\cos\theta-4\left(y^5-y^3+y\right)\cos^2\theta+4y^2[(y-1)y+1]\cos^3\theta+8y^3\cos^4\theta}{(1-y)^4(1-z)(1-\tilde z)^2},$$

$$D^-_{\hat a\hat b}=-\frac{2y(y+1)\left\{(y^4+1)(\cos\theta-2)+2y(y^2+1)(\cos\theta-2)(\cos\theta-1)+y^2\left[\cos\theta\left(9+(\cos\theta-3)\cos\theta\right)-5\right]\right\}}{(1-y)^4(1-\tilde z)^2\nu_i}$$
$$+\frac{2y(y+1)(\cos\theta-1)^2(1+\cos\theta)\left[y^2-2y(2+\cos\theta)+1\right]}{(1-y)^4(1-z)(1-\tilde z)^2}\nu_i. \tag{A3}$$

Note that for identical particles $Z_1Z_2 = Z^2 > 0$ and therefore in the coefficients in this section ν_i is always negative, as can be seen from Eq. (7).

Appendix B: Born approximation

In the following, we present the non-relativistic squared matrix elements in the Born approximation. For simplicity, we specialize to $m_1 = m_2$ and $|Z_{1,2}| = 1$. The matrix elements can be obtained from a quantum field theory calculation, based on the QED Lagrangian, of the Feynman diagrams shown in Fig. 5. The matrix elements are hence given in relativistic normalization $\langle \mathbf{p}|\mathbf{p}'\rangle = (2\pi)^3 2E_{\mathbf{p}}\delta^3(\mathbf{p}-\mathbf{p}')$ and are summed over photon polarizations, averaged over initial and summed over final spins, and averaged over the direction of the emitted photon. We stick to the notation of the main segment and use the variables $\mathbf{k} = \mathbf{p}_2 - \mathbf{p}_4$, $\mathbf{l} = \mathbf{p}_4 - \mathbf{p}_1$ and their directions $\hat{\mathbf{k}} = \mathbf{k}/|\mathbf{k}|$, $\hat{\mathbf{l}} = \mathbf{l}/|\mathbf{l}|$.

The scattering of $e^+e^- \to e^+e^-\gamma$ is dominated by dipole emission and only the unprimed diagrams on the left side of Fig. 5 contribute. To leading order in relative velocity of the colliding pair the squared matrix element reads

$$\left\langle \sum_\lambda |\mathcal{M}_D^{\text{rel.}}|^2\right\rangle_{\hat{\mathbf{q}}} = \frac{128}{3}\frac{(4\pi\alpha)^3}{\omega^4}|\boldsymbol{l}|^2(\hat{\mathbf{k}}\cdot\hat{\mathbf{l}})^2\,. \tag{B1}$$

In turn, for the scattering of $e^\pm e^\pm \to e^\pm e^\pm\gamma$ also the exchange diagrams on the right side of Fig. 5 contribute. In agreement with the original calculation [9] we obtain

$$\left\langle \sum_\lambda |\mathcal{M}_Q^{\text{rel.}}|^2\right\rangle_{\hat{\mathbf{q}}} = \frac{32}{15}\frac{(4\pi\alpha)^3}{\omega^2}|\boldsymbol{k}|^2|\boldsymbol{l}|^2 \times\left(\frac{3+13(\hat{\mathbf{k}}\cdot\hat{\mathbf{l}})^2}{|\boldsymbol{k}|^4}+\frac{3+13(\hat{\mathbf{k}}\cdot\hat{\mathbf{l}})^2}{|\boldsymbol{l}|^4}-\frac{3+7(\hat{\mathbf{k}}\cdot\hat{\mathbf{l}})^2+6(\hat{\mathbf{k}}\cdot\hat{\mathbf{l}})^4}{|\boldsymbol{k}|^2|\boldsymbol{l}|^2}\right). \tag{B2}$$

To obtain the matrix elements (B1) and (B2) we have used a velocity expansion in the relative velocity v_i where $|\mathbf{k}|/\mu$ and $|\mathbf{l}|/\mu$ scale as $\mathcal{O}(v_i)$ and $(\mathbf{k}\cdot\mathbf{l})/\mu^2$ and ω/μ as $\mathcal{O}(v_i^2)$.

The cross sections in Sec. V A can then be obtained from (B1) and (B2) by putting the corresponding matrix elements into Eq. (11) after converting them to non-relativistic normalization, *i.e.*

$$|\mathcal{M}_I|^2 = 2\omega(2m_1)^2(2m_2)^2|\mathcal{M}_I^{\text{rel.}}|^2\,, \tag{B3}$$

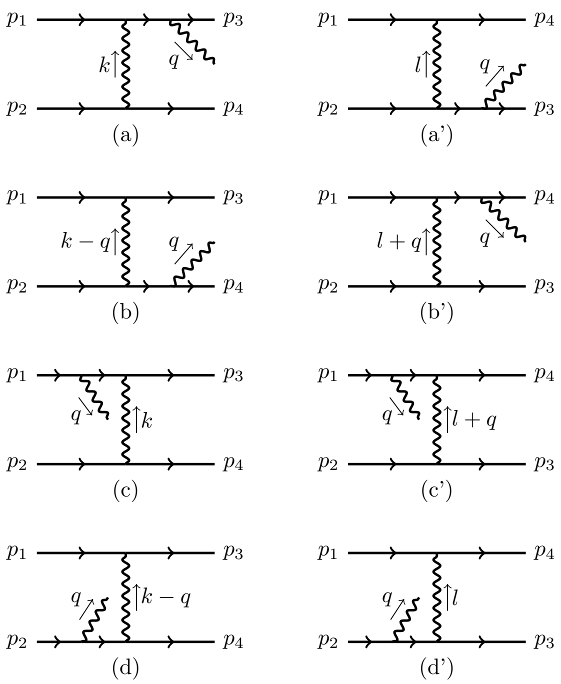

Figure 5. Eight tree level diagrams contributing to e^-e^--bremsstrahlung in the Born limit. Fermion momentum flows from left to right and the direction of the photon momentum is represented by the arrow next to the photon line. For e^+e^--bremsstrahlung only the non-primed diagrams have to be considered and the fermion flow is reversed for positrons.

and setting $|\mathbf{k}|/\mu = |\mathbf{v}_i - \mathbf{v}_f|$, $|\mathbf{l}|/\mu = |\mathbf{v}_i + \mathbf{v}_f|$ and $(\mathbf{k}\cdot\mathbf{l})/\mu^2 = v_i^2 - v_f^2$.

Appendix C: Classical Energy Loss

The effective energy loss $\varepsilon^*\sigma$ can be calculated semi-classically by integrating the intensity of the radiation over the impact parameter ρ and the interaction time t as (see e.g. [22])

$$\varepsilon^*\sigma_I = \int_0^\infty d\rho\, 2\pi\rho \int_{-\infty}^{\infty} dt\, I_I\,. \tag{C1}$$

The intensity I of the dipole or quadrupole radiation respectively is given by

$$I_D = \frac{1}{6\pi} A_D^2 |\ddot{\boldsymbol{d}}(t)|^2, \tag{C2}$$

$$I_Q = \frac{1}{720\pi} A_Q^2 |\dddot{q}^{ab}(t)|^2\,, \tag{C3}$$

with

$$\boldsymbol{d}(t) = e\, \boldsymbol{r}(t), \tag{C4}$$

$$q^{ab}(t) = e\left[3\, r^a(t) r^b(t) - r^2(t)\delta^{ab}\right]. \tag{C5}$$

where $\mathbf{r}(t)$ is the particles' distance and $v = |\dot{\mathbf{r}}|$ will be the magnitude of the relative velocity to be used below. The time integral in Eq. (C1) can be replaced by an integral over the emitted energy ω of the Fourier modes of $\boldsymbol{d}$ and q^{ab}, i.e.

$$\varepsilon^*\sigma = \frac{1}{4\pi}\int d\rho\,\rho \int d\omega \times \left[\frac{2\omega^4}{3} A_D^2 |\tilde{\mathbf{d}}(\omega)|^2 + \frac{\omega^6}{180} A_Q^2 |\tilde{q}^{ab}(\omega)|^2\right]. \tag{C6}$$

with $\ddot{\boldsymbol{d}}(t) = 1/(2\pi)\int_{-\infty}^{\infty} d\omega\, \tilde{\mathbf{d}}(\omega)\, e^{-i\omega t}$ and $\dddot{q}^{ab}(t) = 1/(2\pi)\int_{-\infty}^{\infty} d\omega\, \tilde{q}^{ab}(\omega)\, e^{-i\omega t}$, where we denote Fourier-transformed quantities with a tilde. The particles' distance vector $\boldsymbol{r}(t)$ can be parametrized in a plane spanned by the orthonormal vectors $\hat{\mathbf{e}}_1$ and $\hat{\mathbf{e}}_2$ [22]

$$\mathbf{r}_1 = \frac{\alpha|Z_1Z_2|}{\mu v^2}(\epsilon \pm \cosh\xi)\,\hat{\mathbf{e}}_1, \tag{C7a}$$

$$\mathbf{r}_2 = \frac{\alpha|Z_1Z_2|}{\mu v^2}\sqrt{\epsilon^2-1}\,\sinh\xi\,\hat{\mathbf{e}}_2, \tag{C7b}$$

$$t = \frac{\alpha|Z_1Z_2|}{\mu v^3}(\epsilon\sinh\xi \pm \xi)\,. \tag{C7c}$$

Here, $+(-)$ is to be used for repulsive (attractive) interactions; $r_n = |\mathbf{r}_n|$ is parameterized by the eccentricity ϵ and ξ. For unbound orbits, the eccentricity relates to the impact parameter as $\epsilon^2 = 1 + \mu^2\rho^2 v^4/(\alpha Z_1 Z_2)^2$ and we can rewrite the integral over ρ with $0 < \rho < \infty$ into an integral over ϵ with $1 < \epsilon < \infty$, as we will do in the following.

1. Dipole Emission

For dipole emission in an attractive potential, the differential cross section with respect to the emitted energy is found from the first term in (C6) by omitting the integration over $d\omega$, using the definition (66), and identifying v with v_i [22]

$$\omega\frac{d\sigma_D}{d\omega}\bigg|_{\text{classical}} = \frac{4\alpha^3 Z_1^2 Z_2^2 \omega^4 A_D^2}{3\mu^2 v_i^4}\int_1^\infty d\epsilon\,\epsilon \times \left(|\tilde{r}_1(\omega)|^2 + |\tilde{r}_2(\omega)|^2\right), \tag{C8}$$

where we have used that

$$\tilde{r}_1(\omega) = \int_{-\infty}^{\infty} dt\, r_1\, e^{i\omega t} = \frac{\pi\alpha|Z_1Z_2|}{\mu v_i^2\omega} H_{i\kappa}^{(1)\prime}(i\kappa\epsilon)\,, \tag{C9a}$$

$$\tilde{r}_2(\omega) = \int_{-\infty}^{\infty} dt\, r_2\, e^{i\omega t} = -\frac{\pi\alpha|Z_1Z_2|}{\mu v_i^2\omega}\frac{\sqrt{\epsilon^2-1}}{\epsilon} H_{i\kappa}^{(1)}(i\kappa\epsilon)\,, \tag{C9b}$$

with $\kappa = \alpha |Z_1 Z_2| \omega / (\mu v_i^3)$; the integrals are solved by expressing dt in terms of $d\xi$ using (C7c). For dipole emission, a closed solution for the integral in Eq. (C8) exist. Therefore the differential cross section for an attractive potential $Z_1 Z_2 < 0$ can be written as

$$\omega \frac{d\sigma_D}{d\omega}\bigg|_{\text{classical}} = \frac{4\pi^2}{3} \frac{\alpha^3 Z_1^2 Z_2^2 A_D^2}{\mu^2 v_i^2} \kappa \left| H_{i\kappa}^{(1)}(i\kappa) \right| H_{i\kappa}^{(1)\prime}(i\kappa) \,, \tag{C10}$$

For a repulsive interaction, the respective sign in the parametrization in Eq. (C7) simply leads to an overall factor $\exp(-2\pi\kappa)$ in Eq. (C10).

2. Quadrupole Emission

The cross section for quadrupole emission is found from the second term in (C6) with the quadrupole tensor (C5) and r_n from (C7). The components of $q^{ab}(t)$ are then Fourier-transformed to obtain $\tilde{q}^{ab}(\omega)$. This is then plugged into (C6) to obtain the differential cross section (if the ω integration is omitted), which for attractive potentials $Z_1 Z_2 < 0$ reads

$$\omega \frac{d\sigma_Q}{d\omega}\bigg|_{\text{classical}} = \frac{\alpha^3 Z_1^2 Z_2^2 \omega^6 A_Q^2}{15 \mu^2 v_i^4} \int_1^\infty d\epsilon \; \epsilon \; \Big[|\tilde{r}_{11}(\omega)|^2 + |\tilde{r}_{22}(\omega)|^2 + 3\, |\tilde{r}_{12}(\omega)|^2 - \mathrm{Re}\left(\tilde{r}_{11}(\omega)\; \tilde{r}_{22}^*(\omega)\right) \Big] . \tag{C11}$$

Similarly to the case of dipole emission, the quadrupole emission for a repulsive interaction $Z_1 Z_2 > 0$ can be obtained from (C11) by multiplying it with an overall factor $\exp(-2\pi\kappa)$. The coefficients read

$$\begin{aligned} \tilde{r}_{11}(\omega) &= \int_{-\infty}^{\infty} dt \; r_1^2 \; e^{i\omega t} \\ &= a \left[\frac{\epsilon^2 - 1}{\epsilon} \, \kappa \, H_{i\kappa}^{(1)\prime}(i\kappa\epsilon) - \frac{i}{\epsilon^2} H_{i\kappa}^{(1)}(i\kappa\epsilon) \right] , \end{aligned} \tag{C12}$$

$$\begin{aligned} \tilde{r}_{22}(\omega) &= \int_{-\infty}^{\infty} dt \; r_2^2 \; e^{i\omega t} \\ &= -a \left[\frac{\epsilon^2 - 1}{\epsilon} \kappa \, H_{i\kappa}^{(1)\prime}(i\kappa\epsilon) + i \frac{\epsilon^2 - 1}{\epsilon^2} H_{i\kappa}^{(1)}(i\kappa\epsilon) \right] , \end{aligned} \tag{C13}$$

$$\begin{aligned} \tilde{r}_{12}(\omega) &= \int_{-\infty}^{\infty} dt \; r_1 \; r_2 \; e^{i\omega t} \\ &= a \sqrt{\epsilon^2 - 1} \left[\frac{i}{\epsilon} \, H_{i\kappa}^{(1)\prime}(i\kappa\epsilon) - \frac{\epsilon^2 - 1}{\epsilon^2} \kappa \, H_{i\kappa}^{(1)}(i\kappa\epsilon) \right] , \end{aligned} \tag{C14}$$

with $a = 2\pi\alpha |Z_1 Z_2| / (\mu v_i \omega^2)$.

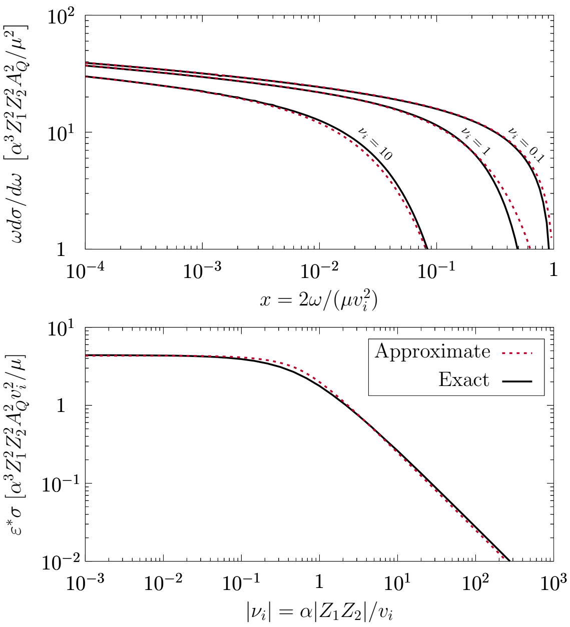

Figure 6. Approximate formula (D1) for non-identical particles compared to the exact result (34). The differential cross section is shown for $\nu_i = 0.1, 1, 10$ in the top panel and the effective energy loss in the bottom panel. The equivalent approximate result for identical particles is *on par* in terms of accuracy w.r.t. the exact result.

3. Asymptotic expressions for large κ

In the limit where $\kappa \gg 1$, which corresponds to the limit assumed in Sec. V B, we can approximate the Hankel functions in terms of Airy functions, *i.e.*,

$$H_{i\kappa}^{(1)}(i\kappa\epsilon) \approx \frac{2^{4/3}}{i(\epsilon\kappa)^{1/3}} \mathrm{Ai}\left(\frac{2^{1/3}(\epsilon - 1)\kappa}{(\epsilon\kappa)^{1/3}} \right) , \tag{C15}$$

$$H_{i\kappa}^{(1)\prime}(i\kappa\epsilon) \approx -\frac{2^{5/3}}{(\epsilon\kappa)^{2/3}} \mathrm{Ai}'\left(\frac{2^{1/3}(\epsilon - 1)\kappa}{(\epsilon\kappa)^{1/3}} \right) . \tag{C16}$$

Putting these expressions into (C8) or (C11) respectively, it can be shown that for $\kappa \to \infty$ the integrand goes to zero everywhere except at $\epsilon = 1$. Thus, expanding the argument of the Airy functions to leading order and the prefactors to fourth order in $(\epsilon - 1)$, one obtains the asymptotic expressions in κ, (52) and (53), which in Sec. V B were obtained from the exact quantum mechanical cross sections.

Appendix D: Approximate Formula for Arbitrary ν_i

For repulsive interactions, and building on our insights on the process in the various kinematic regimes, one may in fact go beyond Eq. (64) and find a "doctored" formula that is not only valid for arbitrary ν_i but also extends the validity away from the soft-photon regime. Although such formula cannot be derived from first principles, it can nevertheless be helpful to obtain reasonably accurate results for quadrupole emission across the entire region in x and ν_i from a simple expression.

For this, we first multiply Eq. (64) by the exponential factor $\exp(-2\pi\kappa)$ that is ubiquitous in the classical formulæ for repulsive interactions. Then we supply a phase space factor $\sqrt{1-x}$ which was neglected in the soft limit and take the x-dependent term in the logarithm to be the one from the full Born cross section. In addition, we add to this the classical cross section for $\kappa \gg 1$ to cover hard photon emission. The resulting approximate formula is

$$\omega\frac{d\sigma_Q}{d\omega} \approx \frac{4}{15}\frac{\alpha^3 Z_1^2 Z_2^2 A_Q^2}{\mu^2}\frac{\sqrt{1-x}}{e^{\pi x|\nu_i|}}\left\{\frac{40\pi^{3/2}}{3^{1/6}\Gamma(1/6)}\left(\frac{x|\nu_i|}{2}\right)^{2/3}\right.$$
$$+\frac{\pi^2\nu_i^2}{\sinh^2\pi\nu_i}\left(6\frac{2+\xi}{\zeta^2+1}-3(2+\xi)+12\ln\zeta\right)$$
$$\left.+26-6\frac{2+\xi}{\zeta^2+1}+12\ln\left(\frac{1}{\zeta}\frac{1+\sqrt{1-x}}{1-\sqrt{1-x}}\right)\right\}, \quad \text{(D1)}$$

with $\zeta = |\nu_i|e^{\gamma+1/2}$ and $\xi = (0)1$ for (non-)identical particles. This approximate cross section is easy to compute numerically in contrast to the exact results (34) and (39) and yields reasonable results in all regimes.

Equation (D1) is essentially exact for arbitrary ν_i for soft photons, as shown in the top panel in Fig. 6. At the kinematic endpoint, for $x \to 1$, it deviates from the exact result. In the Born limit $|\nu_i| \ll 1$, a deviation is only observed very close to $x = 1$ where the Born cross section is already kinematically suppressed. In the classical limit, $|\nu_i| \gg 1$, the deviation is visible for smaller values of x, but in a region where the cross section is already highly Coulomb suppressed. For this reason, Eq. (D1) turns out to be an excellent approximation for the effective energy loss demonstrated in the bottom panel of Fig. 6. The effective energy loss deduced from Eq. (D1) has an error of roughly 1% w.r.t the exact result in the Born regime, in the intermediate regime $\nu_i \sim 1$ the error reaches its maximum of 15% and in the classical regime the exact result is underestimated by 10%.

[1] H. A. Kramers, The London, Edinburgh, and Dublin Philosophical Magazine and Journal of Science **46**, 836 (1923), https://doi.org/10.1080/14786442308565244.
[2] J. R. Oppenheimer, Z. Phys. **55**, 725 (1929).
[3] Y. Sugiura, Phys. Rev. **34**, 858 (1929).
[4] A. Sommerfeld, Ann. Phys. **403**, 257 (1931).
[5] A. Sommerfeld and A. Maue, Ann. Phys. **415**, 589 (1935).
[6] G. Elwert, Ann. Phys. **426**, 178 (1939).
[7] S. Weinberg, Phys. Rev. D **99**, 076018 (2019), arXiv:1903.11168 [astro-ph.GA].
[8] S. Weinberg, Phys. Rev. **140**, B516 (1965).
[9] B. Fedyushin, Zh. Eksperim. Teor. Fiz. **22**, 140 (1952).
[10] R. J. Gould, Phys. Rev. A **23**, 2851 (1981).
[11] R. J. Gould, Astrophys. J. **362**, 284 (1990).
[12] M. S. Maxon and E. G. Corman, Physical Review **163**, 156 (1967).
[13] R. Gould, *Electromagnetic Processes*, Princeton Series in Astrophysics (Princeton University Press, 2006).
[14] E. Haug and W. Nakel, *The elementary process of bremsstrahlung* (2004).
[15] A. Sommerfeld, *Atombau und Spektrallinien II.* (Friedr. Vieweg & Sohn, Braunschweig, 1939).
[16] A. I. Akhiezer and V. B. Berestetskii, *Quantum electrodynamics*, Vol. 2876 (United States Atomic Energy Commission, Technical Information Service Extension, 1953).
[17] V. Berestetskii, E. Lifshitz, and L. Pitaevskii, *Quantum Electrodynamics*, Course of theoretical physics (Butterworth-Heinemann, 1982).
[18] S. Weinberg, *Lectures on quantum mechanics* (Cambridge University Press, 2015).
[19] L. Landau and E. Lifshitz, *Quantum Mechanics: Non-relativistic Theory*, Butterworth-Heinemann (Butterworth-Heinemann, 1977).
[20] M. Abramowitz and I. A. Stegun, *Handbook of mathematical functions with formulas, graphs, and mathematical tables*, Vol. 55 (US Government printing office, 1948).
[21] A. Nordsieck, Phys. Rev. **93**, 785 (1954).
[22] L. Landau and E. Lifshitz, *The Classical Theory of Fields*, Course of theoretical physics (Butterworth-Heinemann, 1975).
[23] F. Low, Phys. Rev. **110**, 974 (1958).
[24] S. Weinberg, Phys. Rev. **138**, B988 (1965).
[25] C. D. Dermer, Astrophys. J. **280**, 328 (1984).
[26] W. J. Karzas and R. Latter, The Astrophysical Journal Supplement Series **6**, 167 (1961).
[27] P. van Hoof, R. Williams, K. Volk, M. Chatzikos, G. Ferland, M. Lykins, R. Porter, and Y. Wang, Mon. Not. Roy. Astron. Soc. **444**, 420 (2014), arXiv:1407.5048 [astro-ph.HE].
[28] J. Chluba, A. Ravenni, and B. Bolliet, Mon. Not. Roy. Astron. Soc. **492**, 177 (2020), arXiv:1911.08861 [astro-ph.CO].
[29] J. Pradler and L. Semmelrock, In preparation.
[30] N. Itoh, Y. Kawana, and S. Nozawa, Nuovo Cimento B Serie **117**, 359 (2002), arXiv:astro-ph/0111040 [astro-ph].
[31] R. Mertig, M. Bohm, and A. Denner, Comput. Phys. Commun. **64**, 345 (1991).
[32] V. Shtabovenko, R. Mertig, and F. Orellana, Comput. Phys. Commun. **207**, 432 (2016), arXiv:1601.01167 [hep-ph].
[33] D. V. Gal'tsov and Y. V. Grats, Soviet Physics Journal **17**, 1713 (1974).
[34] D. V. Gal'stov and Y. V. Grats, Theoretical and Mathematical Physics **28**, 730 (1976).

Part III

Conclusions

CHAPTER 5

Discussion and Outlook

In this thesis, we analyzed emission processes in three publications [1–3] which can be split into two subjects, emission processes of dark states which couple to the SM photon via electromagnetic form factors and bremsstrahlung of photons in collisions of charged particles.

First, we have investigated the phenomenology of a new long lived Dirac fermion χ in the sub-GeV mass range. This fermion is electrically neutral, but couples to the electromagnetic current via higher dimensional operators, which can be induced by heavy charged particles or through compositeness of χ. In Ref. [1], we have analyzed the production of these particles in the high intensity electron beam facilities BaBar, NA64 and mQ as well as in proposed (or ongoing) experiments Belle II, LDMX and BDX. Moreover, we have compared the constraints and sensitivity projections from the high intensity experiments, to constraints from the former high energy collider LEP and found that for these models, the constraints from LEP are the most stringent to this date. With good control of their systematics, Belle II and LDMX will, however, be able to improve on the LEP constraints. Even though electromagnetic form factor models are good candidates to solve the tension between the measured and predicted value of the magnetic moment of the muon, the parameter space capable of solving said tension is excluded by experiments. In addition, we investigate χ as a dark matter candidate, which gives rise to cosmological and astrophysical constraints. It turns out that for magnetic and electric dipole moment interactions, the strongest constraints come from direct detection experiments which—depending on the DM mass—can be up to three orders of magnitude stronger than the LEP bounds. If the dark matter is symmetric in χ and $\bar{\chi}$, the possibility of $\chi\bar{\chi}$-annihilation into an e^+e^--pair constrains the magnetic dipole moment interaction even further. For anapole moment and charge radius interactions, the bounds from direct and indirect detection are weaker than the ones from LEP. For all models it is basically ruled out that these particles make up 100% of the dark matter in a standard freeze-out scenario, except for a narrow region in parameter space around 5 MeV which is not yet ruled out for magnetic dipole moment interactions. It is still possible, however, for such particles to make up all of the dark matter but to be so weakly coupled to the SM that they never reach thermal equilibrium with the latter in the early universe, which was investigated in Ref. [152].

We have then extended our analysis to even smaller masses in Ref. [2] considering the production of a $\chi\bar{\chi}$-pair in stellar objects, i.e. the sun, red giant and horizontal branch stars and the supernova SN1987A. In these objects a pair of dark states can be produced via various channels. We investigated the production via plasmon decay, e^+e^--annihilation, $2 \to 3$ Compton scattering, electron bremsstrahlung and nucleon bremsstrahlung and found that all processes gain relative importance in certain regimes, depending on the model and astrophysical environment. We show that the possibility of producing these dark states in stars strongly constrains the parameter space of magnetic and electric dipole moment interactions for masses smaller than 10-100 keV. Due to a different energy scaling in the production cross section for anapole moment and charge radius interactions, the constraints from stars are weaker than the LEP constraints for these models. However, SN1978A yields strong constraints up to masses of 100 MeV for all four models.

The final open issue regarding probing electromagnetic form factors was tackled in a follow up work by colleagues [153] who investigated the production of dark states in high-intensity proton beam experiments. It turns out that the constraints on the parameter space of dark states with electromagnetic form factors can be improved with these kinds of experiments with respect to the constraints from electron beam facilities for dimension-5 operators, i.e. magnetic and electric dipole moments. But the bounds are weaker with respect to bounds from electron beams for dimension-6 operators, i.e. anapole moments and charge radius interactions.

The second topic presented in this thesis are SM emission precesses. In Ref. [3], we investigated bremsstrahlung of photons accompanying the scattering of two electrically charged spin-1/2 particles. We presented a calculation of the emission cross section and energy loss rates exact to all orders in the Coulomb potential for quadrupole radiation in the collision of two non-relativistic particles. The results are of general validity. They apply to all non-relativistic kinematic regimes, closing a seeming gap in the literature between the perturbative and quasi-classical limit. We show how these limits are derived from the full expressions and compare them to the perturbative and quasi classical treatments. Furthermore, Weinberg [154] recently showed how a generally applicable formula for soft photon emission may be constructed for dipole radiation and we adapt his ansatz to present an equivalent formula for quadrupole radiation. Taking this approach further, we also give an approximate equation, which is applicable in all kinematic regimes beyond the soft photon limit. Finally, we define a Gaunt factor for quadrupole emission in electron-electron scattering, based on the Elwert prescription. They we be tabulated numerically in an upcoming work since the full expressions for the cross sections involve integrals over the hypergeometric functions that lead to cancellations of large numbers and are therefore numerically expensive to evaluate.

Moreover, the results presented in [3] are not only interesting for SM processes, such as electron-electron scattering, but can also be applied to self-interacting dark matter models, where a dark photon can be emitted as bremsstrahlung during particle collisions. In addition to vector boson mediators, SIDM models can have scalar boson mediators, where in the collision of identical particles the interaction is attractive as opposed to the repulsive interaction in QED. Therefore, interesting phenomenology is possible in SIDM models, the investigation of which we also relegate to upcoming work.

To sum up, electromagnetic processes are not only the most dominant processes in our day to day life but are also the most important messenger processes, that tell us about the universe, the particles we know and possibly beyond. This thesis has shown the importance of electromagnetic emission processes in the quest of finding new physics to explain what our universe is made up of, and has presented a detailed exact calculation of a process long known and studied, but to which only approximate solutions have existed. The role of light as a messenger to a dark world is intriguing in many ways. Whether the photon really is a portal to dark matter will only be clarified in the future, but with many efforts being put into designing and building new observational instruments to get a better look at the universe, it is definitely a messenger of the unknown.

Appendix

A Terrestrial and stellar probes of dark sector-photon interactions

A.1 4-body phase space for dark state production at electron accelerators

In this appendix, we present a more thorough derivation of the 4-body phase space discussed in the appendix of Ref. [1]. We are considering the following process

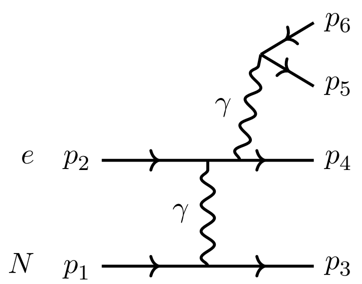

with a nucleus (p_1) and an electron (p_2) in the initial state and a nucleus (p_3), an electron (p_4) and two dark states (p_5 and p_6) in the final state The cross section is

$$\sigma = \int \prod_{i=3}^{6} \left\{ \frac{d^4 p_i}{(2\pi)^4} (2\pi)\delta(p_i^2 - m_i^2)\Theta(p_i^0) \right\} (2\pi)^4 \delta^{(4)} \left(p_1 + p_2 - \sum_{i=3}^{6} p_i \right) |\mathcal{M}|^2, \tag{A.1}$$

where the squared matrix element can be split in a dark matter part, a nuclear part and an electron part,

$$|\mathcal{M}|^2 = \chi_{\mu\nu}(p_5, p_6)\; \eta_{\rho\sigma}(p_1, p_3)\; l^{\mu\nu,\rho\sigma}(p_2, p_4, q_1, q). \tag{A.2}$$

Now, we separate the phase space in the same way, starting with the dark matter part by inserting

$$1 = \int d^4 q\; \delta^{(4)}(q - p_5 - p_6)\Theta(q^0) \tag{A.3}$$

$$1 = \int dM_{56}^2\; \delta(M_{56}^2 - q^2) \tag{A.4}$$

and thereby trading the p_5 and p_6 integration for a q integration

$$\sigma = \frac{1}{(2\pi)^8} \int dM_{56}^2 \int \frac{d^3 q}{2E_{56}} \frac{d^3 p_3}{2E_3} \frac{d^3 p_4}{2E_4} \delta^{(4)} \left(p_1 + p_2 - p_3 - p_4 - q \right)$$

$$\times X_{\mu\nu}(q)\ \eta_{\rho\sigma}(p_1, p_3)\ l^{\mu\nu,\rho\sigma}(p_2, p_4, q_1, q) \tag{A.5}$$

with $q^2 = M_{56}^2 = E_{56}^2 - |\boldsymbol{q}|^2$ and $d^3p/(2E) = d^4p\ \delta(p^2 - m^2)\Theta(p^0)$ and

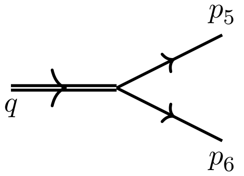

$$= X_{\mu\nu}(q) \tag{A.6}$$

$$= \int \frac{d^3p_5}{2E_5} d^4p_6\ \delta(p_6^2 - m_\chi^2)\delta^{(4)}(q - p_5 - p_6)\ \chi_{\mu\nu}(p_5, p_6) \tag{A.7}$$

$$= \int \frac{d^3p_5}{2E_5}\ \delta((q - p_5)^2 - m_\chi^2)\ \chi_{\mu\nu}(p_5, p_6) \tag{A.8}$$

$$= \int \frac{d^3p_5}{2E_5}\ \delta(q^2 - 2(q \cdot p_5))\ \chi_{\mu\nu}(p_5, p_6) \tag{A.9}$$

$$= \frac{1}{2} \int d\Omega_5^{R56} dE_5^{R56}\ |\boldsymbol{p}_5^{R56}|\ \delta(M_{56}^2 - 2M_{56}E_5^{R56})\ \chi_{\mu\nu}(p_5, p_6) \tag{A.10}$$

$$= \frac{\lambda^{1/2}(M_{56}^2, m_\chi^2, m_\chi^2)}{8M_{56}^2} \int d\Omega_{56}^{R56}\ \chi_{\mu\nu}(\Omega_{56}^{R56}) \tag{A.11}$$

$$= \left(g_{\mu\nu} - \frac{q_\mu q_\nu}{M_{56}^2}\right)\ \lambda^{1/2}(M_{56}^2, m_\chi^2, m_\chi^2)\ f(M_{56}^2) \tag{A.12}$$

with

$$\lambda(a^2, b^2, c^2) = \left[a^2 - (b + c)^2\right]\left[a^2 - (b - c)^2\right] \tag{A.13}$$

where the subscript $R56$ denotes the CM frame of the dark matter particles, i.e. $\boldsymbol{q} = 0$. In (A.12), only the part proportional to the metric contributes, the second part vanishes due to gauge invariance when contracted with the electron part. Now, we insert

$$1 = \int dq_1^2\ \delta(q_1^2 - (p_1 - p_3)^2) \tag{A.14}$$

to get

$$\sigma = \frac{1}{(2\pi)^8} \int dM_{56}^2\ X_{\mu\nu}\left(M_{56}^2\right) \int dq_1^2 \int \frac{d^3p_4}{2E_4} \int \frac{d^3q}{2E_{56}} \frac{d^3p_3}{2E_3} \delta(q_1^2 - (p_1 - p_3)^2)$$
$$\times\ \delta^{(4)}\left(p_1 + p_2 - p_3 - p_4 - q\right)\ \eta_{\rho\sigma}(p_1, p_3)\ l^{\mu\nu,\rho\sigma}(p_2, p_4, q_1, q). \tag{A.15}$$

We can rewrite in the lab frame

$$\int \frac{d^3p_4}{2E_4} = \frac{1}{2} \int d\Omega_4 dE_4\ |\boldsymbol{p}_4| \tag{A.16}$$

to get

$$\sigma = \frac{1}{2(2\pi)^8} \int d\Omega_4 dE_4\ |\boldsymbol{p}_4| \int dM_{56}^2\ X_{\mu\nu}\left(M_{56}^2\right) \int dq_1^2\ N^{\mu\nu}\left(M_{56}^2, q_1^2\right). \tag{A.17}$$

We evaluate $N^{\mu\nu}$ in the CM frame of the electron and the dark matter, i.e. $\boldsymbol{p}_1 + \boldsymbol{p}_2 - \boldsymbol{p}_4 = \boldsymbol{p}_3 + \boldsymbol{q} = 0$, which will be denoted with the superscript $R356$ in the following equation

$$N^{\mu\nu} = \int \frac{d^3p_3}{2E_3} d^4q\ \delta(q^2 - M_{56}^2)\delta(q_1^2 - (p_1 - p_3)^2)\delta^{(4)}\left(p_1 + p_2 - p_3 - p_4 - q\right)\ \eta_{\rho\sigma}\ l^{\mu\nu,\rho\sigma} \tag{A.18}$$

$$= \int \frac{d^3p_3}{2E_3}\ \delta((p_1 + p_2 - p_3 - p_4)^2 - M_{56}^2)\delta(q_1^2 - (p_1 - p_3)^2)\ \eta_{\rho\sigma}\ l^{\mu\nu,\rho\sigma} \tag{A.19}$$

$$= \frac{1}{2}\int d\phi_3^{R356} \int_{-1}^{1} d\cos\theta_3^{R356} \int_{m_3}^{\infty} dE_3^{R356}\ |\boldsymbol{p}_3^{R356}|\ \delta(M_{356}^2 - M_{56}^2 + m_N^2 - 2M_{356}E_3^{R356})$$
$$\times\ \delta(q_1^2 - 2m_N^2 + 2E_1^{R356}E_3^{R356} - 2|\boldsymbol{p}_1^{R356}||\boldsymbol{p}_3^{R356}|\cos\theta_3^{R356})\ \eta_{\rho\sigma}\ l^{\mu\nu,\rho\sigma} \tag{A.20}$$

In (A.20), we have introduced the Lorentz invariant variable $M_{356}^2 = (p_3+q)^2$. It is instructive to write the cross section in terms of the Lorentz invariants M_{356} and $q_2^2 = (p_2 - p_4)^2$ instead of the lab frame variables Ω_4 and E_4. We can do this by introducing

$$1 = \int dM_{356}^2\ \delta(M_{356}^2 - (p_1 + p_2 - p_4)^2), \tag{A.21}$$

$$1 = \int dq_2^2\ \delta(q_2^2 - (p_2 - p_4)^2). \tag{A.22}$$

Using these new delta functions to integrate out Ω_4 and E_4, yields the Jacobian

$$|J| = \frac{1}{2}\left[m_N^4 + \left(s - m_e^2\right)^2 - 2m_N^2\left(s + m_e^2\right)\right]^{-1/2} \tag{A.23}$$

$$\approx \frac{1}{2(s - m_N^2)}, \tag{A.24}$$

where in the second line, we assume $s \gg m_e^2$. From (A.17) we therefore get the cross section in terms of the Lorentz invariant variables M_{356}^2 and q_2^2

$$\sigma = \frac{1}{4(2\pi)^8(s - m_N^2)} \int dM_{356}^2 \int dq_2^2 \int dM_{56}^2\ X_{\mu\nu}\left(M_{56}^2\right) \int dq_1^2\ N^{\mu\nu}\left(M_{56}^2, q_1^2\right). \tag{A.25}$$

To evaluate $N^{\mu\nu}$, the integral over E_3^{R356} in (A.20) is carried out by using the first delta function and the one over $\cos\theta_3^{R356}$ by using the second delta function. What remains, is the integral over ϕ_3^{R356} with some Jacobian factors from rewriting the delta functions, i.e.

$$N^{\mu\nu} = \frac{1}{8M_{356}|\boldsymbol{p}_1^{R356}|} \int d\phi_3^{R356}\ \eta_{\rho\sigma}\ l^{\mu\nu,\rho\sigma} \tag{A.26}$$

$$= \frac{1}{4\lambda^{1/2}(M_{356}^2, m_N^2, q_2^2)} \int d\phi_3^{R356}\ \eta_{\rho\sigma}\ l^{\mu\nu,\rho\sigma} \tag{A.27}$$

and the cross section can be written as

$$\sigma = \frac{1}{16(2\pi)^8(s - m_N^2)} \int dM_{356}^2 \int dq_2^2 \int dM_{56}^2\ f(M_{56}^2)\ \frac{\lambda^{1/2}(M_{56}^2, m_\chi^2, m_\chi^2)}{\lambda^{1/2}(M_{356}^2, m_N^2, q_2^2)}$$

$$\times \int dq_1^2 \int d\phi_3^{R356}\ g_{\mu\nu}\ \eta_{\rho\sigma}\ l^{\mu\nu,\rho\sigma} \tag{A.28}$$

with

$$\lambda^{1/2}(M_{56}^2, m_\chi^2, m_\chi^2) = M_{56}\sqrt{M_{56}^2 - 4m_\chi^2}, \tag{A.29}$$

$$\lambda^{1/2}(M_{356}^2, m_N^2, q_2^2) = \sqrt{\left[M_{356}^2 - \left(m_N + q_2^2\right)^2\right]\left[M_{356}^2 - \left(m_N - q_2^2\right)^2\right]}. \tag{A.30}$$

Now, we have to work out the integration boundaries. For the s-channel cuts, i.e. M_{356} and M_{56}, we get the boundaries by picturing the phase space in the following way

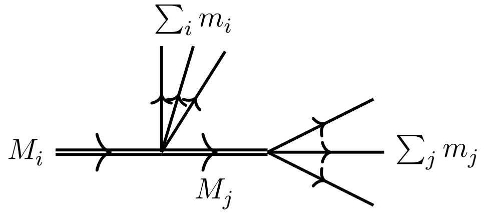

where the lower bound of the respective invariant mass M_j is given by the sum of the masses m_j going out of the vertex at the end of the propagator of M_j and the upper bound is given by the total invariant mass M_i going into the vertex at the beginning of the propagator of M_j minus the sum of the masses m_i going out of this vertex. The corresponding limits for M_{356} and M_{56} are

$$\begin{array}{ccccc} m_N + 2m_\chi & \leq & M_{356} & \leq & \sqrt{s} - m_e, \\ 2m_\chi & \leq & M_{56} & \leq & M_{356} - m_N. \end{array} \tag{A.31}$$

The upper and lower bounds for q_1^2 and q_2^2 can be obtained via Gram determinants for t-channel cuts. For a t-channel of the kind

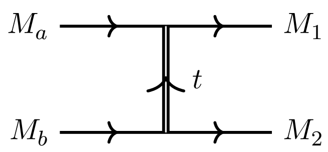

with a total squared invariant mass s, where we denote the masses of the ingoing an outgoing states with capital letters to emphasize that they do not necessarily have to be on shell, the boundaries of t are

$$t^\pm = M_a^2 + M_1^2 - \frac{1}{2s}\left[(s + M_a^2 - M_b^2)(s + M_1^2 - M_2^2) \mp \lambda^{1/2}(s, M_a^2, M_b^2)\ \lambda^{1/2}(s, M_1^2, M_2^2)\right]. \tag{A.32}$$

The corresponding limits for q_1^2 and q_2^2 are

$$\left[q_1^2\right]^\pm = 2m_N^2 - \frac{1}{2M_{356}^2}\left[(M_{356}^2 + m_N^2 - q_2^2)(M_{356}^2 + m_N^2 - M_{56}^2)\right.$$

$$\mp \lambda^{1/2}(M_{356}^2, m_N^2, q_2^2)\, \lambda^{1/2}(M_{356}^2, m_N^2, M_{56}^2)\Big], \tag{A.33}$$

$$\Big[q_2^2\Big]^{\pm} = 2m_e^2 - \frac{1}{2s}\Big[(s + m_e^2 - m_N^2)(s + m_e^2 - M_{356}^2) \mp \lambda^{1/2}(s, m_e^2, m_N^2)\, \lambda^{1/2}(s, m_e^2, M_{356}^2)\Big]. \tag{A.34}$$

The only non-Lorentz invariant variable remaining is the azimuthal angle ϕ_3^{R356} which is unconstrained and runs from 0 to 2π. However, with the use of Gram determinants, it is easy to get the boundaries for one last remaining invariant as a function of M_{56}, M_{356}, q_1^2 and q_2^2. For $u_{23} = (p_2 \cdot p_3)$, requiring that the Gram determinant vanishes, yields the limits

$$\begin{aligned} u_{23} =& \frac{(p_1 \cdot p_2) G_2(p_1, q_2;\, q_2, p_3) - (q_2 \cdot p_2) G_2(p_1, q_2;\, p_1, p_3)}{-\Delta_2(p_1, q_2)} \\ &+ \frac{\sqrt{\Delta_3(p_1, q_2, p_2)\Delta_3(p_1, q_2, p_3)}}{-\Delta_2(p_1, q_2)} \cos\phi_3^{R356}\,, \end{aligned} \tag{A.35}$$

$$\begin{aligned} u_{23}^{\pm} =& \frac{(p_1 \cdot p_2) G_2(p_1, q_2;\, q_2, p_3) - (q_2 \cdot p_2) G_2(p_1, q_2;\, p_1, p_3)}{-\Delta_2(p_1, q_2)} \\ &\mp \frac{\sqrt{\Delta_3(p_1, q_2, p_2)\Delta_3(p_1, q_2, p_3)}}{-\Delta_2(p_1, q_2)}\,, \end{aligned} \tag{A.36}$$

G_n being the Gram determinant of dimension n and Δ_n the respective Cayley determinant (or symmetric Gram determinant). The double differential cross section can therefore be written as

$$\begin{aligned} \frac{d^2\sigma}{dM_{356}^2 dq_2^2} =& \frac{1}{8(2\pi)^8 (s - m_N^2)} \int dM_{56}^2\, f(M_{56}^2)\, \frac{\lambda^{1/2}(M_{56}^2, m_\chi^2, m_\chi^2)}{\lambda^{1/2}(M_{356}^2, m_N^2, q_2^2)} \int dq_1^2 \\ &\times \int du_{23} \frac{f_{23}(M_{356}^2, M_{56}^2, q_1^2, q_2^2)}{\sqrt{1 - f_{23}^2(M_{356}^2, M_{56}^2, q_1^2, q_2^2) u_{23}^2}}\, g_{\mu\nu}\, \eta_{\rho\sigma}\, l^{\mu\nu,\rho\sigma} \end{aligned} \tag{A.37}$$

where the the factor in the second line of (A.37) is the Jacobian of the transformation from ϕ_3^{R356} to u_{23}.

B Photon Emission

B.1 Born Approximation in NR-Quantum Mechanics

In this appendix, we show how to obtain the Born cross sections—which we calculated in in App. B of [3] from a quantum field theory approach—from a non-relativistic quantum mechanics approach starting from Eq. (3) in [3] and taking for the in- and outgoing wave functions the first order Born wave functions, as will be shown below.

Preliminaries. We will work in an abstract basis of initial states $|i\rangle$ and final states $|f\rangle$ denoting the wave function of the relative motion of two particles. Operators will be denoted with a hat, e.g. $\hat{p}$. The projections onto position space are denoted by

$$\chi_{\boldsymbol{p}_i}(\boldsymbol{r}) = \langle \boldsymbol{r}|i\rangle\,, \qquad \chi^*_{\boldsymbol{p}_i}(\boldsymbol{r}) = \langle i|\boldsymbol{r}\rangle\,, \tag{B.38}$$

and the same for final states with

$$\int d^3r\,|\boldsymbol{r}\rangle\,\langle\boldsymbol{r}| = \mathbb{1}, \qquad \langle\boldsymbol{r}|\boldsymbol{r}'\rangle = \delta^{(3)}(\boldsymbol{r}-\boldsymbol{r}'). \tag{B.39}$$

The projections of the momentum and position operator onto position space are

$$\langle\boldsymbol{r}|\,\hat{\boldsymbol{p}}\,|\boldsymbol{r}'\rangle = -i\,\frac{\partial}{\partial\boldsymbol{r}}\delta^{(3)}(\boldsymbol{r}-\boldsymbol{r}'), \tag{B.40}$$

$$\langle\boldsymbol{r}|\,\hat{\boldsymbol{r}}\,|\boldsymbol{r}'\rangle = \boldsymbol{r}\,\delta^{(3)}(\boldsymbol{r}-\boldsymbol{r}'). \tag{B.41}$$

The commutators of $\hat{\boldsymbol{r}}$ and $\hat{\boldsymbol{p}}$ are given by

$$[\hat{r}_i,\hat{p}_j] = i\,\delta_{ij}, \qquad [\hat{r}_i,\hat{r}_j] = 0, \qquad [\hat{p}_i,\hat{p}_j] = 0, \tag{B.42}$$

and a few more helpful relations

$$[\hat{r}_i,\hat{p}_j\hat{p}_k] = i(\hat{p}_j\,\delta_{ik} + \hat{p}_k\,\delta_{ij}), \tag{B.43}$$

$$[\hat{\boldsymbol{p}},V(\hat{\boldsymbol{r}})] = -i\frac{\partial V(\hat{\boldsymbol{r}})}{\partial\hat{\boldsymbol{r}}}. \tag{B.44}$$

The commutator $[\hat{\boldsymbol{r}},\hat{H}]$ can be reformulated in terms of $\hat{\boldsymbol{p}}$ for general $\hat{\boldsymbol{r}}$-dependent potential $V(\hat{\boldsymbol{r}})$ in the following way

$$[\hat{r}_i,\hat{H}] = \frac{1}{2\mu}\underbrace{[\hat{r}_i,\hat{p}_j\hat{p}_j]}_{=2i\hat{p}_i} + \frac{1}{2\mu}\underbrace{[\hat{r}_i,V(\hat{r}_k)]}_{=0} = \frac{i}{\mu}\hat{p}_i. \tag{B.45}$$

The only requirement here is that V is not a function of the momentum, but for any positional dependence of V, this is valid.

We use the same definitions for energies, momenta and masses as in [3].

Reformulation of the dipole matrix element. The dipole matrix element is given by (3) and (4) in [3], which is proportional to $\langle f|\,\hat{\boldsymbol{p}}\,|i\rangle$. With $\omega = E_i - E_f$ we can write

$$\langle f|\,\hat{\boldsymbol{p}}\,|i\rangle = \frac{\mu}{i}\,\langle f|\,[\hat{\boldsymbol{r}},\hat{H}]\,|i\rangle \tag{B.46}$$

$$= \frac{\mu}{i}\Big(\langle f|\,\hat{\boldsymbol{r}}\,\hat{H}\,|i\rangle - \langle f|\,\hat{H}\,\hat{\boldsymbol{r}}\,|i\rangle\Big) \tag{B.47}$$

$$= \frac{\mu}{i}\big(E_i\,\langle f|\,\hat{\boldsymbol{r}}\,|i\rangle - E_f\,\langle f|\,\hat{\boldsymbol{r}}\,|i\rangle\big) \tag{B.48}$$

$$= \frac{\mu\omega}{i}\,\langle f|\,\hat{\boldsymbol{r}}\,|i\rangle\,. \tag{B.49}$$

On the other hand, we can write [154]

$$\langle f|\,\hat{\boldsymbol{p}}\,|i\rangle = \frac{E_i - E_f}{\omega}\,\langle f|\,\hat{\boldsymbol{p}}\,|i\rangle \tag{B.50}$$

$$= \frac{1}{\omega}\big(E_i\,\langle f|\,\hat{\boldsymbol{p}}\,|i\rangle - E_f\,\langle f|\,\hat{\boldsymbol{p}}\,|i\rangle\big) \tag{B.51}$$

$$= \frac{1}{\omega}\Big(\langle f|\,\hat{\boldsymbol{p}}\,\hat{H}\,|i\rangle - E_f\,\langle f|\,\hat{H}\,\hat{\boldsymbol{p}}\,|i\rangle\Big) \tag{B.52}$$

$$= \frac{1}{\omega}\,\langle f|\,[\hat{\boldsymbol{p}},\hat{H}]\,|i\rangle \tag{B.53}$$

$$= \frac{1}{2\mu\omega}\,\langle f|\,[\hat{\boldsymbol{p}},\hat{\boldsymbol{p}}^2]\,|i\rangle + \frac{1}{\omega}\,\langle f|\,[\hat{\boldsymbol{p}},V(\hat{\boldsymbol{r}})]\,|i\rangle \tag{B.54}$$

$$= -\frac{i}{\omega}\,\langle f|\,\frac{\partial V(\hat{\boldsymbol{r}})}{\partial \hat{\boldsymbol{r}}}\,|i\rangle\,. \tag{B.55}$$

For the full calculation of the matrix element in [3], we use the form $\langle f|\,\hat{\boldsymbol{p}}\,|i\rangle$, because then the solution of the Nordsieck integral can be used to solve it analytically. In the Born limit where the hypergeometric functions go to unity, any form of the matrix element,

$$\langle f|\,\hat{\boldsymbol{p}}\,|i\rangle = \frac{\mu\omega}{i}\,\langle f|\,\hat{\boldsymbol{r}}\,|i\rangle = -\frac{i}{\omega}\,\langle f|\,\frac{\partial V(\hat{\boldsymbol{r}})}{\partial \hat{\boldsymbol{r}}}\,|i\rangle\,, \tag{B.56}$$

can be used and solved analytically and leads to the same result. The derivations above can also easily be made in position space, with

$$E_f\,\langle f|\boldsymbol{r}\rangle = E_f\chi^*_{\boldsymbol{p}_f}(\boldsymbol{r}) = -\frac{1}{2\mu}\frac{\partial^2\chi^*_{\boldsymbol{p}_f}(\boldsymbol{r})}{\partial \boldsymbol{r}^2} + V(\boldsymbol{r})\,\chi^*_{\boldsymbol{p}_f}(\boldsymbol{r})\,, \tag{B.57}$$

$$E_i\,\langle \boldsymbol{r}|i\rangle = E_i\chi_{\boldsymbol{p}_i}(\boldsymbol{r}) = -\frac{1}{2\mu}\frac{\partial^2\chi_{\boldsymbol{p}_i}(\boldsymbol{r})}{\partial \boldsymbol{r}^2} + V(\boldsymbol{r})\,\chi^*_{\boldsymbol{p}_i}(\boldsymbol{r})\,. \tag{B.58}$$

The final expressions in position space are

$$\langle f|\,\hat{\boldsymbol{p}}\,|i\rangle = -i\int d^3r\;\chi^*_{\boldsymbol{p}_f}(\boldsymbol{r})\frac{\partial\chi_{\boldsymbol{p}_i}(\boldsymbol{r})}{\partial \boldsymbol{r}}, \tag{B.59}$$

$$\frac{\mu\omega}{i}\,\langle f|\,\hat{\boldsymbol{r}}\,|i\rangle = \frac{\mu\omega}{i}\int d^3r\;\boldsymbol{r}\,\chi^*_{\boldsymbol{p}_f}(\boldsymbol{r})\chi_{\boldsymbol{p}_i}(\boldsymbol{r}), \tag{B.60}$$

$$-\frac{i}{\omega}\,\langle f|\,\frac{\partial V(\hat{\boldsymbol{r}})}{\partial \hat{\boldsymbol{r}}}\,|i\rangle = -\frac{i}{\omega}\int d^3r\;\frac{\partial V(\boldsymbol{r})}{\partial \boldsymbol{r}}\;\chi^*_{\boldsymbol{p}_f}(\boldsymbol{r})\chi_{\boldsymbol{p}_i}(\boldsymbol{r}). \tag{B.61}$$

Reformulation of the quadrupole matrix element. For quadrupole radiation, the matrix element is given by (3) and (5) in [3], which is proportional to $\langle f|\,\hat{r}_i\hat{p}_j\,|i\rangle$. The full amplitude and its projection to position space is

$$\mathcal{M}_Q = \frac{ieA_Q}{\mu\sqrt{2\omega}}\, q_k\epsilon_l^*\,\langle f|\,\hat{r}_k\hat{p}_l\,|i\rangle \tag{B.62}$$

$$= \frac{ieA_Q}{2\mu\sqrt{2\omega}}\, q_k\epsilon_l^* \int d^3r \int d^3r' \int d^3r''\; \underbrace{\langle f|\boldsymbol{r}\rangle}_{=\chi^*_{\boldsymbol{p}_f}(\boldsymbol{r})} \quad \underbrace{\langle \boldsymbol{r}|\,\hat{r}_k\,|\boldsymbol{r}'\rangle}_{=\boldsymbol{r}\,\delta^{(3)}(\boldsymbol{r}-\boldsymbol{r}')} \quad \underbrace{\langle \boldsymbol{r}'|\,\hat{p}_l\,|\boldsymbol{r}''\rangle}_{=-i\,\delta^{(3)}(\boldsymbol{r}'-\boldsymbol{r}'')\frac{\partial}{\partial \boldsymbol{r}}} \quad \underbrace{\langle \boldsymbol{r}''|i\rangle}_{=\chi_{\boldsymbol{p}_i}(\boldsymbol{r}'')} \tag{B.63}$$

$$= \frac{eA_Q}{\mu\sqrt{2\omega}}\, q_k\epsilon_l^* \int d^3r\; \chi^*_{\boldsymbol{p}_f}(\boldsymbol{r})\; r_k\nabla_l\; \chi_{\boldsymbol{p}_i}(\boldsymbol{r}) \tag{B.64}$$

$$= \frac{\sqrt{\omega}A_Q}{\sqrt{2}\mu}\hat{q}_k\epsilon_l^*\, \underbrace{e\int d^3r\; \chi^*_{\boldsymbol{p}_f}(\boldsymbol{r})\; r_k\nabla_l\; \chi_{\boldsymbol{p}_i}(\boldsymbol{r})}_{=\mathcal{Q}_{kl}}\,, \tag{B.65}$$

where from the second to the third line, the two trivial integrals over r' and r'' have been executed, removing the two delta functions. In contrast to the rest of this appendix where the hat is used to indicate operators, in the last line the hat in $\hat{\boldsymbol{q}}$ is used to denote the unit vector, which should be unambiguous since the amplitude is written in position space where all the operators have already been projected.

Squaring the amplitude and averaging over the direction of the emitted particles (denoted by angle brackets) gives

$$\left\langle |\mathcal{M}_Q|^2 \right\rangle_{\hat{\boldsymbol{q}}} = \frac{\omega A_Q^2}{2\mu^2}\,\langle \hat{q}_k\hat{q}_m\epsilon_l^*\epsilon_n\rangle\, Q^*_{kl}Q_{mn} \tag{B.66}$$

$$= \frac{\omega A_Q^2}{30\mu^2}\left[3|Q_{kl}|^2 - |Q_{kk}|^2\right]\,, \tag{B.67}$$

where in the averaging, the photon spin sum $\epsilon_i^*\epsilon_j = \delta_{ij} - \hat{q}_i\hat{q}_j$ was used and therefore with

$$\langle \hat{q}_i\hat{q}_j\rangle = \delta_{ij}/3\,, \tag{B.68}$$

$$\langle \hat{q}_i\hat{q}_j\hat{q}_k\hat{q}_l\rangle = (\delta_{ij}\delta_{kl} + \delta_{ik}\delta_{jl} + \delta_{il}\delta_{jk})/15\,, \tag{B.69}$$

one gets

$$\langle \hat{q}_k\hat{q}_m\epsilon_l^*\epsilon_n\rangle = \frac{1}{15}\,(4\delta_{km}\delta_{ln} - \delta_{kn}\delta_{lm} - \delta_{kl}\delta_{mn})\;. \tag{B.70}$$

Born transition amplitude. If the conditions $\alpha Z_1Z_2/v_i \ll 1$ and $\alpha Z_1Z_2/v_f \ll 1$ are satisfied, we can calculate the inelastic scattering cross section in the Born approximation. For plane waves in the initial and final state, using first order Born approximation in the potential[1]

$$V(r) = \frac{\alpha Z_1Z_2}{r}e^{-m_\phi r}, \tag{B.71}$$

[1] For generality, we start with a Yukawa potential with mediator mass m_ϕ here, but will set $m_\phi = 0$ in the end to relate the results to QED with a massless photon mediator.

the transition amplitude is

$$\mathcal{M}^{(1)} = \langle f^{(1)} | \, \hat{\mathcal{O}}_{\text{emm}} \, | i^{(1)} \rangle \, . \tag{B.72}$$

We will show that in this approximation, the sign of $V(r)$ does not matter. Expanding the wave function to first order, the superscript indicating the order in the Born expansion, we get

$$| i^{(1)} \rangle = | i^{(0)} \rangle + \int \frac{d^3 p}{(2\pi)^3} \frac{\langle p | \, \hat{V} \, | i^{(0)} \rangle}{E_i - E_{\boldsymbol{p}}} \, | p \rangle \tag{B.73}$$

where $|i^{(0)}\rangle$, $|f^{(0)}\rangle$ and $|p\rangle$ are momentum eigenstates, i.e. plane waves, which in position space read

$$\chi^{(0)}_{\boldsymbol{p}_i}(x) = \langle \boldsymbol{r} | i^{(0)} \rangle = e^{i \boldsymbol{p}_i \cdot \boldsymbol{r}} \, , \tag{B.74}$$

$$\chi^{(0)}_{\boldsymbol{p}_f}(x) = \langle \boldsymbol{r} | f^{(0)} \rangle = e^{i \boldsymbol{p}_f \cdot \boldsymbol{r}} \, , \tag{B.75}$$

$$\chi^{(0)}_{\boldsymbol{p}}(x) = \langle \boldsymbol{r} | p \rangle = e^{i \boldsymbol{p} \cdot \boldsymbol{r}} \, . \tag{B.76}$$

Putting this into (B.72) yields

$$\begin{aligned} \mathcal{M}^{(1)} = & \underbrace{\langle f^{(0)} | \, \hat{\mathcal{O}}_{\text{emm}} \, | i^{(0)} \rangle}_{=0} + \underbrace{\int \frac{d^3 p}{(2\pi)^3} \langle f^{(0)} | \, \hat{\mathcal{O}}_{\text{emm}} \, | p \rangle \frac{\langle p | \, \hat{V} \, | i^{(0)} \rangle}{E_i - E_{\boldsymbol{p}}}}_{\mathcal{A}^{(1)}} \\ & + \underbrace{\int \frac{d^3 p}{(2\pi)^3} \frac{\langle f^{(0)} | \, \hat{V} \, | p \rangle}{E_f - E_{\boldsymbol{p}}} \langle p | \, \hat{\mathcal{O}}_{\text{emm}} \, | i^{(0)} \rangle}_{\mathcal{B}^{(1)}} + \mathcal{O}(V^2). \end{aligned} \tag{B.77}$$

B.1.1 Dipole Radiation

The leading order emission operator $\hat{\mathcal{O}}_{\text{emm}}$ for dipole radiation is given by

$$\hat{\mathcal{O}}_D = \frac{e A_D}{\mu \sqrt{2\omega}} \left(\boldsymbol{\epsilon}^* \cdot \hat{\boldsymbol{p}} \right) . \tag{B.78}$$

The amplitude is

$$\mathcal{A}^{(1)} = -i \sqrt{\frac{2\pi}{\omega}} \frac{\alpha^{3/2} A_D}{\mu} \boldsymbol{\epsilon}^* \cdot \int \frac{d^3 p}{(2\pi)^3} \int d^3 x' \, e^{-i \boldsymbol{p}_f \boldsymbol{x}'} \, \boldsymbol{\nabla} e^{i \boldsymbol{p} \boldsymbol{x}'} \int d^3 x \, \frac{e^{-i \boldsymbol{p} \boldsymbol{x}} \, \frac{e^{-m_\phi r}}{r} e^{i \boldsymbol{p}_i \boldsymbol{x}}}{E_i - E} \tag{B.79}$$

$$= -\sqrt{\frac{2\pi}{\omega}} \frac{\alpha^{3/2} A_D}{\mu} \int d^3 p \, \left(\boldsymbol{\epsilon}^* \cdot \boldsymbol{p} \right) \delta^{(3)} \left(\boldsymbol{p}_f - \boldsymbol{p} \right) \frac{4\pi}{|\boldsymbol{p}_i - \boldsymbol{p}|^2 + m_\phi^2} \frac{1}{E_i - E} \tag{B.80}$$

$$= -\sqrt{\frac{2\pi}{\omega}} \frac{\alpha^{3/2} A_D}{\mu} \left(\boldsymbol{\epsilon}^* \cdot \boldsymbol{p}_f \right) \frac{4\pi}{|\boldsymbol{p}_i - \boldsymbol{p}_f|^2 + m_\phi^2} \frac{1}{E_i - E_f} \tag{B.81}$$

$$= -\sqrt{\frac{32\pi^3}{\omega}} \frac{\alpha^{3/2} A_D}{\mu \omega} \frac{\boldsymbol{\epsilon}^* \cdot \boldsymbol{p}_f}{|\boldsymbol{k}|^2 + m_\phi^2}, \tag{B.82}$$

where in the last step we have used $\boldsymbol{k} = \boldsymbol{p}_i - \boldsymbol{p}_f$ and $\omega = E_i - E_f$. Following the same procedure, we get

$$\mathcal{B}^{(1)} = -i\sqrt{\frac{2\pi}{\omega}}\frac{\alpha^{3/2}A_D}{\mu}\boldsymbol{\epsilon}^* \cdot \int \frac{d^3p}{(2\pi)^3}\int d^3x\, \frac{e^{-i\boldsymbol{p}_f\boldsymbol{x}}\,\frac{e^{-m_\phi r}}{r}e^{i\boldsymbol{p}\boldsymbol{x}}}{E_f - E}\int d^3x'\; e^{-i\boldsymbol{p}\boldsymbol{x}'}\;\boldsymbol{\nabla}' e^{i\boldsymbol{p}_i\boldsymbol{x}'} \tag{B.83}$$

$$= -\sqrt{\frac{2\pi}{\omega}}\frac{\alpha^{3/2}A_D}{\mu}\int d^3p\,\left(\boldsymbol{\epsilon}^*\cdot\boldsymbol{p}_i\right)\,\delta^{(3)}(\boldsymbol{p}_i - \boldsymbol{p})\frac{4\pi}{|\boldsymbol{p}_f - \boldsymbol{p}|^2 + m_\phi^2}\frac{1}{E_f - E} \tag{B.84}$$

$$= \sqrt{\frac{2\pi}{\omega}}\frac{\alpha^{3/2}A_D}{\mu}\left(\boldsymbol{\epsilon}^*\cdot\boldsymbol{p}_i\right)\frac{4\pi}{|\boldsymbol{p}_i - \boldsymbol{p}_f|^2 + m_\phi^2}\frac{1}{E_i - E_f} \tag{B.85}$$

$$= \sqrt{\frac{32\pi^3}{\omega}}\frac{\alpha^{3/2}A_D}{\mu\omega}\frac{\boldsymbol{\epsilon}^*\cdot\boldsymbol{p}_i}{|\boldsymbol{k}|^2 + m_\phi^2}. \tag{B.86}$$

Averaging over all directions of the emitted particle yields $\langle\epsilon_i^*\epsilon_j\hat{k}_i\hat{k}_j\rangle = \langle(\delta_{ij} - \hat{q}_i\hat{q}_j)\hat{k}_i\hat{k}_j\rangle = 1 - \langle(\hat{q}\cdot\hat{k})^2\rangle = 2/3$. We then get for the squared transition amplitude

$$\left\langle\left|\mathcal{M}^{(1)}\right|^2\right\rangle_{\hat{\boldsymbol{q}}} = \frac{64\pi^3}{3}\frac{\alpha^3A_D^2}{\mu^2\omega^3}\frac{|\boldsymbol{k}|^2}{\left(|\boldsymbol{k}|^2 + m_\phi^2\right)^2}, \tag{B.87}$$

yielding for the cross section

$$\sigma^{(1)} = \frac{1}{(2\pi)^5}\frac{1}{v}\int d^3p_f\int d^3q\,\left\langle\left|\mathcal{M}^{(1)}\right|^2\right\rangle_{\hat{\boldsymbol{q}}}\delta(E_i - E_f - \omega) \tag{B.88}$$

$$= \frac{8}{3\pi^2}\frac{\alpha^3A_D^2}{\mu p_i}\int dp_f p_f^2 d\Omega_f\int d\omega\frac{1}{\omega}d\Omega_q\;\delta(E_i - E_f - \omega)\frac{p_i^2 + p_f^2 - 2p_ip_f\cos\theta_f}{\left(p_i^2 + p_f^2 - 2p_ip_f\cos\theta_f + m_\phi^2\right)^2} \tag{B.89}$$

$$= \frac{64}{3}\frac{\alpha^3A_D^2}{p_i^2}\int_{m_\phi}^{p_i^2/(2\mu)}d\omega\frac{1}{\omega}\ln\left[\frac{p_i + p_f}{p_i - p_f}\right], \tag{B.90}$$

$$\omega\frac{d\sigma^{(1)}}{d\omega} = \frac{16}{3}\frac{\alpha^3A_D^2}{\mu^2v_i^2}\ln\left[\frac{1 + \sqrt{1-x}}{1 - \sqrt{1-x}}\right]. \tag{B.91}$$

Quantum field theory and quantum mechanics yield the same results for the Born approximation in the non-relativistic limit.

The same calculation can be done using the relation (B.56) which gives

$$\hat{\mathcal{O}}_D = -\frac{ieA_D\sqrt{\omega}}{\sqrt{2}}\left(\boldsymbol{\epsilon}^*\cdot\hat{\boldsymbol{r}}\right). \tag{B.92}$$

Now we want to do the same calculation for $\mathcal{A}$ starting from

$$\mathcal{A}^{(1)} = -ieA_D\sqrt{\frac{\omega}{2}}\boldsymbol{\epsilon}^*\cdot\int\frac{d^3p}{(2\pi)^3}\langle f^{(0)}|\,\boldsymbol{r}\,|p\rangle\frac{\langle p|\,\hat{V}\,|i^{(0)}\rangle}{E_i - E_p}, \tag{B.93}$$

where we have to notice that in our derivation of (B.56) $\omega = E_i - E_f$ are the eigenvalues of the full Hamiltonian $H = p^2/(2m) + V(r)$ whereas in (B.93) E_i and E_p are the eigenvalues of the free Hamiltonian. We will neglect this difference in the following since we assume that our scattering wave function are asymptotically plane waves. This subtlety, however, will give us a different result for $\mathcal{A}$ than we got in (B.110) with the discrepancies only cancelling in the full amplitude $\mathcal{M} = \mathcal{A} + \mathcal{B}$ as we shall see in the following.

First, one needs to rewrite

$$\langle f^{(0)} | \, \boldsymbol{r} \, | p \rangle = \int d^3 r \; \boldsymbol{r} \; e^{-i\boldsymbol{p}_f \boldsymbol{r}} e^{i\boldsymbol{p}\boldsymbol{r}} \tag{B.94}$$

$$= -i \boldsymbol{\nabla}_p \int d^3 r \; e^{-i\boldsymbol{p}_f \boldsymbol{r}} e^{i\boldsymbol{p}\boldsymbol{r}} \tag{B.95}$$

$$= -i \boldsymbol{\nabla}_p \delta^{(3)}\big(\boldsymbol{p}_f - \boldsymbol{p}\big) \, , \tag{B.96}$$

or we can write

$$\langle f^{(0)} | \, \boldsymbol{r} \, | p \rangle = \int d^3 r \; \boldsymbol{r} \; e^{-i\boldsymbol{p}_f \boldsymbol{r}} e^{i\boldsymbol{p}\boldsymbol{r}} \tag{B.97}$$

$$= i \boldsymbol{\nabla}_{p_f} \int d^3 r \; e^{-i\boldsymbol{p}_f \boldsymbol{r}} e^{i\boldsymbol{p}\boldsymbol{r}} \tag{B.98}$$

$$= i \boldsymbol{\nabla}_{p_f} \delta^{(3)}\big(\boldsymbol{p}_f - \boldsymbol{p}\big) \, . \tag{B.99}$$

The first option yields a distributional derivative in the p integral an therefore an additional minus sign when evaluating, leading to the two options yielding the same result, as should be expected. With that, the amplitude is given by

$$\mathcal{A}^{(1)} = \sqrt{2\pi\omega}\alpha^{3/2} A_D \boldsymbol{\epsilon}^* \cdot \int \frac{d^3 p}{(2\pi)^3} \boldsymbol{\nabla}_p \delta^{(3)}\big(\boldsymbol{p}_f - \boldsymbol{p}\big) \int d^3 r \; \frac{e^{-i\boldsymbol{p}\boldsymbol{r}} \, \frac{e^{-m_\phi r}}{r} e^{i\boldsymbol{p}_i \boldsymbol{r}}}{E_i - E} \tag{B.100}$$

$$= -\sqrt{2\pi\omega}\alpha^{3/2} A_D \boldsymbol{\epsilon}^* \cdot \int \frac{d^3 p}{(2\pi)^3} \delta^{(3)}\big(\boldsymbol{p}_f - \boldsymbol{p}\big) \boldsymbol{\nabla}_p \left[\frac{4\pi}{|\boldsymbol{p}_i - \boldsymbol{p}|^2 + m_\phi^2} \frac{1}{E_i - E} \right] \tag{B.101}$$

$$= -\sqrt{32\pi^3\omega}\alpha^{3/2} A_D \left[\frac{\boldsymbol{\epsilon}^* \cdot \boldsymbol{p}_f}{m\omega^2 (|\boldsymbol{k}|^2 + m_\phi^2)} + \frac{2\boldsymbol{\epsilon}^* \cdot \boldsymbol{k}}{\omega (|\boldsymbol{k}|^2 + m_\phi^2)^2} \right] . \tag{B.102}$$

For $\mathcal{B}$ we get

$$\mathcal{B}^{(1)} = \sqrt{32\pi^3\omega}\alpha^{3/2} A_D \left[\frac{\boldsymbol{\epsilon}^* \cdot \boldsymbol{p}_i}{m\omega^2 (|\boldsymbol{k}|^2 + m_\phi^2)} + \frac{2\boldsymbol{\epsilon}^* \cdot \boldsymbol{k}}{\omega (|\boldsymbol{k}|^2 + m_\phi^2)^2} \right] . \tag{B.103}$$

As one can see, the second terms cancel yielding for $\mathcal{M}^{(1)}$ the same result as (B.87).

B.1.2 Quadrupole Radiation (distiguishable particles)

For quadrupole radiation, the leading order emission operator is

$$\hat{\mathcal{O}}_Q = i A_Q \sqrt{\frac{2\pi\alpha}{\omega\mu^2}} (\boldsymbol{q} \cdot \boldsymbol{r})(\boldsymbol{\epsilon} \cdot \boldsymbol{p}) \, , \tag{B.104}$$

and we define the quadrupole tensor $\mathcal{Q}$ as

$$\mathcal{M}^{(1)} = iA_Q \sqrt{\frac{2\pi\alpha}{\omega\mu^2}} q_i \epsilon_j \mathcal{Q}_{ij} \,, \tag{B.105}$$

with

$$\mathcal{Q}_{ij} = \int \frac{d^3p}{(2\pi)^3} \left[\langle f^{(0)} | \, \hat{r}_i \hat{p}_j \, | p \rangle \frac{\langle p | \, \hat{V} \, | i^{(0)} \rangle}{E_i - E_{\boldsymbol{p}}} + \frac{\langle f^{(0)} | \, \hat{V} \, | p \rangle}{E_f - E_{\boldsymbol{p}}} \langle p | \, \hat{r}_i \hat{p}_j \, | i^{(0)} \rangle \right] . \tag{B.106}$$

For simplicity, we switch to a Coulomb potential here, i.e. $m_\phi \to 0$, yielding

$$\begin{aligned}
\mathcal{A}^{(1)} &= -\sqrt{2\pi\omega} \frac{\alpha^{3/2} A_Q}{\mu} n_a \epsilon_b^* \int \frac{d^3p}{(2\pi)^3} \int d^3r' \, e^{-i\boldsymbol{p}_f \cdot \boldsymbol{r}'} \, r'^a \nabla'^b e^{i\boldsymbol{p}\cdot\boldsymbol{r}'} \int d^3r \, \frac{e^{-i\boldsymbol{p}\cdot\boldsymbol{r}} \, \frac{1}{r} e^{i\boldsymbol{p}_i \cdot \boldsymbol{r}}}{E_i - E} && \text{(B.107)} \\
&= i\sqrt{2\pi\omega} \frac{\alpha^{3/2} A_Q}{\mu} n_a \epsilon_b^* \int d^3p \, p^b \frac{4\pi}{|\boldsymbol{p}_i - \boldsymbol{p}|^2} \frac{1}{E_i - E} \partial_p^a \delta^{(3)}(\boldsymbol{p}_f - \boldsymbol{p}) && \text{(B.108)} \\
&= -iA_Q \frac{\sqrt{32\pi^3\alpha^3\omega}}{\mu} n_a \epsilon_b^* \int d^3p \, \delta^{(3)}(\boldsymbol{p}_f - \boldsymbol{p}) \partial_p^a \left(p^b \frac{1}{|\boldsymbol{p}_i - \boldsymbol{p}|^2} \frac{1}{E_i - E} \right) && \text{(B.109)} \\
&= -iA_Q \frac{\sqrt{32\pi^3\alpha^3\omega}}{\mu} n_a \epsilon_b^* \left(\frac{1}{\omega} \frac{\delta^{ab}}{|\boldsymbol{p}_i - \boldsymbol{p}_f|^2} + \frac{1}{\omega} \frac{2(p_i^a - p_f^a) p_f^b}{|\boldsymbol{p}_i - \boldsymbol{p}_f|^4} + \frac{1}{\mu\omega^2} \frac{p_f^a p_f^b}{|\boldsymbol{p}_i - \boldsymbol{p}_f|^2} \right) . && \text{(B.110)}
\end{aligned}$$

Note that if we had carried the mediator mass along up to this point, it would show up in the denominators of (B.110) and we would have to decide to take one of the limits $m_\phi \ll |\boldsymbol{p}_i - \boldsymbol{p}_f|$ or $m_\phi \gg |\boldsymbol{p}_i - \boldsymbol{p}_f|$ at this point of the calculation. For the latter limit, the second term in the brackets of (B.110) is proportional to m_ϕ^{-4} and is therefore negligible with respect to the other terms; we do not show this limit here explicitly. In the massless mediator limit, however, the second term gives an important contribution as will be shown in the following. Following the same procedure, we get

$$\mathcal{B}^{(1)} = -iA_Q \frac{\sqrt{32\pi^3\alpha^3\omega}}{\mu} n_a \epsilon_b^* \left(\frac{1}{\omega} \frac{\delta^{ab}}{|\boldsymbol{p}_i - \boldsymbol{p}_f|^2} - \frac{1}{\omega} \frac{2(p_i^a - p_f^a) p_i^b}{|\boldsymbol{p}_i - \boldsymbol{p}_f|^4} - \frac{1}{\mu\omega^2} \frac{p_i^a p_i^b}{|\boldsymbol{p}_i - \boldsymbol{p}_f|^2} \right) . \tag{B.111}$$

The first term in $\mathcal{A}$ and $\mathcal{B}$ vanishes for a massless mediator since $\boldsymbol{n} \cdot \boldsymbol{\epsilon} = 0$. What remains in the sum is

$$\mathcal{M}^{(1)} = iA_Q \frac{\sqrt{32\pi^3\alpha^3\omega}}{\mu^2\omega^2} n_a \epsilon_b^* \left[\frac{2\mu\omega(p_i^a - p_f^a)(p_i^b - p_f^b)}{|\boldsymbol{k}|^4} + \frac{p_i^a p_i^b - p_f^a p_f^b}{|\boldsymbol{k}|^2} \right] . \tag{B.112}$$

Averaging over all directions of the emitted particle $\langle n_a \epsilon_b^* n_c \epsilon_d \rangle = \delta_{ac}\delta_{bd}/3 - (\delta_{ac}\delta_{bd} + \delta_{ad}\delta_{bc} + \delta_{ab}\delta_{cd})/15$ yields for the squared amplitude

$$\begin{aligned}
\left\langle \left| \mathcal{M}^{(1)} \right|^2 \right\rangle_{\hat{\boldsymbol{q}}} = \frac{32\pi^3\alpha^3 A_Q^2}{\mu^4\omega^3} \langle n_a \epsilon_b^* n_c \epsilon_d \rangle & \left[\frac{2\mu\omega(p_i^a - p_f^a)(p_i^b - p_f^b)}{|\boldsymbol{k}|^4} + \frac{p_i^a p_i^b - p_f^a p_f^b}{|\boldsymbol{k}|^2} \right] \\
\times & \left[\frac{2\mu\omega(p_i^c - p_f^c)(p_i^d - p_f^d)}{|\boldsymbol{k}|^4} + \frac{p_i^c p_i^d - p_f^c p_f^d}{|\boldsymbol{k}|^2} \right]
\end{aligned} \tag{B.113}$$

$$
\begin{aligned}
&= \frac{32\pi^3\alpha^3 A_Q^2}{15\mu^4\omega^3}\left[\frac{2\left(|\boldsymbol{p}_i|^2-|\boldsymbol{p}_f|^2\right)^2+6\left(|\boldsymbol{p}_i|^2|\boldsymbol{p}_f|^2-(\boldsymbol{p}_i\cdot\boldsymbol{p}_f)^2\right)}{|\boldsymbol{k}|^4}\right.\\
&\quad\left.+\frac{2\left(|\boldsymbol{p}_i|^2-|\boldsymbol{p}_f|^2\right)^2|\boldsymbol{p}_i-\boldsymbol{p}_f|^4}{|\boldsymbol{k}|^8}+\frac{4\left(|\boldsymbol{p}_i|^2-|\boldsymbol{p}_f|^2\right)^2|\boldsymbol{p}_i-\boldsymbol{p}_f|^2}{|\boldsymbol{k}|^6}\right] \qquad \text{(B.114)}\\
&= \frac{32\pi^3\alpha^3 A_Q^2}{15\mu^4\omega^3}\frac{|\boldsymbol{l}|^2}{|\boldsymbol{k}|^2}\left[2(\hat{\boldsymbol{k}}\cdot\hat{\boldsymbol{l}})^2+\frac{1}{2}\left(3+(\hat{\boldsymbol{k}}\cdot\hat{\boldsymbol{l}})^2\right)+4(\hat{\boldsymbol{k}}\cdot\hat{\boldsymbol{l}})^2\right] \qquad \text{(B.115)}\\
&= \frac{16\pi^3\alpha^3 A_Q^2}{15\mu^4\omega^3}\frac{|\boldsymbol{l}|^2}{|\boldsymbol{k}|^2}\left[3+13(\hat{\boldsymbol{k}}\cdot\hat{\boldsymbol{l}})^2\right], \qquad \text{(B.116)}
\end{aligned}
$$

where in the second step we have used that

$$
(|\boldsymbol{p}_i|^2-|\boldsymbol{p}_f|^2)^2 = 4\mu^2\omega^2 = |\boldsymbol{k}|^2|\boldsymbol{l}|^2(\hat{\boldsymbol{k}}\cdot\hat{\boldsymbol{l}})^2, \qquad \text{(B.117)}
$$

$$
|\boldsymbol{p}_i|^2|\boldsymbol{p}_f|^2-(\boldsymbol{p}_i\cdot\boldsymbol{p}_f)^2 = \frac{1}{4}|\boldsymbol{k}|^2|\boldsymbol{l}|^2\left[1-(\hat{\boldsymbol{k}}\cdot\hat{\boldsymbol{l}})^2\right]. \qquad \text{(B.118)}
$$

Therefore, we get for the cross section

$$
\omega\frac{d\sigma^{(1)}}{d\omega} = \frac{8}{15}\frac{\alpha^3 A_Q^2}{\mu^2}\left[10\sqrt{1-x}+3(2-x)\ln\left(\frac{1+\sqrt{1-x}}{1-\sqrt{1-x}}\right)\right], \qquad \text{(B.119)}
$$

which agrees with the QFT result.

Again, the same calculation can be done using the relation (B.45) which leads to the radiation operator

$$
\hat{\mathcal{O}}_Q = A_Q\sqrt{\frac{\pi\alpha\omega}{2\mu}}(\boldsymbol{q}\cdot\boldsymbol{r})(\boldsymbol{\epsilon}\cdot\boldsymbol{r}), \qquad \text{(B.120)}
$$

and gives

$$
\begin{aligned}
\mathcal{A}^{(1)} &= A_Q\sqrt{\frac{\alpha^3\pi\omega^3}{2}}n_a\epsilon_b^*\int\frac{d^3p}{(2\pi)^3}\int d^3r'\,e^{-i\boldsymbol{p}_f\cdot\boldsymbol{r}'}\,r'^a r'^b e^{i\boldsymbol{p}\cdot\boldsymbol{r}'}\int d^3r\,\frac{e^{-i\boldsymbol{p}\cdot\boldsymbol{r}}\,\frac{1}{r}e^{i\boldsymbol{p}_i\cdot\boldsymbol{r}}}{E_i-E} \qquad \text{(B.121)}\\
&= -A_Q\sqrt{\frac{\alpha^3\pi\omega^3}{2}}n_a\epsilon_b^*\int d^3p\frac{4\pi}{|\boldsymbol{p}_i-\boldsymbol{p}|^2}\frac{1}{E_i-E}\partial_p^a\partial_p^b\delta^{(3)}(\boldsymbol{p}_f-\boldsymbol{p}) \qquad \text{(B.122)}\\
&= -A_Q\sqrt{8\pi^3\alpha^3\omega^3}n_a\epsilon_b^*\int d^3p\,\delta^{(3)}(\boldsymbol{p}_f-\boldsymbol{p})\partial_p^a\partial_p^b\left(\frac{1}{|\boldsymbol{p}_i-\boldsymbol{p}|^2}\frac{1}{E_i-E}\right) \qquad \text{(B.123)}\\
&= -A_Q\sqrt{8\pi^3\alpha^3\omega^3}n_a\epsilon_b^*\left[\frac{8}{\omega}\frac{(p_i^a-p_f^a)(p_i^b-p_f^b)}{|\boldsymbol{p}_i-\boldsymbol{p}_f|^6}+\frac{2}{\mu\omega^2}\frac{(p_i^a-p_f^a)p_f^b+p_f^a(p_i^b-p_f^b)}{|\boldsymbol{p}_i-\boldsymbol{p}_f|^4}\right.\\
&\quad\left.+\frac{2}{\mu^2\omega^3}\frac{p_f^a p_f^b}{|\boldsymbol{p}_i-\boldsymbol{p}_f|^2}\right], \qquad \text{(B.124)}
\end{aligned}
$$

where we have already omitted the terms proportional to δ_{ab}. With

$$
\mathcal{B}^{(1)} = A_Q\sqrt{8\pi^3\alpha^3\omega^3}n_a\epsilon_b^*\left[\frac{8}{\omega}\frac{(p_i^a-p_f^a)(p_i^b-p_f^b)}{|\boldsymbol{p}_i-\boldsymbol{p}_f|^6}+\frac{2}{\mu\omega^2}\frac{(p_i^a-p_f^a)p_i^b+p_i^a(p_i^b-p_f^b)}{|\boldsymbol{p}_i-\boldsymbol{p}_f|^4}\right.
$$

$$+\frac{2}{\mu^2\omega^3}\frac{p_i^a p_i^b}{|\boldsymbol{p}_i-\boldsymbol{p}_f|^2},\Bigg] \tag{B.125}$$

the first terms cancel and the full amplitude is

$$\mathcal{M}^{(1)} = A_Q\sqrt{\frac{32\pi^3\alpha^3}{\mu^4\omega^3}}n_a\epsilon_b^*\left[\frac{2\mu\omega(p_i^a-p_f^a)(p_i^b-p_f^b)}{|\boldsymbol{k}|^4}+\frac{p_i^a p_i^b-p_f^a p_f^b}{|\boldsymbol{k}|^2}\right], \tag{B.126}$$

yielding the same result as (B.116) for the squared amplitude.

B.2 Nordsieck Integral

In the following, we sketch the solution of the Nordsieck integral as in [151] which we used in Eq. (14) of [3] to solve the transition matrix element for the emission of bremsstrahlung

$$\mathcal{M}_I = -i\frac{eA_I}{\mu\sqrt{2\omega}}\int d^3r\ \chi^*_{\boldsymbol{p}_f}(\boldsymbol{r})\ \mathcal{O}_I\ \left(\boldsymbol{\epsilon}^*_{\boldsymbol{q},\lambda}\cdot\boldsymbol{\nabla}\right)\chi_{\boldsymbol{p}_i}(\boldsymbol{r})\,. \tag{B.127}$$

with the variable definitions as in [3]. The integral to solve is

$$\mathcal{I}_N = \int d^3r\frac{e^{-\lambda r}}{r}e^{i\boldsymbol{k}\cdot\boldsymbol{r}}{}_1F_1\Big(i\nu_f,1,i(p_f r+s_f\ \boldsymbol{p}_f\cdot\boldsymbol{r})\Big){}_1F_1\Big(i\nu_i,1,i(p_i r+s_i\ \boldsymbol{p}_i\cdot\boldsymbol{r})\Big), \tag{B.128}$$

where $-\boldsymbol{k} = s_i\boldsymbol{p}_i + s_f\boldsymbol{p}_f$, $s_{i/f}=\pm1$. We get the dipole and quadrupole transition amplitudes from the solution of the Nordsieck integral by

$$\mathcal{D} = \lim_{\lambda\to0} A_i A_f^*\ p_i\left(\boldsymbol{\epsilon}\cdot\partial_{\boldsymbol{p}_i}\right)\mathcal{I}_N, \tag{B.129}$$

$$\mathcal{Q} = \lim_{\lambda\to0} A_i A_f\left(\boldsymbol{q}\cdot\partial_{\boldsymbol{k}}\right)\left[p_i\left(\boldsymbol{\epsilon}\cdot\partial_{\boldsymbol{p}_i}\right)+i\left(\boldsymbol{\epsilon}\cdot\boldsymbol{p}_i\right)\partial_\lambda\right]\mathcal{I}_N. \tag{B.130}$$

To solve $\mathcal{I}_N$ we rewrite the confluent hypergeometric functions as contour integrals [151],

$${}_1F_1\left(ia,1,z\right) = \frac{1}{2\pi i}\oint_{(0,1)} dt\ t^{ia-1}\left(t-1\right)^{-ia}e^{zt}\,, \tag{B.131}$$

with the contour encircling $t=0$ and $t=1$ in a positive manner, *i.e.*

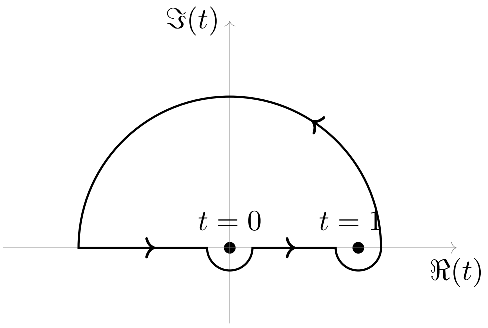

This yields

$$\begin{aligned}\mathcal{I}_N &= -\frac{1}{4\pi^2}\oint dt_f \oint dt_i\, t_i^{ia_i-1}\,(t_i-1)^{-ia_i}\; t_f^{ia_f-1}\,\big(t_f-1\big)^{-ia_f} \\ &\quad\times \int d^3x \frac{1}{r} e^{-\lambda r + i\boldsymbol{k}\cdot\boldsymbol{x} + it_i(p_i r + s_i \boldsymbol{p}_i\cdot\boldsymbol{x}) + it_f(p_f r + s_f\boldsymbol{p}_f\cdot\boldsymbol{x})} && \text{(B.132)} \\ &= \frac{1}{2\pi}\oint dt_f \oint dt_i\, t_i^{ia_i-1}\,(t_i-1)^{-ia_i}\; t_f^{ia_f-1}\,\big(t_f-1\big)^{-ia_f} \\ &\quad\times \frac{1}{\alpha(t_i-1)+\gamma t_i+\beta(t_i-1)t_f+\delta t_i t_f}\,, && \text{(B.133)}\end{aligned}$$

with

$$\alpha = \frac{1}{2}(k^2+\lambda^2), \qquad \beta = s_f\boldsymbol{p}_f\cdot\boldsymbol{k} - i\lambda p_f, \qquad \gamma = -s_i\boldsymbol{p}_i\cdot\boldsymbol{k} + i\lambda p_i - \alpha, \tag{B.134}$$

$$\delta = p_i p_f - s_i s_f \boldsymbol{p}_i\cdot\boldsymbol{p}_f - \beta, \quad a_i = \nu_i, \qquad a_f = \nu_f. \tag{B.135}$$

The solution of the volume integral has a first order pole at

$$t_i = t^* = \frac{\alpha+\beta t_f}{\alpha+\gamma+\beta t_f+\delta t_f}\,, \tag{B.136}$$

situated in the lower half plane outside the t_i contour. Since the integrand is simply connected and analytic with the exception of poles and falls off $\propto t_i^{-2}$ as $t_i\to\infty$, we can extend the contour to infinity and close it at the lower half plane to exclude 0 and 1 and include the pole of the space integration.

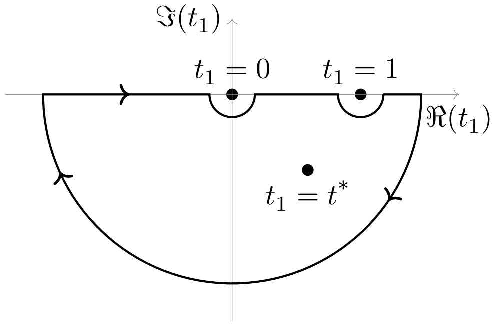

The solution of the t_i integral is then given by the residue at t^* with a minus sign due to the clockwise orientation of the contour, *i.e.*

$$\mathcal{I}_N = \frac{1}{2\pi}\oint dt_f\, t_f^{ia_f-1}\big(t_f-1\big)^{-ia_f}\oint dt_i\, t_i^{ia_i-1}(t_i-1)^{-ia_i}\,\frac{1}{\alpha(t_i-1)+\gamma t_i+\beta(t_i-1)t_f+\delta t_i t_f} \tag{B.137}$$

$$= e^{-\pi a_i}\oint dt_f\, t_f^{ia_f-1}\big(t_f-1\big)^{-ia_f}\big(\gamma+\delta t_f\big)^{-ia_i}\big(\alpha+\beta t_f\big)^{ia_i-1}. \tag{B.138}$$

The integrand has gained two new singularities, $t_f=-\alpha/\beta$ and $t_f=-\gamma/\delta$, all of which have negative imaginary parts and are therefore excluded from the contour.

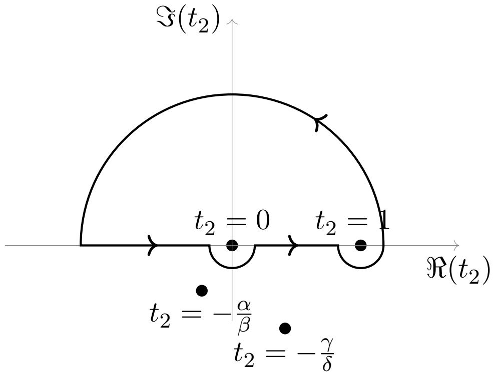

Again, the integrand is simply connected and analytic with the exception of poles and falls off faster than $\propto t_i^{-1}$ as $t_i \to \infty$. One can substitute $t = 1/t$ to get

$$\mathcal{I}_N = -ie^{-\pi a_i} \oint dt \; (1-t)^{-ia_f} (\gamma t + \delta)^{-ia_i} (\alpha t + \beta)^{ia_i - 1} \;, \tag{B.139}$$

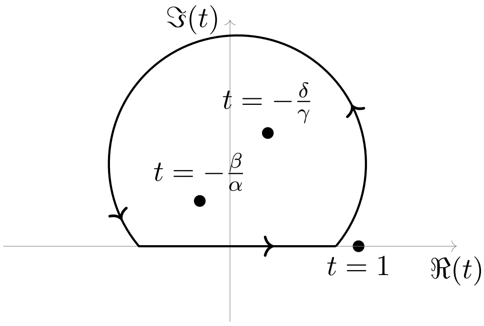

with $t = 1$ excluded from the contour. Now, one can put (B.139) into the standard form of the generalized hypergeometric function

$${}_1F_2\,(a,b,c;z) = \frac{1}{2\pi i} \frac{\Gamma(c)\Gamma(b-c+1)}{\Gamma(b)} \oint_{-\infty}^{(0+,z+)} d\tau \; \tau^{a-c} (1-\tau)^{c-b-1} (\tau - z)^{-a} \,. \tag{B.140}$$

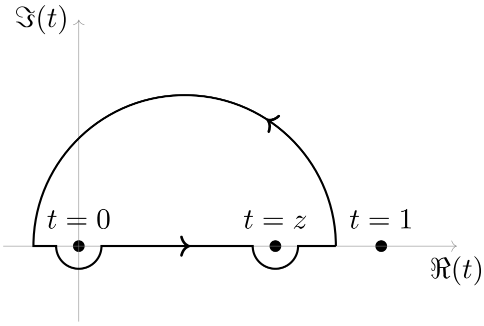

With the transformation $\tau = (\gamma t + \delta)/(\gamma + \delta)$ one gets

$$\mathcal{I}_N = -ie^{-\pi a_i} \frac{1}{\alpha} \left(\frac{\alpha}{\gamma}\right)^{ia_i} \left(\frac{\gamma+\delta}{\gamma}\right)^{-ia_f} \oint_{(x,y)} d\tau \; \tau^{-ia_i} (1-\tau)^{-ia_f} (\tau - z)^{ia_i - 1} \;, \tag{B.141}$$

with

$$z = \frac{\alpha\delta - \beta\gamma}{\alpha(\gamma + \delta)}\,. \tag{B.142}$$

The solution to the Nordsieck integral is

$$\mathcal{I}_N = \frac{2\pi}{\alpha} e^{-\pi a_i} \left(\frac{\alpha}{\gamma}\right)^{ia_i} \left(\frac{\gamma + \delta}{\gamma}\right)^{-ia_f} {}_2F_1\left(1 - ia_i, ia_f, 1, \frac{\alpha\delta - \beta\gamma}{\alpha(\gamma + \delta)}\right). \tag{B.143}$$

Using the properties of the hypergeometric functions

$${}_2F_1\left(a, b, c, z\right) = {}_2F_1\left(b, a, c, z\right)\,, \tag{B.144}$$

$${}_2F_1\left(a, b, c, z\right) = \left(1 - z\right)^{-b} {}_2F_1\left(b, 1 - a, c, \frac{z}{z - 1}\right)\,, \tag{B.145}$$

it can be rewritten to

$$\mathcal{I}_N = \frac{2\pi}{\alpha} e^{-\pi a_i} \left(\frac{\alpha}{\gamma}\right)^{ia_i} \left(\frac{\gamma + \delta}{\gamma}\right)^{-ia_f} \left(1 - \frac{\alpha\delta - \beta\gamma}{\alpha(\gamma + \delta)}\right)^{-ia_f} {}_2F_1\left(ia_i, ia_f, 1, \frac{\beta\gamma - \alpha\delta}{\gamma(\alpha + \beta)}\right). \tag{B.146}$$

C Spin dependent self-interacting dark matter

In this appendix, we discuss a project on spin dependent self-interacting dark matter mentioned in Sec. 2.2.1 that the author of this thesis was working on during his stay at Johns Hopkins University. The work, however, was not published since we ran into numerical problems which we were not able to solve before Ref. [147] appeared on the arXiv, treating exactly the problem that we were trying to tackle.

The idea of this project was to numerically calculate cross sections for SIDM particles with spin-dependent interactions by decomposing the wave functions into partial waves and numerically solving the Schrödinger equation of the scattering potential. A similar analysis was done for spin-independent interactions in Ref. [104]. The status of the unfinished project at the time that Ref. [147] was published, is outlined below.

C.1 Scattering potentials and Born Cross Section

The aim of this appendix is to discuss spin-dependent self-scattering of dark matter particles X with spin $1/2$ and mass m_{X} with a pseudoscalar (PS) or axial vector (AV) mediator with mass m_ϕ. In addition, we want to add interactions with the vector field ϕ^μ where X couples to the field with electric (EDM) or magnetic (MDM) dipole moments. The interaction Lagrangians hence read

$$\mathcal{L} = \begin{cases} i\, g_{\mathrm{PS}}\, \bar{X}\gamma^5 X\,\phi & \text{(pseudo scalar)}, \\ g_{\mathrm{AV}}\, \bar{X}\gamma^\mu\gamma^5 X\,\phi_\mu & \text{(axial vector)}, \\ \frac{1}{2}\mu_{\mathrm{X}}\, \bar{X}\sigma^{\mu\nu} X\,\phi_{\mu\nu} & \text{(magnetic dipole)}, \\ \frac{i}{2}d_{\mathrm{X}}\, \bar{X}\sigma^{\mu\nu}\gamma^5 X\,\phi_{\mu\nu} & \text{(electric dipole)}, \end{cases} \tag{C.147}$$

with $\phi_{\mu\nu} = \partial_\mu\phi_\nu - \partial_\nu\phi_\mu$ and g_{PS} and g_{AV} are dimensionless pseudoscalar and axialvector coupling constants while d_{X} and μ_{X} are dimensionfull dark electric and magnetic dipole moments. The non-relativistic Fourier transforms of the interaction potentials derived from these Lagrangians are

$$\tilde{V}_{\mathrm{PS}}(\boldsymbol{q}) = -\frac{g_{\mathrm{PS}}^2}{|\boldsymbol{q}|^2 + m_\phi^2}\frac{(\boldsymbol{S}_1\cdot\boldsymbol{q})\,(\boldsymbol{S}_2\cdot\boldsymbol{q})}{m_{\mathrm{X}}^2}\,, \tag{C.148a}$$

$$\tilde{V}_{\mathrm{AV}}(\boldsymbol{q}) = -\frac{4g_{\mathrm{AV}}^2}{|\boldsymbol{q}|^2 + m_\phi^2}\left[\frac{(\boldsymbol{S}_1\cdot\boldsymbol{q})\,(\boldsymbol{S}_2\cdot\boldsymbol{q})}{m_\phi^2} + (\boldsymbol{S}_1\cdot\boldsymbol{S}_2)\right]\,, \tag{C.148b}$$

$$\tilde{V}_{\mathrm{MDM}}(\boldsymbol{q}) = -\frac{4\mu_{\mathrm{X}}^2}{|\boldsymbol{q}|^2 + m_\phi^2}\left[(\boldsymbol{S}_1\cdot\boldsymbol{q})\,(\boldsymbol{S}_2\cdot\boldsymbol{q}) - |\boldsymbol{q}|^2\,(\boldsymbol{S}_1\cdot\boldsymbol{S}_2)\right]\,, \tag{C.148c}$$

$$\tilde{V}_{\mathrm{EDM}}(\boldsymbol{q}) = -\frac{4d_{\mathrm{X}}^2}{|\boldsymbol{q}|^2 + m_\phi^2}\,(\boldsymbol{S}_1\cdot\boldsymbol{q})\,(\boldsymbol{S}_2\cdot\boldsymbol{q})\,, \tag{C.148d}$$

with the particle spins $\boldsymbol{S}_{1,2}$, the dark matter mass m_{X}, the mediator mass m_ϕ and the transferred momentum $\boldsymbol{q}$. The scattering potentials can be obtained by Fourier transforming the expressions in Eq. (C.148), i.e.

$$V_{\text{PS}}(\boldsymbol{r}) = \frac{g_{\text{PS}}^2}{4\pi} \frac{e^{-m_\phi r}}{m_{\text{X}}^2} \left[(\boldsymbol{S}_1 \cdot \hat{\boldsymbol{r}})(\boldsymbol{S}_2 \cdot \hat{\boldsymbol{r}}) \left(\frac{3}{r^3} + \frac{3m_\phi}{r^2} + \frac{m_\phi^2}{r} \right) - \boldsymbol{S}_1 \cdot \boldsymbol{S}_2 \left(\frac{1}{r^3} + \frac{m_\phi}{r^2} + \frac{4\pi}{3} \delta^3(\boldsymbol{r}) \right) \right], \tag{C.149a}$$

$$V_{\text{AV}}(\boldsymbol{r}) = \frac{g_{\text{AV}}^2}{\pi} \frac{e^{-m_\phi r}}{m_\phi^2} \left[(\boldsymbol{S}_1 \cdot \hat{\boldsymbol{r}})(\boldsymbol{S}_2 \cdot \hat{\boldsymbol{r}}) \left(\frac{3}{r^3} + \frac{3m_\phi}{r^2} + \frac{m_\phi^2}{r} \right) - \boldsymbol{S}_1 \cdot \boldsymbol{S}_2 \left(\frac{1}{r^3} + \frac{m_\phi}{r^2} + \frac{m_\phi^2}{r} + \frac{4\pi}{3} \delta^3(\boldsymbol{r}) \right) \right], \tag{C.149b}$$

$$V_{\text{MDM}}(\boldsymbol{r}) = \frac{\mu_{\text{X}}^2}{\pi} e^{-m_\phi r} \left[(\boldsymbol{S}_1 \cdot \hat{\boldsymbol{r}})(\boldsymbol{S}_2 \cdot \hat{\boldsymbol{r}}) \left(\frac{3}{r^3} + \frac{3m_\phi}{r^2} + \frac{m_\phi^2}{r} \right) - \boldsymbol{S}_1 \cdot \boldsymbol{S}_2 \left(\frac{1}{r^3} + \frac{m_\phi}{r^2} + \frac{m_\phi^2}{r} - \frac{8\pi}{3} \delta^3(\boldsymbol{r}) \right) \right], \tag{C.149c}$$

$$V_{\text{EDM}}(\boldsymbol{r}) = \frac{d_{\text{X}}^2}{\pi} e^{-m_\phi r} \left[(\boldsymbol{S}_1 \cdot \hat{\boldsymbol{r}})(\boldsymbol{S}_2 \cdot \hat{\boldsymbol{r}}) \left(\frac{3}{r^3} + \frac{3m_\phi}{r^2} + \frac{m_\phi^2}{r} \right) - \boldsymbol{S}_1 \cdot \boldsymbol{S}_2 \left(\frac{1}{r^3} + \frac{m_\phi}{r^2} - \frac{8\pi}{3} \delta^3(\boldsymbol{r}) \right) \right], \tag{C.149d}$$

where $r = |\boldsymbol{r}|$ is the distance between the scattering particles. The problem can be reformulated in terms of dimensionless quantities a and b with

$$a \equiv \frac{v}{2\alpha_{\text{X}}}, \quad b \equiv \frac{\alpha_{\text{X}} m_{\text{X}}}{m_\phi}, \quad \alpha_{\text{X}} \equiv \left\{ \frac{m_\phi^2}{m_{\text{X}}^2} \frac{g_{\text{PS}}^2}{4\pi}, \frac{g_{\text{AV}}^2}{\pi}, \frac{m_\phi^2 \mu_{\text{X}}^2}{\pi}, \frac{m_\phi^2 d_{\text{X}}^2}{\pi} \right\}. \tag{C.150}$$

In the limit where $b \ll 1$, the scattering potential is short ranged and perturbative calculations are possible. On the other hand, even when $b \gg 1$, but $a \gg 1$, perturbativity is guaranteed. We will refer to both cases as the Born limit, where the former is the massive and the latter the massless mediator case. To leading order in relative velocity v, the non-relativistic Born cross section can be written as a function of a and b. Investigating momentum transport between particles, it is often beneficial to calculate the transport cross section σ_T or the viscosity cross section σ_V instead of the standard cross section σ. The respective cross sections are given by

$$\sigma = \int d\Omega \, \frac{d\sigma}{d\Omega}, \qquad \sigma_T = \int d\Omega \, (1 - \cos\theta) \, \frac{d\sigma}{d\Omega}, \qquad \sigma_V = \int d\Omega \, \sin^2\theta \, \frac{d\sigma}{d\Omega}. \tag{C.151}$$

The viscosity (for identical particles) and transport (for distinguishable particles) Born cross sections (with $k = m_X v/2$) can then be written as

$$\frac{k^2}{\pi} \sigma_V = \begin{cases} \frac{1}{a^2} \left[\frac{5+20a^2b^2+16a^4b^4}{4(2a^4b^4+a^2b^2)} \ln\left(4a^2b^2+1\right) - 5 \right] & \text{(scalar/vector)}, \\ \frac{1}{16a^2} \left[\frac{(3+8a^2b^2)^2}{4(2a^4b^4+a^2b^2)} \ln\left(4a^2b^2+1\right) - (9+12a^2b^2-8a^4b^4) \right] & \text{(pseudo scalar)}, \\ \frac{3}{16a^2} \left[\frac{3+12a^2b^2+16a^4b^4}{4(2a^4b^4+a^2b^2)} \ln\left(4a^2b^2+1\right) - 3 \right] & \text{(axial vector)}, \\ \frac{1}{8a^2} \left[\frac{(3+8a^2b^2)^2}{4(2a^4b^4+a^2b^2)} \ln\left(4a^2b^2+1\right) - (9+12a^2b^2-8a^4b^4) \right] & \text{(magnetic dipole)}, \\ \frac{1}{16a^2} \left[\frac{(3+8a^2b^2)^2}{4(2a^4b^4+a^2b^2)} \ln\left(4a^2b^2+1\right) - (9+12a^2b^2-8a^4b^4) \right] & \text{(electric dipole)}, \end{cases} \tag{C.152}$$

$$\frac{k^2}{\pi}\sigma_T = \begin{cases} \frac{1}{2a^2}\left[\ln\left(4a^2b^2+1\right) - \frac{4a^2b^2}{4a^2b^2+1}\right] & \text{(scalar/vector)}, \\ \frac{3}{32a^2}\left[\ln\left(4a^2b^2+1\right) - \frac{4a^2b^2(1+2a^2b^2-8/3\,a^4b^4)}{4a^2b^2+1}\right] & \text{(pseudo scalar)}, \\ \frac{3}{32a^2}\left[\ln\left(4a^2b^2+1\right) - \frac{4a^2b^2}{4a^2b^2+1}\right] & \text{(axial vector)}, \\ \frac{3}{16a^2}\left[\ln\left(4a^2b^2+1\right) - \frac{4a^2b^2(1+2a^2b^2-8/3\,a^4b^4)}{4a^2b^2+1}\right] & \text{(magnetic dipole)}, \\ \frac{3}{32a^2}\left[\ln\left(4a^2b^2+1\right) - \frac{4a^2b^2(1+2a^2b^2-8/3\,a^4b^4)}{4a^2b^2+1}\right] & \text{(electric dipole)}. \end{cases} \tag{C.153}$$

The aim of the numerical treatment, discussed in the following, is to analyse departures from the Born cross sections in regimes where the perturbative approach is not valid.

C.2 Scattering in spin-dependent potentials

The scattering potentials of interest can be written as

$$V(\boldsymbol{r}) = (\boldsymbol{S}_1 \cdot \hat{\boldsymbol{r}})\,(\boldsymbol{S}_2 \cdot \hat{\boldsymbol{r}})\,V_1(r) + (\boldsymbol{S}_1 \cdot \boldsymbol{S}_2)\,V_2(r)\,. \tag{C.154}$$

It is shown in the appendix of Ref. [155] that a partial separation of the Schrödinger equation is possible for spin 1/2 particles in the total angular momentum basis. We write the wave function as

$$\psi_{s,s_z}(r,\theta,\phi) = R_\ell^{s,s_z}(r) Y_{\ell,m}(\theta,\phi)\xi_{s,s_z}\,, \tag{C.155}$$

with $Y_{\ell,m}$ being the spherical harmonics, ξ_{s,s_z} the singlet and triplet spin functions and picking a basis $|s,l,j,j_z\rangle$ which are eigenfunctions of $\{S^2, L^2, J^2, J_z\}$ with eigenvalues $\{s(s+1), \ell(\ell+1), j(j+1), j_z\}$. In this basis, the singlet and triplet spin states for arbitrary ℓ can be represented as

$$\xi_{0,0}:\ |0,j,j,j_z\rangle\,, \qquad \xi_{1,0}:\ |1,j,j,j_z\rangle\,, \qquad \xi_{1,1}:\ |1,j+1,j,j_z\rangle\,, \qquad \xi_{1,-1}:\ |1,j-1,j,j_z\rangle\,. \tag{C.156}$$

Now, it is easy to find eigenvalues and eigenfunctions for the operators $\{(\boldsymbol{S}_1\cdot\boldsymbol{S}_2), (\boldsymbol{S}_1\cdot\hat{\boldsymbol{r}})(\boldsymbol{S}_2\cdot\hat{\boldsymbol{r}})\}$, using $(\boldsymbol{S}_1\cdot\boldsymbol{S}_2) = (\boldsymbol{S}^2 - \boldsymbol{S}_1^2 - \boldsymbol{S}_2^2)/2$ and by rewriting $(\boldsymbol{S}_1\cdot\hat{\boldsymbol{r}})\,(\boldsymbol{S}_2\cdot\hat{\boldsymbol{r}})$ in terms of linear combinations of spherical harmonics, i.e.

$$|0,j,j,j_z\rangle:\ \left\{-\frac{3}{4}, -\frac{1}{4}\right\}, \tag{C.157}$$

$$\frac{1}{\sqrt{2j+1}}\left(\sqrt{j+1}\,|1,j+1,j,j_z\rangle - \sqrt{j}\,|1,j-1,j,j_z\rangle\right):\ \left\{+\frac{1}{4}, -\frac{1}{4}\right\}, \tag{C.158}$$

$$\frac{1}{\sqrt{2j+1}}\left(\sqrt{j+1}\,|1,j-1,j,j_z\rangle + \sqrt{j}\,|1,j+1,j,j_z\rangle\right):\ \left\{+\frac{1}{4}, +\frac{1}{4}\right\}, \tag{C.159}$$

$$|1,j,j,j_z\rangle:\ \left\{+\frac{1}{4}, +\frac{1}{4}\right\}. \tag{C.160}$$

The spin operators can therefore be written as a 4×4 matrix in the singlet/triplet basis

$$(\boldsymbol{S}_1\cdot\boldsymbol{S}_2) = \frac{1}{4}\begin{pmatrix} -3 & 0 & 0 & 0 \\ 0 & 1 & 0 & 0 \\ 0 & 0 & 1 & 0 \\ 0 & 0 & 0 & 1 \end{pmatrix}, \tag{C.161}$$

$$
(\boldsymbol{S}_1 \cdot \hat{\boldsymbol{r}})\,(\boldsymbol{S}_2 \cdot \hat{\boldsymbol{r}}) = \frac{1}{4} \begin{pmatrix} -1 & 0 & 0 & 0 \\ 0 & 1 & 0 & 0 \\ 0 & 0 & -\frac{1}{2j+1} & \frac{2\sqrt{j(j+1)}}{2j+1} \\ 0 & 0 & \frac{2\sqrt{j(j+1)}}{2j+1} & \frac{1}{2j+1} \end{pmatrix}, \tag{C.162}
$$

$$
3\,(\boldsymbol{S}_1 \cdot \hat{\boldsymbol{r}})\,(\boldsymbol{S}_2 \cdot \hat{\boldsymbol{r}}) - (\boldsymbol{S}_1 \cdot \boldsymbol{S}_2) = \frac{1}{2} \begin{pmatrix} 0 & 0 & 0 & 0 \\ 0 & 1 & 0 & 0 \\ 0 & 0 & -\frac{j+2}{2j+1} & \frac{3\sqrt{j(j+1)}}{2j+1} \\ 0 & 0 & \frac{3\sqrt{j(j+1)}}{2j+1} & -\frac{j-1}{2j+1} \end{pmatrix}, \tag{C.163}
$$

where we have to note that this is only valid for $j > 0$ since for $j = 0$ only one triplet state $|1,1,0,0\rangle$ exists. The radial Schrödinger equation to solve is

$$
\left\{ -\frac{d^2}{dr^2} - \frac{2}{r}\frac{d}{dr} + \frac{\ell(\ell+1)}{r^2} + 2\mu[(\boldsymbol{S}_1 \cdot \hat{\boldsymbol{r}})(\boldsymbol{S}_2 \cdot \hat{\boldsymbol{r}})V_1(r) + (\boldsymbol{S}_1 \cdot \boldsymbol{S}_2)V_2(r)] - k \right\} \begin{pmatrix} R_j^{(0,0)}(r) \\ R_j^{(1,0)}(r) \\ R_{j+1}^{(1,1)}(r) \\ R_{j-1}^{(1,-1)}(r) \end{pmatrix} = 0. \tag{C.164}
$$

Note that this is the Schrödinger equation for a fixed j and not for a fixed ℓ. This means that the angular momentum term is different for the components of $R_\ell^{(s,s_z)}(r)$. Another way of saying this is that the short range scattering potential conserves the total angular momentum J^2 but not the orbital angular momentum L^2 whereas the asymptotic solutions for large r are eigenfunctions of J^2 and L^2.

Switching to the dimensionless variables defined in Eq. (12) in [104], i.e.

$$
\chi_\ell^{(s,s_z)} \equiv r R_\ell^{(s,s_z)}, \quad x \equiv \alpha_\mathrm{X} m_\mathrm{X} r, \quad a \equiv \frac{v}{2\alpha_\mathrm{X}}, \quad b \equiv \frac{\alpha_\mathrm{X} m_\mathrm{X}}{m_\phi}, \tag{C.165}
$$

we can reduce the number of parameters from $\{g, m_\mathrm{X}, m_\phi, k\}$ to $\{a, b\}$

$$
\left[\frac{d^2}{dx^2} - \frac{\ell(\ell+1)}{x^2} - (\boldsymbol{S}_1 \cdot \hat{\boldsymbol{x}})\,(\boldsymbol{S}_2 \cdot \hat{\boldsymbol{x}})\,U_1(x) - (\boldsymbol{S}_1 \cdot \boldsymbol{S}_2)\,U_2(x) - a \right] \begin{pmatrix} \chi_j^{(0,0)}(x) \\ \chi_j^{(1,0)}(x) \\ \chi_{j+1}^{(1,1)}(x) \\ \chi_{j-1}^{(1,-1)}(x) \end{pmatrix} = 0, \tag{C.166}
$$

with $\chi_\ell(r) = r R_\ell(r)$. The potentials $U_1(x)$ and $U_2(x)$ for the 4 models are

$$
U_1(x) = e^{-x/b}\left[3\frac{b^2}{x^3} + 3\frac{b}{x^2} + \frac{1}{x} \right], \qquad U_2(x) = -e^{-x/b} \begin{cases} \frac{b^2}{x^3} + \frac{b}{x^2} & \text{(PS)}, \\ \frac{b^2}{x^3} + \frac{b}{x^2} + \frac{1}{x} & \text{(AV)}, \\ \frac{b^2}{x^3} + \frac{b}{x^2} + \frac{1}{x} & \text{(MDM)}, \\ \frac{b^2}{x^3} + \frac{b}{x^2} & \text{(EDM)}. \end{cases} \tag{C.167}
$$

C.2.1 Spin conserving scattering ($s_z = 0$)

If the z-component of the spin of the two particle system vanishes, $s_z = 0$, the orbital angular momentum and the total angular momentum are equal, $\ell = j$. For each orbital angular momentum ℓ, the asymptotic radial wave function $\chi_\ell^{(s,0)}(x)$ far away from the origin of the scattering potential can be decomposed into spherical Bessel functions as

$$\lim_{x\to\infty} \chi_\ell^{(s,0)}(x) = A_\ell \left[j_\ell(ax) - n_\ell(ax)\, \kappa_\ell^{(s,0)}(a) \right] ax \ , \qquad \kappa_\ell^{(s,0)}(a) = \tan \delta_\ell^{(s,0)}(a), \tag{C.168}$$

where j_ℓ and n_ℓ are the spherical Bessel functions of the first and second kind and A_ℓ is the normalization which can be chosen arbitrarily for our purposes. $\kappa_\ell^{(s,0)}(a)$ is the reaction function which we can identify as the tangent of the phase shift $\delta_\ell^{s,0}$. It can be obtained numerically by matching the numerical solution of the wave function to the analytical expression (C.168) at sufficiently large $x = x_m$ (for details see Sec. C.4). The phase shift is then

$$\tan \delta_\ell^{s,0} = \frac{ax_m\, j'_\ell(ax_m) - \beta_\ell^{s,0}\, j_\ell(ax_m)}{ax_m\, n'_\ell(ax_m) - \beta_\ell^{s,0}\, n_\ell(ax_m)} \ , \quad \beta_\ell^{s,0} = \frac{x_m \left[\chi_\ell^{s,0}(x_m) \right]'}{\chi_\ell^{s,0}(x_m)} - 1 \, . \tag{C.169}$$

The differential cross section for a given channel is given by

$$\frac{d\sigma^{s,0}}{d\Omega} = \frac{1}{k^2} \left| \sum_{\ell=0}^{\infty} (2\ell+1) P_\ell(\cos\theta)\, e^{i\delta_\ell^{s,0}} \sin \delta_\ell^{s,0} \right|^2 . \tag{C.170}$$

To obtain the total differential cross section, we have to average over the initial states

$$\frac{d\sigma}{d\Omega} = \frac{1}{2} \sum_{s=0}^{1} \frac{d\sigma^{s,0}}{d\Omega}. \tag{C.171}$$

We can use orthogonality properties of the Legendre polynomials

$$\int_{-1}^{1} dx\, P_\ell(x) P_m(x) = \frac{2}{2\ell+1} \delta_{\ell,m} \, , \tag{C.172}$$

$$\int_{-1}^{1} dx\, (1-x) P_\ell(x) P_m(x) = \frac{2}{2\ell+1} \left[\delta_{\ell,m} - \frac{\ell+1}{2\ell+3} \delta_{\ell,m-1} - \frac{\ell}{2\ell-1} \delta_{\ell,m+1} \right] , \tag{C.173}$$

$$\begin{aligned} \int_{-1}^{1} dx\, (1-x^2) P_\ell(x) P_m(x) = \frac{2}{2\ell+1} \Bigg[& \left(1 - \frac{1-2\ell(\ell+1)}{3-4\ell(\ell+1)} \right) \delta_{\ell,m} - \frac{\ell+1}{2\ell+3} \frac{\ell+2}{2\ell+5} \delta_{\ell,m-1} \\ & - \frac{\ell}{2\ell-1} \frac{\ell-1}{2\ell-3} \delta_{\ell,m+1} \Bigg] , \end{aligned} \tag{C.174}$$

From Eqns. (C.170)–(C.174) it follows that

$$\sigma_{s_z=0} = \frac{4\pi}{k^2} \left(\frac{1}{2} \sum_{s=0}^{1} \right) \sum_{\ell=0}^{\infty} (2\ell+1) \sin^2(\delta_\ell^{s,0}) \, , \tag{C.175}$$

$$\sigma_T^{s_z=0} = \frac{4\pi}{k^2} \left(\frac{1}{2} \sum_{s=0}^{1} \right) \sum_{\ell=0}^{\infty} (\ell+1) \sin^2(\delta_{\ell+1}^{s,0} - \delta_\ell^{s,0}) \, , \tag{C.176}$$

$$\sigma_V^{s_z=0} = \frac{4\pi}{k^2} \left(\frac{1}{2} \sum_{s=0}^{1} \right) \sum_{\ell=0}^{\infty} \frac{(\ell+1)(\ell+2)}{2\ell+3} \sin^2(\delta_{\ell+2}^{s,0} - \delta_\ell^{s,0}) \, . \tag{C.177}$$

C.2.2 Spin changing scattering ($s_z = \pm 1$)

Since the scattering potential matrix is not diagonal for $s_z = \pm 1$, for a pure incoming state $|1, j+1, j, j_z\rangle$ the outgoing state will be a superposition of $|1, j+1, j, j_z\rangle$ and $|1, j-1, j, j_z\rangle$. Therefore, we promote the scattering solution to a matrix

$$\lim_{x\to\infty} \mathbb{F}_j = \mathbb{J}_j(kx) - \mathbb{N}_j(kx)\mathbb{K}_j \ , \tag{C.178}$$

where $\mathbb{K}_j$ is the reaction matrix for a fixed total angular momentum j, i.e.

$$\mathbb{K}_j = \begin{pmatrix} \kappa_{\ell=j+1}^{\uparrow\uparrow\to\uparrow\uparrow} & \kappa_{\ell=j+1}^{\downarrow\downarrow\to\uparrow\uparrow} \\ \kappa_{\ell=j-1}^{\uparrow\uparrow\to\downarrow\downarrow} & \kappa_{\ell=j+1}^{\downarrow\downarrow\to\downarrow\downarrow} \end{pmatrix} , \tag{C.179}$$

where the ℓ denotes the orbital angular momentum of the final state and the subscript depicts the spins of the initial and final states with $\uparrow\uparrow$ representing $s_z = 1$ and $\downarrow\downarrow$ representing $s_z = -1$. The diagonal elements of $\mathbb{K}_j$ can be interpreted as the tangent of the phase shift as in Sec. C.2.1. The off-diagonal elements describe scattering events where the initial spin is not equal to the final spin. Therefore, the outgoing wave function is not just equal to the phase shifted ingoing wave function. $\mathbb{J}_j(kx)$ and $\mathbb{N}_j(kx)$ are diagonal matrices

$$\mathbb{J}_j(kx) = \begin{pmatrix} kx\, j_{j+1}(kx) & 0 \\ 0 & kx\, j_{j-1}(kx) \end{pmatrix} , \qquad \mathbb{N}_j(kx) = \begin{pmatrix} kx\, n_{j+1}(kx) & 0 \\ 0 & kx\, n_{j-1}(kx) \end{pmatrix} . \tag{C.180}$$

By inverting Eq. (C.178), we find

$$\mathbb{K}_j = \left[\mathbb{Y}_j(x)\mathbb{N}_j(kx) - \mathbb{N}_j'(kx)\right]^{-1} \left[\mathbb{Y}_j(x)\mathbb{J}_j(kx) - \mathbb{J}_j'(kx)\right] \ , \qquad \mathbb{Y}_l(x) = \mathbb{F}_j'(x) \left[\mathbb{F}_j(x)\right]^{-1} \ , \tag{C.181}$$

where the primes denote derivatives with respect to x. We define the scattering S-matrix and amplitude for a given total angular momentum j as

$$\mathbb{S}_j = (\mathbb{1} - i\mathbb{K}_j)^{-1}(\mathbb{1} + i\mathbb{K}_j) \, , \tag{C.182}$$

$$\mathbb{T}_j = \mathbb{1} - \mathbb{S}_j \, . \tag{C.183}$$

The total cross section for the scattering of a given initial state $|1, \ell, j, j_z\rangle$ into the same or another final state $|1, \ell', j, j_z\rangle$ is given by the absolute square of the corresponding component of

$$\mathbb{T}_j = \begin{pmatrix} T_j^{\uparrow\uparrow\to\uparrow\uparrow} & T_j^{\downarrow\downarrow\to\uparrow\uparrow} \\ T_j^{\uparrow\uparrow\to\downarrow\downarrow} & T_j^{\downarrow\downarrow\to\downarrow\downarrow} \end{pmatrix} , \quad \text{i.e.,} \tag{C.184}$$

$$\begin{pmatrix} \sigma_j^{\uparrow\uparrow\to\uparrow\uparrow} & \sigma_j^{\downarrow\downarrow\to\uparrow\uparrow} \\ \sigma_j^{\uparrow\uparrow\to\downarrow\downarrow} & \sigma_j^{\downarrow\downarrow\to\downarrow\downarrow} \end{pmatrix} = \frac{4\pi}{k^2} \begin{pmatrix} (2j+3)\left|T_j^{\uparrow\uparrow\to\uparrow\uparrow}\right|^2 & (2j+3)\left|T_j^{\downarrow\downarrow\to\uparrow\uparrow}\right|^2 \\ (2j-1)\left|T_j^{\uparrow\uparrow\to\downarrow\downarrow}\right|^2 & (2j-1)\left|T_j^{\downarrow\downarrow\to\downarrow\downarrow}\right|^2 \end{pmatrix} . \tag{C.185}$$

The total cross section averaged over initial spins is

$$\sigma_{s_z=\pm 1} = \frac{4\pi}{k^2}\frac{1}{2}\sum_{j=1}^{\infty}\left[(2j+3)\left(\left|T_j^{\uparrow\uparrow\to\uparrow\uparrow}\right|^2 + \left|T_j^{\downarrow\downarrow\to\uparrow\uparrow}\right|^2\right) + (2j-1)\left(\left|T_j^{\uparrow\uparrow\to\downarrow\downarrow}\right|^2 + \left|T_j^{\downarrow\downarrow\to\downarrow\downarrow}\right|^2\right)\right] . \tag{C.186}$$

For the total cross section including all possible spin states, we have to sum (C.175) and (C.186) and average over the initial spins, i.e.

$$\sigma = \frac{1}{2}\left(\sigma_{s_z=0} + \sigma_{s_z=\pm 1}\right) \tag{C.187}$$

$$= \frac{4\pi}{k^2}\frac{1}{4}\sum_{j=1}^{\infty}\left[(2j+3)\left(\left|T_j^{\uparrow\uparrow\to\uparrow\uparrow}\right|^2 + \left|T_j^{\downarrow\downarrow\to\uparrow\uparrow}\right|^2\right) + (2j+1)\sum_{s=0}^{1}\left|T_j^{(s,0)}\right|^2 + (2j-1)\left(\left|T_j^{\uparrow\uparrow\to\downarrow\downarrow}\right|^2 + \left|T_j^{\downarrow\downarrow\to\downarrow\downarrow}\right|^2\right)\right]. \tag{C.188}$$

C.3 Treatment of Singular Potentials

The potentials introduced in Sec. C.1 fall into the class of singular potentials. They contain terms proportional to r^{-n} with $n \geq 2$ meaning that the potential is comparable or dominating with respect to the centrifugal barrier. As a consequence the eigenvalues are not bounded from below, i.e. there is an infinite number of bound states with ever decreasing energy; this is clearly unphysical. For scattering problems, i.e. transitions between positive energy states, this issue can be ignored at first sight but the problem here is that the wavelength of the wave function $\lambda \to 0$ as $r \to 0$, making it impossible to specify boundary conditions at the origin.

However, since small distances, can only be probed with sufficiently high energies, it is suggestive to assume that the shape of the potential only holds down to distances $r = r_c$ where UV physics takes over and the theory breaks down. For non-singular potentials, the set of solutions to the potential is independent of the exact nature of the UV physics and of the energy at which the effective theory breaks down. For singular potentials, however, this is no longer true [156]. The solutions will sensitively depend on the cutoff r_c, i.e., on the short range physics. Therefore, we have to renormalize the potential in a way that low energy observables—like the phase shift or cross section—will be invariant under small changes in r_c and the shape of the potential for $r < r_c$ [157, 158].

The potentials we discuss have two terms that have to be taken care of, the singular terms proportional to r^{-n} with $n \geq 2$ and the delta function at the origin $\delta^{(3)}(\mathbf{r})$. In the following, we outline on how to treat them consistently.

The most singular term in the potentials above, is the term proportional to r^{-3}, i.e.

$$\mathcal{V}(r) = r_0^2\frac{e^{-m_\phi r}}{r^3}, \qquad r_0 = \frac{\sqrt{\alpha_{\mathrm{X}}}}{m_\phi}, \tag{C.189}$$

for which we rewrite the couplings defined in the Lagrangians (C.147) in terms of α_{X} in the following way

$$\alpha_{\mathrm{X}} \equiv \left\{\frac{m_\phi^2}{m_{\mathrm{X}}^2}\frac{g_{\mathrm{PS}}^2}{4\pi}, \quad \frac{g_{\mathrm{AV}}^2}{\pi}, \quad \frac{m_\phi^2\mu_{\mathrm{X}}^2}{\pi}, \quad \frac{m_\phi^2 d_{\mathrm{X}}^2}{\pi}\right\}. \tag{C.190}$$

The singular potential $\mathcal{V}(r)$ has to be regulated at a short distances $r < r_c$ and augmented with a series of local operators that parametrize the unknown UV physics [157],

$$\mathcal{V}_{\rm reg}(r) = \mathcal{V}(x)\,\theta(r - r_c) + \mathcal{V}_0\,\theta(r_c - r). \tag{C.191}$$

The short-distance part $\mathcal{V}_0$ of this effective potential is a derivative expansion that can be truncated to the desired order as long as the typical momenta q are much smaller than the cutoff scale. Following [157], we regulate the potential at r_c with a square well of height $\mathcal{V}_0$ encoding the UV data of the relativistic completion. After a functional relation $\mathcal{V}_0(r_c)$ is found through matching to a known observable at an energy scale $\Lambda \ll 1/r_c$, the problem is considered correctly renormalized and $\mathcal{V}_0(r_c)$ is assumed to hold energies smaller then Λ.

Numerically, the delta function can rather easily be taken into account by modelling it as a broadened delta, i.e.

$$\delta^3(\boldsymbol{r}) \to \frac{e^{-r^2/2r_\delta^2}}{(2\pi)^{3/2} r_\delta^3}\,, \tag{C.192}$$

with $r_\delta < r_c$. However, since the renormalization scheme is constructed in a way that the low energy observables are only a function of the cutoff scale r_c and the height of the cutoff $\mathcal{V}_0$ [157–159], it is not necessary to include the delta function. We model the short range part of the potential by a square well of width r_c and the problem is considered correctly renormalized once we are able to vary the width and depth of the short range potential simultaneously in such a way as to keep the phase shifts invariant.

C.4 Numerical treatment

To solve the Schrödinger equation numerically, we adopt the method of Refs. [104, 160]. We work in the $|s, l, j, j_z\rangle$ basis, and only consider scattering processes where the incoming and outgoing states have the same kinetic energy. We impose initial conditions for

$$\boldsymbol{\chi}_j(x) = \begin{pmatrix} \chi_j^{(0,0)}(x) \\ \chi_j^{(1,0)}(x) \\ \chi_{j+1}^{(1,1)}(x) \\ \chi_{j-1}^{(1,-1)}(x) \end{pmatrix}, \tag{C.193}$$

and $\boldsymbol{\chi}_j'(x)$ for a given total angular momentum number j at a point $x = x_i$ close to the origin. For $x_i \ll \min\{b, (\ell+1)/a\}$, the effective potential is dominated by the angular momentum term since we regularize the singular terms of the potential, and we expect $\chi_\ell(x) \propto x^{\ell+1}$. Thus, we take $\chi_\ell^{(s,s_z)}(x_i) = x_i/(\ell+1)$ and $[\chi_\ell^{(s,s_z)}(x_i)]' = 1$; the overall normalization is irrelevant. Note that the orbital angular momentum number is not the same for all components of $\boldsymbol{\chi}_j(x)$, so the initial conditions will also differ.

Our numerical solver finds the solution $\boldsymbol{\chi}_j(x)$ and its derivative at a sufficiently large value x_f. We set the initial wave function to have a distinctive spin s and s_z, implying a distinctive orbital angular momentum ℓ. Since these quantum numbers are not conserved by the potential (C.161), the final state can theoretically be a linear combination of 4 possible initial states

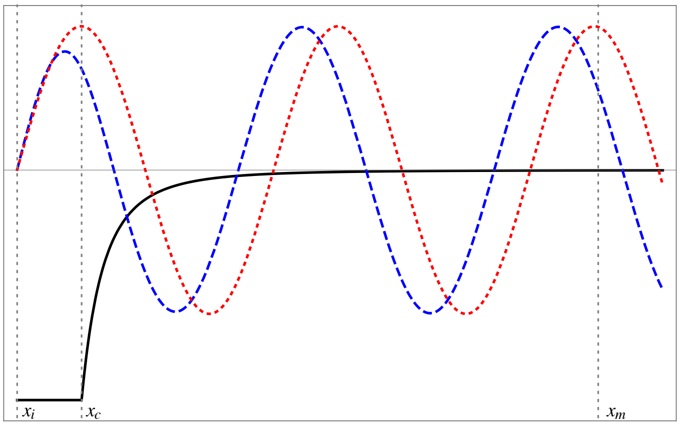

Figure C.2: Numerical treatment of scattering problem for $\ell = 0$ for a scattering potential $X(x) \propto 1/x^3$: The scattering potential, which is cut off at $x = x_c$ is shown in black, the radial scattering wave function in dashed blue and the asymptotic wave function at large x in dotted red. The Schrödinger equation is solved starting at x_i and matched to the asymptotic solution for the calculation of the phase shift at x_m.

(singlet and triplet) We assign the solutions as the row vectors of a 4×4 solution matrix $\mathbb{F}_j$, and we order them such that $\mathbb{F}_j(x_i) = \mathrm{diag}[\boldsymbol{\chi}_j(x_i)]$ is diagonal at the origin where the angular momentum term dominates, and the analytic form of the wave function is known. As the numerical solver evolves to $x > x_i$, off-diagonal terms in $\mathbb{F}_j(x)$ appear, indicating that scattering into other spin states has occurred.

We start out by cutting off the singular parts of the potential at $x_c \ll \min\{b, (\ell{+}1)/a\}$, choose $x_i \ll x_c$ where the angular momentum term dominates and solve Eq. (C.166) numerically within the domain $x_i \leq x \leq x_m$ (as depicted in Fig. C.2). The matching point x_m is determined by the condition $a^2 \gg \exp(-x_m/b)/x_m$, where the potential term is suppressed compared to the kinetic term. At $x = x_m$, we match χ_ℓ (and its first derivative) onto the asymptotic solution, given by Eq. (C.178). Our numerical method makes an initial guess for $\{x_i, x_c, x_m\}$ and computes δ_ℓ, and then successively decreases (increases) x_i (x_m) by 10% (1%) until all phase shifts have converged to 1%. The last step is computing the total cross section σ by summing over all j and averaging over the spins as in Eq. (C.187), truncating at $j_{\max}$ with the requirement that σ converges to 1%.

With the above procedure, we calculate the cross section numerically in the Born regime and vary $\mathcal{V}_0$ for various values of x_c to match the obtained cross section to the Born cross section which we know analytically. This way, we obtain a functional relation $\mathcal{V}_0(x_c)$ for a given a and b. This functional dependence is the renormalization condition for a given potential and should also hold for smaller energies, i.e. smaller a. This way, we can match for a given $a \gg 1$ and b, use the obtained $\mathcal{V}_0(x_c)$ to calculate the cross section for $a \lesssim 1$ and repeat for different values of b to scan the whole parameter space of a and b.

C.5 Numerical difficulties and solution by Agrawal, Parikh and Reece

One caveat in the numerical treatment described above is that one uses the same cutoff and renormalized potential for all partial waves. This makes the matching procedure numerically very expensive since we have to sum up all partial waves to find the numerical cross section to match to the Born result. In addition, the matching has to be done for $a \gg 1$ where the potential is effectively long range and many partial waves have to be summed up. Therefore, we ran into numerical problems where phase shifts and cross sections did not converge which we attributed to the fact that errors in the phase shift accumulate if one has to solve the Schrödinger equation out to very large r and that for large ℓ the numerical values of the wave functions became very large due to the way we normalized them leading to precision loss in Eq. (C.169).

Ref. [147] evaded having to sum many partial waves during the matching by calculating the phase shift induced on the wave function at small $r < m_X^{-1}$ in the Born approximation and using the phase shift obtained this way to set the boundary condition for each partial wave. This way, they found a numerically stable procedure to renormalize each partial wave and only have to sum them up in the end to calculate the cross section.

Bibliography

[1] X. Chu, J. Pradler, and L. Semmelrock, *Light dark states with electromagnetic form factors*. Phys. Rev. **D99** (2019) no. 1, 015040, `arXiv:1811.04095 [hep-ph]`.

[2] X. Chu, J.-L. Kuo, J. Pradler, and L. Semmelrock, *Stellar probes of dark sector-photon interactions*. Phys. Rev. **D100** (2019) no. 8, 083002, `arXiv:1908.00553 [hep-ph]`.

[3] J. Pradler and L. Semmelrock, *Exact Theory of Non-relativistic Electron-Electron Bremsstrahlung*. `arXiv:2007.06592 [hep-ph]`.

[4] **Planck** Collaboration, N. Aghanim *et al.*, *Planck 2018 results. VI. Cosmological parameters*. `arXiv:1807.06209 [astro-ph.CO]`.

[5] **Muon g-2** Collaboration, G. W. Bennett *et al.*, *Final Report of the Muon E821 Anomalous Magnetic Moment Measurement at BNL*. Phys. Rev. **D73** (2006) 072003, `arXiv:hep-ex/0602035 [hep-ex]`.

[6] F. Jegerlehner and A. Nyffeler, *The Muon g-2*. Phys. Rept. **477** (2009) 1–110, `arXiv:0902.3360 [hep-ph]`.

[7] M. Davier, A. Hoecker, B. Malaescu, and Z. Zhang, *Reevaluation of the Hadronic Contributions to the Muon g-2 and to alpha(MZ)*. Eur. Phys. J. **C71** (2011) 1515, `arXiv:1010.4180 [hep-ph]`. [Erratum: Eur. Phys. J.C72,1874(2012)].

[8] A. Keshavarzi, D. Nomura, and T. Teubner, *Muon $g-2$ and $\alpha(M_Z^2)$: a new data-based analysis*. Phys. Rev. **D97** (2018) no. 11, 114025, `arXiv:1802.02995 [hep-ph]`.

[9] R. Pohl *et al.*, *The size of the proton*. Nature **466** (2010) 213–216.

[10] I. Sick and D. Trautmann, *Proton root-mean-square radii and electron scattering*. Phys. Rev. **C89** (2014) no. 1, 012201, `arXiv:1407.1676 [nucl-ex]`.

[11] C. E. Carlson, *The Proton Radius Puzzle*. Prog. Part. Nucl. Phys. **82** (2015) 59–77, `arXiv:1502.05314 [hep-ph]`.

[12] J.-P. Karr and D. Marchand, *Progress on the proton-radius puzzle*. Nature **575** (2019) no. 7781, 61–62.

[13] **BaBar** Collaboration, J. P. Lees *et al.*, *Evidence for an excess of $\bar{B} \to D^{(*)}\tau^-\bar{\nu}_\tau$ decays*. Phys. Rev. Lett. **109** (2012) 101802, `arXiv:1205.5442 [hep-ex]`.

[14] **LHCb** Collaboration, R. Aaij *et al.*, *Measurement of the ratio of branching fractions $\mathcal{B}(\bar{B}^0 \to D^{*+}\tau^-\bar{\nu}_\tau)/\mathcal{B}(\bar{B}^0 \to D^{*+}\mu^-\bar{\nu}_\mu)$*. Phys. Rev. Lett. **115** (2015) no. 11, 111803, `arXiv:1506.08614 [hep-ex]`. [Erratum: Phys. Rev. Lett.115,no.15,159901(2015)].

[15] B. Capdevila, A. Crivellin, S. Descotes-Genon, J. Matias, and J. Virto, *Patterns of New Physics in $b \to s\ell^+\ell^-$ transitions in the light of recent data*. JHEP **01** (2018) 093, arXiv:1704.05340 [hep-ph].

[16] **Planck** Collaboration, N. Aghanim *et al.*, *Planck 2015 results. XI. CMB power spectra, likelihoods, and robustness of parameters*. Astron. Astrophys. **594** (2016) A11, arXiv:1507.02704 [astro-ph.CO].

[17] A. G. Riess, S. Casertano, W. Yuan, L. M. Macri, and D. Scolnic, *Large Magellanic Cloud Cepheid Standards Provide a 1% Foundation for the Determination of the Hubble Constant and Stronger Evidence for Physics beyond ΛCDM*. Astrophys. J. **876** (2019) no. 1, 85, arXiv:1903.07603 [astro-ph.CO].

[18] G. C. F. Chen *et al.*, *A SHARP view of H0LiCOW: H_0 from three time-delay gravitational lens systems with adaptive optics imaging*. Mon. Not. Roy. Astron. Soc. **490** (2019) no. 2, 1743–1773, arXiv:1907.02533 [astro-ph.CO].

[19] W. L. Freedman *et al.*, *The Carnegie-Chicago Hubble Program. VIII. An Independent Determination of the Hubble Constant Based on the Tip of the Red Giant Branch*. arXiv:1907.05922 [astro-ph.CO].

[20] V. Bonvin *et al.*, *H0LiCOW - V. New COSMOGRAIL time delays of HE 0435-1223: H_0 to 3.8 per cent precision from strong lensing in a flat ΛCDM model*. Mon. Not. Roy. Astron. Soc. **465** (2017) no. 4, 4914–4930, arXiv:1607.01790 [astro-ph.CO].

[21] S. Birrer *et al.*, *H0LiCOW - IX. Cosmographic analysis of the doubly imaged quasar SDSS 1206+4332 and a new measurement of the Hubble constant*. Mon. Not. Roy. Astron. Soc. **484** (2019) 4726, arXiv:1809.01274 [astro-ph.CO].

[22] A. Del Popolo and M. Le Delliou, *Small scale problems of the ΛCDM model: a short review*. Galaxies **5** (2017) no. 1, 17, arXiv:1606.07790 [astro-ph.CO].

[23] J. S. Bullock and M. Boylan-Kolchin, *Small-Scale Challenges to the ΛCDM Paradigm*. Ann. Rev. Astron. Astrophys. **55** (2017) 343–387, arXiv:1707.04256 [astro-ph.CO].

[24] E. Di Valentino, A. Melchiorri, and J. Silk, *Planck evidence for a closed Universe and a possible crisis for cosmology*. Nat. Astron. **4** (2019) no. 2, 196–203, arXiv:1911.02087 [astro-ph.CO].

[25] **Supernova Search Team** Collaboration, A. G. Riess *et al.*, *Observational evidence from supernovae for an accelerating universe and a cosmological constant*. Astron. J. **116** (1998) 1009–1038, arXiv:astro-ph/9805201 [astro-ph].

[26] A. G. Riess *et al.*, *A 2.4% Determination of the Local Value of the Hubble Constant*. Astrophys. J. **826** (2016) no. 1, 56, arXiv:1604.01424 [astro-ph.CO].

[27] A. G. Riess *et al.*, *Milky Way Cepheid Standards for Measuring Cosmic Distances and Application to Gaia DR2: Implications for the Hubble Constant*. Astrophys. J. **861** (2018) no. 2, 126, arXiv:1804.10655 [astro-ph.CO].

[28] K. Hotokezaka, E. Nakar, O. Gottlieb, S. Nissanke, K. Masuda, G. Hallinan, K. P. Mooley, and A. Deller, *A Hubble constant measurement from superluminal motion of the jet in GW170817*. Nat. Astron. **3** (2019) no. 10, 940–944, `arXiv:1806.10596 [astro-ph.CO]`.

[29] M. J. Mortonson, D. H. Weinberg, and M. White, *Dark Energy: A Short Review*. `arXiv:1401.0046 [astro-ph.CO]`.

[30] W. L. Freedman, *Cosmology at a Crossroads*. Nat. Astron. **1** (2017) 0121, `arXiv:1706.02739 [astro-ph.CO]`.

[31] S. M. Feeney, D. J. Mortlock, and N. Dalmasso, *Clarifying the Hubble constant tension with a Bayesian hierarchical model of the local distance ladder*. Mon. Not. Roy. Astron. Soc. **476** (2018) no. 3, 3861–3882, `arXiv:1707.00007 [astro-ph.CO]`.

[32] E. Di Valentino, A. Melchiorri, and J. Silk, *Reconciling Planck with the local value of H_0 in extended parameter space*. Phys. Lett. **B761** (2016) 242–246, `arXiv:1606.00634 [astro-ph.CO]`.

[33] E. Di Valentino, A. Melchiorri, E. V. Linder, and J. Silk, *Constraining Dark Energy Dynamics in Extended Parameter Space*. Phys. Rev. **D96** (2017) no. 2, 023523, `arXiv:1704.00762 [astro-ph.CO]`.

[34] E. Di Valentino, E. V. Linder, and A. Melchiorri, *Vacuum phase transition solves the H_0 tension*. Phys. Rev. **D97** (2018) no. 4, 043528, `arXiv:1710.02153 [astro-ph.CO]`.

[35] S. Kumar and R. C. Nunes, *Probing the interaction between dark matter and dark energy in the presence of massive neutrinos*. Phys. Rev. **D94** (2016) no. 12, 123511, `arXiv:1608.02454 [astro-ph.CO]`.

[36] T. Karwal and M. Kamionkowski, *Dark energy at early times, the Hubble parameter, and the string axiverse*. Phys. Rev. **D94** (2016) no. 10, 103523, `arXiv:1608.01309 [astro-ph.CO]`.

[37] E. Mörtsell and S. Dhawan, *Does the Hubble constant tension call for new physics?* JCAP **1809** (2018) no. 09, 025, `arXiv:1801.07260 [astro-ph.CO]`.

[38] V. Poulin, T. L. Smith, T. Karwal, and M. Kamionkowski, *Early Dark Energy Can Resolve The Hubble Tension*. Phys. Rev. Lett. **122** (2019) no. 22, 221301, `arXiv:1811.04083 [astro-ph.CO]`.

[39] J. Colin, R. Mohayaee, M. Rameez, and S. Sarkar, *Evidence for anisotropy of cosmic acceleration*. Astron. Astrophys. **631** (2019) L13, `arXiv:1808.04597 [astro-ph.CO]`.

[40] P. Peebles and B. Ratra, *The Cosmological Constant and Dark Energy*. Rev. Mod. Phys. **75** (2003) 559–606, `arXiv:astro-ph/0207347`.

[41] J. de Swart, G. Bertone, and J. van Dongen, *How Dark Matter Came to Matter*. `arXiv:1703.00013 [astro-ph.CO]`. [Nature Astron.1,0059(2017)].

[42] F. Zwicky, *Die Rotverschiebung von extragalaktischen Nebeln.* Helv. Phys. Acta **6** (1933) 110–127. [Gen. Rel. Grav.41,207(2009)].

[43] S. Smith, *The Mass of the Virgo Cluster.* Astrophys. J. **83** (1936) 23–30.

[44] E. Holmberg, *A Study of Double and Multiple Galaxies Together with Inquiries into some General Metagalactic Problems*Annals of the Observatory of Lund **6** (Jan., 1937) 1–173.

[45] F. Zwicky, *On the Masses of Nebulae and of Clusters of Nebulae.* Astrophys. J. **86** (1937) 217–246.

[46] K. C. Freeman, *On the disks of spiral and SO Galaxies.* Astrophys. J. **160** (1970) 811.

[47] V. C. Rubin and W. K. Ford, Jr., *Rotation of the Andromeda Nebula from a Spectroscopic Survey of Emission Regions.* Astrophys. J. **159** (1970) 379–403.

[48] J. P. Ostriker, P. J. E. Peebles, and A. Yahil, *The size and mass of galaxies, and the mass of the universe.* Astrophys. J. **193** (1974) L1–L4.

[49] J. Einasto, A. Kaasik, and E. Saar, *Dynamic evidence on massive coronas of galaxies.* Nature (London), v. 250, no. 5464, pp. 309-310 .

[50] A. A. Penzias and R. W. Wilson, *A Measurement of excess antenna temperature at 4080-Mc/s.* Astrophys. J. **142** (1965) 419–421.

[51] **WMAP** Collaboration, C. Bennett *et al.*, *The Microwave Anisotropy Probe (MAP) mission.* Astrophys. J. **583** (2003) 1–23, `arXiv:astro-ph/0301158`.

[52] **Planck** Collaboration, *The Scientific programme of Planck.* `arXiv:astro-ph/0604069`.

[53] K. Garrett and G. Duda, *Dark Matter: A Primer.* Adv. Astron. **2011** (2011) 968283, `arXiv:1006.2483 [hep-ph]`.

[54] R. Massey, T. Kitching, and J. Richard, *The dark matter of gravitational lensing.* Rept. Prog. Phys. **73** (2010) 086901, `arXiv:1001.1739 [astro-ph.CO]`.

[55] D. Clowe, A. Gonzalez, and M. Markevitch, *Weak lensing mass reconstruction of the interacting cluster 1E0657-558: Direct evidence for the existence of dark matter.* Astrophys. J. **604** (2004) 596–603, `arXiv:astro-ph/0312273`.

[56] D. Clowe, M. Bradac, A. H. Gonzalez, M. Markevitch, S. W. Randall, C. Jones, and D. Zaritsky, *A direct empirical proof of the existence of dark matter.* Astrophys. J. Lett. **648** (2006) L109–L113, `arXiv:astro-ph/0608407`.

[57] E. Bertschinger and J. M. Gelb, *Cosmological N-Body Simulations.* Computers in Physics **5** (1991) no. 2, 164. `https://doi.org/10.1063/1.4822978`.

[58] V. Springel, S. D. M. White, A. Jenkins, C. S. Frenk, N. Yoshida, L. Gao, J. Navarro, R. Thacker, D. Croton, J. Helly, J. A. Peacock, S. Cole, P. Thomas, H. Couchman, A. Evrard, J. Colberg, and F. Pearce, *Simulations of the formation, evolution and clustering of galaxies and quasars*Nature **435** (June, 2005) 629–636. `https://doi.org/10.1038/nature03597`.

[59] M. Boylan-Kolchin, V. Springel, S. D. M. White, A. Jenkins, and G. Lemson, *Resolving cosmic structure formation with the Millennium-II Simulation*Monthly Notices of the Royal Astronomical Society **398** (Sept., 2009) 1150–1164. https://doi.org/10.1111/j.1365-2966.2009.15191.x.

[60] R. E. Angulo, V. Springel, S. D. M. White, A. Jenkins, C. M. Baugh, and C. S. Frenk, *Scaling relations for galaxy clusters in the Millennium-XXL simulation*Monthly Notices of the Royal Astronomical Society **426** (Oct., 2012) 2046–2062. https://doi.org/10.1111/j.1365-2966.2012.21830.x.

[61] M. Vogelsberger, S. Genel, V. Springel, P. Torrey, D. Sijacki, D. Xu, G. F. Snyder, D. Nelson, and L. Hernquist, *Introducing the Illustris Project: Simulating the coevolution of dark and visible matter in the Universe*. Mon. Not. Roy. Astron. Soc. **444** (2014) no. 2, 1518–1547, arXiv:1405.2921 [astro-ph.CO].

[62] M. Vogelsberger, S. Genel, V. Springel, P. Torrey, D. Sijacki, D. Xu, G. F. Snyder, S. Bird, D. Nelson, and L. Hernquist, *Properties of galaxies reproduced by a hydrodynamic simulation*. Nature **509** (2014) 177–182, arXiv:1405.1418 [astro-ph.CO].

[63] R. Weinberger, V. Springel, L. Hernquist, A. Pillepich, F. Marinacci, R. Pakmor, D. Nelson, S. Genel, M. Vogelsberger, J. Naiman, and P. Torrey, *Simulating galaxy formation with black hole driven thermal and kinetic feedback*Monthly Notices of the Royal Astronomical Society **465** (Nov., 2016) 3291–3308. https://doi.org/10.1093/mnras/stw2944.

[64] G. Kauffmann, S. D. M. White, and B. Guiderdoni, *The formation and evolution of galaxies within merging dark matter haloes*. Monthly Notices of the Royal Astronomical Society **264** (1993) no. 1, 201–218.

[65] A. Klypin, A. V. Kravtsov, O. Valenzuela, and F. Prada, *Where Are the Missing Galactic Satellites?* Astrophys. J. **522** (1999) no. 1, 82.

[66] B. Moore, S. Ghigna, F. Governato, G. Lake, T. Quinn, J. Stadel, and P. Tozzi, *Dark Matter Substructure within Galactic Halos*. Astrophys. J. Lett. **524** (1999) no. 1, L19.

[67] R. Cen and J. P. Ostriker, *Where are the baryons?* Astrophys. J. **514** (1999) 1–6, arXiv:astro-ph/9806281.

[68] R. Cen and J. P. Ostriker, *Where are the baryons? 2. feedback effects*. Astrophys. J. **650** (2006) 560–572, arXiv:astro-ph/0601008.

[69] M. Boylan-Kolchin, J. S. Bullock, and M. Kaplinghat, *Too big to fail? The puzzling darkness of massive Milky Way subhaloes*Monthly Notices of the Royal Astronomical Society: Letters **415** (June, 2011) L40–L44. https://doi.org/10.1111/j.1745-3933.2011.01074.x.

[70] E. Papastergis, R. Giovanelli, M. P. Haynes, and F. Shankar, *Is there a "too big to fail" problem in the field?*Astronomy & Astrophysics **574** (Feb., 2015) A113. https://doi.org/10.1051/0004-6361/201424909.

[71] W. J. G. de Blok, *The Core-Cusp Problem*. Advances in Astronomy **2010** (2010) 1–14. https://doi.org/10.1155/2010/789293.

[72] J. F. Navarro, C. S. Frenk, and S. D. White, *The Structure of cold dark matter halos*. Astrophys. J. **462** (1996) 563–575, arXiv:astro-ph/9508025.

[73] K. A. Oman *et al.*, *The unexpected diversity of dwarf galaxy rotation curves*. Mon. Not. Roy. Astron. Soc. **452** (2015) no. 4, 3650–3665, arXiv:1504.01437 [astro-ph.GA].

[74] D. N. Spergel and P. J. Steinhardt, *Observational evidence for selfinteracting cold dark matter*. Phys. Rev. Lett. **84** (2000) 3760–3763, arXiv:astro-ph/9909386.

[75] M. R. Buckley, J. Zavala, F.-Y. Cyr-Racine, K. Sigurdson, and M. Vogelsberger, *Scattering, Damping, and Acoustic Oscillations: Simulating the Structure of Dark Matter Halos with Relativistic Force Carriers*. Phys. Rev. **D90** (2014) no. 4, 043524, arXiv:1405.2075 [astro-ph.CO].

[76] M. Vogelsberger, J. Zavala, C. Simpson, and A. Jenkins, *Dwarf galaxies in CDM and SIDM with baryons: observational probes of the nature of dark matter*. Mon. Not. Roy. Astron. Soc. **444** (2014) no. 4, 3684–3698, arXiv:1405.5216 [astro-ph.CO].

[77] M. Vogelsberger, J. Zavala, F.-Y. Cyr-Racine, C. Pfrommer, T. Bringmann, and K. Sigurdson, *ETHOS – an effective theory of structure formation: dark matter physics as a possible explanation of the small-scale CDM problems*. Mon. Not. Roy. Astron. Soc. **460** (2016) no. 2, 1399–1416, arXiv:1512.05349 [astro-ph.CO].

[78] A. Kamada, M. Kaplinghat, A. B. Pace, and H.-B. Yu, *How the Self-Interacting Dark Matter Model Explains the Diverse Galactic Rotation Curves*. Phys. Rev. Lett. **119** (2017) no. 11, 111102, arXiv:1611.02716 [astro-ph.GA].

[79] **LUX** Collaboration, D. Akerib *et al.*, *The Large Underground Xenon (LUX) Experiment*. Nucl. Instrum. Meth. A **704** (2013) 111–126, arXiv:1211.3788 [physics.ins-det].

[80] **DAMA** Collaboration, R. Bernabei *et al.*, *The DAMA/LIBRA apparatus*. Nucl. Instrum. Meth. A **592** (2008) 297–315, arXiv:0804.2738 [astro-ph].

[81] G. Angloher *et al.*, *Results from 730 kg days of the CRESST-II Dark Matter Search*. Eur. Phys. J. C **72** (2012) 1971, arXiv:1109.0702 [astro-ph.CO].

[82] **SENSEI** Collaboration, M. Crisler, R. Essig, J. Estrada, G. Fernandez, J. Tiffenberg, M. Sofo haro, T. Volansky, and T.-T. Yu, *SENSEI: First Direct-Detection Constraints on sub-GeV Dark Matter from a Surface Run*. Phys. Rev. Lett. **121** (2018) no. 6, 061803, arXiv:1804.00088 [hep-ex].

[83] **SENSEI** Collaboration, O. Abramoff *et al.*, *SENSEI: Direct-Detection Constraints on Sub-GeV Dark Matter from a Shallow Underground Run Using a Prototype Skipper-CCD*. Phys. Rev. Lett. **122** (2019) no. 16, 161801, arXiv:1901.10478 [hep-ex].

[84] J. Cortina, F. Goebel, and T. Schweizer, *Technical Performance of the MAGIC Telescopes*arXiv e-prints (July, 2009) arXiv:0907.1211, `arXiv:0907.1211 [astro-ph.IM]`.

[85] **H.E.S.S.** Collaboration, J. Hinton, *The Status of the H.E.S.S. project*. New Astron. Rev. **48** (2004) 331–337, `arXiv:astro-ph/0403052`.

[86] T. Weekes *et al.*, *VERITAS: The Very energetic radiation imaging telescope array system*. Astropart. Phys. **17** (2002) 221–243, `arXiv:astro-ph/0108478`.

[87] **Fermi-LAT** Collaboration, M. Ackermann *et al.*, *The Fermi Large Area Telescope On Orbit: Event Classification, Instrument Response Functions, and Calibration*. The Astrophysical Journal Supplement Series **203** (2012) no. 1, 4. `https://doi.org/10.1088/0067-0049/203/1/4`.

[88] M. Casolino *et al.*, *Launch of the Space experiment PAMELA*. Adv. Space Res. **42** (2008) 455–466, `arXiv:0708.1808 [astro-ph]`.

[89] **AMS 02** Collaboration, R. Battiston, *The antimatter spectrometer (AMS-02): A particle physics detector in space*. Nucl. Instrum. Meth. A **588** (2008) 227–234.

[90] **BaBar** Collaboration, B. Aubert *et al.*, *The BaBar detector*. Nucl. Instrum. Meth. **A479** (2002) 1–116, `arXiv:hep-ex/0105044 [hep-ex]`.

[91] A. Abashian *et al.*, *The Belle Detector*. Nucl. Instrum. Meth. **A479** (2002) 117–232.

[92] **ATLAS** Collaboration, G. Aad *et al.*, *The ATLAS Experiment at the CERN Large Hadron Collider*. JINST **3** (2008) S08003.

[93] **CMS** Collaboration, G. L. Bayatian *et al.*, *CMS Physics: Technical Design Report Volume 1: Detector Performance and Software*.

[94] **NA64** Collaboration, D. Banerjee *et al.*, *Search for vector mediator of Dark Matter production in invisible decay mode*. `arXiv:1710.00971 [hep-ex]`.

[95] A. A. Prinz *et al.*, *Search for millicharged particles at SLAC*. Phys. Rev. Lett. **81** (1998) 1175–1178, `arXiv:hep-ex/9804008 [hep-ex]`.

[96] **COHERENT** Collaboration, D. Akimov *et al.*, *Observation of Coherent Elastic Neutrino-Nucleus Scattering*. Science **357** (2017) no. 6356, 1123–1126, `arXiv:1708.01294 [nucl-ex]`.

[97] R. Bernabei *et al.*, *Final model independent result of DAMA/LIBRA-phase1*. Eur. Phys. J. C **73** (2013) 2648, `arXiv:1308.5109 [astro-ph.GA]`.

[98] R. Bernabei *et al.*, *No role for muons in the DAMA annual modulation results*. Eur. Phys. J. C **72** (2012) 2064, `arXiv:1202.4179 [astro-ph.GA]`.

[99] **SABRE** Collaboration, M. Antonello *et al.*, *The SABRE project and the SABRE Proof-of-Principle*. Eur. Phys. J. C **79** (2019) no. 4, 363, `arXiv:1806.09340 [physics.ins-det]`.

[100] **AMS** Collaboration, M. Aguilar *et al.*, *First Result from the Alpha Magnetic Spectrometer on the International Space Station: Precision Measurement of the Positron Fraction in Primary Cosmic Rays of 0.5–350 GeV*. Phys. Rev. Lett. **110** (2013) 141102.

[101] **AMS** Collaboration, L. Accardo *et al.*, *High Statistics Measurement of the Positron Fraction in Primary Cosmic Rays of 0.5–500 GeV with the Alpha Magnetic Spectrometer on the International Space Station*. Phys. Rev. Lett. **113** (2014) 121101.

[102] **XENON** Collaboration, E. Aprile *et al.*, *Observation of Excess Electronic Recoil Events in XENON1T*. `arXiv:2006.09721 [hep-ex]`.

[103] S. Tulin and H.-B. Yu, *Dark Matter Self-interactions and Small Scale Structure*. Phys. Rept. **730** (2018) 1–57, `arXiv:1705.02358 [hep-ph]`.

[104] S. Tulin, H.-B. Yu, and K. M. Zurek, *Beyond Collisionless Dark Matter: Particle Physics Dynamics for Dark Matter Halo Structure*. Phys. Rev. D **87** (2013) no. 11, 115007, `arXiv:1302.3898 [hep-ph]`.

[105] L. G. van den Aarssen, T. Bringmann, and C. Pfrommer, *Is dark matter with long-range interactions a solution to all small-scale problems of ΛCDM cosmology?* Phys. Rev. Lett. **109** (2012) 231301, `arXiv:1205.5809 [astro-ph.CO]`.

[106] M. Markevitch, A. Gonzalez, D. Clowe, A. Vikhlinin, L. David, W. Forman, C. Jones, S. Murray, and W. Tucker, *Direct constraints on the dark matter self-interaction cross-section from the merging galaxy cluster 1E0657-56*. Astrophys. J. **606** (2004) 819–824, `arXiv:astro-ph/0309303`.

[107] J. Jaeckel, M. Lamont, and C. Vallée, *The quest for new physics with the Physics Beyond Colliders programme*. Nature Physics **16** (2020) no. 4, 393–401.

[108] **ATLAS, CMS, LHCb** Collaboration, E. Graverini, *Flavour anomalies: a review*. J. Phys. Conf. Ser. **1137** (2019) no. 1, 012025, `arXiv:1807.11373 [hep-ex]`.

[109] A. J. Krasznahorkay *et al.*, *Observation of Anomalous Internal Pair Creation in Be8 : A Possible Indication of a Light, Neutral Boson*. Phys. Rev. Lett. **116** (2016) no. 4, 042501, `arXiv:1504.01527 [nucl-ex]`.

[110] A. Krasznahorkay *et al.*, *New evidence supporting the existence of the hypothetic X17 particle*. `arXiv:1910.10459 [nucl-ex]`.

[111] J. L. Feng, B. Fornal, I. Galon, S. Gardner, J. Smolinsky, T. M. P. Tait, and P. Tanedo, *Particle physics models for the 17 MeV anomaly in beryllium nuclear decays*. Phys. Rev. D **95** (2017) no. 3, 035017, `arXiv:1608.03591 [hep-ph]`.

[112] G. Raffelt, *Stars as laboratories for fundamental physics: The astrophysics of neutrinos, axions, and other weakly interacting particles*. 5, 1996.

[113] K. Saikawa and T. T. Yanagida, *Stellar cooling anomalies and variant axion models*. JCAP **03** (2020) 007, `arXiv:1907.07662 [hep-ph]`.

[114] I. G. Irastorza and J. Redondo, *New experimental approaches in the search for axion-like particles*. Prog. Part. Nucl. Phys. **102** (2018) 89–159, `arXiv:1801.08127 [hep-ph]`.

[115] T. Aoyama *et al.*, *The anomalous magnetic moment of the muon in the Standard Model*. `arXiv:2006.04822 [hep-ph]`.

[116] **Muon g-2** Collaboration, G. Bennett *et al.*, *Measurement of the negative muon anomalous magnetic moment to 0.7 ppm*. Phys. Rev. Lett. **92** (2004) 161802, `arXiv:hep-ex/0401008`.

[117] **Muon g-2** Collaboration, J. Grange *et al.*, *Muon (g-2) Technical Design Report*. `arXiv:1501.06858 [physics.ins-det]`.

[118] **J-PARC g-'2/EDM** Collaboration, N. Saito, *A novel precision measurement of muon g-2 and EDM at J-PARC*. AIP Conf. Proc. **1467** (2012) 45–56.

[119] S. N. Gninenko and N. V. Krasnikov, *The Muon anomalous magnetic moment and a new light gauge boson*. Phys. Lett. **B513** (2001) 119, `arXiv:hep-ph/0102222 [hep-ph]`.

[120] B. Batell, N. Lange, D. McKeen, M. Pospelov, and A. Ritz, *Muon anomalous magnetic moment through the leptonic Higgs portal*. Phys. Rev. D **95** (2017) no. 7, 075003, `arXiv:1606.04943 [hep-ph]`.

[121] W. Marciano, A. Masiero, P. Paradisi, and M. Passera, *Contributions of axionlike particles to lepton dipole moments*. Phys. Rev. D **94** (2016) no. 11, 115033, `arXiv:1607.01022 [hep-ph]`.

[122] M. Bauer, M. Neubert, S. Renner, M. Schnubel, and A. Thamm, *Axion-like particles, lepton-flavor violation and a new explanation of a_μ and a_e*. Phys. Rev. Lett. **124** (2020) no. 21, 211803, `arXiv:1908.00008 [hep-ph]`.

[123] R. Essig, J. Mardon, and T. Volansky, *Direct Detection of Sub-GeV Dark Matter*. Phys. Rev. D **85** (2012) 076007, `arXiv:1108.5383 [hep-ph]`.

[124] R. Essig, A. Manalaysay, J. Mardon, P. Sorensen, and T. Volansky, *First Direct Detection Limits on sub-GeV Dark Matter from XENON10*. Phys. Rev. Lett. **109** (2012) 021301, `arXiv:1206.2644 [astro-ph.CO]`.

[125] R. Essig, T. Volansky, and T.-T. Yu, *New Constraints and Prospects for sub-GeV Dark Matter Scattering off Electrons in Xenon*. Phys. Rev. D **96** (2017) no. 4, 043017, `arXiv:1703.00910 [hep-ph]`.

[126] P. J. Fox and E. Poppitz, *Leptophilic Dark Matter*. Phys. Rev. D **79** (2009) 083528, `arXiv:0811.0399 [hep-ph]`.

[127] J. Kopp, V. Niro, T. Schwetz, and J. Zupan, *DAMA/LIBRA and leptonically interacting Dark Matter*. Phys. Rev. D **80** (2009) 083502, `arXiv:0907.3159 [hep-ph]`.

[128] J. E. Felten, R. J. Gould, W. A. Stein, and N. J. Woolf, *X-Rays from the Coma Cluster of Galaxies*The Astrophysical Journal **146** (Dec., 1966) 955. https://doi.org/10.1086/148972.

[129] J. H. Chang, D. Egana-Ugrinovic, R. Essig, and C. Kouvaris, *Structure Formation and Exotic Compact Objects in a Dissipative Dark Sector*. JCAP **03** (2019) 036, arXiv:1812.07000 [hep-ph].

[130] R. Essig, S. D. Mcdermott, H.-B. Yu, and Y.-M. Zhong, *Constraining Dissipative Dark Matter Self-Interactions*. Phys. Rev. Lett. **123** (2019) no. 12, 121102, arXiv:1809.01144 [hep-ph].

[131] J. Fan, A. Katz, L. Randall, and M. Reece, *Double-Disk Dark Matter*. Phys. Dark Univ. **2** (2013) 139–156, arXiv:1303.1521 [astro-ph.CO].

[132] J. Fan, A. Katz, and J. Shelton, *Direct and indirect detection of dissipative dark matter*. JCAP **1406** (2014) 059, arXiv:1312.1336 [hep-ph].

[133] J. Fan, A. Katz, L. Randall, and M. Reece, *Dark-Disk Universe*. Phys. Rev. Lett. **110** (2013) no. 21, 211302, arXiv:1303.3271 [hep-ph].

[134] P. Agrawal and L. Randall, *Point Sources from Dissipative Dark Matter*. JCAP **1712** (2017) no. 12, 019, arXiv:1706.04195 [hep-ph].

[135] M. R. Buckley and A. DiFranzo, *Collapsed Dark Matter Structures*. Phys. Rev. Lett. **120** (2018) no. 5, 051102, arXiv:1707.03829 [hep-ph].

[136] R. Foot, *Dissipative dark matter halos: The steady state solution*. Phys. Rev. **D97** (2018) no. 4, 043012, arXiv:1707.02528 [astro-ph.GA].

[137] R. Foot, *Galactic structure explained with dissipative mirror dark matter*. Phys. Rev. **D88** (2013) no. 2, 023520, arXiv:1304.4717 [astro-ph.CO].

[138] R. Foot and S. Vagnozzi, *Dissipative hidden sector dark matter*. Phys. Rev. **D91** (2015) 023512, arXiv:1409.7174 [hep-ph].

[139] A. Yu. Ignatiev and R. R. Volkas, *Mirror dark matter and large scale structure*. Phys. Rev. **D68** (2003) 023518, arXiv:hep-ph/0304260 [hep-ph].

[140] L. Randall and J. Scholtz, *Dissipative Dark Matter and the Andromeda Plane of Satellites*. JCAP **1509** (2015) no. 09, 057, arXiv:1412.1839 [astro-ph.GA].

[141] R. Foot, *Dissipative dark matter explains rotation curves*. Phys. Rev. **D91** (2015) no. 12, 123543, arXiv:1502.07817 [astro-ph.GA].

[142] R. Foot, *Dissipative dark matter and the rotation curves of dwarf galaxies*. JCAP **1607** (2016) no. 07, 011, arXiv:1506.01451 [astro-ph.GA].

[143] R. Foot, *A dark matter scaling relation from mirror dark matter*. Phys. Dark Univ. **5-6** (2014) 236–239, arXiv:1303.1727 [astro-ph.CO].

[144] R. Foot and S. Vagnozzi, *Solving the small-scale structure puzzles with dissipative dark matter*. JCAP **1607** (2016) no. 07, 013, arXiv:1602.02467 [astro-ph.CO].

[145] A. Das and B. Dasgupta, *New dissipation mechanisms from multilevel dark matter scattering.* Phys. Rev. **D97** (2018) no. 2, 023002, `arXiv:1709.06577 [hep-ph]`.

[146] C. Itzykson and J.-B. Zuber, *Quantum Field Theory -.* Courier Corporation, New York, 2006.

[147] P. Agrawal, A. Parikh, and M. Reece, *Systematizing the Effective Theory of Self-Interacting Dark Matter.* `arXiv:2003.00021 [hep-ph]`.

[148] V. Berestetskii, E. Lifshitz, and L. Pitaevskii, *Quantum Electrodynamics.* Course of theoretical physics. Butterworth-Heinemann, 1982.

[149] L. Landau and E. Lifshitz, *Quantum Mechanics: Non-relativistic Theory.* Butterworth-Heinemann. Butterworth-Heinemann, 1977.

[150] A. Sommerfeld and A. Maue, *Über den Bremsverlust von Kathodenstrahlen beim Auftreffen auf Atomkerne*Ann. Phys. **415** (Sept., 1935) 589–596. `https://doi.org/10.1002/andp.19354150702`.

[151] A. Nordsieck, *Reduction of an Integral in the Theory of Bremsstrahlung*Phys. Rev. **93** (Feb., 1954) 785–787. `https://doi.org/10.1103/PhysRev.93.785`.

[152] J. H. Chang, R. Essig, and A. Reinert, *Light(ly)-coupled Dark Matter in the keV Range: Freeze-In and Constraints.* `arXiv:1911.03389 [hep-ph]`.

[153] X. Chu, J.-L. Kuo, and J. Pradler, *Dark sector-photon interactions in proton-beam experiments.* `arXiv:2001.06042 [hep-ph]`.

[154] S. Weinberg, *Soft Bremsstrahlung.* Phys. Rev. D **99** (2019) no. 7, 076018, `arXiv:1903.11168 [astro-ph.GA]`.

[155] J. Kraus and W. Baltensperger, *Scattering of a dipole by a dipole.* Solid State Communications **44** (1982) no. 11, 1523 – 1528.

[156] K. M. Case, *Singular Potentials*Phys. Rev. **80** (Dec, 1950) 797–806.

[157] B. Bellazzini, M. Cliche, and P. Tanedo, *Effective theory of self-interacting dark matter.* Phys. Rev. **D88** (2013) no. 8, 083506, `arXiv:1307.1129 [hep-ph]`.

[158] S. Beane, P. F. Bedaque, L. Childress, A. Kryjevski, J. McGuire, and U. van Kolck, *Singular potentials and limit cycles.* Phys. Rev. A **64** (2001) 042103, `arXiv:quant-ph/0010073`.

[159] “, How to renormalize the Schrodinger equationt,” in *8th Jorge Andre Swieca Summer School on Nuclear Physics*, pp. 135–180. 2, 1997. `arXiv:nucl-th/9706029`.

[160] K. K. Boddy, M. Kaplinghat, A. Kwa, and A. H. G. Peter, *Hidden Sector Hydrogen as Dark Matter: Small-scale Structure Formation Predictions and the Importance of Hyperfine Interactions.* Phys. Rev. **D94** (2016) no. 12, 123017, `arXiv:1609.03592 [hep-ph]`.